CHAPTER 1

INTRODUCTION

Research programs in the new millennium are geared toward developing the technology to deploy a future fleet of "Generation IV" reactors. In the meantime, a new fleet of Generation III+ reactors will be constructed, providing the nuclear industry with a more active role in the energy sector. Life extensions of licensed reactors have become routine, and the potential for further license extension is already being discussed. The role of structural material integrity for life extensions, new reactor construction and licensing, and future reactor design is a critical component to ensuring the safety and performance of the nuclear fleet. Materials for nuclear power applications are exposed to harsh environments, combining high temperature, corrosion, cyclic loading and radiation damage. For this reason, research aimed at ensuring material integrity in these environments and developing advanced materials with improved performance is of paramount importance to the nuclear community.

Austenitic stainless steels (SS) are among the most widely used alloys for structural components in light water nuclear reactors. Iron-chromium-nickel steels were recognized for their corrosion resistance dating back to the early 1800s. However, it wasn't until the early 1900s that alloys with sufficiently low carbon content could be produced, and it was in 1915 that stainless steel became popularized [1].

Stainless steels are characterized by a minimum of 10.5 wt% Cr in order to form a passive Cr_2O_3 layer. The Fe-Cr-Ni alloys have excellent corrosion resistance due to surface passivation which protects the metal from further corrosion. Meanwhile, austenitic stainless steels also have additions of Ni to stabilize austenite with a face-centered cubic (FCC) crystal structure [2].

The two most common grades of austenitic stainless steels are the 304 and 316 grades. 316SS has excellent weldability, good machinability, reasonable high-temperature strength, resistance to chloride pitting, and high toughness even down to cryogenic temperatures. Many of the reactor vessel internal components in nuclear reactors are made of 316-type stainless steel.

Some of the early problems with 316SS came to light in the 1960s with issues of stress corrosion cracking (SCC). Intergranular SCC had been found in other high temperature aqueous environments involving stainless steels. However, the combination of high temperature, an aqueous environment and radiation appeared to increase the susceptibility to SCC and increase the rate of cracking. By the 1990s irradiation-assisted stress corrosion (IASCC) was a widely recognized problem in the industry as it affected many components, such as the reactor core shroud, baffle bolts and other important components for reactor safety and performance.

The mechanism of IASCC has been studied for many years, and there have been a great number of theories as to what causes the increased susceptibility. Although the primary mechanisms for IASCC are still being sorted out, it is known that changes to the microstructure and grain boundary microchemistry play some role. One mechanism that has long been proposed is the highly localized changes in bulk concentration, called radiation-induced segregation (RIS) that occur at grain boundaries at intermediate temperatures. These changes develop at low radiation doses of less than 1 displacement per atom (dpa) and continue until the segregation saturates after several dpa.

RIS is characterized by a decrease in Cr content at the grain boundary with a corresponding increase in Ni content. Grain boundaries were also found to usually have a decrease in Fe and a large enrichment in minor impurity atoms such as Si and P [3]. In the 1970s researchers started to investigate RIS through experimental measurements to quantify its effect. Simultaneously, computational studies explored the mechanisms which were responsible for causing the non-equilibrium grain boundary segregation. RIS was believed to cause loss of passivation at the grain boundary due to Cr depletion, and this in turn could cause crack initiation at the grain boundary that would lead to stress corrosion cracking.

Although Cr depletion often correlated well with SCC susceptibility, there was growing skepticism by the 1990s that RIS was the primary driver for IASCC susceptibility, in part because SCC was found even for low temperature irradiations where RIS would not occur because of slow point defect diffusion [4]. In 2002 Busby et al. [5] conducted post-irradiation annealing experiments to show how, even when RIS disappeared with annealing, susceptibility to IASCC remained. These experiments, far from ruling out RIS as playing a role in IASCC, at the very least identified that RIS is just one part of the complex process that occurs from radiation damage to cause stress corrosion cracking.

Soon after RIS was discovered and connected to the problems with stress corrosion cracking, work was already underway to find ways to reduce the amount of RIS that occurs due to irradiation. Mansur et al. [6] developed a computational model to assess whether or not the addition of solute impurity atoms to the stainless steel would have an effect on point defect concentrations and RIS. The authors concluded that with a sufficiently large attractive force between the solute atom and a point defect, RIS could be substantially reduced or even eliminated.

Experimental work did not start until years later, but sufficient studies have now demonstrated that oversized solute additions may be trapping vacancy defects and increasing the amount of recombination in the matrix to ultimately reduce RIS. The studies have separately examined different irradiation particle types, temperatures and oversized solute types, and many have shown a strong correlation between oversized solute addition and RIS reduction. None of the studies, however, have focused on covering a range of parameters, such as solute concentration or temperature or solute type, to prove the mechanism of how these solute additions actually affect RIS.

The objective of this work is to determine the mechanism by which oversized solute additions to austenitic stainless steels affect the radiation-induced grain boundary segregation of Cr. The second chapter of this thesis will cover the large body of background literature, both experimental and computational, for RIS, changes to irradiated microstructure, and how oversized solute additions affect these radiation-induced changes. Chapter 3 will state the objectives of the work presented here. Chapter 4 will give a detailed overview of all of the experimental procedures used in pursuing this

research. Chapter 5 will present the experimental results for RIS, loop microstructure, and oversized solute remaining in solution as a function of irradiation dose. Chapter 6 will present the modified kinetic rate-theory model developed to simulate oversized solutes and their role in reducing RIS in addition to atomistic *ab initio* simulations. Chapter 7 will discuss the experimental results and compare them with model results to demonstrate a thorough understanding of the mechanism for RIS reduction with oversized solute addition. Finally, chapter 8 will present the conclusions of this thesis.

CHAPTER 2

BACKGROUND

Irradiation can have a profound consequence on the microchemistry, microstructure and phase stability of a material. The effects are seen in composition changes at the grain boundaries, the production of dislocation loops, hardening and embrittlement, swelling from the creation of voids and He bubbles, radiation-enhance diffusion and creep, and even amorphization, and phase transformation. These changes can have an enormous impact on the integrity of nuclear reactor components because of their effect on corrosion, mechanical property degradation and irradiation-assisted stress corrosion cracking. Developing new materials to mitigate the effects of radiation and increase component or lifetimes has been a major effort in nuclear materials research.

2.1 Radiation-Induced Segregation

Radiation-induced segregation (RIS) is the non-equilibrium segregation of alloying elements near grain boundary sinks. These microchemical changes at grain boundaries and other point defect sinks are the consequence of irradiation-produced defects. This phenomenon, called radiation-induced segregation (RIS), has long been considered a primary cause of irradiation-assisted stress corrosion cracking [7, 8]. In trying to isolate the mechanisms for IASCC, however, more recent results show that RIS alone is not responsible for IASCC [5, 9, 10]. Rather RIS is more likely one part of a more complex mechanism that depends on many factors that ultimately lead to an increase in cracking susceptibility in high temperature water during exposure to radiation. This

section will explore the process of RIS and the potential mechanisms and experimental evidence for RIS.

2.1.1 Cause of RIS

Radiation-induced segregation is the result of high temperature irradiation which causes segregation of solute and impurity atoms at point defect sinks in a metal. RIS is due to a coupling of the defect fluxes with fluxes of solute atoms. When irradiation occurs, equal numbers of interstitials and vacancies are created. Those escaping recombination will diffuse to sinks that can accommodate the defects, such as grain boundaries. During the diffusion process, any coupling of a defect flux with an alloying element or impurity will cause the enrichment or depletion of that element at a sink. Once a concentration gradient exists, back diffusion of the segregating elements will work against the concentration gradient, decreasing the rate of segregation until the concentration gradient reaches some maximum at steady state and the net flux of solute is zero.

When considering a binary alloy of 50%A and 50%B atoms, high temperature irradiation can cause segregation where one type of atom enriches and the other depletes. The segregation process is demonstrated in figure 2.1, taken from [11], showing defect and solute atom concentrations and vectors with the direction and magnitude of the fluxes. Figure 2.1(a) plots the vacancy concentration gradient as a function of distance from a grain boundary, where the flux of vacancies toward the boundary is offset by the flux of A and B atoms away from the boundary. In this case, the coupling of A atoms preferentially in the vacancy flux causes a higher flux of A atoms relative to B atoms to diffuse away from the boundary. Figure 2.1(b) shows the same for the interstitial concentration. Here, the B atoms are preferentially bound to the interstitial flux and therefore more B atoms flow toward the grain boundary than A atoms with the interstitial flux. The resulting concentrations for A and B atoms are shown in figure 2.1(c) where a coupling of A atoms with the vacancy flux corresponds to grain boundary depletion and a coupling of B atoms with the interstitial flux results in grain boundary enrichment. The significance is that enrichment and depletion can occur through either the vacancy or

interstitial fluxes, and the magnitude of segregation depends on the strength of association between a solute and a defect type.

2.1.2 RIS Sensitivity

RIS is sensitive to a number of factors such as the irradiation temperature, radiation dose, dose rate, and size effects. These sensitivities will be discussed further through experimental RIS data in section 2.1.3, but the behavior of RIS as a function of these factors will briefly be mentioned first.

RIS depends to a great extent on the irradiation temperature and occurs only within a certain temperature regime for a given dose rate [8, 12]. This is illustrated in figure 2.2. for a concentration profile as a function of distance from a grain boundary for a number of temperatures [11]. At the lowest temperature of 200°C, RIS occurs within a very shallow depth of the boundary. Increasing the temperature increases the depth to which segregation occurs. RIS becomes more severe while back diffusion broadens the segregation profile. By 800°C RIS has extended to a great distance from the boundary, but notice that the concentration at the boundary shows less segregation than lower temperatures due to the extent of back diffusion. Generally if the temperature is too low, the low point defect diffusion rates prevent the migration of defects to sinks, and the recombination of point defects dominates, inhibiting the evolution of RIS. At high temperatures, back diffusion of elements at the grain boundary prevents large concentration gradients from developing, again with the result that RIS is inhibited.

RIS is also sensitive to dose rate [12], and both temperature and dose rate combined have a significant impact on the RIS effect. Figure 2.3 highlights this fact demonstrating that as dose rate increases, maximum segregation occurs at a higher temperature [11]. Put another way, higher dose rates require higher temperatures for RIS to occur. This is due to how the temperature and dose rate combine to affect defect migration. Considering a low temperature, a lower dose rate will result in more segregation than a higher dose rate. This is because, for any given dose, the time scale over which the irradiation occurs is much longer and allows more time for defects to diffuse to grain boundary sinks. At low temperatures, the defect migration rate is very

7

low, so an increasing dose rate simply means a higher fraction of point defects will recombine in the matrix rather than diffuse to grain boundaries to cause RIS.

At a higher temperature, the defect migration rate increases, so now RIS may increase with increasing dose rate. With more defects going to the grain boundary, a low dose rate and high temperature allows more time for segregation to be removed through back diffusion. Conversely, segregation profiles can be established quickly with the high dose rate with insufficient time for back diffusion to remove the segregation. Hence, RIS is a complex process that depends on both temperature and dose rate to determine the magnitude of defect recombination in the matrix, diffusion of defects to sinks, and back diffusion of solute at the boundary. These in turn will affect the amount of grain boundary segregation.

A strong correlation has also been developed between size effects, or volume misfit, and RIS. Building on work by King [13], Kornblit et al. [14] developed a relationship to determine the direction of segregation. Base on the understanding that a smaller substitutional atom in an alloy will diffuse preferentially through the interstitial flux and a larger atom will exchange preferentially with the vacancy flux, the prediction is made that undersized atoms will enrich and oversized atoms will deplete at a grain boundary. Table 2.1 presents volume misfit and segregation results from Kornblit for a variety of binary alloys. Note that a (+) volume misfit represents an oversized solute atom and a predicted depletion; conversely, (-) misfit solute should enrich. Without exception, for the examples presented by Kornblit et al. [14], the volume misfit correlation accurately predicts the measured trends in segregation.

More recently, in computer simulations using a first-principles approach with the Vienna *ab-initio* Simulation Package (VASP), Janotti et al. [15] and Krčmar et al. [15, 16] demonstrate that larger atoms can diffuse more quickly through vacancies than smaller atoms. The primary cause was found to be due to bonding directionality, where the electronic structure of the atoms determines the diffusion barrier energy, thus affecting the ratio of the point defect diffusivities for the larger and smaller elements. Their work suggests that Cr is more likely to diffuse through vacancies because it is the larger element relative to other major elements Fe and Ni. This would imply that RIS

develops, at least in part, because Cr is a faster diffuser through vacancies than Ni, with Fe lying somewhere in between.

These factors highlight some of the irradiation and material parameters that can have a large impact on RIS. The remaining parts of this section will go into greater detail, discussing past experiments involving RIS measurements, other factors that can affect RIS, and the underlying proposed mechanisms which lead to the development of RIS in austenitic stainless steels.

2.1.3 Experiments in RIS

A great deal of work has been done to measure RIS at grain boundaries, especially for austenitic stainless steels. While only a sampling of the work will be covered here, some highlights will be given to demonstrate the behavior that has been shown over a variety of temperature and dose regimes along with different irradiation particle types.

Figure 2.4 shows the minimum-measured Cr content for a variety of austenitic alloys, plotted as a function of radiation dose [17]. The data comes from a variety of neutron-irradiated commercial and high-purity austenitic steels over a variety of doses. One common theme from the data is that RIS develops exponentially with dose until saturating at some grain boundary concentration, typically between 3 – 5 dpa for most alloys.

Kenik [3] measured RIS in commercial purity (CP) and high purity (HP) 304-type stainless steels after neutron irradiation at 288°C to dose of 2.0 x 10^{25} n/m^2. Both CP and HP alloys contained the same concentrations of Ni and Cr, while the CP alloy contained higher concentrations of impurities Si, P, C, and S. After irradiation, segregation profiles were measured along a grain boundary, where figure 2.5(a) shows, for the commercial purity alloy, concentration as a function of distance from the boundary for the major alloying elements, Fe, Cr and Ni and figure 2.5(b) shows the same profiles for Si, S, and P. Figure 2.5(c) and 2.5(d) plot concentration profiles, this time for the HP alloy for Fe, Cr, Ni, and Si and P, respectively.

The CP alloy showed higher levels of Si and P segregation than the HP alloy, and this is not surprising given the higher concentrations of the impurities in the alloys.

9

However, the CP alloy also showed more depletion of Cr and enrichment of Ni at the grain boundary compared to the HP alloys. Moreover, while the HP alloy showed only a small depletion of Fe at the grain boundary, the CP alloy measured much more Fe depletion, close to 5 at%. Kenik suggested a possible synergism between segregation of Si and increased segregation for the major elements. The work demonstrates that, all things being equal, commercial purity alloys tend to have more solute segregation at sinks than high purity alloys.

Busby et al. [18] studied a series of high purity 304 stainless steels where each alloy contained a single impurity addition, with proton irradiations performed at 360°C to doses of 5.5 dpa. In particular, additions of Si or Mo both resulted in increases of grain boundary Cr depletion and Ni enrichment, as shown in figure 2.6. The results are similar to work by Kenik suggesting that impurity additions, particularly Si, can increase grain boundary segregation of Cr and Ni.

Similar work by Jensen et al. [19] involved grain boundary measurements of unirradiated and neutron irradiated CP and HP 304 and 316 stainless steels. Neutron fluences ranged from 3×10^{24} to 9×10^{25} n/m^2 at 275°C. CP alloys again had higher concentrations of Si, P and C impurities. Measurements of the irradiated alloys showed heat-to-heat variations in RIS, which was related back to unirradiated sample conditions. Jensen et al. found that enrichment of Mo and Cr of the heat-treated alloys varied considerably among the alloys prior to irradiation. And this pre-irradiation segregation then had an effect on the irradiated grain boundary concentrations. The work also confirmed results shown by Kenik, where CP alloys generally had higher amounts of segregation than the HP alloys due to higher concentrations of impurities like Si, which enrich at the grain boundary.

RIS has also been studied in austenitic stainless steels using ion irradiations, as shown in figure 2.7 [5, 20-29]. The figure shows the amount of Cr depletion as a function of dose representing numerous proton, electron, and He$^+$ irradiations. Electron irradiation data is shown in open symbols while proton irradiation data has closed, grey symbols and He$^+$ irradiation data has x symbols. Notice that electron irradiations typically represent higher radiation doses, principally because the high dose rate allows for high doses to be reached quickly. Notice for all of the data that segregation develops

quickly and can be substantial even at low doses, but that generally, the amount of segregation tends to saturate after several dpa.

One such ion irradiation done by Kinoshita et al. [22] studied the effect of Cr and Ni content on the amount of RIS after 1 MeV electron irradiation to 7 dpa at 450°C. Starting with the variation of Ni content, figure 2.8 plots the amount of segregation for Fe, Cr and Ni as a function of %Ni concentration. The largest variation is in the Ni enrichment. Cr depletion varies only by a few percent over the entire range of Ni concentrations. Meanwhile, Ni enrichment increases up to 35% bulk Ni concentration, then decreases due to a decreasing lattice constant, such that size effects for grain boundary segregation become less important.

When measuring the amount of segregation as a function of Cr concentration, as is shown in figure 2.9, the amount of Cr depletion appears to increase linearly with Cr concentration, with no change in Ni enrichment [22]. The authors concluded that for the fixed bulk Ni concentration (20%), Ni enrichment was insensitive to Cr concentration. Yet, returning to the authors' conclusion that a changing lattice constant should affect grain boundary segregation, it seems apparent that increasing the Cr concentration would increase the lattice constant, and this in turn should have an effect on segregation (i.e. Ni enrichment).

Damcott [30, 31] studied the effects of temperature on RIS through the use of proton irradiations in austenitic stainless steels. In a comprehensive study where temperatures were systematically varied between 300 and 600°C in 100°C increments, austenitic alloys of Fe-16Cr-24Ni, Fe-20Cr-24Ni, Fe-24Cr-24Ni, Fe-24Cr-19Ni, and Fe-Cr-9Ni were irradiated to doses ranging from 0.1 to 3.0 dpa. Selecting just one of these alloys, figure 2.10 shows RIS for the Fe-20Cr-24Ni alloy as a function of dose. Notice that RIS has saturated by only 1 dpa. By the higher dose of 3 dpa, the figure actually shows slightly more Cr concentration at the grain boundary.

The same 20Cr-24Ni alloy was irradiated to just 0.5 dpa from 300 – 600°C, shown in figure 2.11 [31]. Importantly, the highest degree of RIS measured was at 500°C. For the given dose rate of 10^{-6} dpa/s, the maximum RIS was estimated to occur somewhere between 400°C and 500°C. RIS decreases above this intermediate temperature due to back-diffusion of solute to the grain boundary, while below this

11

temperature, a higher fraction of recombination of point defects in the matrix prevents RIS from becoming more severe.

Allen et al. [32] found similar results in experimental studies where Fe-20Cr-24Ni, Ni-18Cr-9Fe, and Ni-18Cr alloys were irradiated with protons to 0.5 – 1.0 dpa with temperatures ranging from 200 – 600°C. The minimum grain boundary Cr concentration was found for the Ni-base alloys to occur around 400°C, with Fe-20Cr-24Ni having more Cr depletion at 500°C. The results were then compared to a RIS model to demonstrate that the maximum in segregation occurred between 400 – 500°C [33]. Further discussion of theses comparisons between model and experiment for RIS is presented in section 2.2.

2.1.4 Effect of Irradiation Particle Type on RIS

Ion irradiations are often used in place of neutron irradiations largely because they enable accelerated testing to obtain high doses in a relatively short amount of time, at lower cost, and often with little or no activation of the specimens. But RIS in metals can be sensitive to the irradiating particle type [12]. The type of particle determines the damage morphology of the irradiated material via ballistic collision cascades and the displacement rate. And the effect of the different damage morphologies on RIS depends in part on the efficiency of the particle for producing freely migrating defects, because RIS occurs only through the diffusion of freely migrating defects to defect sinks, such as grain boundaries[12]. Displacement rates for ions tend to be much higher because ions lose energy through electronic excitations in addition to elastic collisions [34]. In addition, neutrons have a larger mean-free-path for ballistic collisions [11]. Combined, these effects make the energy deposition rates, and thus displacement rates, much higher for ions than for neutrons.

Electrons, with a very small mass, transfer only a small fraction of their kinetic energy during ballistic collisions. If the electron energy is large enough, collisions will create isolated point defect pairs in the material. Typically, electron irradiations have a very high displacement rate, typically on the order of 10^{-3} displacements per atom (dpa) per second. This is due both to the high electron currents of modern TEM's and the very high energy deposition rates. With these isolated defects, electron irradiations create 'freely migrating' defects with an assumed 100% efficiency [35].

At the other extreme heavy ion and neutron irradiations transfer a large amount of energy in a single collision, resulting in energetic primary knock-on atoms (PKA) that have large, dense cascades of point defects. Heavy ions and neutrons may have as little as 2-4% of defects survive the collapse of the damage cascade [12]. Despite the similarity in collision cascades, heavy ions, like Ni^{++} irradiations, are performed with large accelerator currents and also have high energy deposition rates typical of ions in general. The result is a much higher displacement rate compared to the low displacement rates typical of neutrons from a light water reactor.

Proton irradiations, in the mean time, lie between these two extremes. Damage cascades are more widely dispersed than heavy ions because the mean-free-path for collisions is larger. The damage cores are still large, but are smaller than for neutrons or heavy ions because energy transfer in ballistic collisions is less due to the lighter mass of a proton as compared to heavy ions. Typical displacement rates for protons range between 10^{-5} and 10^{-6} dpa/s, with damage cascade efficiencies of around $10 - 20\%$.

2.1.5 Effects of Dislocation Loops on RIS

Dislocation loop microstructure is often analyzed before and after irradiation to determine the damage morphology, since void nucleation and swelling does not take place except at temperatures above 300°C under neutron irradiation [36]. Sakaguchi et al. [37] linked a rate-theory RIS model to dislocation evolution by including the growth rate of faulted dislocation loops and network dislocations. The rate equations, following the work of Stoller and Odette [38] and Garner and Wolfer [39], are incorporated into the model as shown:

$$\frac{\partial N_j^{loop}}{\partial t} = K_{growth}^{j-1} N_{j-1}^{loop} - K_{unf}^{j-1} N_{j-1}^{loop} - K_{growth}^{j} N_j^{loop} ,$$

(2.1)

$$\frac{\partial \rho}{\partial t} = \sum 2\pi \cdot r_j^{loop} K_{unf}^{j} N_j^{loop} + K_{B-H}\rho - K_{pair}\rho^2 .$$

(2.2)

Equation 2.1 describes the growth rate of faulted dislocation loops while equation 2.2 is for network dislocation loops. $K_{reaction}$ is the reaction rate constants for each process, N_j^{loop} is the faulted dislocation loop number density, r_j^{loop} is the loop radius in

each class of loops, where each class is tracked by size, and ρ is the network dislocation number density. In addition, the interstitial reaction rate equation includes an added term to count the nucleation of interstitial loops, shown by:

$$\frac{\partial C_i}{\partial t} = -\nabla J_i + K_0 - K_{vi}C_vC_i - S_iD_iC_i - K_{ii}C_i^2 , \tag{2.3}$$

where C_i is the interstitial concentration, $-\nabla J_i$ is the divergence of the interstitial flux, K_0 is the defect production rate. The recombination rate, $K_{iv}C_vC_i$, is the product of the recombination coefficient, K_{iv}, and C_v is the vacancy concentration. The sink term is described by $S_iD_iC_i$, where S_i is the sink density and D_i is the interstitial diffusion coefficient. Finally, K_{ii} is the coefficient for loop nucleation.

The results show that initially, the faulted dislocation loops dominate the microstructure, while network dislocations form and become the dominant feature only after several dpa. The relationship between loop and network dislocations as a fraction of the total dislocation density is shown in figure 2.12 [37]. Because grain boundaries act as sinks for point defects, the area around a grain boundary forms a "denuded zone," where dislocation formation does not take place. Sakaguchi et al. [40] studied the formation of dislocation-free zones (DLFZ) with electron irradiation at 523 K up to doses of 10 dpa. The initial result was a relatively wide area on either side of the grain boundary that remained free of dislocations, as shown in figure 2.13. One can see in both figures 2.14 and 2.15 how the DLFZ decreases over time (e.g. dose) as more dislocations either nucleate or diffuse into the denuded zone.

Sakaguchi et al. [40] propose that the formation of a DLFZ around the grain boundary is due to a lack of point defect super-saturation around the boundary, where point defects will migrate to and be absorbed by the boundary rather than cluster in the matrix. The authors correlate the width of RIS profiles as being linearly proportional to the DLFZ width, with an increase in RIS width as a function of dose corresponding to a decrease in the width of the DLFZ. The authors' correlation is:

$$W_{DLFZ}\big|_{t\to0} = W_{RIS}\big|_{t\to\infty} = r_c^{gb} \propto \sqrt[4]{D_v} . \tag{2.4}$$

The initial DLFZ width is assumed to be equal to the steady-state RIS profile width. The width is calculated as being equal to the grain boundary capture radius for point defects,

r_c^{gb}, and proportional to the fourth root of the vacancy diffusivity. The value for r_c^{gb} is described by:

$$r_c^{gb} = \sqrt{\frac{2D_i C_i^*}{G_{dpa}}} , \qquad (2.5)$$

$$C_i^* = \sqrt{\frac{D_v G_{dpa}}{R_{vi} D_i^2}} . \qquad (2.6)$$

Here, C_i^* is the matrix interstitial concentration, G_{dpa} is the point defect production rate, R_{vi} is the vacancy-interstitial recombination rate, and D_i and D_v are the interstitial and vacancy diffusion coefficients, respectively. Watanabe et al. [41] further relate the RIS and DLFZ width to the temperature by the relationship:

$$W_{DLFZ} \propto W_{RIS} \propto e^{\left(-\frac{E^{irr}/2}{kT} \right)} . \qquad (2.7)$$

Sakaguchi et al. [37] state that the formation of RIS and DLFZ profiles are influenced by the same kinetic and thermodynamic behavior. The authors further conclude that dislocation evolution and sink strength have only a weak effect on the resulting RIS composition due to the formation of the DLFZ near grain boundaries. One should note, however, that the described dislocation evolution and, in particular, the correlation of DLFZ width to RIS profile width, may be specific only to electron irradiation studies, where cascade damage does not occur. Edwards et al. [36] report the creation of DLFZ (or denuded zones) near grain boundaries after neutron irradiation at 275°C but find consistent differences in the widths between 304SS and 316SS alloys. Furthermore, no DLFZ's were found at all in the high-purity alloys of either 304 or 316 at doses as low as 1 dpa. These results suggest that cascade damage morphology has a strong influence on the dislocation microstructure, and dislocation studies performed using electron irradiations may have limited relevance to radiation damage studies of heavy ion and neutron irradiations. Finally, proton irradiation studies examining the microstructure of austenitic stainless steels have never reported the observation of DLFZ's near grain boundaries, despite a host of grain boundary examinations over a range of alloys, temperatures, and doses [27, 42-44].

Prior cold work to stainless can cause a dense dislocation microstructure which can enhance point defect recombination and prevent RIS at low doses. Eventually this dislocation microstructure will be removed and replaced with an irradiated microstructure of faulted loops and segregation at grain boundaries. However, an initial dislocation microstructure can act as a sink for point defects to prevent RIS. Likewise, the development of a defect microstructure with irradiation dose can increase the matrix defect sinks and decrease the amount of RIS [45].

2.1.6 Effects of Void Swelling on RIS

In correlating RIS with the defect microstructure, Johnson et al. [46] used their RIS model to scope out temperature and dose rate effects of segregation at voids. The study included the effects of void size and density on surface segregation and preliminary work on incorporating the use of an interstitial-solute binding mechanism to describe the process by which RIS develops. One conclusion is that no segregation occurs at the surface of very small voids, becomes significant with increasing void sizes up to a certain size, and then decreases again for large voids in excess of 10 nm. This is due to a decreasing interstitial flux at the void surface with increasing void size. The model is not based on the inverse Kirkendall mechanism and input parameters bias results to an interstitial-driven RIS mechanism, as will be discussed in section 2.2 in work by Johnson et al. [47] and Wiedersich et al. [48].

The development of RIS around voids has been measured previously [49]. In particular, significant Ni enrichment had been seen around voids and helium bubbles [50]. The effect of this composition change around voids is to change the capture efficiency for defects [51, 52]. The greater the segregation at voids, the less efficient the void becomes at capturing additional vacancies. For stainless steels, the enrichment of Ni and depletion of Cr at the surface of a void can reduce the void growth rate [45]. Void nucleation and growth near grain boundary surfaces could affect the local microchemistry that could in turn have an impact on grain boundary chemistry.

Point defects, which are the cause of RIS, also result in the nucleation of dislocation loops and at sufficient temperatures result in void nucleation and swelling. A process in the matrix that can enhance point defect recombination will reduce the point

defect super-saturation and also the magnitude of the defect flux to grain boundaries, which should consequently reduce RIS. Changes in RIS behavior may then signal a change in the morphology of the microstructure. In this way, RIS and microstructure are linked, since changes in radiation damage to the microstructure may reflect changes to grain boundary segregation as well.

2.1.7 Effects of Grain Boundary Orientation on RIS

The degree of segregation that develops at a grain boundary also depends, as it turns out, on grain boundary misorientation. Typically, the sink strength of a grain boundary is assumed to be constant, but in fact, the ability of the grain boundary to readily absorb point defects depends upon the grain boundary misorientation, or tilt angle [53]. As the sink strength of a boundary increases, the RIS similarly increases.

Watanabe et al. [41] alter the point defect reaction rate equations to include a dependence upon the tilt angle of the grain boundary. The rate equations as shown in equations Y and Z incorporate the sink strengths, S_v and S_i, into the following term:

$$S^{GB} = A \sin\left(\frac{\theta}{2}\right).$$

(2.8)

The constant A is the nominal sink strength of the grain boundary and θ is the tilt angle.

Watanabe et al. [41] find that the sink strength increases as the grain boundary tilt angle increases. The justification is that as the tilt angle increases, the misorientation is better able to accommodate point defects; a random, high angle boundary has stronger sink strength than a coherent or low-energy (low angle) grain boundary. This is demonstrated experimentally in figure 2.16(a) and 2.16(b), where the interfacial grain boundary character has a strong effect on the resulting segregation behavior.

Sakaguchi et al. [54] further demonstrate this behavior by including a grain boundary energy relationship with the sink strength, where the grain boundary energy depends on the coherence of the grain boundary. Grain boundary energy continues to increase with increasing tilt angle, but is greatly reduced at certain coincident site lattice (CSL) boundaries. These CSL boundaries represent particular orientations where a fraction of the atoms between the two neighboring boundaries are aligned, or coincident, thus reducing the grain boundary energy. The larger the grain boundary energy, the

larger the sink strength of the boundary and the more segregation occurs. The relationship for the grain boundary sink strength now depends on:

$$S^{GB} = S^{GB}(\theta_\Sigma + \theta_{dev})\sin\frac{|\theta_{dev}|}{\theta_{dev}^{Max}} + S_\Sigma^{GB}\left[1 - \sin\frac{|\theta_{dev}|}{\theta_{dev}^{Max}}\right],$$ (2.9)

where θ_{dev}^{Max} is the maximum deviation angle from coincidence [54], determined by

$$\theta_{dev}^{Max} = 15°\Big/\sqrt{\Sigma},$$ (2.10)

where S_Σ^{GB} is the CSL boundary sink strength of the Σ coincidence boundary, θ_{dev} is the deviation angle, and θ_Σ is the misorientation angle for the exact coincidence relationship.

The result of this work is to demonstrate that RIS varies not only with tilt angle, but also has a large dependence on CSL boundaries. Figure 2.17 shows the Ni and Cr concentration of a Fe-15Cr-20Ni alloy after electron irradiation to 3 dpa at 623 K for a <110> boundary [54]. Although segregation increases with tilt angle misorientation, the lower Σ boundaries which have a larger tilt angle actually demonstrate less segregation than CSL boundaries with lower tilt angle. For example, the $\Sigma 3$ boundary shows virtually no Cr depletion or Ni enrichment. A $\Sigma 3$ boundary implies that one in three atoms along the boundary is coincident and the coincident boundary has low sink strength, resulting in less RIS. Since CSL boundaries typically represent only a fraction of the total boundaries, RIS measurements generally try to avoid CSL or low angle boundaries.

2.2 Mechanisms of RIS

Soon after the discovery of solute segregation occurring at grain boundaries due to irradiation, progress was made toward understanding this phenomenon. This section will discuss the early work in understanding RIS, moving to binary and then ternary alloy systems to determine mechanistically the causes for RIS.

2.2.1 Early Work in RIS Mechanisms

      Because radiation-induced segregation is such a complex process, any attempt to simulate the phenomenon must capture the primary variables, such as irradiation dose rate, efficiency for producing freely migrating defects, and temperature, to name a few. More difficult is to accurately simulate the diffusion process that leads to RIS. Because RIS can be described by a chemical potential gradient that exists at grain boundaries, the simplest case that can be modeled is a binary alloy. Even in such cases, however, any model must account not only for point defect behavior in the alloy system, but also the differences in interactions between the chemical species of the alloy and how they interact both with the point defects and with one another. As the number of chemical species of the alloy increases, the complexity of a model will increase exponentially.

      Some of the first attempts at understanding RIS were made by Anthony et al. [55, 56]. The authors assumed two different mechanisms to explain segregation. First, the preferential diffusion of one type of solute atom in the vacancy flux can cause the depletion of that solute from a grain boundary. Second, the association of vacancies with a particular solute can create vacancy-solute complexes that would effectively drag the solute toward a boundary.

      Johnson et al. built upon this work to identify a third mechanism, where a coupling between a solute atom and the interstitial flux would drag the solute to a boundary and cause enrichment [47]. The authors considered a binary alloy where segregation occurs through the migration of solute with either the vacancy flux or via interstitial binding of the solute through the formation of interstitial dumbbells. Because interstitials are significantly more mobile at lower temperatures, interstitial migration became the dominant mechanism for RIS at low temperatures.

      Johnson's model includes many complex interactions as the model was primarily used to analyze changes in point defect concentrations rather than grain boundary solute concentrations. The work considers eight different concentrations, for interstitials, vacancies, impurities, interstitial-impurity complexes with both type A and type B atoms, vacancy-impurity complexes, and the explicit treatment of sink concentrations (i.e. sink strength) for both interstitials and vacancies. To make the matter more complicated, twelve different reaction rate constants were needed to consider all of the relevant

reactions. Concentrations were plotted as a function of time, but the results did little to provide any insight into the actual mechanisms causing segregation.

Figure 2.18, for example, plots these concentrations as a function of irradiation time at the center of a thin foil with an irradiation temperature of $0°C$, where C_i^c is the solute concentration, C_v^c is for vacancies, C_{vi}^c is for vacancy-solute complexes, C_{Iia}^c and C_{Iib}^c are for interstitial-solute complexes with atoms A and B, respectively, C_I^c is the interstitial concentration, and C_i^s is the solute concentration at the surface. Clearly, the relative importance of each mechanism is lost in such a treatment.

2.2.2 RIS Mechanisms for Binary Alloy System

Wiedersich outlines a basic kinetic segregation model for a binary alloy [48]. Since the segregation is due to the diffusion of point defects, the defect rate equations are described by:

$$\frac{\partial C_v}{\partial t} = -\nabla J_v + K_0 - R, \tag{2.11}$$

$$\frac{\partial C_i}{\partial t} = -\nabla J_i + K_0 - R, \tag{2.12}$$

where $-\nabla J_v$ and $-\nabla J_i$ are the divergences of the vacancy and interstitial fluxes, K_0 is the defect production rate and the recombination rate is $R = K_{iv}C_vC_i$, and K_{iv} is the recombination constant. The conservation equations for atoms A and B can be described likewise:

$$\frac{\partial C_A}{\partial t} = -\nabla J_A, \tag{2.13}$$

$$\frac{\partial C_B}{\partial t} = -\nabla J_B, \tag{2.14}$$

Since it is assumed that all diffusion of vacancies and interstitials takes places through A and B atoms, then the diffusion equations for vacancies and interstitials are written as:

$$J_i = J_A^i + J_B^i, \tag{2.15}$$

$$J_v = -\left(J_A^v + J_B^v\right), \tag{2.16}$$

20

Of course, A and B atoms diffusing through interstitials travel in the same direction as the interstitial flux while the flux of vacancies is opposing the flux of A and B atoms diffusing through the vacancy flux.

Partial diffusion coefficients are used to describe the concentration gradients for the defect and solute fluxes, shown by:

$$D_A^v = \frac{1}{6}\lambda_A^2 Z_A N_v \omega_A^v f_A^v .$$ (2.17)

In equation 2.17, λ_A is the jump distance for A atoms, Z_A is the number of nearest neighbors to A atoms, N_v is the fraction of vacancies, ω_A^v is the jump frequency for an A atom jumping to a vacancy lattice site, and f_A^v is the correlation factor for A atoms diffusing through vacancies. Since the correlation factor is composition dependent, it is ignored here. This gives a partial diffusion coefficient of A atoms migrating through vacancies as:

$$D_A^v = \frac{1}{6}\lambda_A^2 Z_A N_v \omega_A^v ,$$ (2.18)

and a partial diffusion coefficient of vacancies exchanging with A atoms as:

$$D_v^A = \frac{1}{6}\lambda_A^2 Z_A N_v \omega_v^A .$$ (2.19)

Since the frequency of exchange of A atoms through vacancies is the same as vacancy exchange with A atoms, then $\omega_v^A = \omega_A^v$. As a result a common diffusivity coefficient can be written as:

$$d_{Av} = \frac{1}{6}\lambda_A^2 Z_A \omega_v^A ,$$ (2.20)

and the partial diffusion coefficients can be simplified to:

$$D_A^v = d_{Av} N_v ,$$ (2.21)

$$D_v^A = d_{Av} N_A .$$ (2.22)

The partial diffusion coefficients for B atoms can be described similarly as:

$$D_B^v = d_{Bv} N_v ,$$ (2.23)

$$D_v^B = d_{Bv} N_A .$$ (2.24)

The expressions for the partial diffusion coefficient for atoms A and B migrating through interstitials are similar to equations 2.21 to 2.24 and are shown by:

$$D_A^i = d_{Ai} N_i, \tag{2.25}$$

$$D_i^A = d_{Ai} N_A, \tag{2.26}$$

$$D_B^i = d_{Bi} N_i, \tag{2.27}$$

$$D_i^B = d_{Bi} N_B. \tag{2.28}$$

Total diffusion coefficients are now written to combine equations 2.21 through 2.28 and are expressed as follows:

$$D_A = d_{Av} N_v + d_{Ai} N_i, \tag{2.29}$$

$$D_B = d_{Bv} N_v + d_{Bi} N_i, \tag{2.30}$$

$$D_v = d_{Av} N_A + d_{Bv} N_B, \tag{2.31}$$

$$D_i = d_{Ai} N_i + d_{Bi} N_B, \tag{2.32}$$

Having identified the total and partial diffusion coefficients and the diffusivity, the fluxes can be rewritten as:

$$J_A = -D_A \alpha \nabla C_A + d_{Av} N_A \nabla C_v - d_{Ai} N_A \nabla C_i, \tag{2.33}$$

$$J_B = -D_B \alpha \nabla C_B + d_{Bv} N_B \nabla C_v - d_{Bi} N_B \nabla C_i, \tag{2.34}$$

$$J_v = d_{Av} N_v \alpha \nabla C_A + d_{Bv} N_v \alpha \nabla C_A - D_v \nabla C_v, \tag{2.35}$$

$$J_i = d_{Ai} N_i \alpha \nabla C_A + d_{Bi} N_i \alpha \nabla C_A - D_i \nabla C_i. \tag{2.36}$$

The thermodynamic factor, $\alpha = \left(1 + \dfrac{\partial \ln \gamma_A}{\partial \ln N_A}\right) = \left(1 + \dfrac{\partial \ln \gamma_B}{\partial \ln N_B}\right)$, describes the difference chemical potential gradient between alloy atoms A and B and the concentration gradient. The terms γ_A and γ_B are the activity coefficient. Although the thermodynamic factor is less than one for non-ideal solutions, no one has yet considered the relevance of this factor in the RIS models.

Only three of the four flux equations are independent according to the equation,

$$J_A + J_B = -J_v + J_i, \tag{2.37}$$

because the atom fluxes must balance the defect fluxes. Using equations 2.33 through 2.36, we can insert the fluxes into the original concentration rate equations to find:

$$\frac{\partial C_A}{\partial t} = \nabla \left[D_A \alpha \nabla C_A + \Omega C_A (d_{Ai} \nabla C_i - d_{Av} \nabla C_v) \right], \tag{2.38}$$

$$\frac{\partial C_v}{\partial t} = \nabla \left[-(d_{Av} - d_{Bv}) \alpha \Omega C_v \nabla C_A + D_v \nabla C_v \right] + K_0 - R, \tag{2.39}$$

$$\frac{\partial C_i}{\partial t} = \nabla \left[-(d_{Ai} - d_{Bi}) \alpha \Omega C_i \nabla C_A + D_i \nabla C_i \right] + K_0 - R, \tag{2.40}$$

where Ω is the average alloy atomic volume. The concentration for atom B can easily by found by $C_B = 1 - C_A$.

Wiedersich et al. is more successful in describing a binary alloy under irradiation by analyzing two different mechanisms [48]. The first mechanism does not consider a preferential coupling of the solute atoms with either vacancies or interstitials but instead assumes segregation occurs solely through the differences in diffusivity ratios of vacancies to interstitials for A and B atoms. This is demonstrated by the inequality:

$$\frac{D_A^V}{D_B^V} > \frac{D_A^I}{D_B^I}. \tag{2.41}$$

In equation 2.41, A atoms will deplete while B atoms enrich. Shown schematically already in figures 2.1(a), (b), and (c), A atoms deplete if they have a higher diffusivity through vacancies than interstitials relative to B atoms [57]. And B atoms enrich because they have a higher diffusivity through interstitials than A atoms.

The second mechanism used by Wiedersich is the coupling of interstitials with undersized solute atoms by using a binding energy to form interstitial-solute complexes [48]. If a preferential binding exists between atoms A and the interstitial flux, the equations describing the concentrations of A and B atoms expressing this preferential binding would be shown as:

$$C_{Ai} = C_i \frac{C_A \exp\left(E_b^{Ai} / kT\right)}{C_A \exp\left(E_b^{Ai} / kT\right) + C_B}, \tag{2.42}$$

$$C_{Bi} = C_i \frac{C_B}{C_A \exp\left(E_b^{Ai} / kT\right) + C_B}, \tag{2.43}$$

where E_b^{Ai} is the interstitial binding energy with A atoms and represents the energy difference between an A and B interstitial. In the case of an AB alloy, the atom that binds more strongly to the interstitial flux will enrich at the grain boundary.

2.2.3 RIS Mechanisms for a Ternary Alloy System

Lam et al. [58] extending the simple system of a binary alloy to a more complex ternary alloy system. The following equations form the basis of ternary alloy rate theory RIS models today. The basic kinetic equations do not change, but now the defect fluxes can be partitioned between three atom types A, B and C, shown by:

$$J_i = J_i^A + J_i^B + J_i^C,$$ (2.44)

$$J_v = J_v^A + J_v^B + J_v^C.$$ (2.45)

For the defect fluxes, the equations are:

$$J_i^x = J_x^i,$$ (2.46)

but,

$$J_v^x = -J_x^v,$$ (2.47)

and

$$J_i = \sum_x J_x^i,$$ (2.48)

$$J_v = -\sum_x J_x^v,$$ (2.49)

where x is for atoms A, B, and C. So the flux of atoms A through interstitials is in the same direction as the flux of interstitials through atoms A, but the direction of the vacancy flux through atoms A is in the opposite direction of atoms A through the vacancy flux.

The kinetic equations for the solute atoms are the same as in the binary model when written as the divergence of the flux by:

$$\frac{\partial C_A}{\partial t} = -\nabla J_A,$$ (2.50)

$$\frac{\partial C_B}{\partial t} = -\nabla J_B,$$ (2.51)

$$\frac{\partial C_C}{\partial t} = -\nabla J_C.$$ (2.52)

The fluxes for atoms A, B and C can be written as the sum of partial defect fluxes by:

$$J_x = J_x^v + J_x^i.$$ (2.53)

Writing the defect flux as a function of the concentration gradients of the solute atoms, the equations are:

$$J_x^i = -D_x^i \alpha \nabla C_x - D_i^x \nabla C_i,$$ (2.54)

$$J_x^v = -D_x^v \alpha \nabla C_x - D_v^x \nabla C_v,$$ (2.55)

where D_x^i and D_x^v are the partial diffusion coefficients of atoms x through interstitials and vacancies, and D_i^x and D_v^x are the partial diffusion coefficients of interstitials and vacancies through atoms x. The partial diffusion coefficients can be written as:

$$D_x^j = d_{xj} N_j,$$ (2.56)

$$D_j^k = d_{xj} N_x,$$ (2.57)

where j is for vacancies or interstitials, $N_j = \Omega C_j$ and $N_x = \Omega C_x$ are the atomic fractions for the defects and the solute atoms, Ω is the average atomic volume for the alloy, and d_{xj} represent the diffusivity coefficients for the different combinations of atom-defect pairs. They can be written as:

$$d_{xj} = \frac{1}{6} \lambda_x^2 Z_x \omega_{xj}^{eff},$$ (2.58)

The jump distance is λ_x^2, Z_x is the number of nearest neighbor atoms to x, and ω_{xj}^{eff} is the effective jump frequency for the atom-defect pair.

The total diffusion coefficients interstitials and vacancies is expressed by:

$$D_i = \sum_x d_{xi} N_x,$$ (2.59)

$$D_v = \sum_x d_{xv} N_x,$$ (2.60)

and for atoms,

25

$$D_x = d_{xi}N_i + d_{xv}N_v. \tag{2.61}$$

Using the diffusion coefficients, the fluxes can incorporate the diffusion terms for new expressions, shown by the following:

$$J_A = -D_A\alpha\nabla C_A + d_{Av}N_A\nabla C_v - d_{Ai}N_A\nabla C_i, \tag{2.62}$$

$$J_B = -D_B\alpha\nabla C_B + d_{Bv}N_B\nabla C_v - d_{Bi}N_B\nabla C_i, \tag{2.63}$$

$$J_C = -D_C\alpha\nabla C_C + d_{Cv}N_C\nabla C_v - d_{Ci}N_C\nabla C_i, \tag{2.64}$$

$$J_i = -(d_{Ai} - d_{Ci})N_i\alpha\nabla C_A - (d_{Bi} - d_{Ci})N_i\alpha\nabla C_B - D_i\nabla C_i, \tag{2.65}$$

$$J_v = -(d_{Av} - d_{Cv})N_v\alpha\nabla C_A - (d_{Bv} - d_{Cv})\alpha\nabla C_A - D_v\nabla C_v. \tag{2.66}$$

Assuming that $C_A + C_B + C_C = 1$ and $\nabla C_C = -(\nabla C_A + \nabla C_B)$, then of the three solute atom fluxes and two defect fluxes, only four are independent, since

$$J_A + J_B + J_C = -J_v + J_i \tag{2.67}$$

Finally, the kinetic rate equations for the concentrations incorporate the new flux terms, where only four are needed because the concentration for C_C atoms can be found according to $C_C = 1 - C_A - C_B$. The remaining equations are shown by:

$$\frac{\partial C_A}{\partial t} = \nabla[D_A\alpha\nabla C_A + N_A(d_{Ai}\nabla C_i - d_{Av}\nabla C_v)], \tag{2.68}$$

$$\frac{\partial C_B}{\partial t} = \nabla[D_B\alpha\nabla C_B + N_B(d_{Bi}\nabla C_i - d_{Bv}\nabla C_v)], \tag{2.69}$$

$$\frac{\partial C_C}{\partial t} = \nabla[D_C\alpha\nabla C_C + N_C(d_{Ci}\nabla C_i - d_{Cv}\nabla C_v)], \tag{2.70}$$

$$\frac{\partial C_v}{\partial t} = \nabla[-(d_{Av} - d_{Cv})\alpha N_v\nabla C_A - (d_{Bv} - d_{Cv})\alpha N_v\nabla C_B + D_v\nabla C_v] \\ + K_0 - R \tag{2.71}$$

$$\frac{\partial C_i}{\partial t} = \nabla[-(d_{Ai} - d_{Ci})\alpha N_i\nabla C_A - (d_{Bi} - d_{Ci})\alpha N_i\nabla C_B + D_i\nabla C_i] + K_0 - R. \tag{2.72}$$

Lam et al. [58] also consider RIS with the mechanism of preferential solute binding to the interstitial flux. This can again be accommodated in a similar treatment to the binary alloy, shown by:

$$C_{Ai} = C_i \frac{C_A \exp\left(E_b^{Ai} / kT\right)}{C_A \exp\left(E_b^{Ai} / kT\right) + C_B + C_C}, \tag{2.73}$$

$$C_{Bi} = C_i \frac{C_B}{C_A \exp\left(E_b^{Ai} / kT\right) + C_B + C_C}, \tag{2.74}$$

$$C_{Ci} = C_i \frac{C_C}{C_A \exp\left(E_b^{Ai} / kT\right) + C_B + C_C}. \tag{2.75}$$

In this case, the authors use E_b^{Ai} to denote the energy gained through the conversion of B or C interstitials into A interstitials. This mechanism assumes that only one atom type forms interstitial-solute complexes, though all solute atoms can diffuse through the interstitial flux. Knowing E_b^{Ai} the ratio of A, B and C atoms as interstitials can be found, which in turn could be used to determine RIS arising from differences in solute participation in the interstitial flux.

Segregation is the result of the diffusion of both interstitials and vacancies toward sinks. As has been discussed, three mechanisms for RIS have been proposed: solute-defect complexes which drag solute to the boundary, preferential binding of solute atoms with the interstitial flux, and the preferential diffusion of solute atoms through the vacancy flux. According to Perks et al. [59], however, migration of solute-defect complexes can occur only when the migration energy of the complex is less than the dissociation energy of the complex. This condition is unlikely for vacancy complexes and is true for interstitial-solute complexes only for alloys with a relatively large size mismatch, where dissociation of the interstitial is less favorable. The large size mismatch does not represent, however, a ternary Fe-Cr-Ni alloy, where atom sizes are similar. So Perks argues that diffusion of solute-defect complexes toward the grain boundary cannot be the mechanism for RIS.

In the work done by Perks et al. [60] and based on previous work by Marwick et al. [61] and random alloy theory by Manning [62], both interstitial and vacancy diffusion are treated explicitly. Perks derived thermodynamic factors based on diffusion data from Rothman et al. [63] and derivations by Million et al. [64]. The diffusivity of element k through defect j is described by:

$$d_{kj} = d_0^{kj} \exp\left(\frac{-E_m^{kj}}{kT}\right),$$ (2.76)

where

$$d_0^{kj} = \frac{1}{6}\lambda_j^2 Z_j \nu_{kj} \exp\left(\frac{S_m^j}{k}\right),$$ (2.77)

and ν_{ji} is the jump frequency, Z_j is the number of nearest neighbor atoms, and λ_j is the jump distance. But the interstitial jump rates, used to calculate the solute-interstitial diffusivities, are independent of composition [59]. Perks defines the solute-interstitial diffusion coefficient in equation 2.77 as:

$$d_{ki} = \frac{2}{3}\nu_{ki}\lambda^2.$$ (2.78)

The jump frequency is expressed as a function of the interstitial jump frequency ν_i and the relative jump rate, ω_k^i, of j atoms through an interstitial, shown by:

$$\nu_{ki} = \omega_k^i \nu_i.$$ (2.79)

The only variable for the interstitial diffusivity coefficient is in the relative jump rate of solute atoms through vacancies. Since it is assumed that $\omega_{Fe}^i = \omega_{Cr}^i = \omega_{Ni}^i = 1$, the interstitial mechanism plays no role in segregation. Segregation is the result, then, only of differences in vacancy diffusion pre-exponentials arising from the differences in jump frequencies between the atoms.

Watanabe et al. [65] take the alternative mechanism by using constant vacancy migration energies and varying the interstitial migration energy, with a higher energy for Ni at 0.9 eV compared to 0.3 eV for Cr and Fe. Ni enrichment occurs through the binding of Ni atoms to the interstitial flux with a similarly large energy of 0.75 eV. The larger migration energy for Ni implies that Ni diffusion for interstitials occurs more slowly than that for Cr and Fe, contrary to conventional understanding that Ni is more likely to exchange with interstitials due to its lower atomic volume as compared to Fe and Cr. The authors conclude that the primary mechanism for segregation occurs through dumbbell interstitial migration because boundary migration has been observed even at low temperatures [66] where vacancies were not highly mobile. However, others have

demonstrated segregation behavior through preferential vacancy exchange at this temperature, even at the high dose rates of 5×10^{-3} dpa/s [21, 32, 59, 67, 68].

Using the determinant of the atom gradient ratios for a ternary alloy derived by Watanabe and Takahashi [69], Allen et al. [32] was able to predict the grain boundary depletion or enrichment of Fe, which depends upon the relative concentrations of Cr and Ni in the alloy. Comparing the qualitative behavior of grain boundary measurements after proton irradiation at 400°C as a function of composition to model predictions, Allen demonstrates that the vacancy mechanism alone is sufficient to explain segregation behavior. This is significant because it requires that there be no bias in the diffusion of interstitial species to a grain boundary; that is, interstitials migrate without preference to any of the primary solvent species.

Allen et al. [32, 33] used the Perks' model to demonstrate that defect coupling with the vacancy flux alone could explain segregation behavior. The work was extended to include diffusivities for a ternary Fe-Cr-Ni alloy that are dependent on local composition. The vacancy diffusivities are calculated from vacancy migration energies that incorporate short-range ordering effects based on a model by Grandjean et al. [70]. Since Manning's [71] random alloy theory no longer applies, because there exists a preferential ordering of Ni-Cr pairs, thermodynamic and correlation factors from Perk's model are no longer considered. The new composition-dependent ternary alloy model is referred to as the modified inverse Kirkendall (MIK) model.

Starting with equation 2.80, the vacancy migration energy is the difference between the saddle point energy and the equilibrium energy, described here for Cr as:

$$E_m^{Cr,v} = ES_{Fe-Cr-Ni}^{Cr} - E_{eq}^{Cr} . \tag{2.80}$$

The migration energy $E_m^{Cr,v}$ is the energy required for an atom to move from its equilibrium lattice position E_{eq}^{Cr} through the point of maximum potential $ES_{Fe-Cr-Ni}^{Cr}$ before moving to a new lattice position. This is shown in figure 2.20 which illustrates this migration energy difference between equilibrium and saddle point [33]. The equilibrium energy is defined as the interaction energy between nearest neighbor atoms, shown by:

$$E_{eq}^{Cr} = Z\left[C_{Cr}E_{CrCr} + C_{Ni}E_{CrNi} + C_{Fe}E_{CrFe} + C_{v}E_{Cr-v}\right], \tag{2.81}$$

where C is the atomic concentration, E_{kj} is the pair interaction energy between two solute atoms or a solute and defect. Pair interaction energies are approximated by using a linear average of the like-atom pair energies minus the ordering energy, E_{kj}^{ord}, shown by:

$$E_{CrNi} = \frac{E_{CrCr} + E_{NiNi}}{2} - E_{CrNi}^{ord}, \tag{2.82}$$

$$E_{CrFe} = \left(\frac{E_{CrCr} + E_{FeFe}}{2}\right) - E_{CrFe}^{ord}, \tag{2.83}$$

$$E_{FeNi} = \left(\frac{E_{FeFe} + E_{NiNi}}{2}\right) - E_{FeNi}^{ord}, \tag{2.84}$$

Interaction energies for like-atom pairs are a function of the cohesive energy, E_{coh}^{Cr}, divided by the number of nearest neighbor bonds, expressed by the following:

$$E_{CrCr} = E_{coh}^{Cr}/(Z/2), \tag{2.85}$$

$$E_{FeFe} = E_{coh}^{Fe}/(Z/2), \tag{2.86}$$

$$E_{NiNi} = E_{coh}^{Ni}/(Z/2). \tag{2.87}$$

Both Cr and Fe have BCC crystal structures as opposed to the FCC crystal structure for austenitic stainless steel. Consequently, the cohesive energies require correction terms that account for the energy required to convert from BCC to FCC for a proper description of the equilibrium cohesive energy. The FCC cohesive energy, $E_{coh}^{Cr,fcc}$, is a combination of the BCC cohesive energy plus the change in Gibbs free energy, $\Delta G_{Cr}^{bcc \rightarrow fcc}$, shown by:

$$E_{coh}^{Cr,fcc} = E_{coh}^{Cr,bcc} + \Delta G_{Cr}^{bcc \rightarrow fcc}, \tag{2.88}$$

$$E_{coh}^{Fe,fcc} = E_{coh}^{Fe,bcc} + \Delta G_{Fe}^{bcc \rightarrow fcc}. \tag{2.89}$$

Although Allen does not include equations 2.88 and 2.89 explicitly in the MIK model, the changes in Gibbs free energy are assumed as a part of the cohesive energies used for input parameters, where the free energy difference is assumed to be 0.01 eV for Fe and -0.10 eV for Cr from reference 72.

Pair interaction energies between atoms and vacancies account for the vacancy formation energy, E_{vf}^k, of k atoms in a pure metal system, since there is no cohesive energy for a vacancy, and the equation is shown as:

$$E_{kv} = \left(\frac{E_{coh}^k + E_{vf}^k}{Z} \right).$$

(2.90)

Equations 2.81 to 2.90 are used to determine the equilibrium energy, but the saddle point energy must still be calculated in order to determine vacancy migration energies. The pure element saddle point energies should reproduce the pure metal vacancy migration energy. In a pure metal, the extraction of an atom and a vacancy requires energy described by:

$$E_k = Z\left(C_k E_{k,k} + C_v E_{k,v} \right),$$

(2.91)

$$E_v = Z\left(C_v E_{v,v} + C_k E_{k,v} \right).$$

(2.92)

Combining the two equations, since $C_k + C_v = 1$ and $C_v \ll C_k$, equations 2.91 and 2.92 become the following:

$$E_k + E_v = Z\left(E_{k,k} + E_{k,v} \right).$$

(2.93)

Notice that equation 2.93 is the definition for the equilibrium energy for an atom k in a pure metal system. Knowing this, the pure metal vacancy migration energy is defined as the difference in the saddle point energy and the equilibrium energy from the right hand side of equation 2.93, shown by:

$$E_{vm}^{pure,k} = ES_{pure}^k - Z\left(E_{k,k} + E_{k,v} \right).$$

(2.94)

Solving for the saddle point energy:

$$ES_{pure}^k = E_{vm}^{pure,k} + Z\left(E_{k,k} + E_{k,v} \right).$$

(2.95)

Finally, the saddle point energy for atom k in a Fe-Cr-Ni system can be approximated as the average of the alloy average, $ES_{Fe-Cr-Ni}^{avg}$, plus the pure metal, ES_{pure}^k, saddle point energies, with the following:

$$ES_{Fe-Cr-Ni}^k = \frac{ES_{pure}^k + ES_{Fe-Cr-Ni}^{avg}}{2},$$

(2.96)

where the alloy average is defined as:

$$ES^{avg}_{Fe-Cr-Ni} = \sum_{k=Fe,Cr,Ni} ES^{k}_{pure} C_k \ . \tag{2.97}$$

These saddle point energies are correct when the equilibrium energies for each of the elements are the same as the equilibrium energy for the alloy; although this is not necessarily true, equations 2.96 and 2.97 are a sufficient approximation.

Combining equations 2.80 through 2.84, the migration energies for Cr, Ni and Fe through vacancies can be expressed as,

$$E^{Cr,v}_m = ES^{Cr}_{Fe-Cr-Ni} - Z\left[\frac{1}{2}(C_{Cr}+1)E_{CrCr} + \frac{C_{Ni}}{2}E_{NiNi} + \frac{C_{Fe}}{2}E_{FeFe} + C_v E_{Cr-v}\right]$$
$$+ ZC_{Ni}E^{ord}_{NiCr} + ZC_{Fe}E^{ord}_{FeCr} \tag{2.98}$$

$$E^{Ni,v}_m = ES^{Ni}_{Fe-Cr-Ni} - Z\left[\frac{1}{2}(C_{Ni}+1)E_{NiNi} + \frac{C_{Cr}}{2}E_{CrCr} + \frac{C_{Fe}}{2}E_{FeFe} + C_v E_{Ni-v}\right]$$
$$+ ZC_{Cr}E^{ord}_{NiCr} + ZC_{Fe}E^{ord}_{FeNi} \tag{2.99}$$

$$E^{Fe,v}_m = ES^{Fe}_{Fe-Cr-Ni} - Z\left[\frac{1}{2}(C_{Fe}+1)E_{FeFe} + \frac{C_{Ni}}{2}E_{NiNi} + \frac{C_{Cr}}{2}E_{CrCr} + C_v E_{Fe-v}\right]$$
$$+ ZC_{Fe}E^{ord}_{FeCr} + ZC_{Ni}E^{ord}_{FeNi} \tag{2.100}$$

Allen et al. adjusts the pre-exponential factors (namely, the jump frequencies and their ratios) such that the resulting diffusion coefficients calculated at 1200°C best match experimental diffusion data by Rothman et al. [63] over a wide range of Fe-Cr-Ni compositions. Results from the MIK model, compared to Perk's model calculations in figure 2.21, show better agreement between calculated Cr concentration levels and the concentrations found from auger electron spectroscopy (AES) measurements in proton-irradiated Fe-Cr-Ni and Ni-Cr high purity alloys at temperatures between 200 – 600°C [73, 74].

The MIK model is also very good at calculating RIS at the intermediate temperature range of 400 – 500°C for a Fe-based 20Cr-24Ni alloy. Figure 2.22 shows the MIK model calculations for Cr concentration vs. AES measurements as a function of temperature [33]. Although the model over-predicts Cr depletion at lower temperatures and under-predicts segregation at the highest temperature, it is most effective at the intermediate temperature. Moreover, figure 2.23 shows that the model is effective in

calculating the concentration profile for Cr as a function of dose up to 3 dpa. By this point, it is clear that RIS has saturated, so no appreciable change in the model calculations or degree of segregation is expected.

Allen et al. [29, 32, 33] are able to show good agreement between model and experiment using only one mechanism for RIS where segregation results from preferential diffusion of one atom type through the vacancy flux. Unfortunately, the model requires ordering energies as fitting parameters to help reproduce the segregation data. The ordering energies do not have any basis in experimental measurements. Moreover, they are also not used in a self-consistent manner in that they are not accounted for in the thermodynamic factor.

Faulkner et al. [75-78] have also focused considerable attention on RIS modeling and the segregation of impurity atoms in austenitic stainless steels. They rely upon a solute-defect drag mechanism, whereby the binding energy between a particular solute type and the defect flux enables the diffusion of the defect flux to effectively "drag" particular types of solute atoms to sinks, including the grain boundary. This work has focused primarily on segregation in binary and ternary systems of Fe with impurity atoms, such as Si, C, B or P, where the model is used to calculate maximum segregation according to the equation, in this case for P, shown by:

$$C_P^{\max} = C_g \frac{E_b}{E_f} \left[\frac{C_b^j \exp\left(E_b^j/kT\right)}{\sum_j C_g^j \exp\left(E_b^j/kT\right)} \right] \left[1 + \frac{\xi K_0 F(\eta)}{ADk^2} \exp\left(E_f^j/kT\right) \right], \tag{2.101}$$

where C_g is the concentration of all impurities in the grain, E_b^j is the binding energy between the impurity atom j and self-interstitial, E_f^j is the interstitial formation energy and C_g^j is the concentration of impurity atom j. Basically, all impurity atoms have to compete for self-interstitial sites, which are represented in the denominator of the first bracketed term, and the competition depends, of course, on the binding energy. Meanwhile, ξ is the defect production efficient, K_0 is the defect production rate, $F(\eta)$ is the recombination term, A represents the vibrational entropy surrounding the defect, D is the diffusion coefficient, and k^2 is the sink efficiency.

33

Faulkner et al. has assessed impurity segregation in Fe-Cr-Ni alloys, but the models are not constructed to determine bulk concentration segregation, such as Cr depletion. While these models offer an interesting perspective on solute-interstitial binding, they are not necessarily applicable to RIS modeling for Fe, Cr and Ni. Furthermore, recent work by Tucker et al. [79] has suggested that some of the assumed interstitial-solute binding energies may be unrealistically large values.

2.3 RIS and Oversized Solute Additions

Oversized solute additions have been made to austenitic stainless steels to examine the effect on the radiation-induced microstructural evolution and radiation-induced segregation (RIS). The term 'oversized' is a generic term that describes any solute type that is larger than the matrix atoms. More specifically, one could think of the oversized atoms as having a larger-than-average atomic volume. For a ternary Fe-Cr-Ni alloy, this includes many transition elements, many of which have been studied in detail.

Oversized solutes are thought to create a localized strain field through their size difference with the matrix and thus act through vacancy or interstitial trapping mechanisms to enhance recombination of point defects [6, 80]. The increase in recombination leads to fewer point defects that can diffuse to sinks and cause changes in microstructure or microchemistry. In effect, the oversized solutes are intended to 'heal' the matrix from damage induced by radiation.

To study the effect of oversized solute additions, many irradiations have been performed using neutrons, protons, heavy ions, and electrons at a variety of temperatures and many different doses. The results of these irradiations have reported some widely varying results but have generally shown an improvement in radiation stability through the use of oversized elements. The remainder of this section will present experimental measurements that have demonstrated RIS reduction with oversized solutes.

2.3.1 Effects of Oversized Solute Additions on RIS

Gessel and Rowcliffe [81] were some of the first to propose that additions of Nb atoms could act as recombination sites for trapped vacancies and diffusing interstitials

and result in less RIS. A number of studies followed that examined experimentally the role of oversized solute additions on RIS. Figure 2.24 shows selected Cr depletion data as a function of dose for a variety of irradiation experiments covering He^+, p^+, e^- and neutron irradiations [18, 21, 23, 24, 28, 82, 83]. The figure breaks the data into groups along the lines of oversized solute type and also irradiation particle type. Symbol shading represents the particle type, with grey, closed symbols for proton irradiations, black, closed symbols for neutron irradiations, cross-hatch symbols for He^+ irradiations, and open symbols for electron irradiations. Meanwhile, symbol shape represents the oversized solute type, with square symbols for Zr, diamonds for Hf, triangles for Ti and circles for Nb. All alloys are a 316-type SS with the exception of the data from Busby et al. [18] which is for 304L. The purpose of the figure is to demonstrate some of the differences between particle types and also differences in effectiveness of different solute types.

In work done by Kato et al. [23], six different oversized solute additions, V, Ti, Nb, Ta, Zr, and Hf, were made to 316L alloys. The samples were irradiated using in a high voltage electron microscope (HVEM) at 1 MeV to a dose of 10.8 dpa at 500˚C. Shown in figure 2.25, the segregation results were mixed. According to the figure, while V and Ti demonstrated a moderate reduction in RIS at the grain boundary, neither Nb nor Ta appeared to have any effect on the RIS. Meanwhile Hf and Zr showed almost complete suppression of segregation. The authors attributed the poor RIS results for both Ta and Nb to be due to a low vacancy binding energy. Estimates were made of the binding energies, shown in table 2.2, both for vacancies and interstitials, even though a binding of oversized solutes with the interstitial flux seems unlikely due to size effects. Mysteriously, Ti was estimated to have the lowest binding energy of 0.14 eV compared to 0.18 eV for Nb, despite the fact that Ti showed better segregation behavior than the Nb alloy did. Unfortunately, no estimates of vacancy binding energies were given for Zr and Hf in order to demonstrate the binding energy necessary for complete RIS suppression.

Sakaguchi et al. [21] did a combined computational and experimental study of the effects of 0.5 at% Ti, Nb, Hf and Zr addition to a 316SS using 1 MeV electron irradiation at 500°C. Although the authors' work is covered in greater detail later, the highlights of the work is that Hf and Zr addition resulted in nearly complete suppression of RIS, with

less RIS reductions shown for Nb and Ti. What is interesting is that Nb and Ti results do not appear to be that different, contrary to the work of Kato et al. [23]. In fact, figure 2.26 shows that with increasing Nb concentration, considerable reductions in both Cr depletion and Ni enrichment are seen.

The RIS measurements were used to estimate a solute-vacancy binding energy, as given in figure 2.27. Nb and Ti binding energies were estimated ranging between 0.3 – 0.4 eV, somewhat higher than the value estimated by Kato et al. [23]. Zr and Hf had the largest estimated solute-vacancy binding energies because they demonstrated the most reduction in RIS, with Hf having the highest binding energy approaching 1.0 eV.

Kasahara et al. [24] show different results from both Kato and Sakaguchi. Irradiating a 316SS with 0.2%Zr using 1 MeV electrons to 10 dpa, a decrease in RIS was still measured, but it was not the near-complete suppression of RIS as demonstrated by previously, as shown in figure 2.28. The figure also shows data for an alloy with 10% Mn additions, which is not relevant to the discussion here, but the data for Zr clearly shows that, although the segregation is less than the reference alloy, Cr depletion is still evident, perhaps half the Cr depletion as the reference. In this case, there is a temperature dependence of the effectiveness of Zr addition in reducing RIS, with the difference between reference and oversized solute decreasing with increasing temperature. This is shown in figure 2.29 where the amount of Cr depletion and Mn depletion is plotted as a function of temperature. The results are significant because they offer experimental evidence that the oversized solute is less effective at mitigating RIS at higher temperatures.

Shigenaka et al. [20] performed 400 keV He$^+$ irradiation of 316L using Zr at 0.07, 0.21 and 0.41 wt% at 500°C to doses of 0.85 and 3.4 dpa. A strong correlation was found between increasing Zr content and decreasing RIS, presented in figure 2.30 with Cr depletion plotted against solute concentration for the two radiation doses. The figure depicts almost complete suppression of RIS at 3.4 dpa with 0.41 mass% Zr. The implication of Shigenaka's study is that increasing oversized solute concentrations should not only decrease the amount of segregation that occurs but also decrease the size of dislocation loops, as will be discussed in the next section. This depends, of course, on the concentration of oversized solute that remains in solution, as precipitation of the solute

will prevent their ability to act as trapping sites and enhance point defect removal. Shigenaka observed the presence of precipitates, but only in the highest Zr sample at 0.41 wt% and furthermore states that they had formed only during irradiation.

In more recent work, irradiations of 0.3 at% Hf and Pt in high purity (HP) 316SS were done at 500˚C to 50 dpa using Ni-ions and at 400˚C to 2.5 dpa using protons [25, 44]. The purpose of the study was to examine the influence of mass-misfit vs. size-misfit on microstructure. Both elements have similar mass-misfits but largely different size-misfits, with Pt having a size-misfit of 9.84 % and Hf at 25.04 %.

Examination of the RIS measurements for the proton-irradiated samples showed that both the 316+Pt and 316+Hf demonstrated better retention of Cr at the grain boundary than the reference alloy at 2.5 dpa, with Hf showing slightly better performance [25]. By 5 dpa, however, the Hf alloy showed a small marginal decrease in RIS as compared to the reference alloy, suggesting that the effect of the solute addition was merely to delay the onset of RIS. The data is presented in table 2.3 and offers both matrix and grain boundary concentrations for major and minor alloying elements, along with oversized solute concentrations. It is worth noting that no change in oversized solute concentration was measured at the grain boundary for the Pt or Hf alloys.

One important factor that may have contributed to more segregation for the oversized solute alloys at 5 dpa is the irradiation-induced precipitation of the oversized solute. Shigenaka et al. [20] saw the precipitation of Zr during irradiation in the alloy with the highest Zr content, but similar precipitation did not occur in the low-Zr alloys. If the Hf alloys in this study underwent precipitation of the solute atom during irradiation, or saturation of the trapping strength of the Hf, it would remove the ability to trap point defects and would explain the onset of RIS and void swelling. Another important insight to gain from this study is the effect of mass misfit and size misfit. While size misfit clearly plays a role in altering the microstructure, mass misfit does not appear to play a role in reducing RIS.

In a recent study examining the RIS behavior of proton-irradiated 316SS at 400°C [28], the effect of Zr addition on segregation is unclear. Figure 2.31, shows Ni enrichment and Cr depletion for a reference Fe-18Cr-8Ni-1.25Mn alloy without Zr and two similar alloys with 0.04 and 0.16 at% Zr. Looking at the alloy compositions, it

37

should be pointed out that there was no true reference alloy to compare to the +Zr alloys for Cr depletion and Ni enrichment. The changes in Ni and Mn content are small, but it is difficult assess their full impact on Cr depletion. Furthermore, even though the authors concluded that there was no observed benefit of Zr on the amount of Cr depletion, comparisons between the alloys were not even made at the same dose, with 0.5 dpa for the reference and the higher dose of 1.0 dpa for the +Zr alloys, where RIS should be higher anyway. Finally, the results showed that Ni enrichment was dramatically reduced for Zr addition, while Cr depletion mysteriously increased, suggesting that a different element was enriching to account for the Cr depletion.

Neutron irradiation results further complicate the assessment of oversized solutes [28]. 304L doped with 0.25% Zr was irradiated with neutrons to doses of 0.38 – 19 dpa, between 430 - 444°C. Table 2.4 shows the measured grain boundary concentration for Fe, Cr and Ni at the three irradiation doses for the +Zr alloy. At 0.38 dpa, despite the fact that no radiation damage was observed in the specimen, grain boundary Cr depletion was measured at 11 wt%. The high level of RIS measured at 0.38 dpa is far more than seen in the literature [5, 26-29, 84] and significantly higher than predicted by the MIK model [32], where Cr depletion is expected to be < 5 wt% for 304-type alloys in this temperature range. And whereas the amount of Cr depletion should increase with increasing dose, the amount of Cr depletion actually decreased from 11 wt% to 9 wt% between 0.38 to 19 dpa. Grain boundary Ni enrichment is also much higher than seen in the literature [17, 25, 26, 28, 33], with enrichment of 38 wt% at 19 dpa. Without a reference alloy for the study, there was no point of comparison to understand or explain the higher-than-expected RIS, making the data not credible. The results from this study of Zr additions on RIS cannot be supported by other literature data and are inconsistent with RIS modeling. Consquently, no consideration is given to the RIS results from this study for assessing oversized solute effects on RIS.

Still, differences among the ion irradiation studies on solute effectiveness on RIS, combined with electron irradiation results that show complete suppression of RIS with Hf and Zr, illustrate that the behavior of these oversized solutes is not yet well understood. Although many authors have studied experimental results, and while Sakaguchi et al. [21] has done a best fit of rate theory calculations to experimental data, none have

satisfactorily explained how the oversized solutes affect point defect behavior and consequently, RIS. Furthermore, there is no explanation for why RIS results vary so widely between experiments.

2.3.2 Effect of Oversized Solutes on Microstructure

The proposed effect by oversized solutes of enhanced recombination means that the point defect flux to sinks, such as grain boundaries, should decrease. This also translates into fewer point defects forming the defect microstructure, with either a reduction in dislocation loop density or size, or a combination of both. This section will discuss the defect microstructure as a consequence of oversized solute additions.

In work done by Watanabe et al. [66], Ti and Nb were used in Fe-16Cr-17Ni to evaluate the effect on microstructural evolution during 1 MeV electron irradiation. The alloys contained 0.025 and 0.1 at% Nb and 0.25 at% Ti. The alloy with Ti had a higher vacancy cluster density than the Nb alloys at low dose, 0.1 dpa. This is shown in figure 2.32 where the vacancy cluster density for the Ti alloy is actually similar to the reference alloy at higher doses. However, the average size of the vacancy clusters is not reported. This is significant because by 2.0 dpa, Ti showed the strongest reduction in swelling of the two elements, demonstrated in figure 2.33. The lower swelling for the Ti alloy as compared to the reference or the Nb alloy indicates that despite the high vacancy cluster density, the average size of these clusters is small and make overall void swelling less significant. Interestingly, despite the higher void density, the Ti alloy showed the lowest loop density at all temperatures, shown in Arrhenius plot of loop density versus inverse temperature in figure 2.34. These differences in behavior between the Ti and Nb alloys was explained by a lower binding energy between Nb atoms and vacancies as compared to Ti, thus making Ti more effective in enhancing recombination and reducing the point defect concentration.

Shigenaka et al. [21] studied loop microstructure on 316L with 0.07 and 0.21 wt% Zr additions after 400 keV He$^+$ irradiation. Table 2.5 lists the dislocation loop data as for the reference, 0.07 wt% and 0.21 wt% alloys. The authors reported a decrease in average loop diameter with increasing Zr and an overall decrease in the dislocation density at 0.07 and 0.21 mass% Zr compared to the reference alloy. However, the higher Zr sample at

0.21 mass% had a higher dislocation density than the lower Zr sample, suggesting more loop nucleation with further increases in the amount of oversized solute while average dislocation sizes decreased.

Zr was used in a proton irradiation study of HP304SS with 0.04% and 0.16% Zr to doses of 1.0 dpa at 400 °C [85]. Here, both loop and void densities showed large decreases with increasing Zr, while the sizes generally remained the same. This contradicts the theory that oversized solutes act as dislocation nucleation sites and increase their density [20]. However, the effect of Zr addition did follow the expected trend of reducing the overall swelling with increased oversized solute concentration.

Microstructure studies with Pt and Hf additions were also carried out using high purity 316SS irradiated with p^+ at 400°C and Ni^{++} at 500°C [25, 44]. For the Ni-ion irradiation, there was no void formation or swelling for either of the 316+Hf alloys at doses up to 10 dpa. At higher dose, swelling seemed to depend on the pre-irradiation heat treatment of 900°C or 1100°C, with annealing at 1100˚C for 30 minutes continuing to suppress void formation and swelling up to 50 dpa. The percent void swelling is shown in figure 2.35 as a function of radiation dose. Notice that swelling for 316+Pt, on the other hand, is actually higher than the reference alloy at all studied doses suggesting that Pt had a negative impact on defect microstructure.

The loop volume fraction is presented in figure 2.36, which shows the combination of loop size and density in the loop volume fraction as a function of dose [44]. Overall, the loop volume fraction is lowest in the 316+Hf (1100°C) sample. But the behavior for the alloys is somewhat complicated. While the reference alloy volume fraction quickly saturates, 316+Pt is highest at low dose, then decreases to a similar level as 316+Hf (1100°C) at 50 dpa, while 316+Hf (900°C) increases slowly to exceed the reference value by 50 dpa. Similar to Shigenaka's work, dislocation loop sizes were smaller in diameter with a higher density for the 316+Hf compared to the base 316SS, as shown in figure 2.37 for loop diameter as a function of dose. 316+Pt, however, showed a small increase in loop size and density at intermediate doses, though only the increase in loop density persisted at 50 dpa.

For proton irradiation to 2.5 dpa at 400°C, the results were similar to the Ni-ion irradiations. The 316+Pt experienced an increase in both loop and void diameters and

densities relative to the reference alloy, while the 316+Hf has increased loop densities, but decreased loop diameter with no swelling observed. While dislocation loop formation in the alloys was similar between the two different irradiations, void swelling is greatly increased in the 316+Pt alloy relative to the reference alloy after proton irradiation.

Although RIS results for neutron irradiations showed little effect on RIS behavior due to oversized solute additions, Ohnuki et al. [86] demonstrated that oversized solutes can have a substantial impact on void swelling. Using fast neutron irradiation at 425°C, 520°C, and 600°C, Ohnuki studied 316L with additions of V, Ti, Ta, Zr, and Hf at doses from 30 – 35 dpa. Among the smaller oversized solutes, V, Ti and Ta still showed substantial void swelling. However, Zr and Hf results were markedly different, with very little void swelling at 425°C, and complete swelling suppression at the higher two temperatures.

The alloys used in the study by Ohnuki et al. [86] were the same alloys studied with electron irradiation by Kato et al. [23]. These alloys were very low carbon, < 0.01 wt% carbon, with the 316L-Zr having only 0.003 wt% C, to prevent XC carbides from forming in the matrix. The authors report no precipitate formation in the unirradiated alloy. However, at 520°C and 600°C, fine-scale precipitation was reported due to irradiation for both the Zr and Hf alloys. The precipitates were studied with x-ray diffraction (XRD) and determined to be ZrC and HfC, contrary to Allen et al. [83] who reported $ZrNi_5$ and $HfNi_5$ precipitates both before and after irradiation. Interestingly enough, Kato et al. [23] reported no precipitate formation after electron irradiation in the same alloys, so the conclusion is that neutron irradiation, with the lower dose rates over longer time scales, was able to induce radiation-induced precipitation of the oversized solutes, shown in figure 2.38 both the Zr and Hf alloys after irradiation to 35 dpa at 600°C. And these radiation-induced precipitates, inferred as being coherent in nature, were able to act as point defect sinks to enhance recombination. Ohnuki et al. conclude, then, that Zr and Hf show superior void swelling suppression due to stronger vacancy trapping and additional defect recombination at precipitate sinks.

2.4 RIS Mechanisms in Oversized Solute Alloys

Understanding the effects of impurity additions on RIS has long been studied using kinetic rate-theory modeling. Some authors have focused on both undersized and oversized solute additions and their effects on creep [6] or swelling [6, 87] with the conclusion that both vacancies and interstitials can be trapped by the solutes and have the effect of reducing defects by enhancing recombination. Similar assumptions were made for early work on the modeling of RIS and the impact of solute additions [88]. Only more recently has work focused on a single mechanism for enhanced recombination with oversized solute additions. A discussion of the mechanisms for reducing RIS through oversized solute addition will be presented in more detail in this section. This section will start with a correlation of relative sizes of solute atoms to explain their effects on solute segregation. A detailed discussion of the solute-defect binding mechanisms will be presented, and the section will end with a brief description of an alternative interstitial-impurity model

2.4.1 Linear Size Factors of Oversized Solutes

As identified already, size effects can play a large role in segregation behavior. King [13] developed a relationship that described the size differences between two components in an alloy using atomic sizes to calculate what he termed a linear size factor, L_{sf}. This is shown as:

$$L_{sf} = \left[\left(\Omega_{solute} \middle/ \Omega_{solvent} \right)^{1/3} - 1 \right] \times 100\%, \tag{2.102}$$

where Ω_{solute} is the atomic volume of the oversized solute atom and $\Omega_{solvent}$ is the atomic volume of the matrix. The linear size factors were used to predict the direction of segregation for elements in a binary alloy model and some discrepancies arose. These were corrected by Kornblit et al. [14] by developing an alternative. They proposed a volume misfit parameter based on the metallic radii of the solute and solvent atoms. The authors reason that, when considering diffusion processes, distances between an

oversized solute atom and its nearest neighbors are more important than the average volume for the atoms of each element individually. The volume misfit is defined by

$$\left[\left(r_{solute} \Big/ r_{solvent}\right) - 1\right] \times 100\% ,$$ (2.103)

where r is the atomic radius (i.e. not the lattice parameter) of the solute and solvent. As discussed already, with data presented in table 2.1, the new relationship was able to explain the discrepancies in RIS trends for several systems.

Fournier et al. calculated linear size factors of a variety of oversized solute atoms based on atomic volumes for the oversized solutes and a Fe-Cr-Ni system. These experimentally-determine linear size factors are shown in table 2.6.

2.4.2 Solute-Defect Binding

Mansur et al. [6, 80], modeled the effects of impurity atoms (either oversized or undersized) on swelling and creep. The authors developed a trapping model that included both interstitial and vacancy trapping. For oversized solute atoms, only one mechanism, that for trapping vacancies, is logical, but Mansur assumed that both vacancies and interstitials can be trapped by an impurity, though obviously not both at the same time. The effects of the impurity were modeled indirectly by adding three additional terms to the rate equations for vacancy and interstitial concentrations. These terms include 1) a trapping mechanism, whereby freely migrating interstitials are captured by the oversized solute atom, forming a vacancy-solute complex, 2) a recombination mechanism by which freely migrating interstitials are able to recombine with the bound vacancy when the interstitial travels through the recombination volume of the vacancy-solute complex, and 3) a release mechanism, where bound vacancies are able to dissociate from the vacancy-solute complex. These terms are reflected in the reaction rate equations shown by:

$$\frac{\partial C_v}{\partial t} = -\nabla \cdot J_v + G_v - RC_v C_i - K_v C_v - C_v \sum_l \kappa_{vl} \left(C_l^{t,0} - C'_{vl} - C'_{il}\right) - $$
$$C_v \sum_l R_{il} C'_{il} + \sum_l \tau_{vl} C'_{vl}$$ (2.104)

43

$$\frac{\partial C_i}{\partial t} = -\nabla \cdot J_i + G_i - RC_v C_i - K_i C_i - C_i \sum_l \kappa_{il} \left(C_l^{t,0} - C'_{vl} - C'_{il} \right) -$$
$$C_i \sum_l R_{vl} C'_{vl} + \sum_l \tau_{il} C'_{il} \qquad (2.105)$$

The equations are rather complicated but each of the terms will be explained in detail. The first term is the divergence of the defect flux, $-\nabla \cdot J_x$, where x is for the defect type, G_x is the defect production rate, R is the recombination coefficient for the concentrations of vacancies and interstitials, C_v and C_i, respectively, while K_x is the term for defect removal at sinks. There are three remaining parts to these equations, shown by:

$$C_i \sum_l \kappa_{il} \left(C_l^{t,0} - C'_{vl} - C'_{il} \right), \qquad (2.106)$$

which represents the trapping term, in this case for interstitials, taking the sum of all of the traps, l, where κ_{il} is the trapping coefficient, $C_l^{t,0}$ is the original trap concentration for trap type l, while C'_{vl} and C'_{il} are the concentration of vacancies and interstitials already trapped by the trap type l. The next term,

$$C_i \sum_l R_{vl} C'_{vl}, \qquad (2.107)$$

is for the recombination of defects at the traps, again summed for all traps, where R_{vl} is the recombination coefficient for the recombination of free interstitials with trapped vacancies. Finally the term,

$$\sum_l \tau_{il} C'_{il}, \qquad (2.108)$$

is for the dissociation of trapped interstitials with the impurity atom, where τ_{il}^{-1} is the dissociation coefficient. A similar equation describes the dissociation of vacancies.

Three of the variables require further definition, namely the trapping, recombination and dissociation coefficients. First, the trapping coefficient represents a trapping volume around the impurity, shown by:

$$\kappa_{xl} = 4\pi r'_{xl} D_x N_D, \qquad (2.109)$$

where r'_{xl} is the trapping radius, D_x is the diffusion coefficient for the defect type x, and N_D is the average atomic density. The recombination coefficient is similar, where:

$$R_{xl} = 4\pi r_{xl} D_x N_D \,,$$

and r_{xl} is the recombination radius. The last term is described by:

$$\tau_{xl}^{-1} = \left(\frac{b^2}{D_x^0}\right) \exp\left[\frac{\left(E_{xl}^b + E_x^m\right)}{kT}\right],$$ (2.110)

where b is the jump distance, D_x^0 is the pre-exponential factor of the diffusion coefficient, E_{xl}^b is the binding energy between the defect and the trap l, E_x^m is the migration energy of the defect, k is Boltzmann's constant, and T is the temperature. Since the $D_x = D_x^0 \exp\left(-E_x^m/kT\right)$, then τ can also be written as:

$$\tau_{xl}^{-1} = \left(\frac{b^2}{D_x}\right) \exp\left[\frac{\left(E_{xl}^b\right)}{kT}\right].$$ (2.111)

In Mansur's dissociation equation, the time constant reduces to the ordinary diffusion coefficient for a vacancy when $E_\alpha^b \to 0$. This matches the expectation for a freely migrating defect and makes this the preferred equation to describe solute-vacancy dissociation.

The rate equations for the traps, l, can now be written. A rate equation will be needed for each trap type, but for simplicity, just two equations are shown, one each for vacancies and interstitials, shown by:

$$\frac{\partial C_v'}{\partial t} = C_v \sum_l \kappa_{vl} \left(C_l^{t,0} - C_{vl}' - C_{il}'\right) - C_v \sum_l R_{il} C'_{il} - \sum_l \tau_{vl}^{-1} C_{vl}' \,,$$ (2.112)

$$\frac{\partial C_i'}{\partial t} = C_i \sum_l \kappa_{il} \left(C_l^{t,0} - C_{vl}' - C_{il}'\right) - C_i \sum_l R_{vl} C'_{vl} - \sum_l \tau_{il}^{-1} C_{il}' \,.$$ (2.113)

The trap concentration can also be written as:

$$\frac{\partial C_l^t}{\partial t} = C_l^{t,0} - \sum_l \left(C_{vl}' + C_{il}'\right).$$ (2.114)

Note that since it is not an independent equation, it need not be solved, since the trap concentration can be solved by:

$$C_l^t = C_l^{t,0} - \sum_l \left(C_{vl}' + C_{il}'\right).$$ (2.115)

Based on the rate equations, Mansur calculated the fraction of traps occupied as a function of the binding energy. The results are shown in figure 2.39 which includes one line for calculations at a dose rate of 10^{-3} dpa/s at 650°C, and the other line for 10^{-6} dpa/s at 500°C [6]. At the lower dose rate and temperature, which would be more representative of proton irradiations, even a binding energy of 0.5 eV only manages to have a trap occupation of less than 1% at any given time. Admittedly, the subsequent effect on RIS is not easy to determine based on this alone. Unfortunately, no attempt at calculating grain boundary segregation was made. Nevertheless, Mansur concluded that for the trapping mechanism to be effective in reducing radiation damage, binding energies up to 1.0 eV were necessary.

Sakaguchi et al. [21] used their RIS model, based on kinetic rate equations very similar to mechanisms employed in the Perks' and MIK model as presented earlier [29, 32, 33, 59, 60] to simulate the effects of an oversized solute present in solution in a Fe-Cr-Ni alloy. The mechanisms for trapping are similar to the work by Mansur. There are two exceptions, however. First, while Mansur includes multiple traps capable of trapping either vacancies or interstitials, the work by Sakaguchi only considers one oversized solute type which can trap vacancies. Second, Sakaguchi inaccurately describes solute-defect dissociation by including the coordination number in the dissociation term.

Otherwise, the mechanism remains the same, namely that the oversized solute can trap vacancies, lead to recombination events between trapped vacancies and freely migrating interstitials, and result in the dissociation of solute-defect complexes. The defect reaction rate equations are somewhat more straightforward, described by:

$$\frac{\partial C_v}{\partial t} = -\nabla \cdot J_v + G_{dpa} - K_{iv}C_vC_i - S_vD_v\left(C_v - C_v^{eq}\right) - $$
$$K_vC^sC_v + \tau_vC_vC_v^s \qquad \qquad (2.116)$$

$$\frac{\partial C_i}{\partial t} = -\nabla \cdot J_i + G_{dpa} - K_{vi}C_vC_i - S_iD_iC_i - R_vC_v^sC_i. \qquad (2.117)$$

In these equations, $-\nabla \cdot J_x$ is the divergence of the defect flux, G_{dpa} is the defect production rate, $K_{iv}C_vC_i$ represents the recombination of vacancies and interstitials, and $S_vD_v\left(C_v - C_v^{eq}\right)$ and $S_iD_iC_i$ represent the loss of vacancies or interstitials to sinks. The

remaining terms of equations 2.116 and 2.117 represent the trapping mechanism, where $K_v C^s C_v$ is for the trapping of freely-migrating vacancies, $R_v C_v^s C_i$ is for the recombination of trapped vacancies with freely migrating interstitials, and $\tau_v C_v^s$ is for the release of vacancies from trapping sites. As for the individual variables in the equations, K_{iv} is the recombination coefficient, D_x is the diffusion coefficient, C_x is the concentration, S_x is the sink density, and C_v^{eq} is the thermal equilibrium concentration for vacancies. Here, x represents the defect type, either vacancies or interstitials.

The term $K_v C^s C_v$ represents the trapping of free vacancies, where C^s is the oversized solute concentration, and K_v is the capture coefficient,

$$K_v = 4\pi \cdot r_v' D_v N_D \tag{2.118}$$

with r_v' as the capture radius.

The last term of the vacancy rate equation is $\tau_v C_v^s$, where the dissociation coefficient of the vacancy-solute complex is τ_v. This was defined by Mansur et al. [80] already in equation 2.111, but Sakaguchi has a slightly different definition, described by:

$$\tau_v = \frac{Z D_v}{a_0^{\ 2}} \exp\left[-\frac{E_v^b}{k_B T} \right], \tag{2.119}$$

where Z is the coordination number, a_0 is the lattice spacing, k_B is Boltzmann's constant, T is the irradiation temperature, and E_v^b is the binding energy of the vacancy-solute complex. This is equivalent to equation 2.111 except for the coordination number Z. Since it was already pointed out that τ_v should reduce to the ordinary diffusion coefficient as $E_\alpha^b \to 0$, then it would indicate that Sakaguchi et al. erroneously included the coordination number in the equation for vacancy dissociation of solute-vacancy complexes.

The last term of the interstitial rate equation, shown by $R_v C_v^s C_i$, includes the recombination coefficient, R_v, of the vacancy-solute complexes, where:

$$R_v = 4\pi \cdot r_v D_v N_D . \tag{2.120}$$

The recombination coefficient includes the recombination radius, r_v. Unfortunately, Sakaguchi et al. provide no values for or insight into the determination of the capture and recombination radii, r_v' and r_v, respectively. Without values for these terms, it is difficult to compare the model results between Sakaguchi et al. and Mansur et al.

The oversized solute terms result in two additional rate equations for tracking the creation of vacancy-solute complexes and the loss of unbound solute atoms. These terms are represented by:

$$\frac{\partial C_v^s}{\partial t} = K_v C^s C_v - \tau_v C_v^s - R_v C_v^s C_i,$$ (2.121)

$$\frac{\partial C^s}{\partial t} = -K_v C^s C_v + \tau_v C_v^s + R_v C_v^s C_i,$$ (2.122)

where C_v^s is the concentration of vacancy-solute complexes.

Note that equation 2.122 does not need to be solved because, when incorporated into the rate theory model, it is no longer an independent equation. The concentration of unbound solute atoms can be found by:

$$C^s = C_0^s - C_v^s,$$ (2.123)

where C_0^s is the initial unbound solute concentration.

From this exercise Sakaguchi et al. [21] find that, although solute-vacancy binding can be effective in reducing the amount of grain boundary segregation, the mechanism is sensitive to the binding energy of the complexes and oversized solute concentration. The results, however, are rather contradictory. For example, figure 2.40 plotted the difference between grain boundary and matrix concentrations for Ni and Cr as a function of binding energy at two different temperatures, 573K and 773K. The data was plotted to a dose of 3 dpa with a solute concentration of 0.5 at%. Focusing just on the trends for Cr for now, one can see that at 723 K, differences in Cr depletion are not evident until binding energies are greater than 0.5 eV. Even then, at the binding energy of 1.0 eV, Cr depletion is still ~ 7 at%, compared to 12 at% at 0 eV. But figure 2.27 shows experimental and calculated depletion data, plotted this time as function of binding energy or linear size factor, on the same x-axis. Here, experimental measurements show virtually no Cr depletion for Zr and Hf, both with 0.5 at% additions and estimated

binding energies between 0.8 and 1.0 eV. This time, theoretical calculations match the experimental measurements in calculating virtually no Cr depletion. It should be pointed out that figure 2.40 was for a Fe-15Cr-20Ni alloy and figure 2.27 was for a Fe-18Cr-12Ni alloy with solute irradiated to 10.8 dpa. But these factors mean that in figure 2.27, the theoretical calculations should have resulted in even more Cr depletion because of the higher alloy Cr content and higher dose.

The theoretical results given in figure 2.26, where composition changes for Ni and Cr are plotted as a function of Nb concentration, also demonstrate discrepancies from figure 2.40. In the case of figure 2.26, Nb was assumed to have a binding energy of 0.4 eV, with irradiation temperature of 773 K. At 0.5 at% Nb, the model calculated only 2 at% Cr depletion. But figure 2.40 shows more than 10 at% Cr depletion at 0.4 eV with 0.5 at% additive. And figure 2.27 shows a model calculated Cr depletion of 3 at% at 0.4 eV. Even the measured values of Cr depletion for 0.5 at% Nb differ between figures 2.26 and 2.27.

In spite of the serious discrepancies that have been highlighted, the results of figure 2.40 from the work by Sakaguchi et al. do demonstrate one of the most important factors in the solute-vacancy trapping mechanism on RIS, namely the solute-vacancy binding energy.

2.4.3 Interstitial Impurity Trapping

A model developed by Nastar et al. [89] was used to simulate the trapping of interstitials by impurity atoms to explain the reduction in RIS shown experimentally with oversized solute additions. Assuming diffusion of interstitials as split dumbbells (along the [100] direction), the pure element interstitial migration energies are used to fit effective migration energies for the different interstitial pairs. Since there are 9 interstitial configurations and 3 different elements that can be displaced when the dumbbell diffuses, then there are 27 frequencies for interstitial diffusion that are defined. Rather than simplifying other RIS models, of course, this method introduces new complexities in trying to use interstitial diffusion to replicate RIS results with very little experimental diffusion data on which to parameterize the model. The result is nothing more than an array of fitting parameters that are used to match model results to existing

49

RIS data. The matrix of exchange frequencies can be tweaked to make the model match experimental data, but the values will not necessarily have any physical meaning based on experimental data.

Although this example pertains to how bulk interstitial diffusion is treated, more generally it highlights a significant problem with modeling oversized solutes to determine RIS. Ternary alloy systems already confront a lack of experimental data to parameterize interactions between the solvent atoms. Adding a fourth element to the system would make the model too complex and experimental values for the incorporation would be lacking. In the case of modeling an oversized solute, the only alternative is to simulate solute effects indirectly without explicitly defining the element mathematically, but this has the disadvantage of preventing the model to account for solute thermodynamics. The solute becomes immobile and effects such as solute-defect drag or solute enrichment or depletion at sinks are lost. This does not imply, however, that useful information about how oversized solutes affect RIS cannot be obtained. Even with the limitations, important insights can be made into how the solute atoms interact with point defects and change the irradiated grain boundary microchemistry.

Table 2.1 Segregation predictions based on volume misfit of solute in a binary alloy. Taken from [14].

$r_{solv}(\text{Å})$	Structure	Alloy	$r_{sol}(\text{Å})$	Structure of the solute when crystal	Volume misfit % $(r_{sol}/r_{solv})^3 - 1$	Direction of segregation (from ref. 1)
		Pd–Cu	1.278	fcc	−20	+
		Pd–Fe	1.24115	bcc	−27	+
1.3775	fcc	Pd–Mo	1.36255	bcc	−3	+
		Pd–Ni	1.2458	fcc	−26	+
		Pd–W	1.37095	bcc	−2	+
		Al–Ge	1.2249	diamond	−37	+
1.4315	fcc	Al–Si	1.17585	diamond	−45	+
		Al–Zn	1.3347	hcp	−19	+
		Cu–Ag	1.4447	fcc	+44	−
1.278	fcc	Cu–Be	1.1130	hcp	−34	+
		Cu–Fe	1.24115	bcc	−8	+
		Cu–Ni	1.2458	fcc	−7	+
		Ni–Al	1.4315	fcc	+52	−
		Ni–Au	1.44205	fcc	+55	−
		Ni–Be	1.1130	hcp	−29	+
		Ni–Cr	1.2490	bcc	+1	
1.2458	fcc	Ni–Ge	1.2249	diamond	−5	+
		Ni–Mn	1.36555	fcc (γ-phase)	+32	−
		Ni–Mo	1.36255	bcc	+31	−
		Ni–Si	1.450	rhomboh.	+58	−
		Ni–Si	1.17585	diamond	−16	+
		Ni–Ti	1.4478	hcp	+57	−
1.4478	hcp	Ti–Al	1.4315	fcc	−3	+
		Ti–V	1.3112	fcc	−26	+
1.24115	bcc	Fe–Cr	1.2490	bcc	+2	−
1.59855	hcp	Mg–Cd	1.4894	hcp	−19	+

51

Table 2.2 Estimated binding energies for oversized solutes in a 316L stainless steel [23]

Steel	Binding energy of additive-vacancy (eV)	Binding energy of additive-interstitial (eV)
316L-V	not estimated	~ 0
316L-Ti	0.14	~ 0
316L-Nb	0.18	~ 0.1
316L-Ta	not estimated	~ 0.1
316L-Zr	not estimated	~ 0.5
316L-Hf	not estimated	~ 0.5

Table 2.3 RIS data for a series of 316SS with Pt or Hf additions, irradiated with protons at 400°C to doses of 2.5 and 5 dpa [25].

Alloy	Dose (dpa)	# GB	# GB meas.	Fe	Cr	Ni	Mo	Mn	Si	Pt	Hf
316SS											
Avg. GB comp.	2.5	2	6	63.3	12.4	22	1.4	0.8	0.1		
Bulk comp				65.5	17.5	13.3	2.4	1.3	<0.1		
316SS + Pt											
Avg. GB comp.	2.5	2	6	64.9	15.4	15.7	2	1	<0.1	1	
Bulk comp				65.3	16.9	13.6	2	1.2	<0.1	1	
316SS + Hf											
Avg. GB comp.	2.5	2	6	64.3	15.9	15.6	2.5	1.1	<0.1		0.6
Bulk comp				65	17.1	13.6	2.4	1.3	<0.1		0.6
316SS											
Avg. GB comp.	5	2	6	59	10.8	27.9	1.7	0.6	<0.1		
Bulk comp				65.8	16.8	14.4	1.8	1.2	<0.1		
316SS + Hf											
Avg. GB comp.	5	2	6	63.3	12.3	22.2	1.5	0.7	<0.1		--
Bulk comp				64.6	17.4	14	2.2	1.2	<0.1		0.6

Table 2.4 Grain boundary concentration data for a FeCrNi alloy with Zr additions after neutron irradiation [83].

Table B10. Grain Boundary Compositions measured in the FeCrNi + Zr Alloy

Condition	Cr (wt%)	Fe (wt%)	Ni (wt%)	Zr (wt%)
19 dpa 430°C	9.6	33.8	52.1	2.5
3.7 dpa 431°C	8.1	51.3	40	0.4
0.38 dpa, 444°C	7.6	45.8	38.8	7.8
Matrix	18.5	67.3	14	0.25

Table 2.5 A 316+Zr alloy after 1 MeV electron irradiation to doses of 0.85 and 3.4 dpa with, (a) the average void diameter, and (b) the void density, as a function of temperature [24]

Zr Concentration (wt%)	Average Loop Density (m^{-3})	Average Loop Diameter (nm)	Total Dislocation Density (m^{-2})
0	8.0×10^{20}	82	2.0×10^{14}
0.07	3.9×10^{20}	35	4.3×10^{13}
0.21	1.2×10^{21}	23	8.7×10^{13}

Table 2.6 Experimentally-determine linear size factors of oversized solute atoms in a Fe-Cr-Ni alloy [25]

Element	Atomic number	Atomic mass (g)	Density (g cm^{-3})	Atomic volume (cm^{-3})	Linear size factor (%)
V	23	50.94	6.09	8.36	6.81
Pt	78	195.08	21.45	9.09	9.84
Ti	22	47.88	4.51	10.62	15.68
Nb	41	92.91	8.58	10.83	16.44
Ta	73	180.95	16.68	10.85	16.51
Zr	40	91.23	6.51	14.01	26.87
Hf	72	178.46	13.31	13.41	25.04
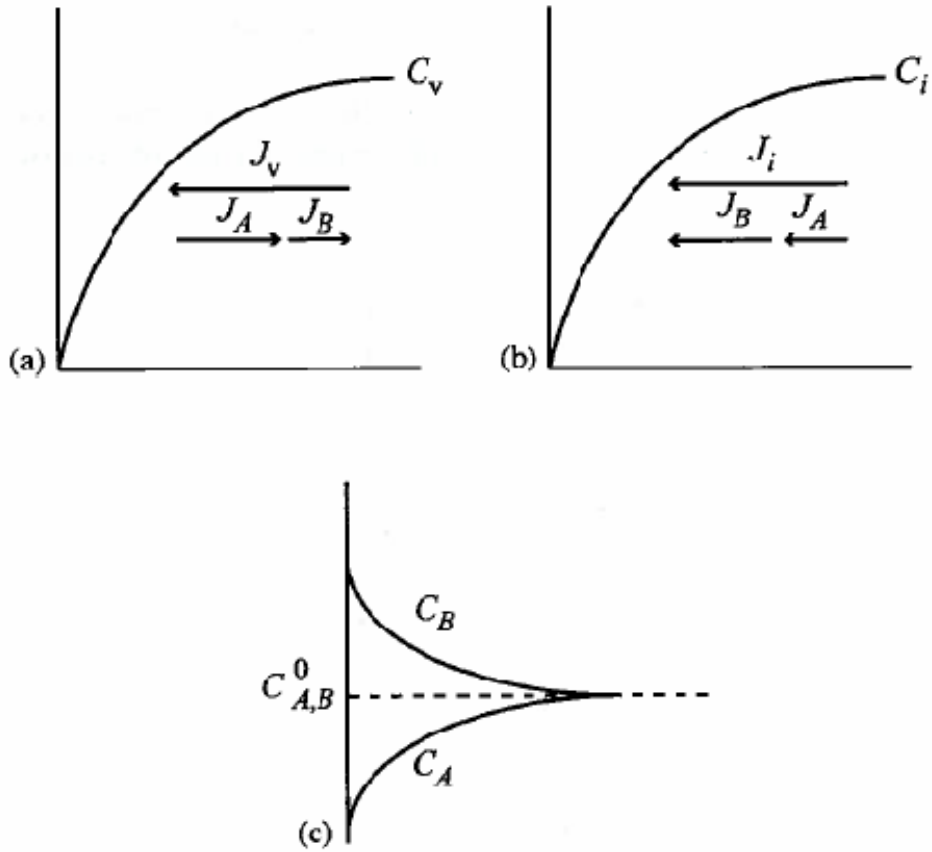
Figure 2.1 (a) The diffusion of A atoms through the vacancy flux is greater than the diffusion of B atoms through the vacancy flux; (b) the diffusion of B atoms through the interstitial flux is greater than A atoms; and (c) the resulting concentration profile shows the enrichment of B atoms and depletion of A atoms at the grain boundary [11].
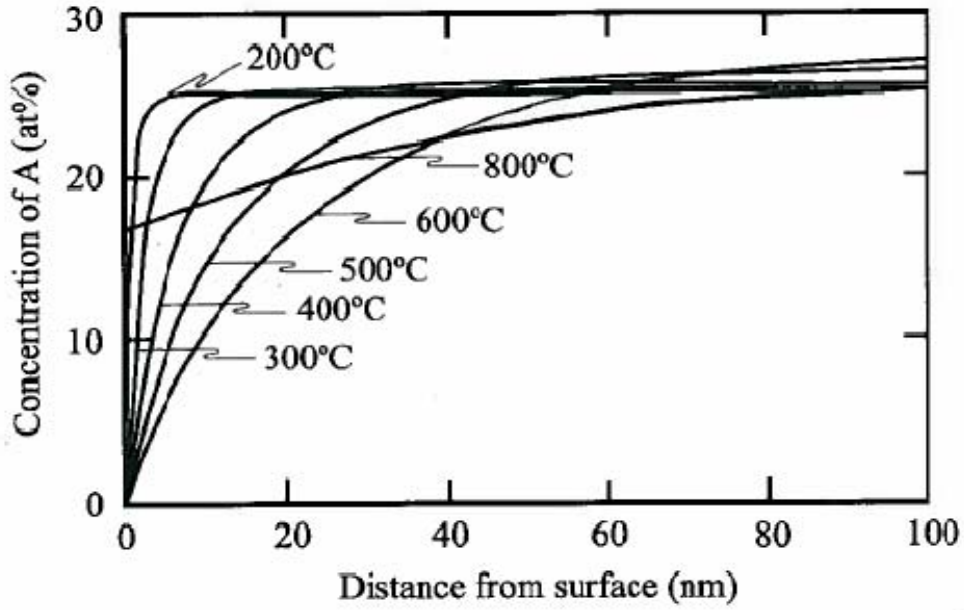
Figure 2.2 Calculated steady-state concentration profiles of element A in a B-25%A alloy as a function of distance from the grain boundary. The dose rate is 10^{-3} dpa/s. Taken from [11].
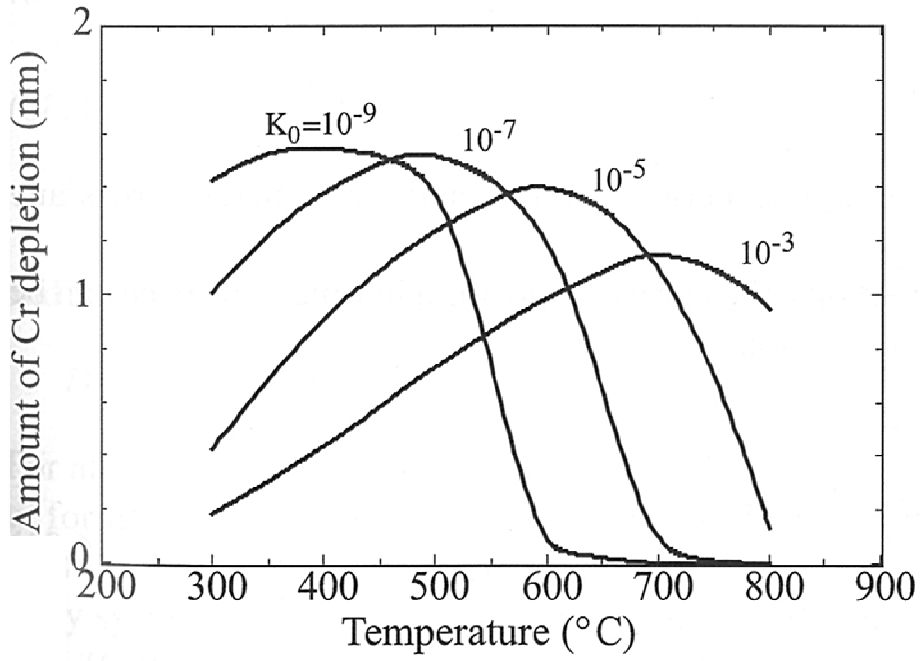
Figure 2.3 The temperature and dose rate regime in which stainless steels are susceptible to RIS [90].
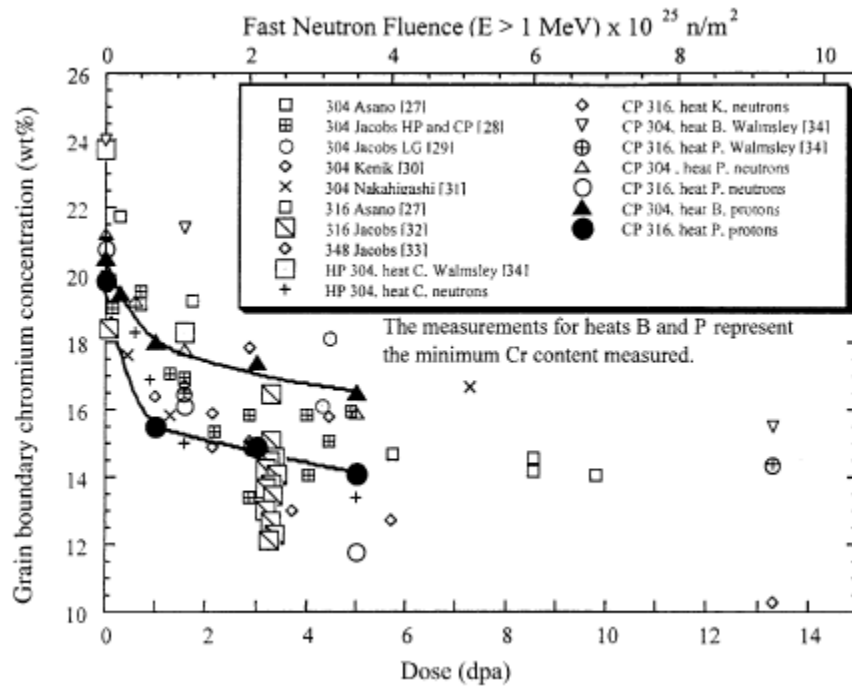
Figure 2.4 Experimental Cr GB measurements after neutron irradiation for 300 series stainless steels at various temperatures [91].
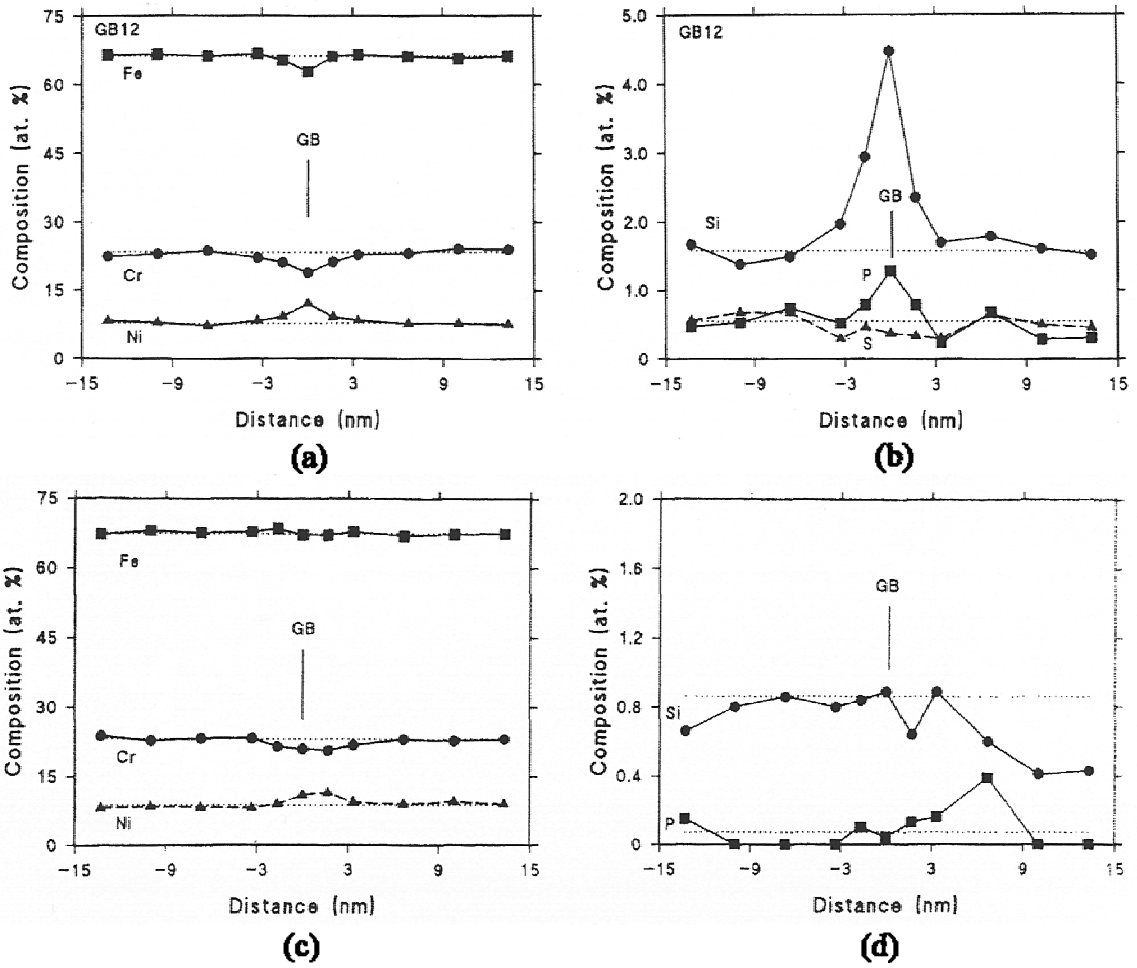
Figure 2.5 Concentration profiles of 304SS irradiated with neutrons at 288°C for a commercial purity alloy, showing (a) Fe, Cr and Ni, and (b) Si, P and S grain boundary concentrations; a high purity alloy, showing the grain boundary concentration for (c) Fe, Cr and Ni, and (d) Si and P.
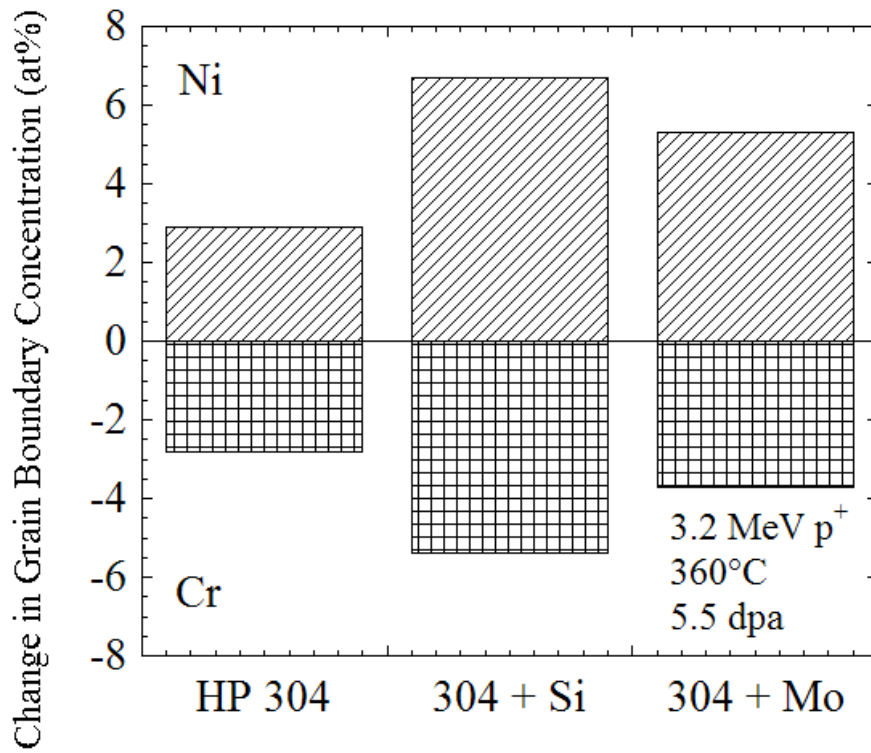
Figure 2.6 Change in grain boundary Ni and Cr concentrations for a series of HP 304SS with additions of Si or Mo after proton irradiation at 360°C to a dose of 5.5 dpa (Adapted from Ref. 18).
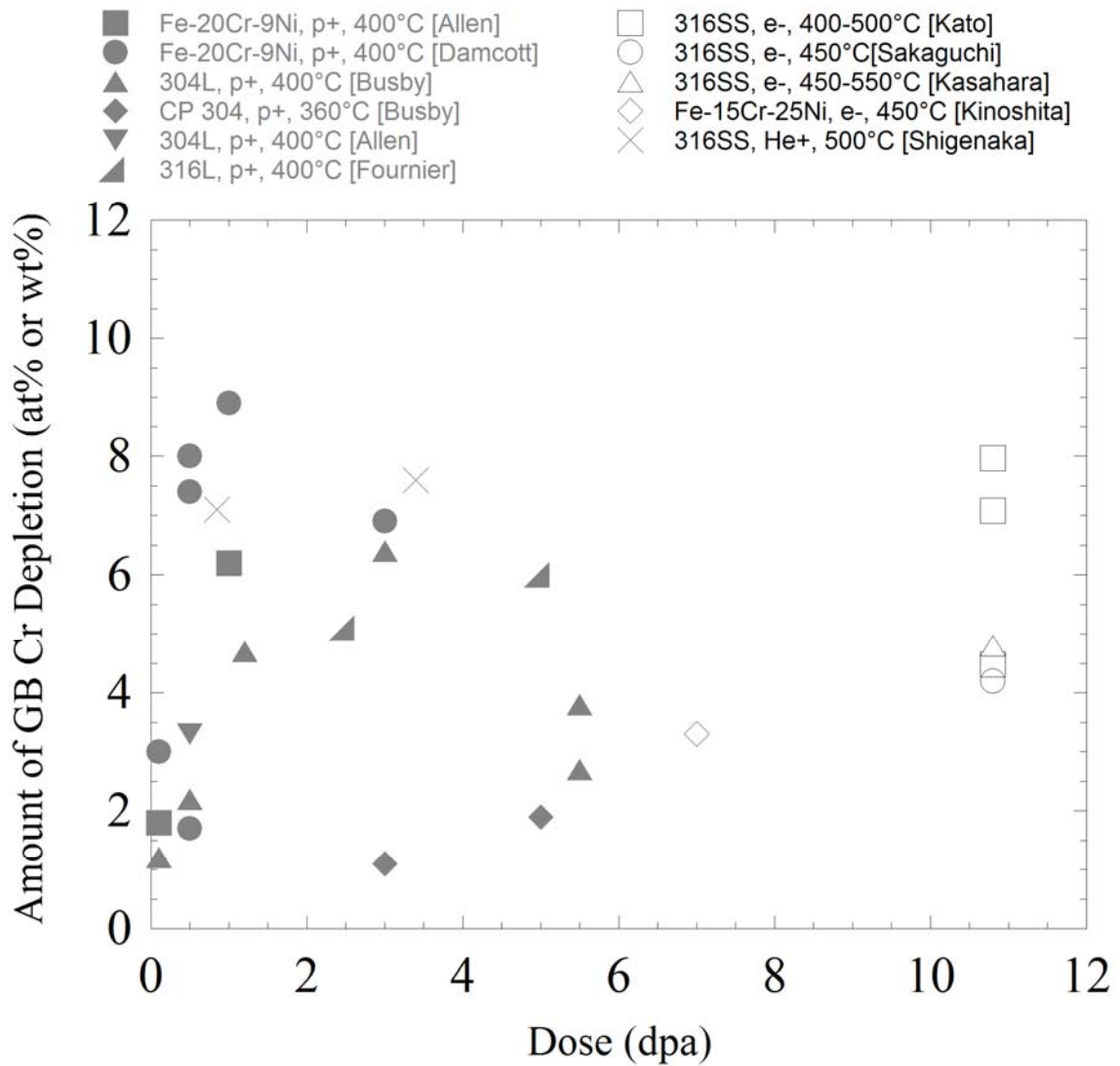
Figure 2.7 Amount of Cr depletion at the grain boundary as a function of radiation dose for a variety of Fe-based, 304 and 316 stainless steels. Symbol shading represents the particle type, with grey, closed symbols for proton irradiations, open symbols for electron irradiations, and x symbols for He$^+$ irradiations [5, 20-29].
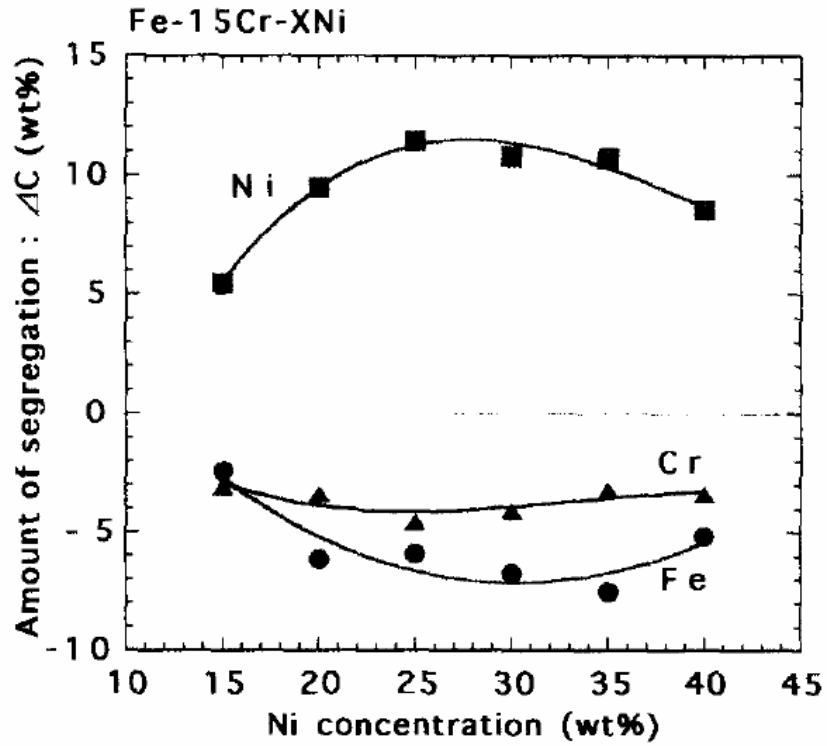
Figure 2.8 Grain boundary segregation for Ni, Cr and Fe as a function of Ni concentration for a constant 15Cr alloy after electron irradiation at 500°C to 7 dpa [22].
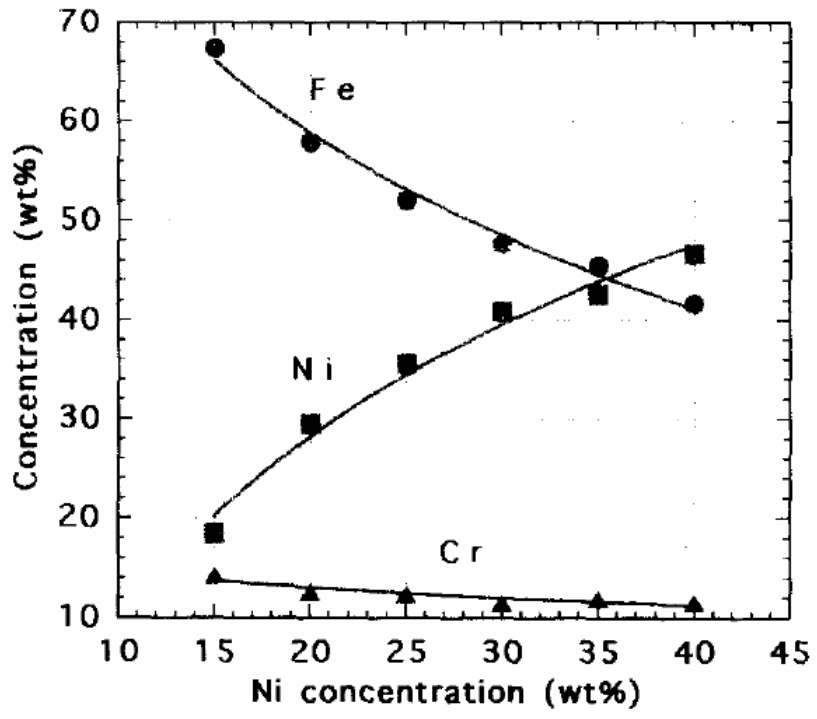
Figure 2.9 Grain boundary segregation for Ni, Cr and Fe as a function of Cr concentration for a constant 20Ni alloy after electron irradiation at 500°C to 7 dpa [22].
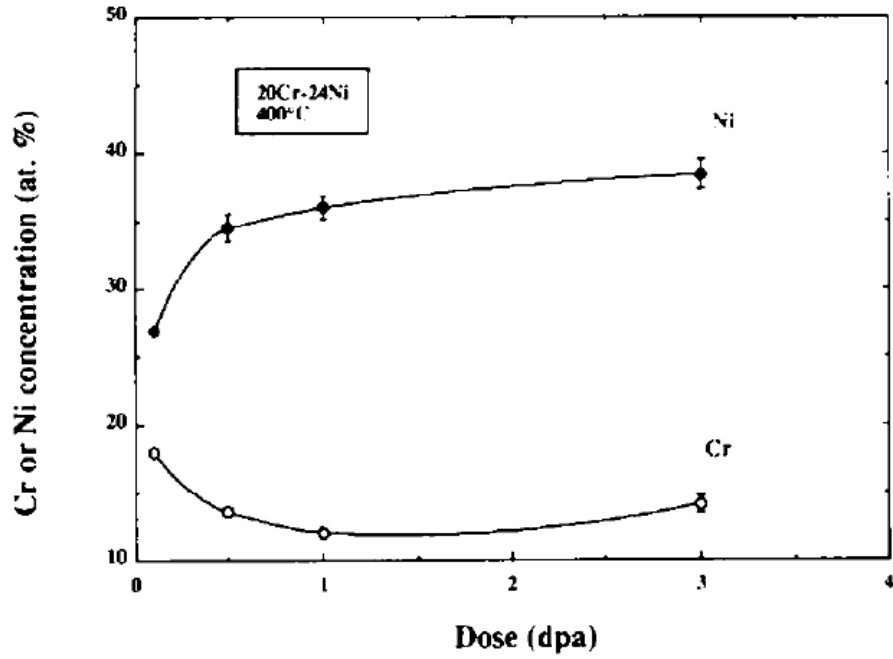
Figure 2.10 Ni and Cr grain boundary concentration as a function of dose after proton irradiation of a Fe-20Cr-24Ni alloy at 400°C [26].
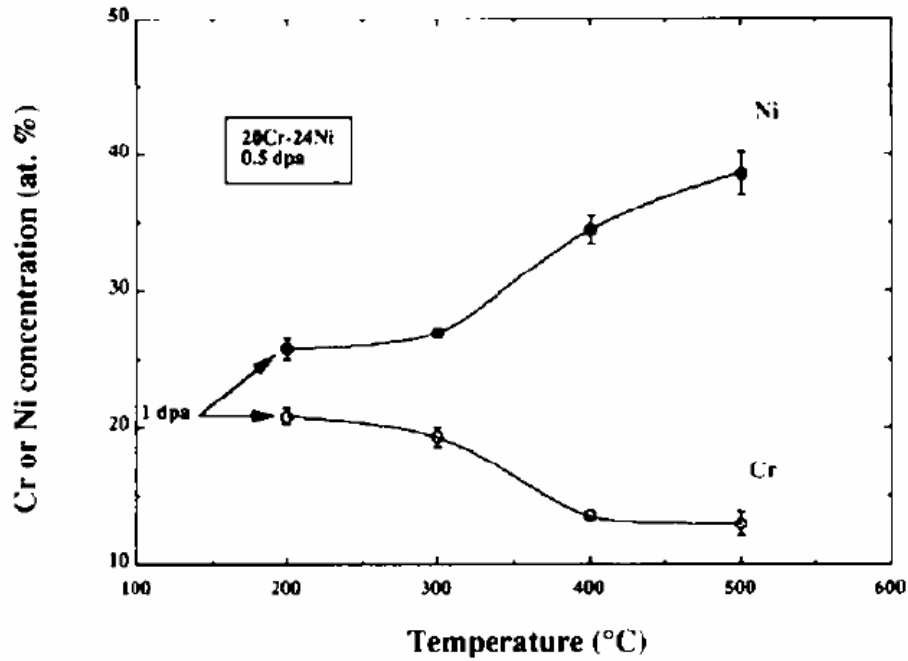
Figure 2.11 Ni and Cr grain boundary concentration as a function of temperature after proton irradiation of a Fe-20Cr-24Ni alloy to a dose of 0.5 dpa [26].
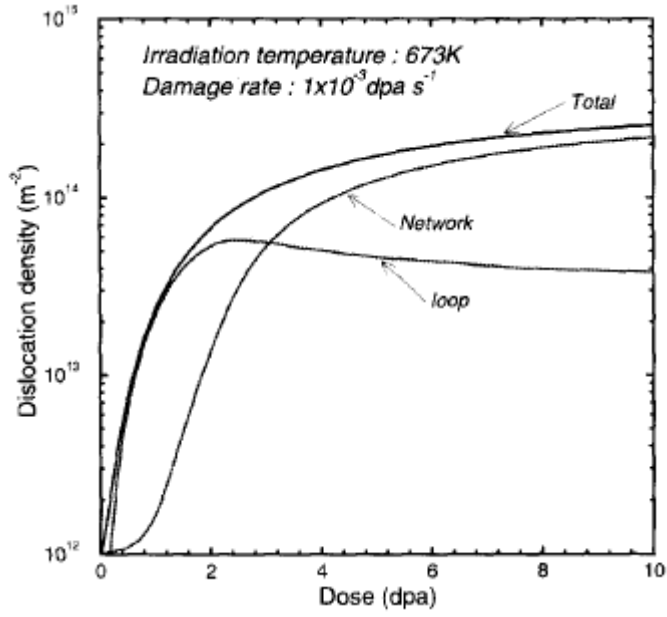
Figure 2.12 Network, loop and total dislocation density as a function of dose [37].
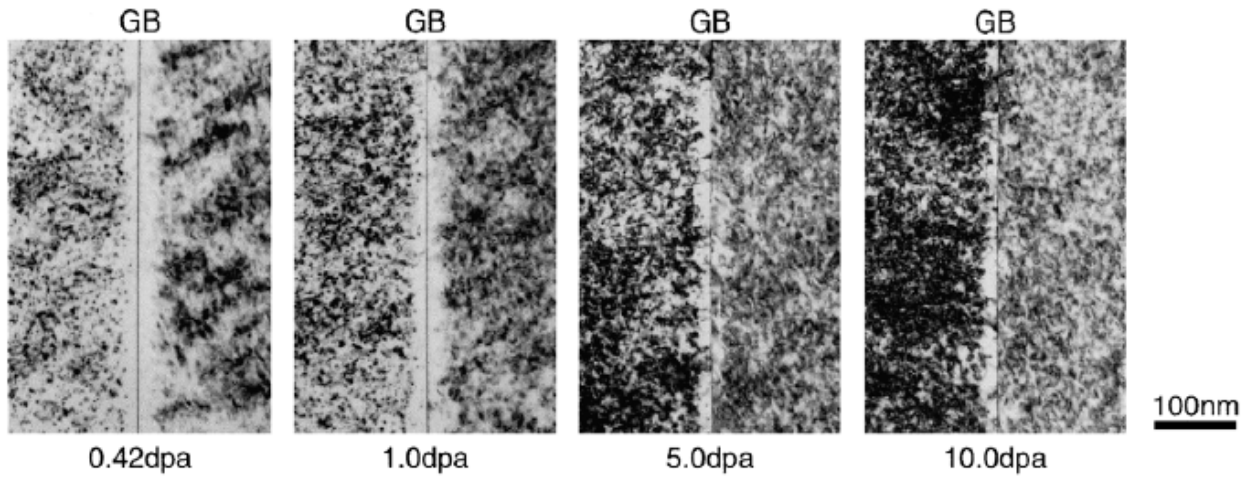
Figure 2.13 The formation and loss of DLFZ near a grain boundary as a function of dose [40].
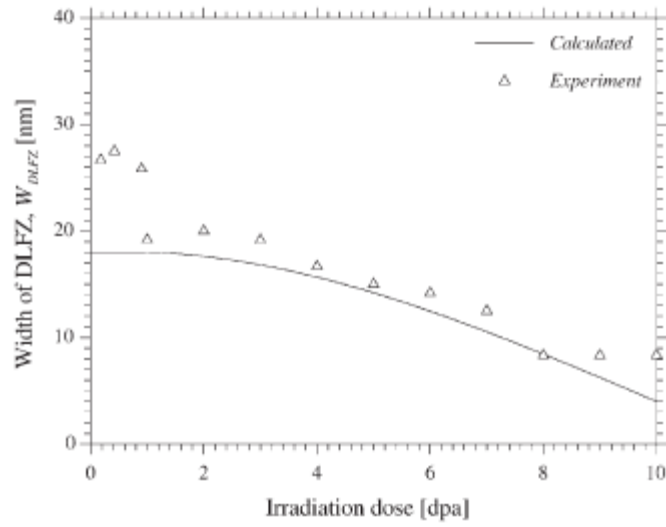
Figure 2.14 Dose dependence of the DLFZ width under 1 MeV electron irradiation at 523 K [40].
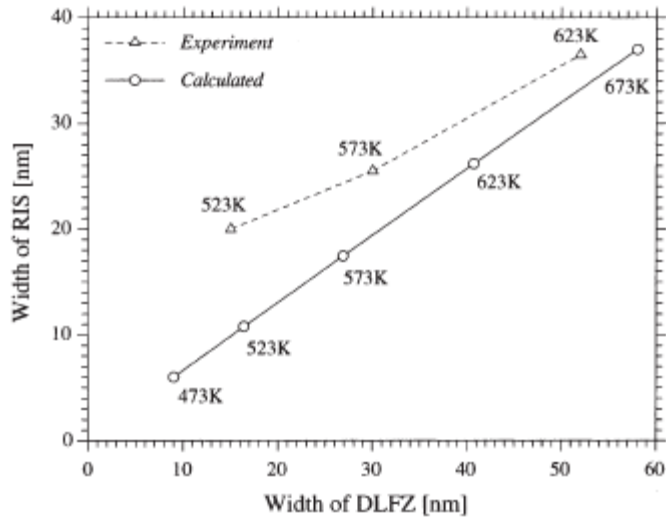
Figure 2.15 Width of RIS profile relative to the width of the DLFZ under 1 MeV electron irradiation at 1 dpa. The calculated solid line is not convoluted to match the experimental measurements [40].
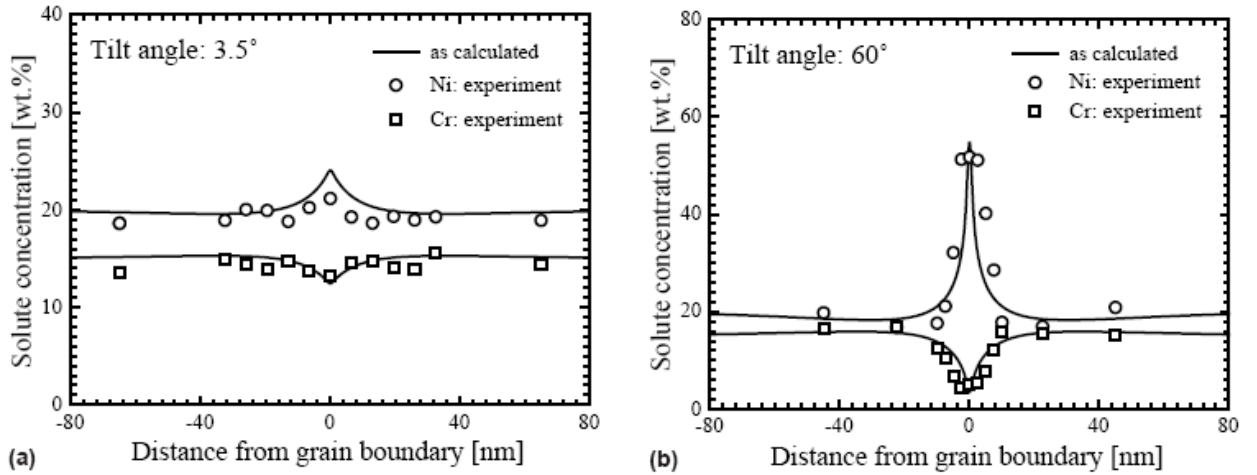
Figure 2.16 The tilt angle between two grain boundaries has a strong effect on the resulting RIS profile, with increasing tilt angle corresponding to increasing RIS. Depletion is small for (a) a small tilt angle of 3.5° and (b) a large tilt angle of 60° [41].
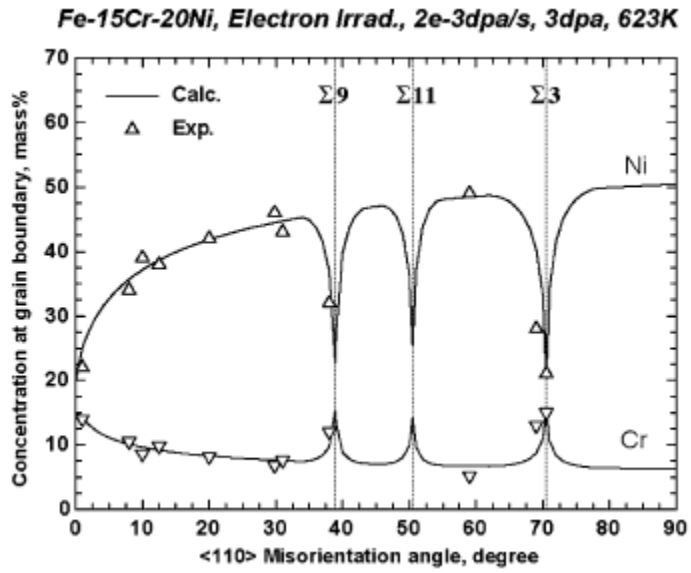
Figure 2.17 RIS dependence on misorientation tilt angle after electron irradiation at 350°C [41,54].
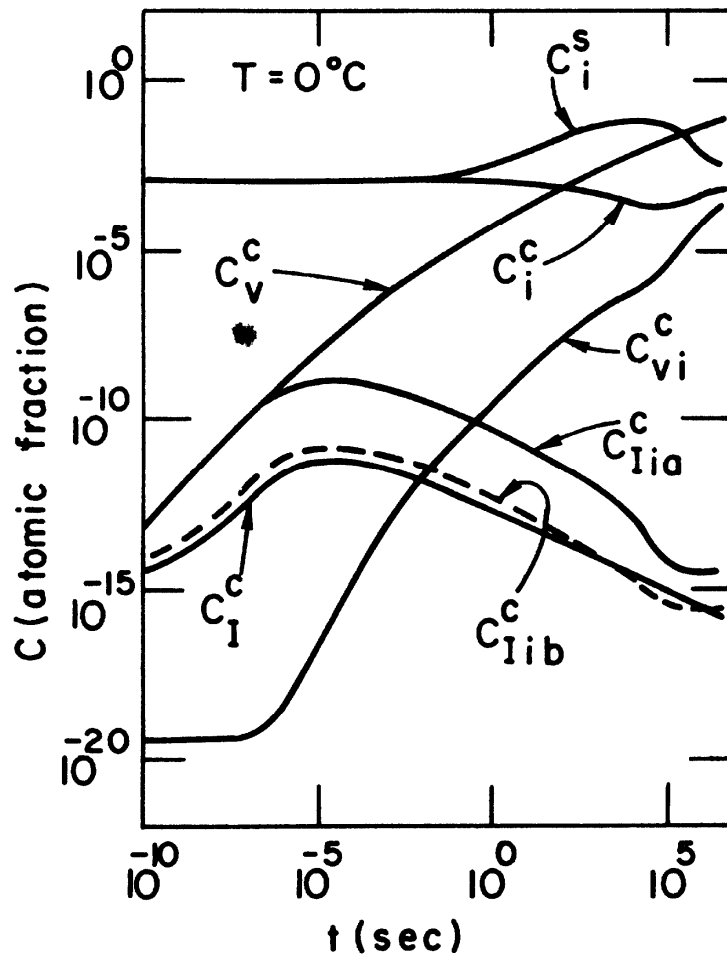
Figure 2.18 Concentrations of point defects and defect-solute complexes at the center of a thin foil irradiated at 0°C as a function of irradiation time [47].
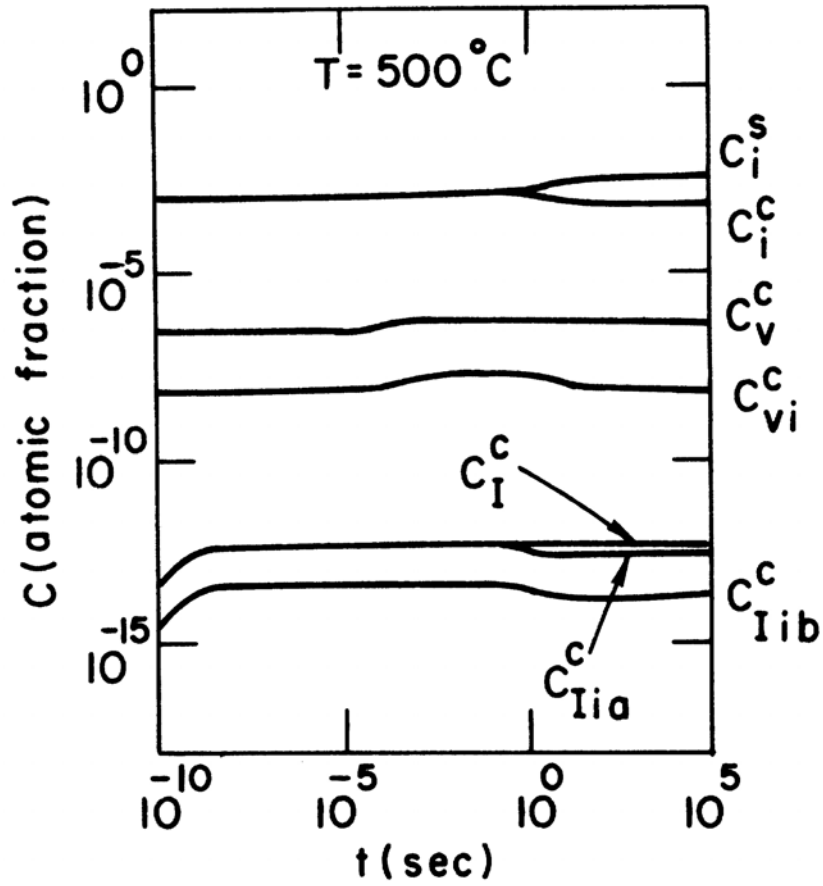
Figure 2.19 Concentrations of point defects and defect-solute complexes at the center of a thin foil irradiated at 500°C as a function of irradiation time [47].
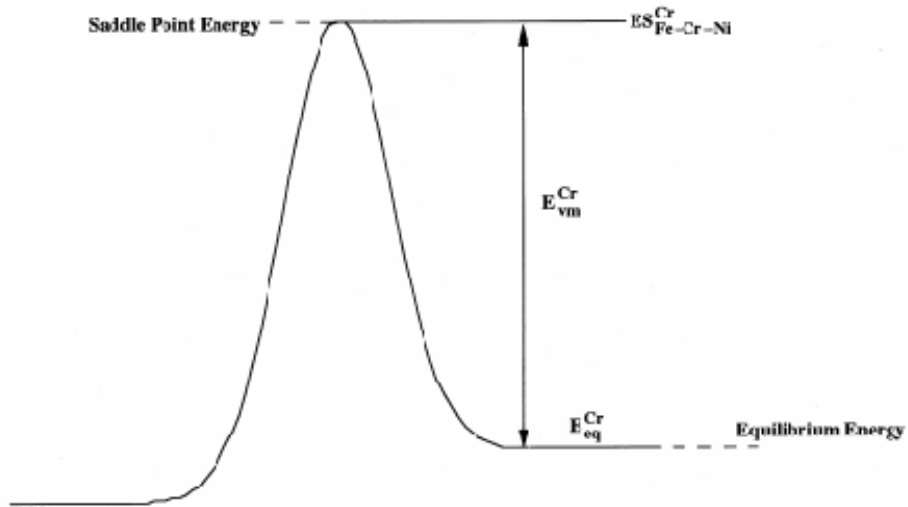
Figure 2.20 Representation of the migration energy, defined as the different between the equilibrium energy and the saddle point energy [33].
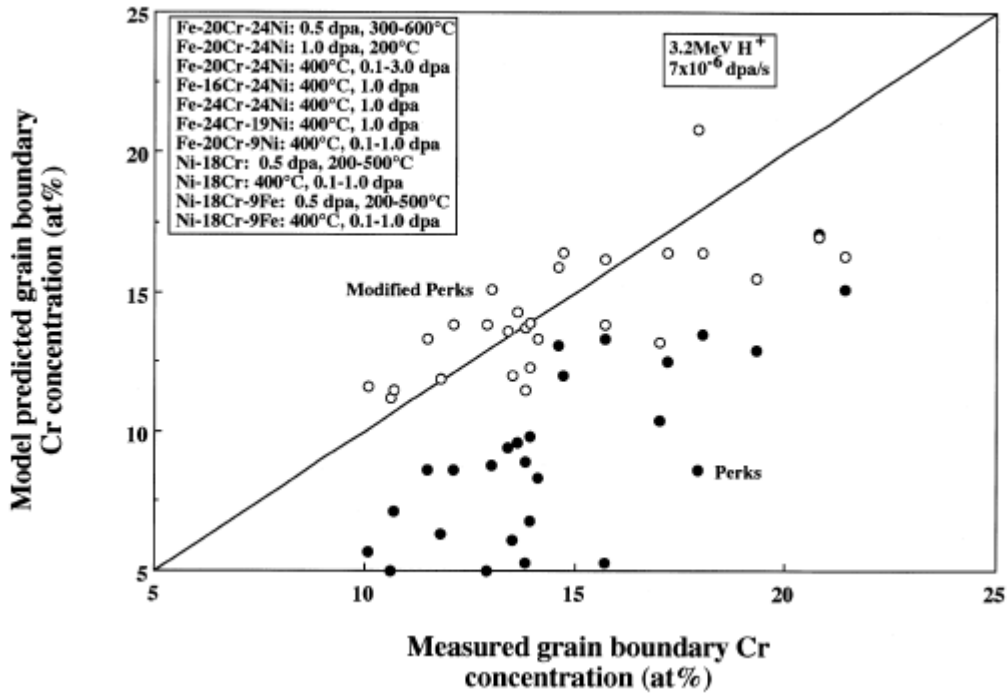
Figure 2.21 Comparing experimental Cr concentration levels from proton-irradiated stainless steels to calculated concentrations from the MIK model [33].
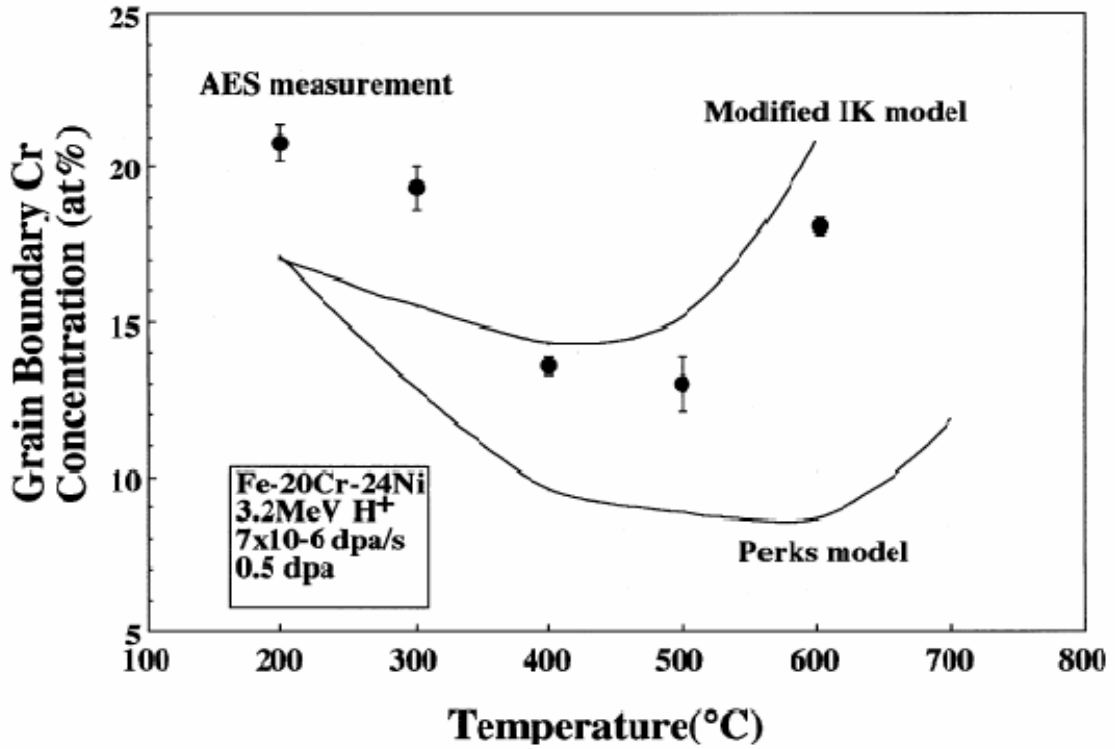
Figure 2.22 Cr concentration at the grain boundary as a function of temperature for proton-irradiated Fe-20Cr-24Ni after 0.5 dpa. The symbols represent AES measurements, the upper line is the MIK model calculated Cr concentration, while the lower line is calculated by the Perks model. Taken from [33].
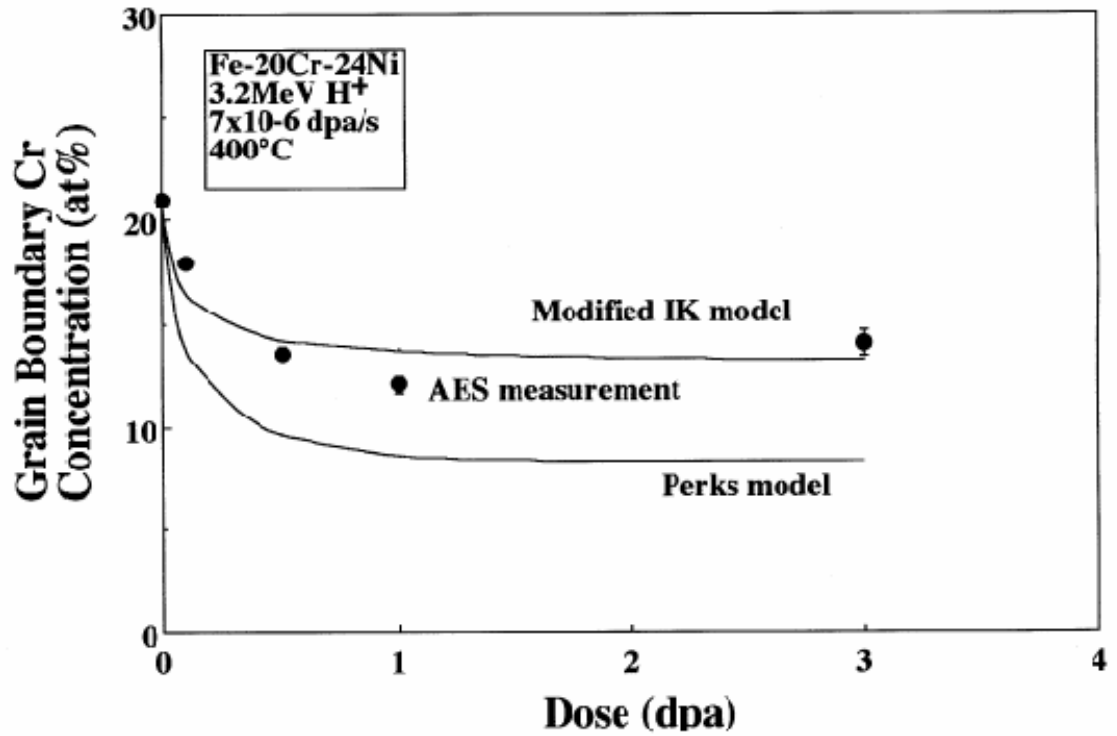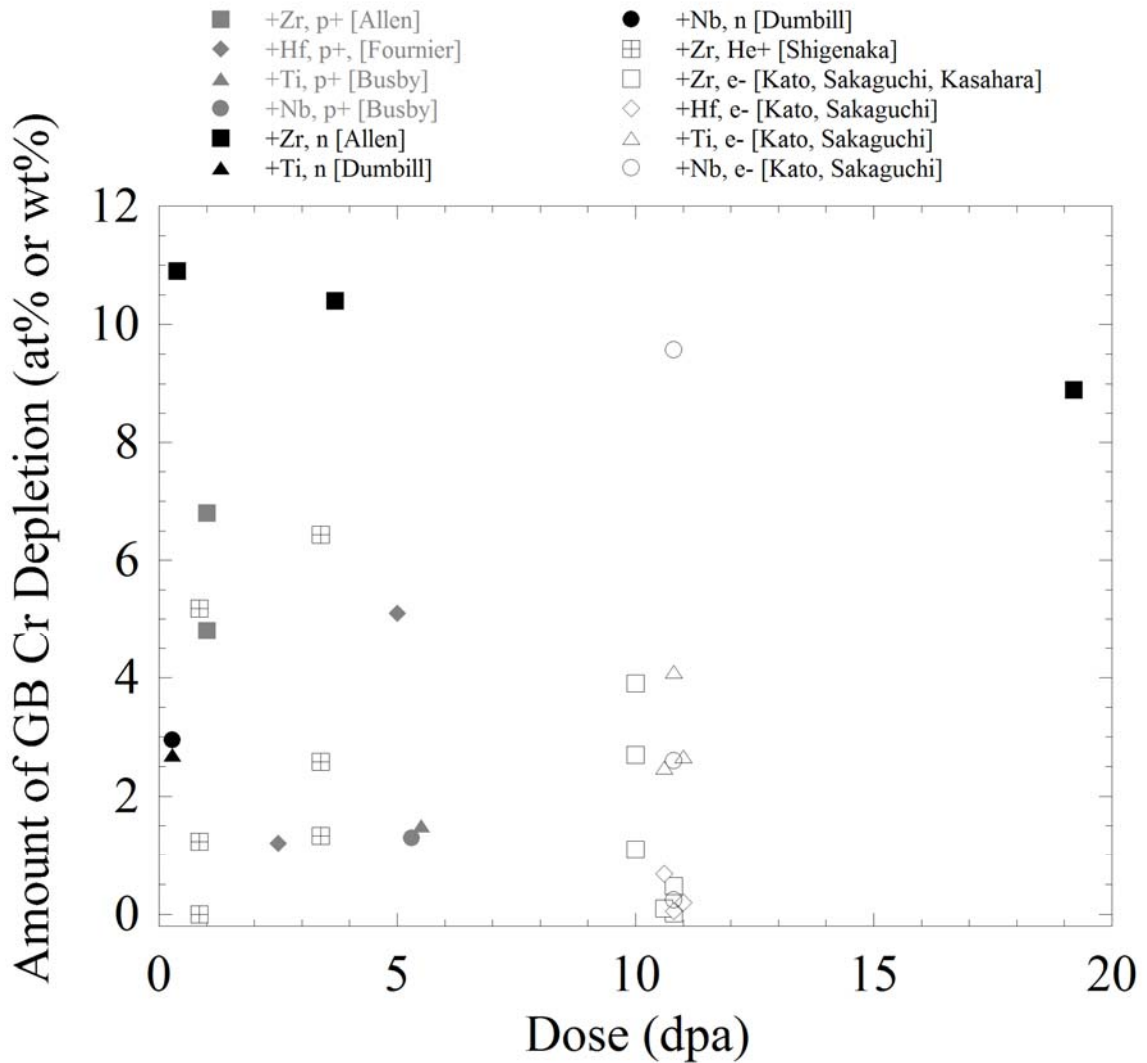
Figure 2.23 Cr concentrations at the grain boundary as a function of dose for proton-irradiated Fe-20Cr-24Ni at 400°C. The symbols represent AES measurements, the upper line is the MIK model calculated Cr concentration, while the lower line is calculated by the Perks model. Taken from [33].

Figure 2.24 Grain boundary Cr depletion as a function of dose for a variety of 304 and 316 stainless steel alloys. The oversized solute additions include Zr, Hf, Ti, and Nb. Symbol shading represents the particle type, with grey, closed symbols for proton irradiations, black, closed symbols for neutron irradiations, cross-hatch symbols for He^{+} irradiations, and open symbols for electron irradiations. Meanwhile, symbol shape represents the oversized solute type, with square symbols for Zr, diamonds for Hf, triangles for Ti and circles for Nb [21, 23, 24, 28, 82, 83, 92].
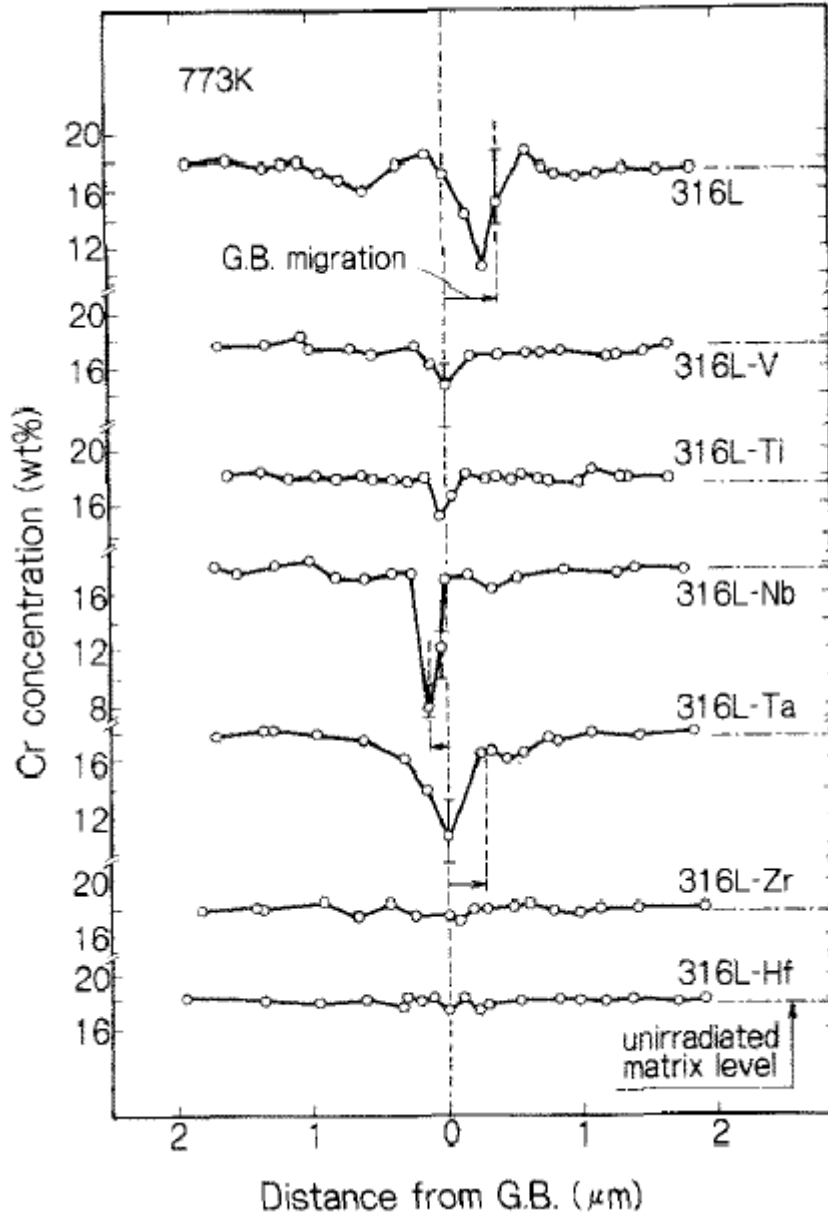
Figure 2.25 Chromium grain boundary concentration profiles for various oversized solute alloys after 1 MeV electron irradiation to 10.8 dpa at 500°C [23]. Not all oversized solute additions resulted in a decrease in Cr depletion.
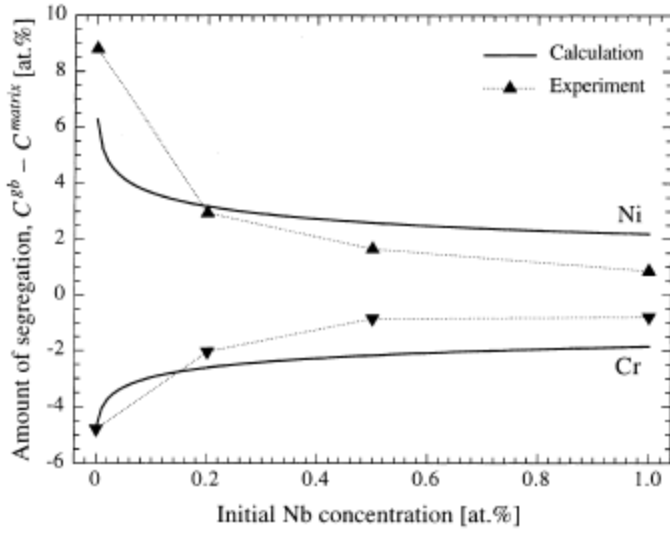
Figure 2.26 Grain boundary segregation as a function of Nb concentration after electron irradiation to 7.2 dpa at 773 K in Fe-16Cr-13Ni [21].
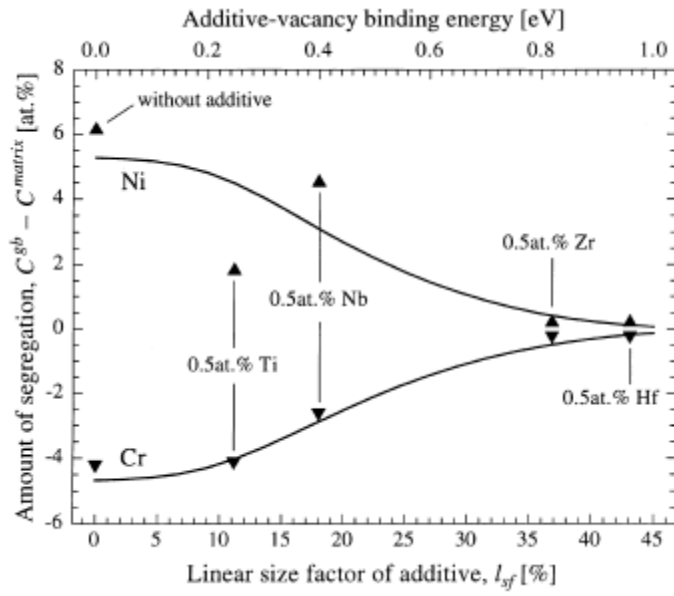
Figure 2.27 Grain boundary segregation versus linear size factor and vacancy-solute binding energy for solute additions of 0.5 at% of Ti, Nb, Zr, and Hf in Fe-18Cr-12Ni after electron irradiation to 10.8 dpa at 723 K [21].
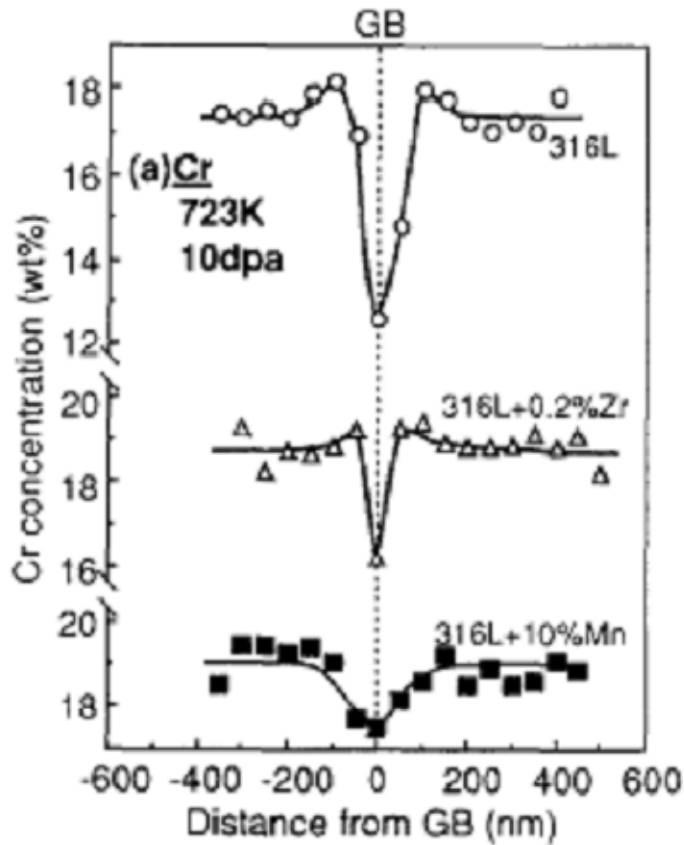
Figure 2.28 Cr concentration profile as a function of distance from the grain boundary for 316L and 316+0.2%Zr alloys after irradiation with 1 MeV electrons to a dose of 10 dpa at 450°C [24].
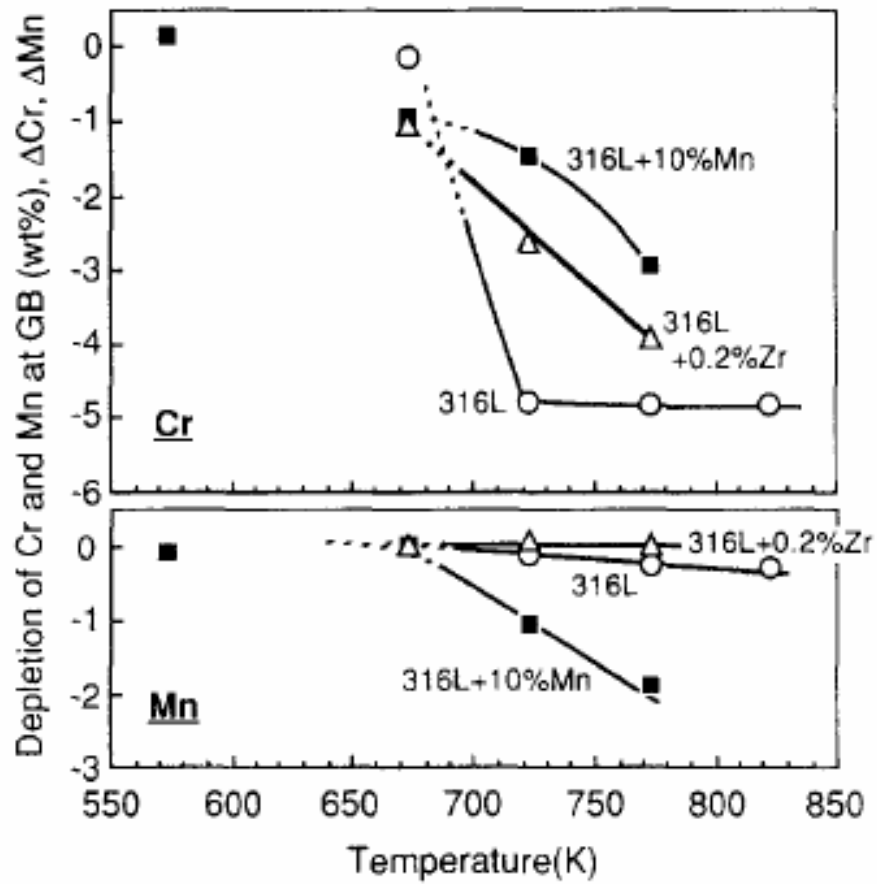
Figure 2.29 Focusing on Cr, the grain boundary depletion as a function of temperature for 316L and 316+0.2%Zr after 1 MeV electron irradiation [24].
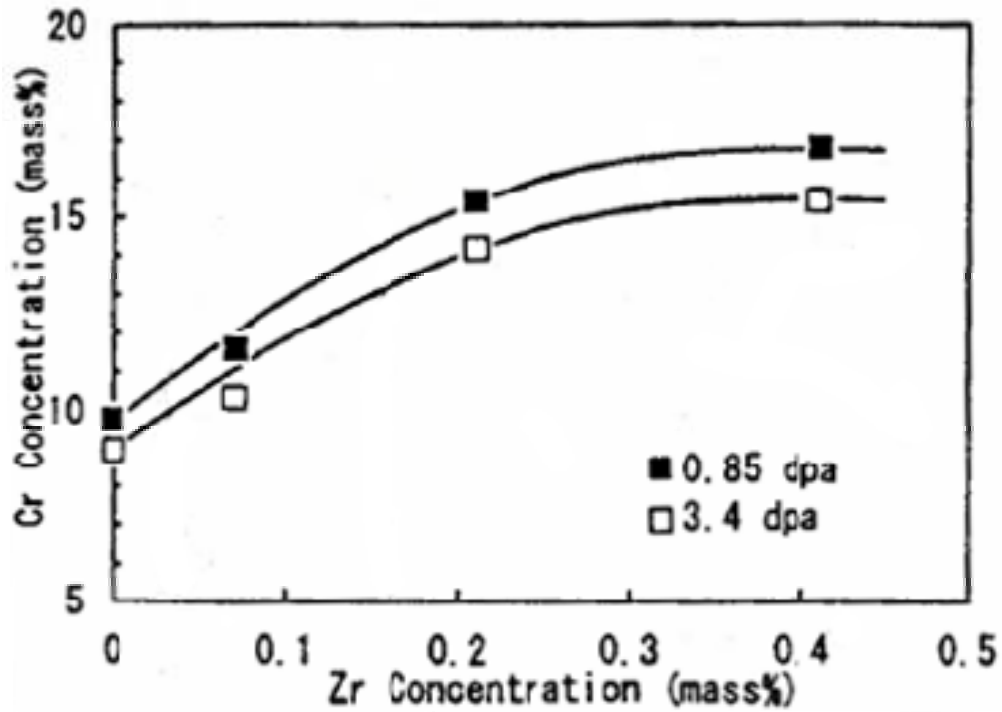
Figure 2.30 Cr concentration as a function of the Zr alloy concentration after 400 keV He$^+$ irradiation at 500°C. The closed symbols represent a dose of 0.85 dpa and the open symbols are for 3.4 dpa [20].
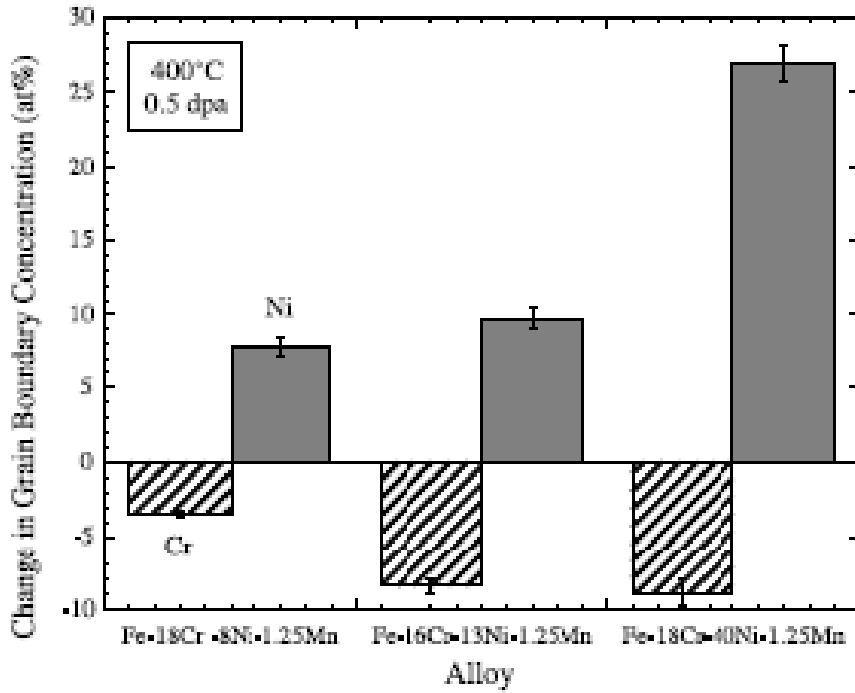
Figure 2.31 The change in grain boundary Cr concentration for a reference Fe-18Cr-8Ni, 1.25Mn irradiated with protons at 400°C to a dose of 0.5 dpa, compared to two similar oversized solute alloys with 0.04 and 0.16at% Zr irradiated to 1.0 dpa [28].
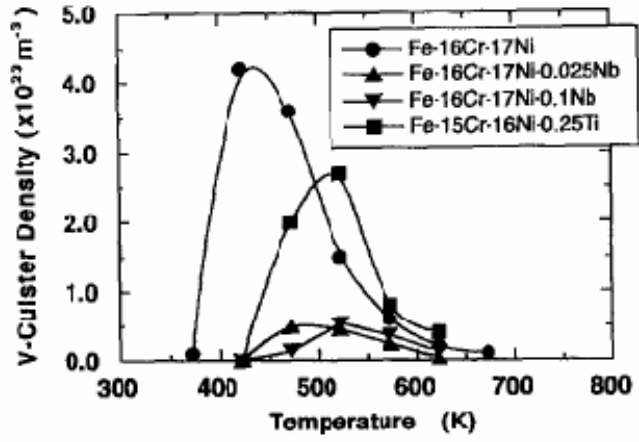
Figure 2.32 The vacancy-cluster density of Fe-16Cr-17Ni alloys with Nb and Ti additions after 1 MeV electron irradiation to 0.1 dpa [66].
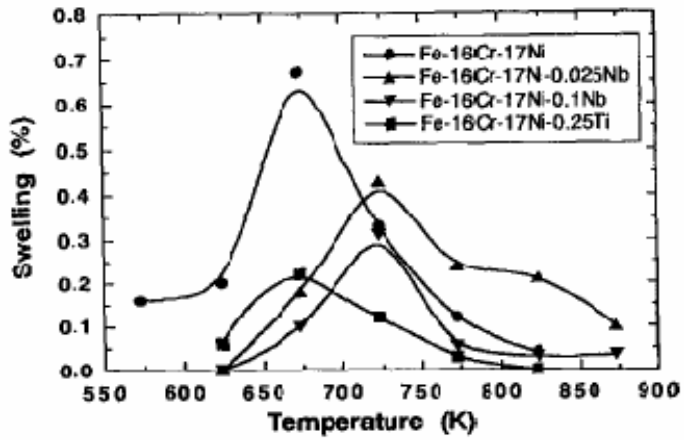
Figure 2.33 Void swelling as a function of temperature after 1 MeV electron irradiation to 2.0 dpa for Fe-16Cr-17Ni alloys with Nb and Ti additions [66].
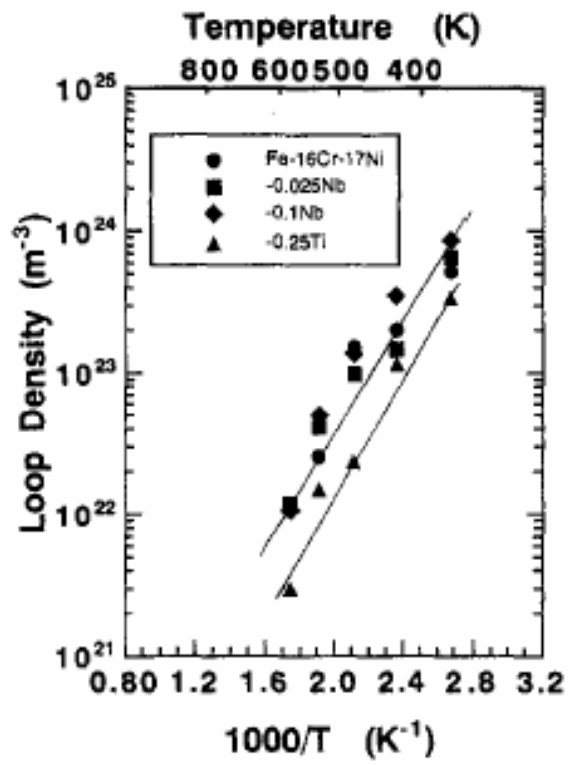
Figure 2.34 Arrhenius plot of the interstitial loop density in Fe-16Cr-17Ni with additions of Nb or Ti.
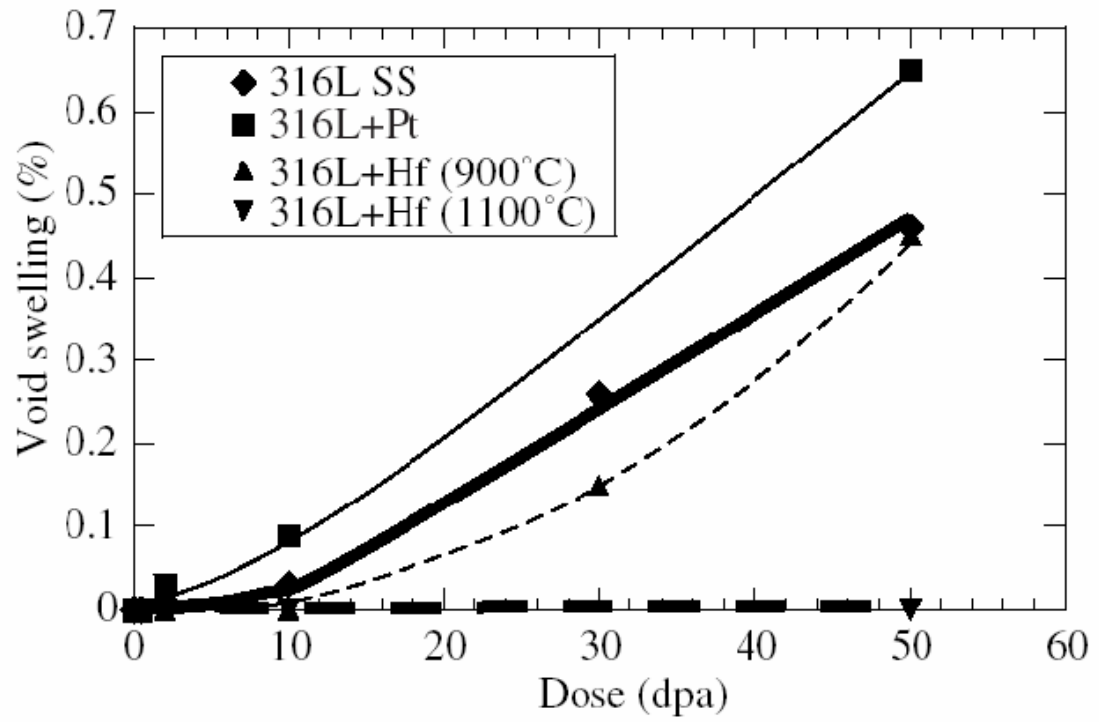
Figure 2.35 Void swelling as a function of dose for Hf and Pt-modified 316SS after Ni^{++} irradiation at 500°C [44].
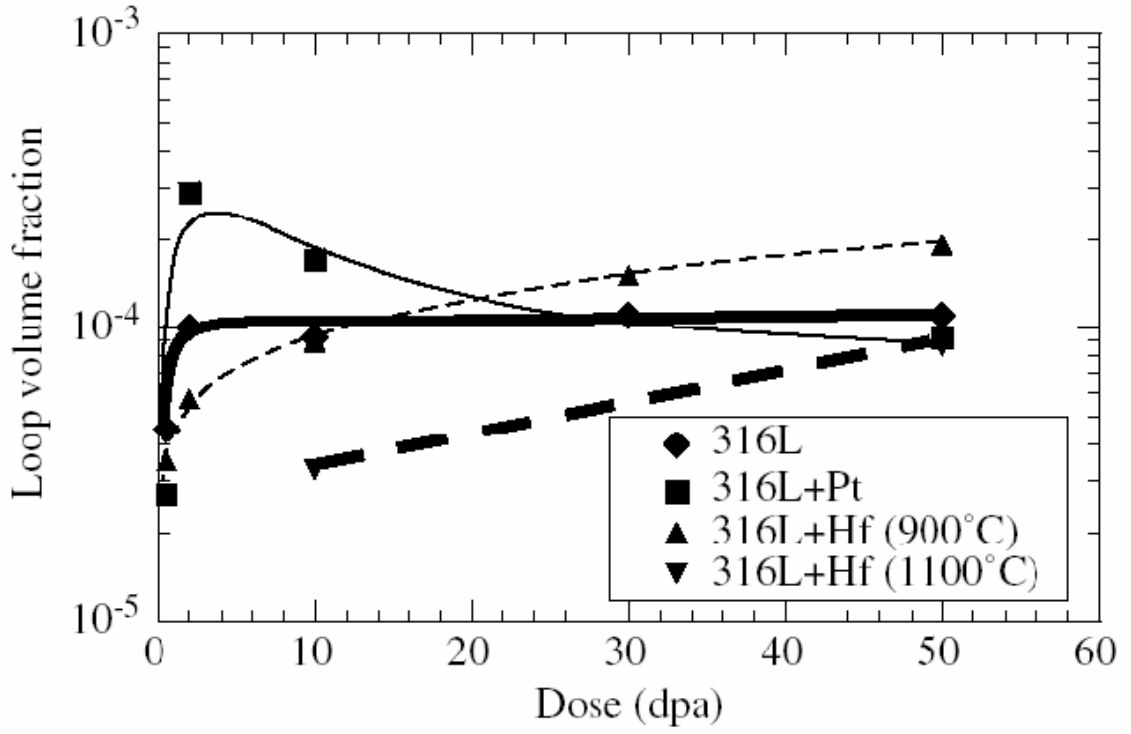
Figure 2.36 Loop volume fraction as a function of dose for Hf and Pt-modified 316SS after Ni^{++} irradiation at 500°C [44].
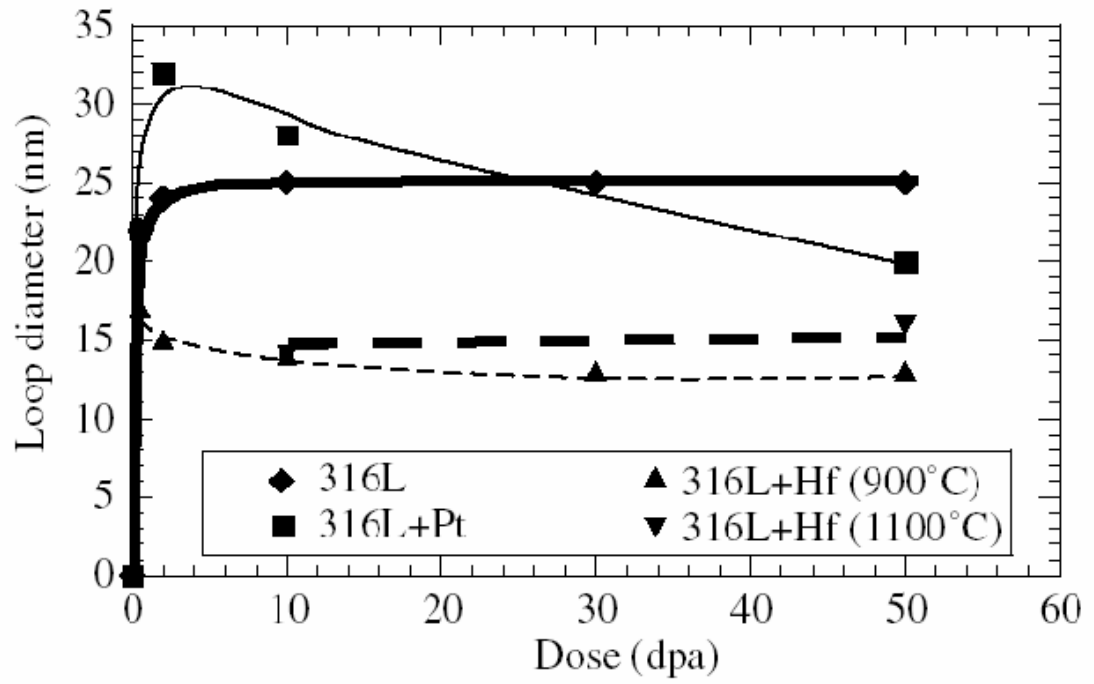
Figure 2.37 Loop diameter as a function of dose for Hf and Pt-modified 316SS after Ni^{++} irradiation at 500°C [44].
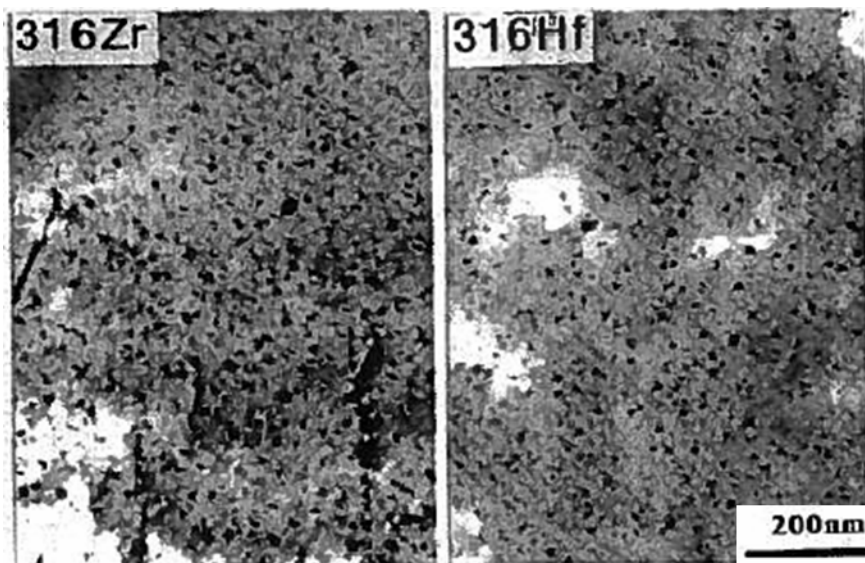
Figure 2.38 Fine-scale precipitate formation of ZrC and HfC after fast neutron irradiation to 35 dpa at 600°C [86].
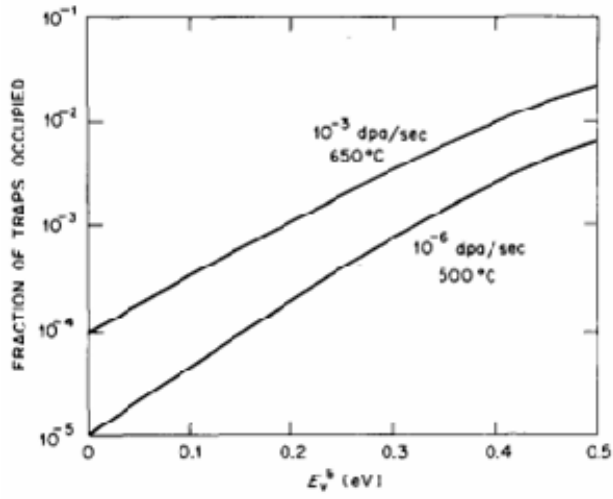
Figure 2.39 The fraction of occupied solute-defect traps as a function of the binding energy for defect trapping. Fractions are shown for 650°C at 10^{-3} dpa/s and 500°C at 10^{-6} dpa/s [6].
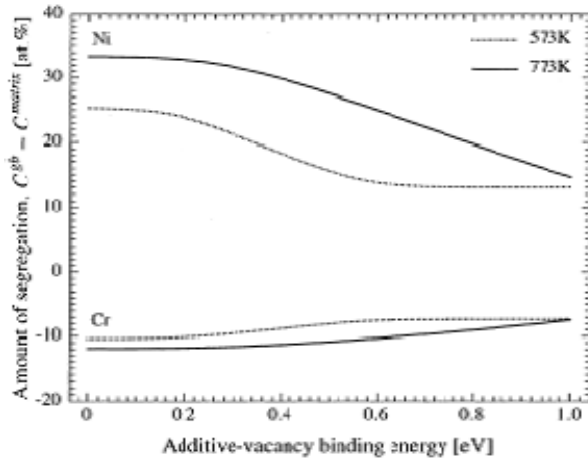
Figure 2.40 Amount of segregation for Ni and Cr as a function of binding energy for irradiation at 573K and 773K for a Fe-15Cr-20Ni alloy [21].

CHAPTER 3

OBJECTIVE

The objective of this work is to determine the mechanism by which oversized solute additions to austenitic stainless steels affect the radiation-induced grain boundary segregation of Cr. Based on previous work in this field, it is hypothesized that substitutional oversized solute atoms, when in solution, exert a compressive stress on surrounding atoms. This stress acts as a trap for vacancy defects, holding them and preserving their identity until they are either released or interact with interstitials to remove the defects. The enhanced recombination reduces the flow of defects to sinks such as the grain boundary, with a resulting suppression of radiation-induced segregation (RIS).

To achieve this objective, the work can be broken into four different sections, each listed as a sub-objective. These will be listed below.

The first sub-objective is the adoption of a trapping, release and recombination mechanism into an existing (MIK) model for RIS. This trapping MIK model will allow prediction of the effect of oversize solutes on grain boundary chromium concentration following irradiation. This objective also includes a sensitivity analysis to determine the critical parameters governing the change in grain boundary chromium depletion due to oversized solutes.

The second sub-objective is the determination of the binding energy. The binding energy is shown to be one of the most sensitive variables in the trapping MIK model, and therefore an important variable to understand. Using a first-principles approach, the Vienna Ab-initio Simulation Package (VASP) is used to assess the binding energy

quantitatively and provide a basis for the binding energy used to calculate RIS in the trapping MIK model.

The next sub-objective is the experimental determination of the effect of oversize solutes on grain boundary chromium content over a range of temperatures and doses to determine if the behavior fits that predicted by the modified MIK model.

The last part of the objective is an assessment of experimental and model results to determine whether the mechanism of oversize solute addition is plausible.

CHAPTER 4

EXPERIMENTAL PROCEDURES

This chapter describes the sample preparation, experimental techniques and measurements associated with the experimental portion of this research. The procedures utilized during this study are detailed in the following sections: 1) Alloys and Sample Preparation, 2) Sample Irradiation, 3) Hardness Testing, 4) Post-Irradiation Specimen Preparation, 5) Radiation-Induced Segregation Measurements, 6) Dislocation Loop Imaging, 7) Determination of Oversized Solute in Solution, and 8) Error Analysis.

4.1. Alloys and Sample Preparation

To study the effect of oversized solute additions on radiation-induced segregation (RIS) in Fe-Cr-Ni alloys, two different oversized solutes were selected: Zr and Hf. These particular solutes were selected because of their large size relative to the matrix material. A series of austenitic stainless steel alloys containing Zr or Hf were fabricated in order to complete the experimental studies necessary to fulfill the objective of this research.

4.1.1 Alloys

Four different austenitic stainless steel alloys were selected for testing in order to determine the mechanism of oversized solute additions in reducing RIS. Two alloy contained Zr at 0.19 and 0.28 at% and the other two alloys contained Hf at 0.05 and 0.37 at%. In addition, both the Zr and Hf alloy series had reference alloys that closely matched the composition but without the oversized solute. Compositions are provided in table 4.1.

Alloys are designated by their solute type and relative concentration. So the Zr alloys are referred to as 316+LoZr and 316+HiZr, where the relative concentration of the oversized solute is thus obvious. The reference alloys are similarly designated: 316-Ref-Zr and 316-Ref-Hf. Two reference alloys were necessary because of some small variations in composition between the +Zr and +Hf alloy series.

4.1.2. Alloy Processing

The +Hf alloys and 316-Ref-Zr were provided by the General Electric Global Research Center. The alloys 316+LoZr and 316+HiZr were fabricated by MetalMen Inc. Because the alloys were not all fabricated simultaneously, processing conditions varied somewhat between the different alloys, although all thermo-mechanical heat treatments were performed with the goal of achieving a roughly 20 μm grain size. The different processing conditions for the alloys are listed in detail in table 4.2 to highlight the steps taken to achieve the desired grain size.

In order to obtain the 20 μm grain sizes, stock materials were solution annealed at 1200°C for homogenization. This is particularly important for the oversized solute alloys to ensure a more uniform distribution of the solute atoms. The materials were then cold rolled, with cold rolling performed with a target of 2% reduction in each pass through the rolling mill. Cold rolling was followed by a re-crystallization process that varied in time and temperature to obtain the desired grain size. Re-crystallization heat treatments were always followed with a water quench to retain the austenite microstructure. Re-crystallization heat treatments were performed in a Lindberg Model 54232 furnace.

Once the reference condition thermo-mechanical treatments had been performed, transmission electron microscope (TEM) bars were machined using electrical discharge machining (EDM). The EDM process places a copper wire between 10 and 100 μm away from the area of the material that needs to be removed. High frequency sparks are applied across the gap between the wire and the material and cause the removal of sample material. This technique was chosen for use in these experiments because it eliminates the large amounts of cold working that can occur during conventional machining. Sample TEM bars had dimensions of 2.0 X 2.0 X 20 mm. Figure 4.1 illustrates the sample geometry for the specimens used in this study.

4.1.3. Preparation

Following the EDM process, a smooth, flat polishing block was placed on a hot plate. The hot plate temperature was just high enough to melt resin wax which was used to bond sample bars to the polishing block. The samples were carefully wet polished from a starting grit of 320 to a final grit of 1200 using Struers® SiC paper on the back side of the sample, or in other words, the side of the sample that will be placed face down onto the irradiation stage. After each polishing step of SiC grit, samples were visually inspected to ensure that scratches from the previous grit SiC paper had been removed.

After finishing the polishing process, samples were reheated on the hot plate, removed from the polishing block, and ultrasonically cleaned in acetone. The samples were then remounted onto the block for further polishing. This time, the polishing was done on the face of the samples to be irradiated, starting at 320 grit and ending with 4000 grit SiC paper, using the same procedures as mentioned already.

After polishing, samples were again cleaned ultrasonically in acetone. This was followed by electropolishing to remove the plastically deformed layer resulting from mechanical polishing. The electropolishing conditions were selected in order to provide a mirror surface with no pitting or etching.

Electropolishing consisted of immersion in a solution of 400 mL of 10% perchloric acid plus 90% methanol. The solution was cooled by placing the primary container into a secondary container and using a combination of methanol and dry ice to rapidly cool the acid/alcohol polishing solution. Samples were immersed in the solution at a temperature of -55°C for 30 seconds. The potential was set to ~ 30 V and verified through the use of a digital multi-meter connected across the cathode and anode. The voltage corresponds to a current of ~ 100 mA. A magnetic stirring bead was used at 60% of full speed to create a circular flow of the solution with a vortex of approximately ½ to ¾ inches. This created sufficient agitation to remove bubbles from the surface of the sample as they commonly formed during electropolishing and had the potential to create pits on the sample surface if not removed through agitation. After electropolishing, samples were quickly immersed in acetone, then methanol to remove any residual polishing solution. Samples were finally cleaned ultrasonically in methanol before storing the samples in plastic vials until the time of irradiation.

4.2. Sample Irradiation

Sample irradiations were carried out at the Michigan Ion Beam Laboratory using the General Ionex Tandetron accelerator. Irradiations were conducted using either 2 MeV or 3.2 MeV protons. This section will describe the setup and techniques used to achieve these proton irradiations. Specifically, this section will describe the irradiation setup, how to calculate the displacement damage and determine the radiation dose, the setup of the irradiation stage, including apertures, beam scanning and thermocouples, the monitoring of the irradiation, and finally, the subsequent sample activation and beta activity which can be used to determine dose uniformity.

4.2.1 Overview of Irradiation Setup

During all irradiations, the accelerator beam-line pressure was kept below 3 x 10^{-8} torr. Samples were mounted in a specially designed irradiation stage attached to the accelerator beam-line. The irradiation stage was designed such that it was electrically isolated from the accelerator while maintaining sample temperature control through the use of electrical resistance heaters and an air cooling system. These systems are shown in a schematic drawing shown in figure 4.2(a) and (b) [17]. Figure 4.2(a) shows a cross-section view of the stage chamber, with the copper stage, heater in the back, specimen stage, and positioning of an infrared pyrometer. Figure 4.2(b) provides greater detail of the stage, including the samples mounted on front, and aperture connected to the stage with ceramic insulator posts. Each of these features shall receive further discussion.

The standard loading for an irradiation stage consisted of 8 TEM samples plus 2 guide bars. The maximum width of all samples that could be irradiated was 18 mm. This irradiation width provided for some beam overlap onto the guide bars in order to ensure a uniform dose across the TEM samples. A photograph of the samples mounted on the stage, as seen through the hole in the aperture, in show in figure 4.3. Further discussion of the aperture system, aperture alignment and beam overlap onto the samples will be given in section 4.2.4.

TEM samples were held in place on the irradiation stage using hold-down bars with a triangular cross section in order to decrease the amount of thermal reflection onto

the stage. The hold-down bars were attached to the irradiation stage using four set screws. The hold-down bar and set screw arrangement were utilized to guarantee good thermal contact with the irradiation stage. A series of drawings of the hold-down bars is shown in figure 4.4, which outlines all of the dimensions. The figure shows how they were mounted onto the stage over the samples in the lower right-hand corner of the drawing. The hold-down bars can also be viewed in figure 4.5. This photograph shows two of the aperture wires used to connect the tantalum aperture plates to the feed-through for current measurements. The image also depicts the hold-down bars and one of the thermocouple wires. The thermocouple wires are described in more detail in section 4.2.5.

Irradiation stage thermal control was regulated through the use of a resistance heating cartridge in combination with an air cooling system. These were presented in figure 4.2(b). The resistance heating cartridge was inserted into the rear of the copper block forming the base of the irradiation stage. Cooling lines ran through the copper block to remove heat from the copper stage during the irradiation. The samples were mounted to the front of this copper block. A shim was placed between the samples and the copper block. This shim was used to hold a layer of either indium or tin in place. Since the irradiation temperature was much higher than the melting temperature of the metals, a solid/liquid/solid interface formed between the samples, the indium or tin, and the copper irradiation block. This interface maximized the thermal control and temperature stability during irradiation. Indium was used at an irradiation temperature of 400°C, where the melting temperature is 156°C, while tin, with a higher melting temperature of 232°C, was used for irradiation temperatures of 500°C.

Because of the risk of alloying between the Ni in austenitic stainless steels and the liquid metal under the samples, particularly with tin at irradiation temperatures of 500°C, a protective coating was needed on the unirradiated sides of the samples which would come into contact with the liquid metal during irradiation. As it turns out, Cr will not alloy with tin or indium. Since Cr was already present in the stainless steels, a thin layer of Cr deposited on the unirradiated sides of the samples was used to prevent alloying during irradiation. This proved to be an effective barrier that protected the surfaces of the samples and prevented leaks of liquid metal between the samples on to the irradiated

surface of the samples during irradiation testing. Preventing these leaks was particularly important because any liquid metal deposited onto the irradiated surface would prevent irradiation of the sample and result in alloying or sputtering of the liquid metal into the irradiated region of the sample, requiring the irradiation to be terminated.

Cr depositions were performed using a Magnetron sputtering system. Samples were placed in the Magnetron sputtering chamber with the highly polished face that was to be irradiated placed down so that only the sides and backside of the specimens would have a Cr layer deposition. With a partial argon pressure of $\sim 4\times10^{-3}$ torr, a pure Cr metal target was used for sputtering. The power supply was set to 6% and the stage was rotated during deposition. Deposition times of approximately 10 minutes gave a Cr layer thickness of several hundred nanometers.

4.2.2 Determining Displacement Damage

Prior to irradiation, the displacement damage was calculated using the program Stopping and Range of Ions in Matter (SRIM) 2006™ [93]. This displacement damage is defined as the number of displacements produced per unit length per ion and is calculated as a function of depth into the irradiated material. The SRIM calculations were detailed calculations with full damage cascades using a total of 500,000 ions. This large number of ions was chosen because it gave a smooth, more accurate damage profile.

Displacement damage was calculated in SRIM using a displacement energy of 40 eV as recommended by ASTM E 521-89 for metal and alloy samples [94]. Figure 4.6 illustrates the SRIM generated irradiation damage profile obtained using 2 MeV and 3.2 MeV protons in austenitic stainless steel for a standard Fe-16Cr-13 Ni alloy. Note that the use of proton irradiation results in a fairly uniform damage profile up to 35 μm of the irradiation depth for 3.2 MeV protons, or up to 15 μm of the irradiation depth for 2 MeV protons.

Figure 4.7 provides a closer view of the damage curve. Since the displacement damage increases with increasing depth into the material, an average damage is chosen to be representative of the irradiated region to be analyzed. For this work, the average was chosen to be at a depth equal to 60% of the maximum damage depth. In the case for 3.2 MeV protons, with a maximum damage depth of 43 μm, the average displacement

damage was chosen to be 5.3×10^{-5} displacements/Å/ion at a depth of 26 μm. Similarly, for 2 MeV protons, with a maximum damage depth of 20 μm, the average damage rate was chosen as 8.0×10^{-5} displacements/Å/ion at a depth of 12 μm.

4.2.3 Calculating Radiation Dose

The stage beam current represents the amount of accelerator current hitting the samples the irradiation stage. This stage current was measured throughout the irradiation. A wire was attached to the outside of the stage chamber and connected to a monitoring computer to measure and record the current. The stage was electrically isolated from the rest of the accelerator by a large ceramic connector. Also, the aperture was electrically isolated from the stage by ceramic pieces, with current passing to the feed-through. As a result, all of the current measured on the outside of the stage chamber represented the beam current hitting the samples during irradiation.

The current that passed to the monitoring computer was integrated and arbitrarily set such that one "count" was recorded for every μC of charge collected. The accelerator measured the charge collected during the irradiation, and converted the charge into counts, where 1 count = 1 μC. The number of counts recorded during the irradiation was used as a measure of the radiation dose.

The duration of an irradiation was determined by the number of protons required to reach a certain dose. In a sense, this was a determination of the amount of charge on the samples required for the number of displacements per atom (dpa) desired. The key, then, was to calculate the number of "counts", as measured by the computer, needed per dpa, given a known displacement rate from SRIM. The equation relating counts to dpa is given as:

$$
\frac{Counts}{DPA} = \frac{N\left(\frac{at}{cm^3}\right) \cdot q\left(\frac{C}{unit, charge}\right) \cdot Area(cm^2) \cdot \left(\frac{counts}{C}\right)\left(\frac{unit, charge}{ion}\right)}{Displacement, Rate\left(\frac{displacements}{\text{Å} \cdot ion}\right)} \qquad (4.1)
$$

In equation 4.1, N is the atom density, q is the Coulomb charge per ion, and the *Area* refers to the area inside the aperture, which was equivalent to the sample area that was irradiated. The *Area* is 1.8 cm^2 for these experiments and is set by the aperture

dimensions, as will be discussed later. The atom density is assumed to be a constant for all of the alloys at 8.48×10^{22} atoms/cm^3. The Coulomb charge is 1.6×10^{-19} C/p$^+$. There are 10^6 counts/C and just 1 unit charge per ion.

For 2 MeV protons with an average displacement rate of 8.0×10^{-5} displacements/Å/ion, the number of counts per dpa was calculated to be 3.05 million. For 3.2 MeV protons with an average displacement rate of 5.3×10^{-5} displacements/Å/ion, the number of counts per dpa was calculated to be 4.61 million.

4.2.4 Aperture System and Beam Scanning

A stage aperture system was used to ensure that the accelerator beam was aligned on the samples. Prior to irradiation, a laser was used to check that the apertures were in a correctly aligned position. A misplaced aperture would result in shadowing the leftmost or rightmost sample from the ion beam, so proper aperture alignment was important.

For alignment, the stage was set on its side, in the same orientation that would be used as if the stage were mounted inside the accelerator. Using a bench-top-mounted laser pointer positioned roughly 15 feet away from the stage, a small piece of plastic was placed over the laser pointer to diffuse the beam. The alignment setup is demonstrated in figure 4.8 [17]. The laser was positioned such that most of the beam intensity hit the center of the aperture. Turning off the room lights, the laser beam intensity could be seen as it passed through the aperture and hit the samples. From here, the aperture position was adjusted until it was clear that the beam hit all of the samples, the edges of each guide bar, and the entire beam was centered between the hold-down bars. A schematic showing proper beam alignment is provided in figure 4.9 to highlight laser intensity over the samples with proper alignment.

The aperture used in this study had dimensions of 10 mm x 18 mm for a total irradiation area of 1.8 cm^2. The aperture consisted of four separate tantalum plates, connected by ceramic insulators in the shape of a rectangle with a rectangular hole in the middle to allow the proton beam to pass through. A simple schematic of the aperture is provided in figure 4.10 showing the dimensions of the inner gap that permitted the beam to pass through. The aperture plates were each connected separately by metal wires to a

feed-through that passed to a monitoring computer. The computer measured the beam current hitting each of the aperture plates independently.

The measurements were important for two reasons. First, in order for complete irradiation of all samples on the stage, the beam had to overlap onto all of the apertures. So when aligning the beam during startup, a current was always measured on each of the apertures. Second, in order to have uniform irradiation on each of the samples, a certain ratio between stage current and aperture current had to be maintained throughout the irradiation. The proper ratio depended on the proton beam size.

A beam size of 3-mm full-width at half-maximum (FWHM) or less was used for the irradiations. For complete dose uniformity, one full beam size had to be scanned onto the apertures. This required an aperture overlap of 3 mm, given a 3-mm beam size. With a stage area of 1.8 cm^2 inside the aperture, the total beam area would be 3.8 cm^2 (for an aperture area of 2.0 cm^2), so the stage-to-aperture current ratio would be roughly 1:1. A schematic including the aperture with overlaying beam pattern is demonstrated in figure 4.11 which shows how the beam would overlap the stage and aperture to obtain a 1:1 ratio of stage-to-aperture current. This ratio would ensure the beam would raster completely off the stage onto the apertures.

The tantalum aperture plates are limited in the amount of current they can receive without melting, roughly 25 μA total for the whole aperture. This relatively low aperture current would have limited the amount of stage current that could be used during irradiation if the 1:1 ratio was followed. In practice, a ratio of less than 2:1 stage-to-aperture current was maintained; in other words, the stage current never exceeded twice the aperture current. From experience, this stage-to-aperture current ratio was sufficient for uniform irradiation of the stage samples, in part because of the use of guide bars on each end of the stage which did not require the uniform irradiation like the stage samples.

Irradiations were conducted by scanning the proton beam over the surface of the samples. The beam was scanned in the horizontal and rastered on the vertical directions at 255 Hz and 2061 Hz, respectively. The length of one beam scanning cycle was 3.9 ms. The ratio of the two scanning cycles was 8.08. By scanning such that the ratio of the two cycles was not an integer, the beam path would be offset from previous scans, further

ensuring spatial uniformity. This complex scanning pattern is demonstrated in figure 4.12 with an outline of the apertures in the background [17].

Beam size was measured by using a Beam Profile Monitor (BPM). The BPM was a device able to measure the intensity distribution and position of a beam of charged particles. It consisted of a single wire formed into a 45° helix rotated about the central axis of the helix. The BPM would sweep across the beam in two orthogonal directions in every cycle. As the BPM intercepted the beam, secondary electrons would be emitted and the current could be measured using an oscilloscope. The signals on the oscilloscope gave information on the position and size of the beam.

The BPM device is provided in an image in figure 4.13, showing the correct position of the selector knob during operation of the BPM. Figure 4.14 shows the oscilloscope with the fiduciary marks where the beam profiles would be centered. The two peaks of the beam, representing beam size in the X and Y direction, are shown centered correctly in figure 4.15. Note, however, that the peaks should be of equal height, even though this is not represented precisely in the image. Notice also that the grid marks on the oscilloscope represent actual spatial measurements of the beam. With the TIME/DIV selector knob set at 5 ms, which is shown in the upper right hand corner of figure 4.15, the grid represents a spacing of 1 cm. Changing the TIME/DIV selector knob to 2 ms expanded the view of the beam, where the grid then represented a spacing of just 2 mm. At this setting, the X and Y dimensions were measured to ensure beam size was 3 mm or less. Focusing of the beam could be performed until the beam size was measured at 3 mm or less on the BPM.

4.2.5 Thermocouples

During irradiation, temperature was monitored using a set of four thermocouples. The series of J-type thermocouples, usable up to temperatures of 600°C, consisted of 0.005" iron and constantan wires threaded through insulating sheath. The insulator was used to protect the wires and prevent them from contacting one another and causing a short in the thermocouple. The standard setup was to use four thermocouples on the irradiation stage to provide some redundancy in measurement and to check for uniformity of temperature over the samples. In order to attach the thermocouples to the sage, the

two wires of the thermocouples were crossed and spot welded at the intersection using a portable spot welder with a power setting of 30% and time setting of 2.5%. The thermocouples were placed such that they were close to the irradiated area but not directly in the ion beam since the proton charge may affect their behavior. Also, the thermocouples were spot-welded around the hold-down bars and not over top of them, ensuring that no insulating sheath rested above the stage samples. An image of the thermocouples can be seen in figure 4.5 which shows the thermocouples wrapping around the hold-down bars to connect to the feed-through which sent the temperature readings to a monitoring computer used to record irradiation data throughout the experiment. This image demonstrates the proper arrangement of thermocouples spot-welded onto the irradiation stage.

4.2.6 Irradiation Monitoring

Sample temperature was monitored using both the thermocouples and an IRCON Stinger thermal imaging system. The position of the imaging system outside of the accelerator relative to the stage was shown previously in figure 4.2(a). The main purpose of the thermocouples was to calibrate the Stinger camera at the planned irradiation temperature prior to the start of the irradiation. An additional thermocouple was inserted into a port in the rear of the copper block to measure the back temperature of the irradiation stage.

The primary means of temperature measurement and control during an irradiation was through the Stinger thermal imaging system. Temperature was monitored in the Stinger software through the use of an Area of Interest (AOI). Each AOI measured up to four pixels in width and six pixels in height and was created as an area that fit entirely within one sample to measure the temperature of a region within that sample. Three AOI's were created on each sample and the emissivity of each AOI was calibrated, at the planned irradiation temperature, but prior to the start of irradiation. The AOI emissivity values were calibrated to reflect the average thermocouple temperatures. The AOI's were monitored continuously throughout the irradiation and temperature data for each AOI was output to the Stinger computer every second. A total of 60 data points were averaged and then a single value was recorded, each minute giving one data point per

AOI per minute. Using the dual thermocouple/Stinger system, sample temperatures for each AOI were controlled such that all temperatures remained within ±10°C of the set irradiation temperature.

If the irradiation temperature for any AOI drifted outside of the ±10°C range, audible alarms sounded, and a combination of the stage current, heating cartridge voltage, and cooling air pressure was adjusted in order to return the AOI's within the desired temperature range. For minor adjustments in temperature, only the heating cartridge voltage was adjusted to return the stage temperature back to the normal range. Changing the heater voltage allowed for the finest control over stage temperature, as compared to changing the cooling air pressure, for which temperature adjustments were more coarse. Although temperature occasionally drifted outside the desired ±10°C range, it did so only by a degree or two and for such an insignificant duration compared to the total irradiation time that the average and standard deviation of the temperature for each sample remained well within the desired range of the irradiation temperature.

Irradiation parameters were monitored continuously using a PC-based system. Over the course of the irradiation, sample temperature, beam current, stage and aperture current, and irradiation dose were monitored. Irradiation monitoring was implemented using the Labview™ program. The software recorded the stage current, aperture current, Stinger AOI temperatures, and five thermocouple temperatures. The system allowed for continuous monitoring and recorded each parameter to provide an irradiation history. Alarms were also incorporated to warn the operator when parameters exceeded defined limits. Figure 4.16 is a Stinger pyrometer temperature history for an irradiation, showing the number of measured temperature data points for all samples on the irradiation stage. The figure shows the target irradiation temperature of 500°C, the average temperature for the entire irradiation, and the 2σ value of the measured temperatures, denoted by dashed lines on the figure. Included are solid lines showing the ±10°C range of the target irradiation temperature.

4.2.7 Radioactivity and Beta Counting

During irradiation, the 3.2 MeV protons undergo nuclear reactions with elements in the target specimens. There are a number of potential isotopes that may be created in

the alloys based on the (p^+,n) reaction energy thresholds that are below 3.2 MeV. Not all of the isotopes are radioactive, and even fewer are of radiological concern if they have a very short or very long half-life. However, an assessment of the amount of induced radioactivity is important because of regulatory limits for work involving radioactive specimens. A detailed discussion of the radioactivity induced by proton irradiation can be found in Appendix A. The appendix includes the radioactive isotopes produced and estimates of the amount of radioactivity per specimen based on 2 MeV, 3 MeV and 3.2 MeV proton irradiations.

Following irradiation, samples must be allowed to decay for ~1 day in order to allow for the short-lived isotopes, notably ^{61}Cu, and ^{64}Cu, to be reduced to lower radiation levels. Beta counting can then be performed for each specimen. The purpose of beta counting is twofold: to assess the dose uniformity among samples that were irradiated, and to compare beta activity to previous irradiations to establish the absolute dose of each of the irradiated specimens. The first purpose assumes that all of the samples have a near-uniform composition; large composition variations between samples will prevent a true comparison in dose uniformity. For the second purpose of beta counting, an empirical model of expected beta activity is required. A modified version of the empirical beta activity is provided in figure 4.17. The figure includes a combination of two exponential equations that model beta activity as a function of decay time from the end of the irradiation. Note that the beta activity model is applicable only to 3.2 MeV proton irradiations. Activity for lower energy proton irradiations will result in a lower beta activity because some of the isotopes may not be created due to the reaction energy thresholds.

Each TEM bar was counted for five minutes in a Tennelec LB 5100 2π alpha/beta counter. Each sample was placed in a metal disk with the irradiated face up toward the detector to be counted. Beta counts were normalized over the area of the samples in order to correct for size differences between the samples. The activity was also normalized to radiation dose and finally normalized to Fe content. For alloys with similar compositions, but with small variations in Fe content, the beta activity can be roughly normalized to account for these differences in composition. Note that this will

only work for alloys that are similar in composition to 304SS and 316SS, as the empirical model was developed based on activity from these alloy types.

4.3 Post-Irradiation Sample Preparation

A number of post-irradiation analytical techniques were performed after the completion of post-irradiation hardness measurements. The analyses required first the careful preparation of TEM discs for the analysis of radiation-induced segregation (RIS) and dislocation loop imaging. The TEM discs were also utilized in preparing sharp-tip specimens using focused-ion beam (FIB) for atomic resolution characterization with field ion microscopy. This section will describe the procedures used for preparation of TEM specimens.

4.3.1 TEM Preparation

TEM bars were bonded using wax resin to round aluminum polishing blocks with the irradiated side facing down to leave the unirradiated face exposed for wet grinding from 320 – 4000 grit SiC paper to remove most of the thickness from the 2 mm bars. Sample bars were thinned typically to less than 300 μm during the wet grinding process to decrease the amount of time required for slurry drill cutting ot TEM samples. Sample thickness was checked during the thinning process using a digital micrometer until the samples reached the desired thickness.

The thinned TEM bars were then mounted using wax resin on a graphite block and placed in a South Bay Technologies slurry drill cutter. A 3-mm inner diameter brass drill bit was used to drill out discs to perforation through the TEM bar. Slurry consisting of 600 grit SiC powder with distilled water was added between the drill bit and the TEM sample for use as an abrasive in the cutting process. A total of 3 irradiated discs can be cut from each TEM sample, starting from the center of the bar, and then drilling out discs on either side as closely as possible to ensure that each of the TEM discs lay fully within the irradiated region of the sample. Since the TEM bar had a width of only 2 mm, the TEM discs were oval shaped with dimensions of 2 mm by 3 mm, as shown in figure 4.18.

After cutting TEM discs, the TEM samples were mounted once again on the polishing block with the irradiated face down to expose the unirradiated surface onto a Gatan 623 sample polishing unit. Individual discs were carefully thinned using 4000 grit SiC paper to ensure a flat planar surface down to a thickness of ~ 100 μm.

Thinned TEM discs were mounted in a SouthBay Technologies, Inc. single-jet electropolishing unit. A solution of 5% perchloric acid and 95% methanol was chilled to -55°C using dry ice, and the solution was used as the electrolyte. Samples were first thinned from the irradiated face for approximately 30 seconds to remove ~ 10 μm of material from the irradiated face. The sample pedestal was then cleaned in acetone, then methanol, and the sample was remounted on the unirradiated face to electrolytically polish from the unirradiated face just until perforation of the sample. Typical time until perforation was approximately 8 – 10 minutes, depending on the actual thickness of the specimen. Once the sample had been perforated in the center of the disc, the sample was analyzed in an optical microscope to ensure an adequate hole in the sample. If the hole was too small, additional thinning could be done from the unirradiated face for a few seconds to enlarge the hole slightly.

4.3.2 Ion Milling

The prepared TEM discs were inspected for adequate thin area in a JEOL 2010F TEM. The operating voltage of 200 keV and electron intensity (current) was the same as the instrument, the Philips CM200, to be used for RIS analysis so that electron transparency of the thin area of the sample would appear similar between microscopes. If there was inadequate thin area or contamination of organics on the surface, the sample was mounted in a Gatan Model 691 Precision Ion Polishing System to enhance the thin area of the specimen and remove any residual contamination. The samples were ion milled with Ar at an operating voltage of 4 keV and typical ion currents of 15 – 20 μA at angles ranging from 5 – 7°. Samples were rotated during the milling process to ensure uniform removal of material. Milling was usually done from the unirradiated face first, for times ranging from 10 – 20 minutes. Additional milling was then done from both the unirradiated and the irradiated face for 5 – 10 minutes to thin both sides and remove any

material from the irradiated face that may have been sputtered onto the surface during the milling process.

4.4 Radiation-Induced Segregation

Measurements of RIS were made using scanning transmission electron microscopy (STEM) with electron-dispersive X-ray spectroscopy (EDS). This is a commonly used technique for high-resolution composition measurements, especially for spatial composition measurements such as those made across a grain boundary. The remainder of this section will describe instrumentation and methods used for RIS measurements.

4.4.1 STEM Instrumentation

Microchemistry measurements of grain boundaries were made with a Philips CM200/FEG at Oak Ridge National Laboratory using scanning transmission electron microscopy (STEM) with energy dispersive X-ray spectroscopy (EDS) with a probe size of approximately 1.5 nm diameter (full-width, tenth-maximum) at 200 kV with a beam current of typically 1 nA or more. A Philips Compustage, room-temperature double-tilt specimen holder was used to minimize specimen drift during analysis and allowed for sufficient tilt control to align grain boundaries. Prior to analysis, the Compustage holder and samples were both plasma cleaned using a Southbay PC150 plasma cleaner. Plasma cleaning removed the hydrocarbons from the foil surface, drastically reducing the formation of contamination on the specimen. The holder with a mounted sample was cleaned for 10 minutes in an Ar plasma, followed by 10 minutes in an O_2 plasma with 10 watts of forward power for both plasmas. After cleaning, the holder with sample was inserted into the CM200 microscope.

Microchemistry data was collected and analyzed using Emispec ES Vision software. The Emispec software allowed for automated control of the electron probe and STEM imaging system. The software also provided for automatic acquisition of composition profiles, allowing the user to input the number of points to be taken along a

defined line, along with the spacing of those points and the acquisition time for each point.

4.4.2 STEM/EDS Measurements of RIS

RIS measurements were performed after alignment of grain boundaries 'edge-on' to the incident electron probe to maximize beam exposure of the grain boundary. Grain boundaries in thin areas were measured in order to minimize beam broadening. A drawing of an 'edge-on' grain boundary is shown in figure 4.19 showing the excitation volume from the electron beam as it passes through a specimen with a grain boundary aligned edge-on. An image taken in STEM mode of an aligned grain boundary is shown in figure 4.20. The magnification for the image is 700,000X, the magnification used to make grain boundary measurements in STEM mode. Notice in the figure that the grain boundary is represented by a line with high contrast whereas the matrix on either side of the boundary should have low contrast when the boundary is aligned 'edge-on'. The figure also illustrates the beam damage that can occur from the STEM probe during RIS measurements.

During grain boundary alignment, several factors were considered in the selection of grain boundaries for alignment. When possible, only boundaries that intersected at triple points were aligned; this ensured that the boundary was not a twin boundary and was also likely to be high-angle boundary. Boundaries were aligned such that they exhibited low contrast on either side of the boundary, meaning that the grains on either side of the boundary would not be strongly diffracting. A strongly diffracting grain would significantly increase beam broadening through the specimen and decrease the grain boundary resolution for the measurement. In addition, grain boundary alignment was only performed in the positive b tilting direction for the holder as this ensured that the sample was tilted toward the EDS detector. Measurements performed with the holder in a negative b direction would have resulted in little or no x-ray signal entering the EDS detector window and would have prevented chemical analysis of the grain boundary.

Analysis involved measurement of two or more grain boundaries for each alloy condition, with typically six profile measurements across each boundary. Line profile measurements were 30 nm in length with a total of 21 measurements per line, for a 1.5

nm spacing of each measurement. Results for all boundaries and measurements were averaged together to determine the average depletion or enrichment for each element at the grain boundary due to irradiation. The amount of segregation was taken as the difference between the grain boundary measurement and the bulk composition measurement away from the boundary.

Two matrix area measurements were also made for each specimen in order to determine the *k*-factors, which will be discussed in the next section. Matrix measurements were made in raster scan mode over a larger area, between $10 - 20$ μm square. The measurements were made away from the boundary and over a large area to ensure that local variations in composition would not influence the bulk composition measurement.

4.4.3 STEM/EDS Composition Calculation

After data acquisition of a line profile, the concentration, in at%, was calculated to determine the grain boundary composition. For all of the alloys, the major and minor alloying elements (Fe, Cr, Ni, Mn, and Mo) were analyzed along with the impurity Si and the oversized solute addition, Zr or Hf. Table 4.3 presents the elements that were analyzed in addition to the K_α or L_α X-ray energies used in the analysis.

X-ray intensity data for each element was integrated over a certain energy window in order to sum the number of counts received for the element. These energy windows were used consistently for each of the alloys and the values are also shown in table 4.3.

The ratio of the concentration of atom A to atom B in a material is proportional to the ratio of the measured intensities by the Cliff-Lorimer equation [95]:

$$\frac{C_A}{C_B} = k_{AB} \frac{I_A}{I_B} \tag{4.2}$$

where k_{AB} is known as the Cliff-Lorimer factor, or *k*-factor. The *k*-factor is not a physical constant and will vary on the basis of the STEM/EDS system and beam energy used. Similarly, for a ternary alloy,

$$\frac{C_A}{C_C} = k_{AC} \frac{I_A}{I_C} \tag{4.3}$$

and,

$$\frac{C_B}{C_C} = k_{BC}\frac{I_B}{I_C} \qquad\qquad (4.4)$$

This relation can easily be extended to any number of elements. Also, assuming that no other elements are present in the material, then the following is true:

$$C_A + C_B + C_C = 1 \qquad\qquad (4.5)$$

Equations 4.2 – 4.4 can be solved simultaneously. If the factors k_{AB} and k_{AC} are known, the concentrations of each element can be readily calculated. The k-factors are calculated using the matrix area measurements with the bulk composition based on the alloy composition data from table 4.1.

In this study, the k-factors were all calculated relative to Cr, as in k_{CrFe} k_{CrFe} k_{CrMn}, etc. For each matrix area measurement, the set of k-factors was calculated, and then the k-factors were averaged. These average values were used to determine the concentration for all measurements taken. A set of k-factors was calculated for each specimen examined, but the k-factors for the same element pair was not necessarily the same for different alloys. The differences were due in part to different absorption arising from differences in bulk compositions between alloys.

4.5 Dislocation Loop Imaging

Irradiation-induced microstructure was characterized using a JEOL 2010F TEM at the North Campus Electron Microscopy Analysis Laboratory at the University of Michigan. The TEM operates at 200 kV and is equipped with a 1024x1024 pixel charge-coupled device (CCD) and with a Gatan double-tilt, room-temperature holder. A dark-field imaging technique was used to image dislocation loops that form as a result of irradiation. This technique and the imaging results will be discussed further in the next two sections.

4.5.1 Dark-field Technique

Stacking-fault defects such as dislocations form a 'spike' that is oriented along the direction that is normal to the defect plane. This 'spike' represents a reciprocal-space

lattice rod, or rel-rod, reflection. These reflections create additional spots in the diffraction pattern which can be used for imaging.

Dislocation loops for a face-centered cubic (FCC) lattice lie on the (111) planes. There are four (111) planes in the FCC lattice, with a 70.5° angle between the planes. The dislocation loops can be imaged by tilting off the <011> zone axis and inserting the objective aperture around the rel-rod streaks that form along the $\mathbf{g}$ = <113> reflection between the $\mathbf{g}$ = <200> and $\mathbf{g}$ = <111> reflections. Two diffraction patterns showing this condition are presented in figure 4.21 to show the faint streaks that can appear from the faulted loops [36]. In this condition, Frank loops from two of the (111) planes will be visible while the others will not appear. So only ¼ of the loops will be visible, and the number of loops must be multiplied by a factor of 4 to obtain the actual number of loops. In order to image the loops, the objective aperture must be carefully centered on one of the rel-rod streaks, with imaging in dark field showing only the faulted loops, which show up as bright lines. Rel-rod streaks from the images were measured and counted to provide a dislocation loop size and density.

The rel-rod technique images only the faulted dislocation loops and is therefore a powerful analytical tool. At the same time, since imaging relies on the rel-rod streaks that form due to faulted loops, the technique can be very challenging when loop size and/or density are low, roughly < 1 x 10^{22} #/m$^{2.}$, because there are not enough loops to form the streaks. As a result, image quality is sometimes poor for those samples in which loop density is small.

4.5.3 Loop Measurements

Dislocation loop images were typically taken at a magnification of 50,000X. After loop images were taken, the images were analyzed for loop size and density.   The length of each rel-rod streak was measured in order to calculate an average loop diameter. In addition, loop densities were calculated by using the image area and sample thickness to determine the sample volume. For each specimen, the total number of loops was added together and then multiplied by the correction factor of 2 to come up with a loop density. In addition, the volume for each image of a particular specimen was added

together to come up with a total sample volume. Then the loop population was divided by the total sample volume in order to determine the loop density for a specimen.

4.6 Determination of Oversized Solute in Solution

The solubility of Zr or Hf in Fe-Cr-Ni alloys is not known, but looking at phase diagrams of Zr or Hf in Fe or Cr or Ni, it can be assumed that the solubility will be very low. A clear first step in the analysis of the precipitate phases involved quantification of the composition, and there are many ways in which this can be done. A variety of techniques was employed to attempt to determine the amount of oversized solute remaining in solution. The techniques included a determination of the precipitate area through secondary electron microscopy (SEM) combined with energy dispersive spectroscopy (EDS), X-ray diffraction to determine the amount of precipitate phase present in the alloys, and field ion microscopy using a local electrode atom probe (LEAP) with sample preparation using focused ion beam (FIB). Each of these techniques had certain limitations and drawbacks, but in concert they could determine the presence of oversized solute remaining in solution. A description of each of the techniques is listed below, covering x-ray diffraction, SEM imaging, and LEAP analysis.

4.6.1 X-ray Diffraction

To help determine which type of precipitate is present in the alloys, a study of the precipitate phases was performed using x-ray diffraction (XRD). Using information from x-rays that scatter off the electrons within a crystal, a determination can be made about the crystallographic orientation of atoms within a material, as well as positions and lattice spacing. This is because crystallographic materials have long range order where the diffraction of x-rays from the atoms produces patterns that correspond to the planar spacing of the atoms. Comparing the diffraction information to a library database, a lattice parameter can be found which corresponds to the phase/material being examined. In the case of a material where two different phases exist, two different lattice parameters will be found, and these can be used to identify the phases as well as calculate the relative abundance of each phase.

X-ray diffraction was performed at Lockheed Martin's Knolls Atomic Power Laboratory using a Bruker D8 Discover general area detector diffraction system (GADDS) and a Rigaku Dmax B. Unirradiated specimens were first wet-polished using a series of 320, 600, and 1200 grit SiC paper to remove surface deformation from the EDM machining process.

Multiple scans were made of each alloy condition to ensure the accuracy of results. The duration of each scan varied depending upon the range of diffraction angles being measured, but typical scans would last 30 minutes or more. After obtaining the x-ray diffraction data, a search was made for peaks that could identify the presence of the precipitate phases, in particular the presence of ZrC in the +Zr alloys and HfC in the +Hf alloys. Intensity peaks in the x-ray diffraction pattern angles represented the different phases present in each of the samples. These intensity peaks were compared to a large database of known crystallographic materials in order to identify each phase.

Lattice parameter calculations of the primary phase – austenite – and the estimated concentrations of the precipitate phases were performed using the Jade Whole Pattern Fitting software package [96]. The (331) and (420) peaks of the face-centered cubic structured austenite samples were used for the matrix lattice parameter calculations. These calculations included a Si external standard (SRM 640B) which was used to correct for systematic error in the instrument.

The peak intensity for each phase corresponded to the volume fraction of that phase in the material. A volume fraction of precipitate phase with oversized solute was calculated from the Jade Whole Pattern Fitting software, and the results were used to estimate the amount of oversized solute still remaining in solution.

4.6.2 SEM Imaging

A second analysis of the precipitate microstructure relied on SEM with the use of a backscatter electron (BSE) detector. Backscattered electrons are those electrons from the original electron beam which are scattered out of the specimen back toward the detector. These electrons contain high contrast information and can be used to highlight regions of composition variation where the variations are due to differences in the atomic

number. Regions with a higher Z will show a higher contrast and appear brighter in the image.

Since austenitic stainless steel consists of a single homogeneous phase, BSE imaging should not reveal any variations in contrast on the sample. However, secondary phases such as precipitates may have a different average Z and therefore can be imaged using a BSE detector due to the contrast difference. An example of this contrast difference is shown in figure 4.22 for HiZr, revealing the precipitate phases present in the alloy.

These contrast differences existed for precipitate phases of high Zr or Hf content in the oversized solute alloys. Using a JEOL JSM-6480 SEM equipped with a BSE and EDS detector, an analysis of the secondary phases was performed in order to try to identify these precipitate phases. For the imaging analysis, one sample for each alloy was polished to a mirror finish with a final step using 0.02 μm silica. Each sample was imaged at 2000X magnification. Using EDS on the precipitate phases, the presence of Zr or Hf was identified in the precipitates to confirm the nature of these precipitates as being solute-rich phases.

4.6.3 TEM Imaging

Using a JEOL 2010F TEM, the HiZr and HiHf alloys were imaged to identify and quantify the precipitate phases in the matrix of the alloys. Using a small objective aperture for high-contrast imaging, a total of 5 images were collected per alloy. Using Scion Image for Windows [97], a diameter for each of the precipitates was measured. Based on the diameter, the area of each precipitate was calculated and the total precipitate area was summed. Using the lattice parameter for ZrC and HfC, the total precipitate area was compared relative to the matrix area, and based on this ratio, the amount of oversized solute remaining in solution was calculated.

4.6.4 FIB and LEAP

A final technique for quantifying the oversized solute in solution rested on the local-electrode atom probe (LEAP). The method combines time-of-flight spectroscopy and field ion microscopy (FIM) to create three-dimensional composition maps with

atomic resolution. Using a specimen with a sharp tip, typically with a tip radius of 100 nm or less, a high voltage is pulsed between the tip of the specimen and a local electrode. The voltage pulse creates an electrical field that is carefully controlled to ionize and evaporate a single atom at a time which, based on the time-of-flight, can be identified with high-spatial resolution according to the mass-to-charge ratio of the atom. The use of a local electrode allows for a larger field of view and higher data acquisition rates compared to other atom probes.

Analysis of specimens in a LEAP system required specially prepared samples where a sharp needle-like tip protrudes from the end of the specimen. The tip must be free of secondary tips surrounding the primary tip in order for analysis to be successful. To this end, two different methods were used to prepare samples for analysis in LEAP. The first method for unirradiated samples consisted of sample bars that were electropolished from one end of the sample bar to create the sharp tips necessary for analysis. All four oversized solute alloys used this method for solute quantification in the unirradiated condition.

A second method for sample preparation utilized a focused ion beam (FIB). The FIB combines a standard secondary electron microscope with a focused beam of gallium ions. Using a liquid metal ion source, gallium is melted to coat a tungsten filament. Passing a large voltage across the filament causes the ionization and field emission of the gallium ions to form the ion beam. The purpose of the gallium ions are for destructive sputtering that can be used for micro-and even nano-scale machining of samples.

Using a sample lift-out method that is described in Appendix B, sharp-tip specimens were prepared using the FEI Nova 200 Dual-Beam FIB at Oak Ridge National Laboratory. The FIB employed a combination of Pt deposition and Ga^+ milling for sample lift-out and Ga^+ milling for tip fabrication. In the ideal case, the multi-step process resulted in specimens with less than 100 nm diameter tips with minimal Ga^+ implantation into the specimen.

After preparation with FIB, samples were loaded into an Imago Scientific Instruments Local Electrode Atom Probe®. Samples were cooled to liquid He temperature before being inserted into the specimen chamber for analysis. A minimum of one million atoms was required in order to obtain an adequate data set for composition

analysis. Samples with fewer than the one million atoms in the data set were deemed insufficient and no analysis was performed on these data sets. Sample sets with a sufficient number of atoms were collected for each of the four oversized solute alloys in the unirradiated condition. In addition, irradiated specimens were analyzed for 316+HiZr at 3 and 7 dpa, 316+LoZr at 3 and 7 dpa, and 316+HiHf at 3 dpa.

4.7 Error analysis

Measurements of the grain boundary microchemistry, radiation hardening and dislocation loop density all require some error to be associated with the measured value. The purpose, of course, is to provide some level of confidence in the measured value and a range in which one might expect to find the value for a measurement made under identical conditions.   In this work, the standard deviation of the data set is provided, described by the following equation:

$$\sigma = \sqrt{\frac{1}{N} \cdot \sum_{i=1}^{N} (x_i - \bar{x})^2} \tag{4.7}$$

where N is the total number of measurements in the data set, σ is the standard deviation, x_i is a measurement in the data set, and $\bar{x}$ is the average of the measurements.

In many cases, values are reported that are actually an indirect measurement from two directly measured values. In this case, each directly measured value has a standard deviation, so taking the sum or difference, etc. of the two measured values requires consideration of the standard deviation from each measurement. One must then consider the propagation of error to determine a new standard deviation. The rules for propagation of error analysis are listed in table 4.3.

Table 4.1 Summary of bulk alloy compositions (wt%) determined by chemical analysis

Sample Composition (wt%)										
Alloy	Fe	Cr	Ni	Mo	C	Mn	Si	P	Zr	Hf
Ref-Zr	bal.	14.34	13.5	0.16	0.050	1.21	0.38	0.005	<0.01	<0.01
LoZr	bal.	14.40	13.55	0.18	0.050	1.30	0.38	0.021	0.310	<0.01
HiZr	bal.	13.91	13.48	0.17	0.050	1.18	0.40	0.021	0.450	<0.01
Ref-Hf	bal.	17.65	13.85	2.23	0.022	1.00	0.12	0.011	<0.01	<0.01
LoHf	bal.	17.42	13.45	2.18	0.025	1.01	0.14	0.012	-	0.160
HiHf	bal.	17.03	13.6	2.18	0.028	1.01	0.10	0.010	-	1.170

Table 4.2 Thermo-mechanical heat treatments and processing steps taken to achieve an average grain size of approximately 20 μm for each alloy

Alloy	Steps Thermo-Mechanical Processing
Ref-Zr	1) Homogenization at 1200°C for 2 hours in flowing hydrogen. 2) Cold roll to 50% total reduction, with target of ~ 2% reduction per pass. 3) Homogenization at 1200°C for 2 hours in flowing hydrogen. 4) Cold roll to 25% total reduction, with target of ~ 2% reduction per pass. 5) Recrystrallization at 950°C for 2 hours in flowing hydrogen.
LoZr HiZr	1) Homogenization at 1200°C for 24 hours in flowing argon. 2) Cold roll to 66% total reduction, with target of ~ 2% reduction per pass. 3) Recrystallization at 1000°C for 1 hour.
Ref-Hf LoHf HiHf	1) Homogenization at 1200°C for 24 hours in flowing argon. 2) Hot roll at 1100C to 25% total reduction 3) Homogenization at 1250°C for 1 hour. 4) Cold roll to 50% total reduction, with target of ~ 2% reduction per pass. 5) Recrystallization at 1000°C for 1 hour.

Table 4.3 X-ray emission energies for elements analyzed in composition analysis, including the energy window used for each window in the Emispec ES Vision software

	K energy	L energy	Energy window
Si	1.740		1.675 - 1.825
Zr		2.042	1.975 - 2.125
Mo		2.293	2.192 - 2.392
Cr	5.415		5.290 - 5.546
Mn	5.899		5.830 - 6.043
Fe	6.930		6.258 - 6.549
Ni	7.478		7.348 - 7.608
Hf		7.899	7.825 - 7.975

Table 4.4 Rules for calculating the propagation of error for Z based on two quantities, A and B, each of which have an associated error

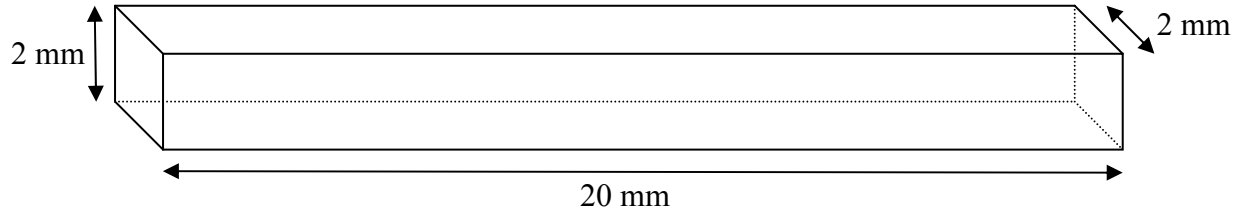| Relation between Z and (A,B)	Relations between error ΔZ and $(\Delta A, \Delta B)$
1 $Z = A \pm B$	$(\Delta Z)^2 = (\Delta A)^2 + (\Delta B)^2$
2 $Z = AB$	$\left(\dfrac{\Delta Z}{Z}\right)^2 = \left(\dfrac{\Delta A}{A}\right)^2 + \left(\dfrac{\Delta B}{B}\right)^2$
3 $Z = A/B$	$\left(\dfrac{\Delta Z}{Z}\right)^2 = \left(\dfrac{\Delta A}{A}\right)^2 + \left(\dfrac{\Delta B}{B}\right)^2$
4 $Z = A^n$	$\dfrac{\Delta Z}{Z} = n\dfrac{\Delta A}{A}$
5 $Z = \ln[A]$	$\Delta Z = \dfrac{\Delta A}{A}$
6 $Z = e^A$	$\dfrac{\Delta Z}{Z} = \Delta A$

Figure 4.1 TEM sample bar design produced by electron-discharge machining for proton irradiation.

a)

Infrared
pyrometer

3.2 MeV p+ beam

Specimen stage

Ceramic
isolator

b)

Copper stage   Ceramic standoff

Heater

Air cooling
loop

3.2 MeV
p+ beam

Tantalum
Aperture

Indium layer between specimen
and stage

Hold-down bar

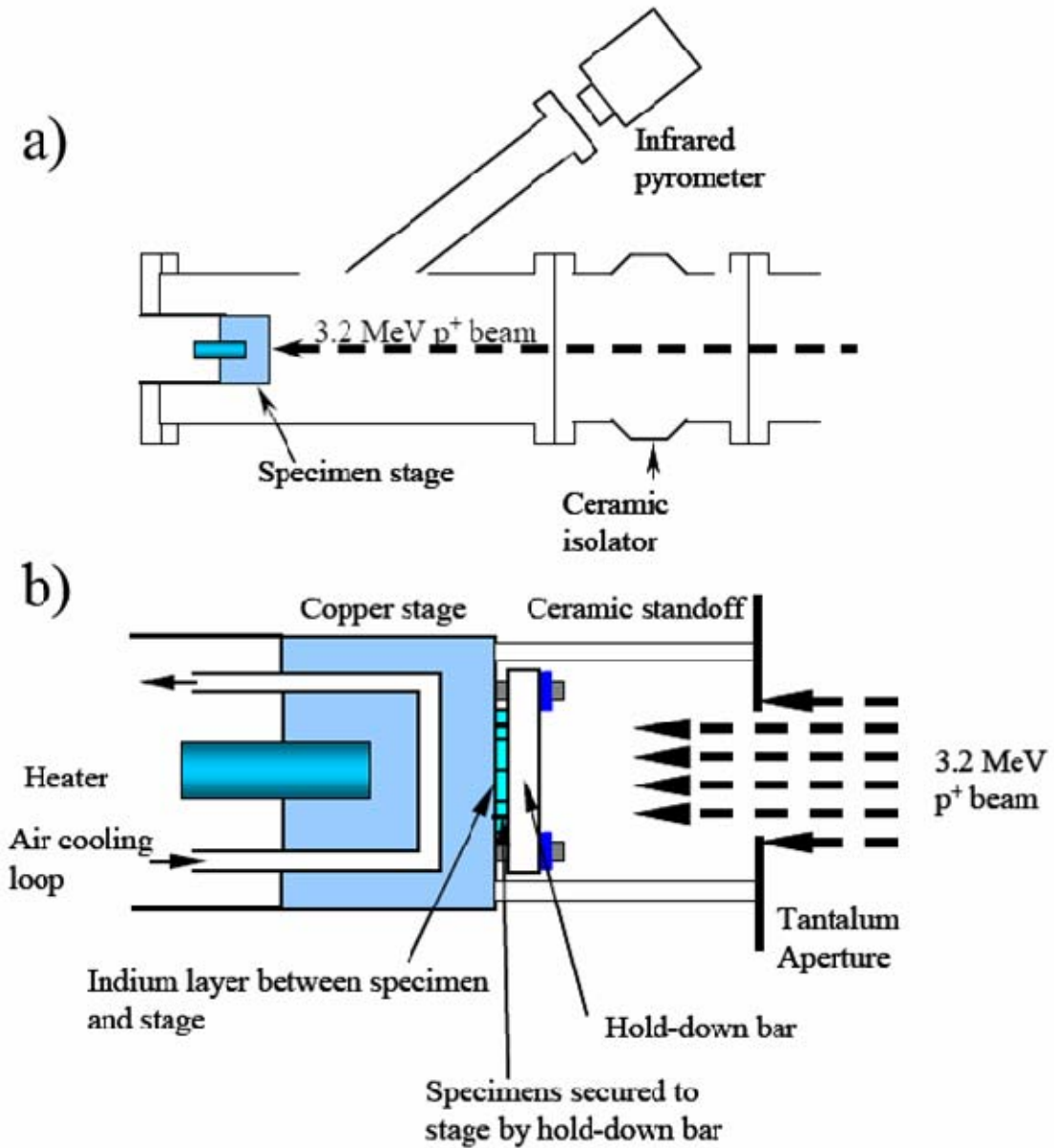Specimens secured to
stage by hold-down bar

Figure 4.2 (a) Position of the Stinger thermal imager in capturing infrared radiation from the samples during irradiation, and (b) illustration of the sample stage that was used for proton irradiation of the TEM bars. Taken from [17].
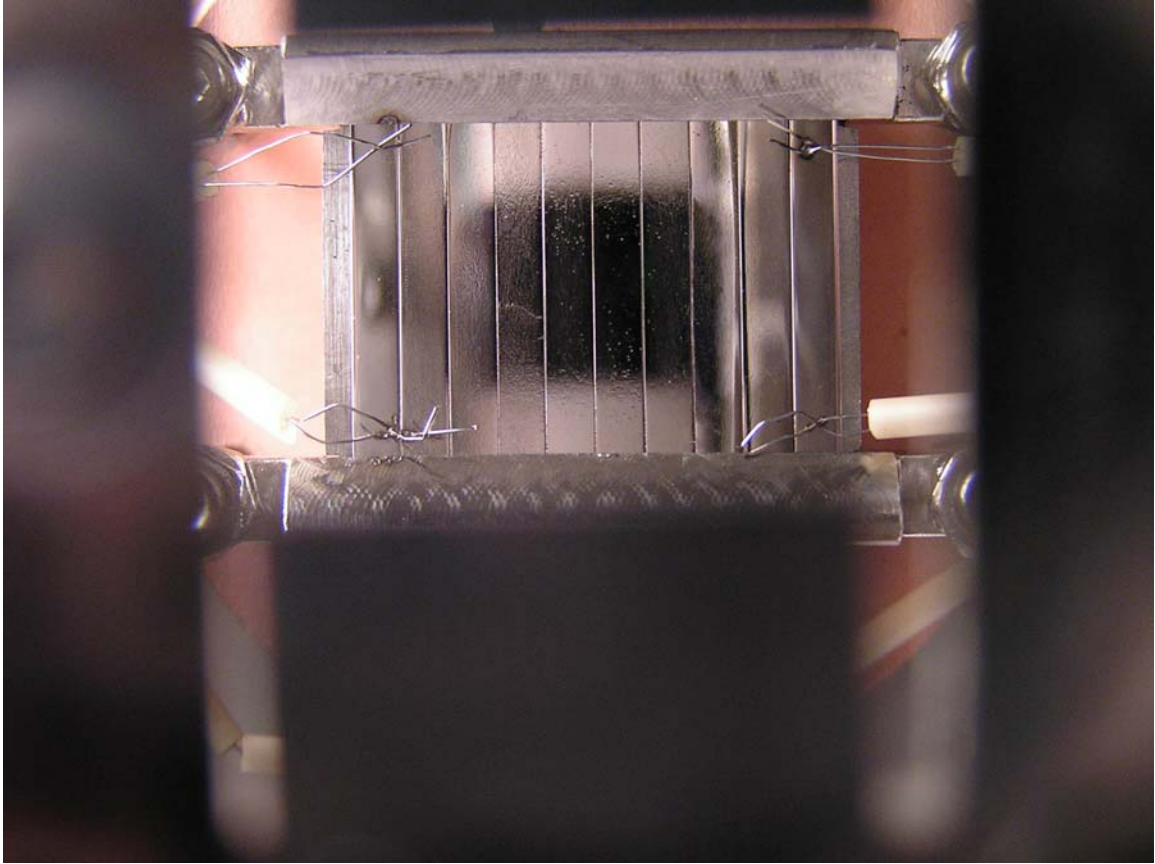
Figure 4.3 Photograph of eight samples plus two guide bars mounted on the stage prior to irradiation. The image shows thermocouples spot-welded onto the samples.

All dimensions are in mm

25

40.15°

3

3

2

2mm ID

3.556

21*

3

6   4

10

* Hold down bars were
machined to fit on the
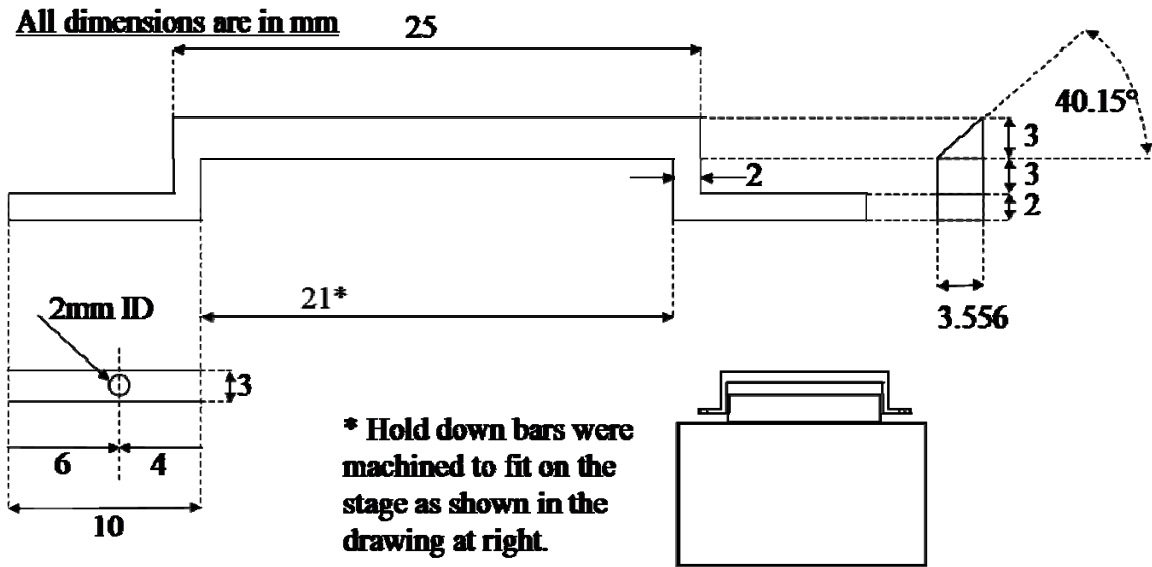stage as shown in the
drawing at right.

Figure 4.4 A drawing of the hold-down bars used to secure samples on the stage during irradiation.
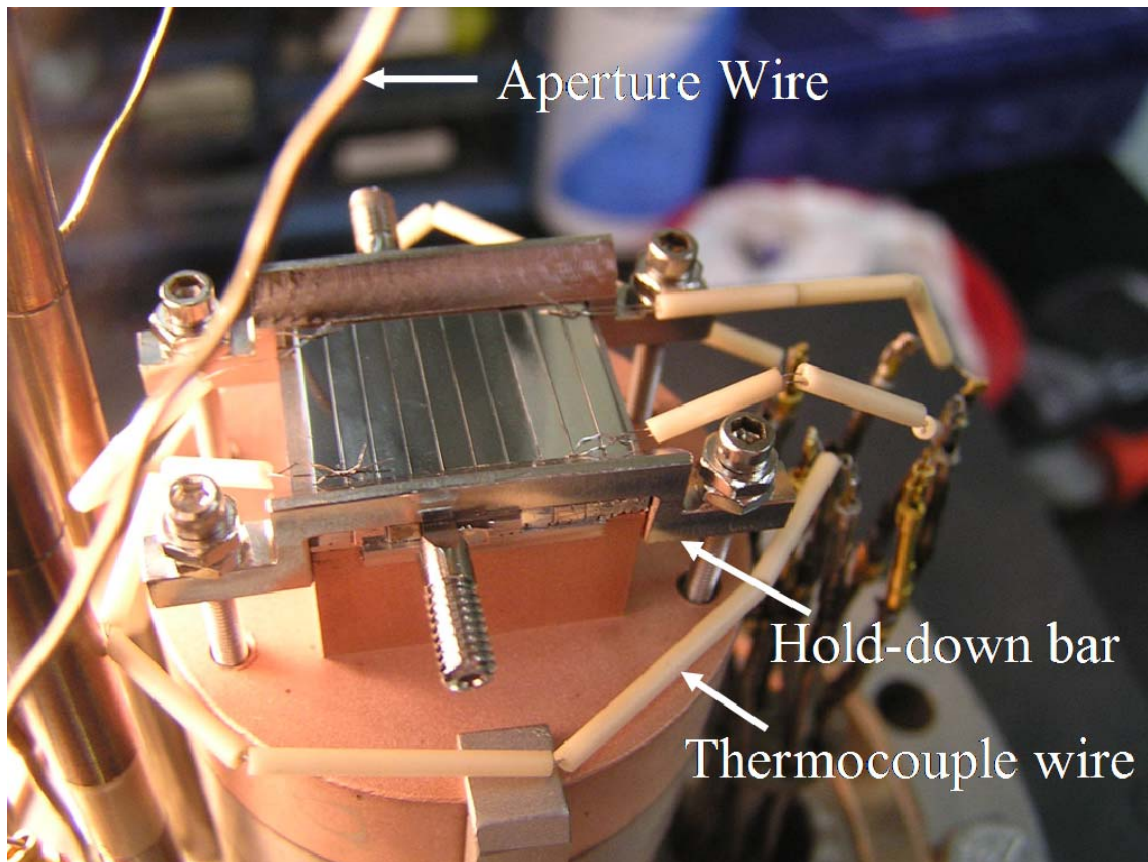
Figure 4.5 View of the copper stage with samples mounted, thermocouple wires, and hold-down bars.
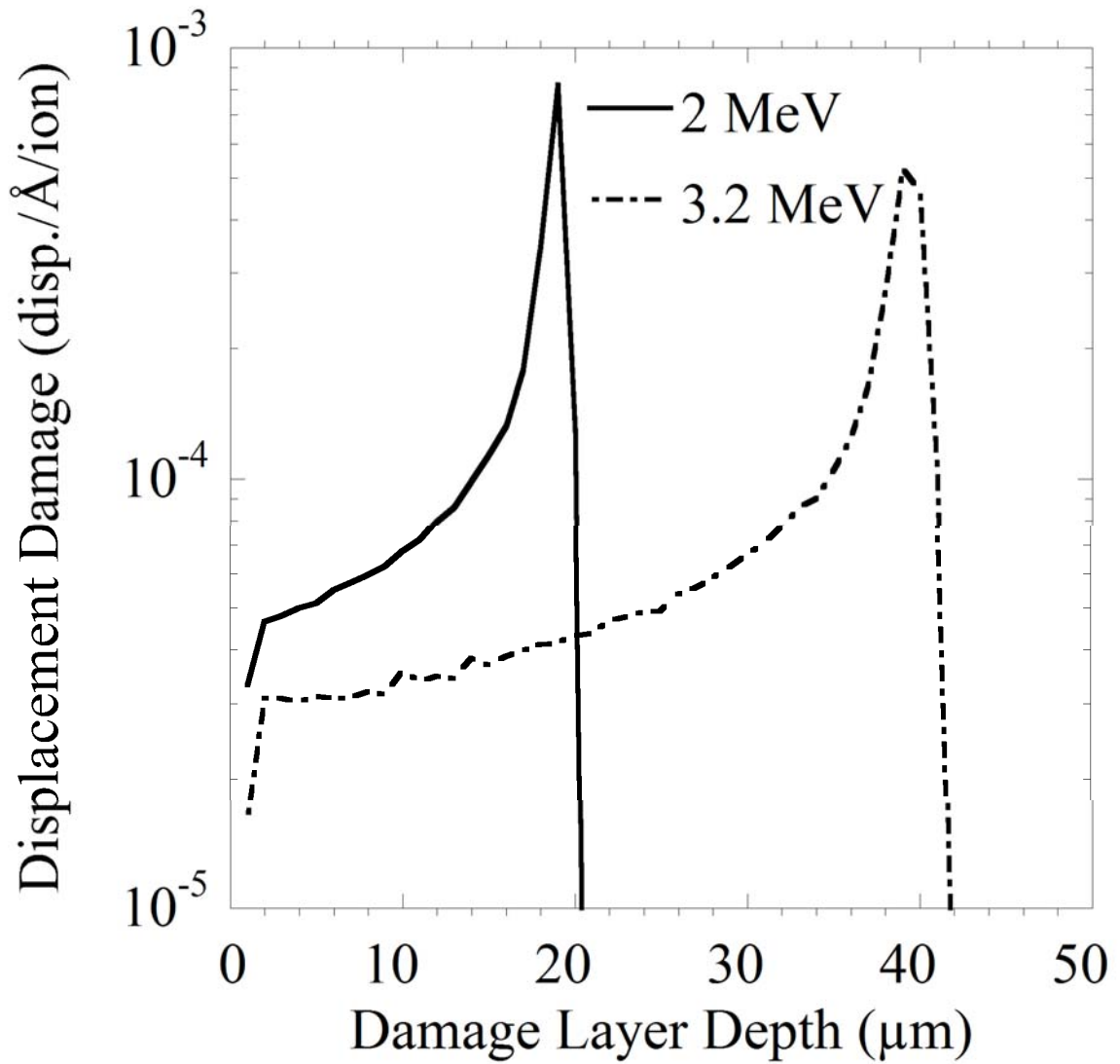
Figure 4.6 A view of the damage rate as a function of depth into the irradiated surface as calculated by SRIM 2006 [93] for 3.2 MeV protons in Fe-16Cr-13Ni alloy. A relatively uniform damage region is created from a depth of 5 – 35 μm, with a maximum damage depth at ~ 43 μm.
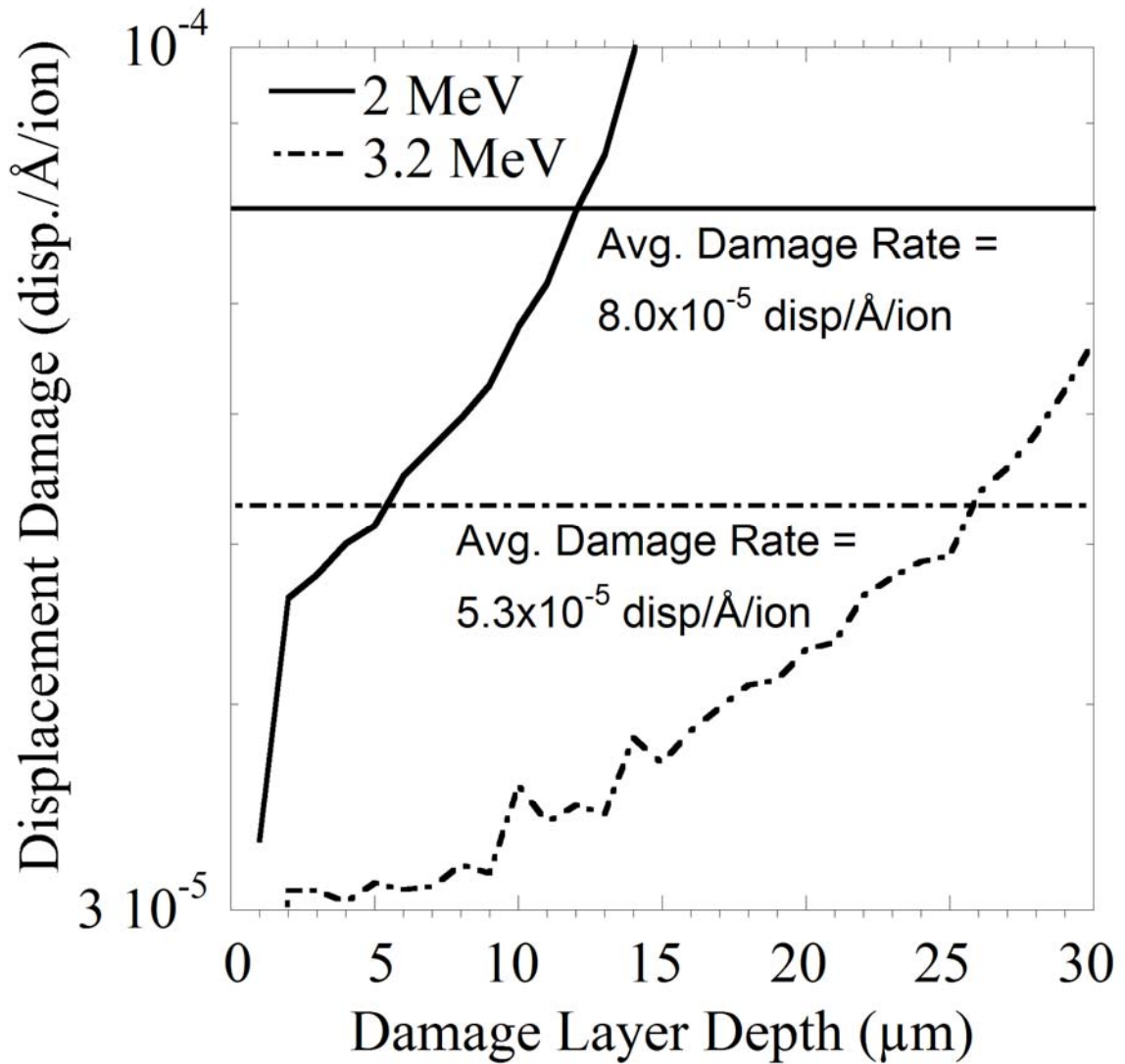
Figure 4.7 A closer view of the displacement rate as a function of damage layer depth as calculated by SRIM 2006 [93]. An average displacement rate is taken at ~ 26 μm for 3.2 MeV p[+], where the displacement rate is 5.3x10^{-5} displacements/Å/ion, and at ~ 12 μm for 2.0 MeV p[+], where the displacement rate is 8.0x10^{-5} displacements/Å/ion.
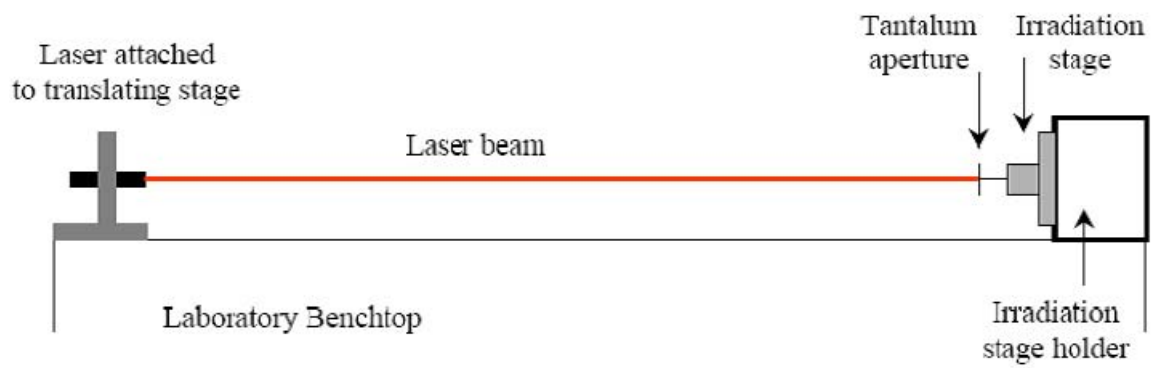
Figure 4.8 Setup of the laser alignment procedure for proper alignment of the aperture system on the irradiation stage. Taken from [17].
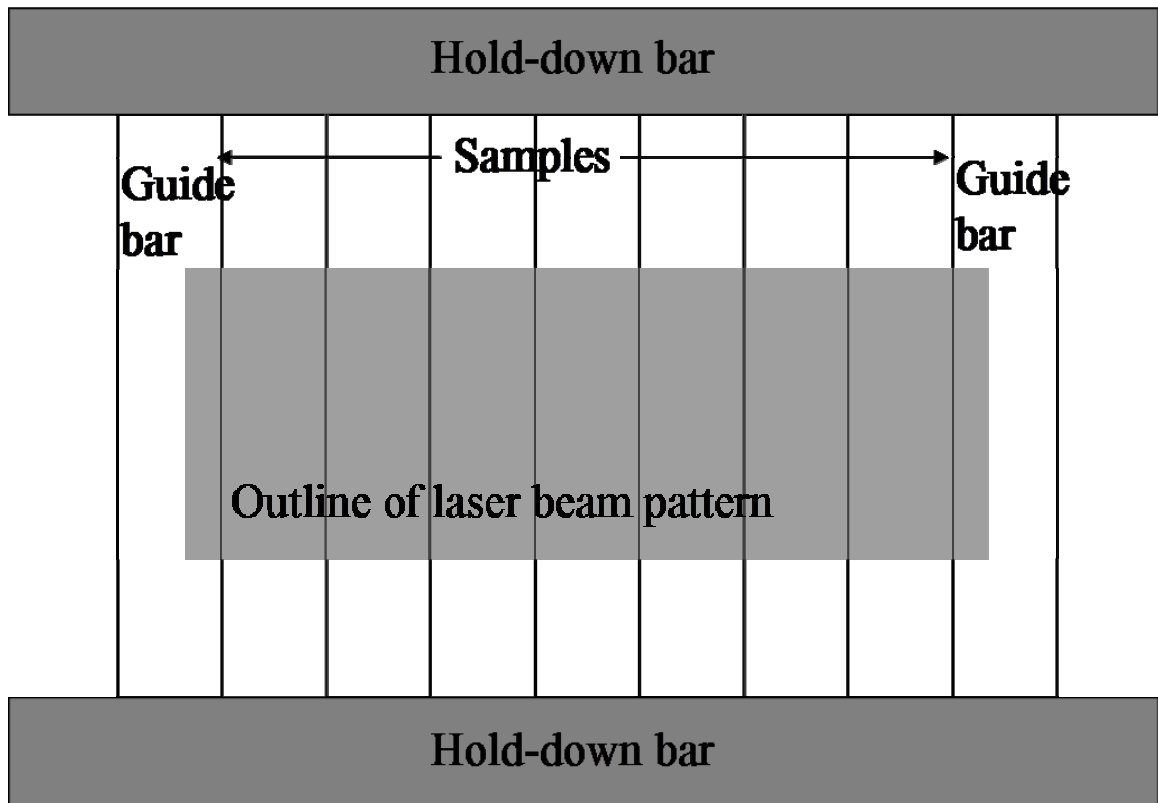
Figure 4.9 Representation of the laser beam pattern hitting the samples with a properly aligned stage.
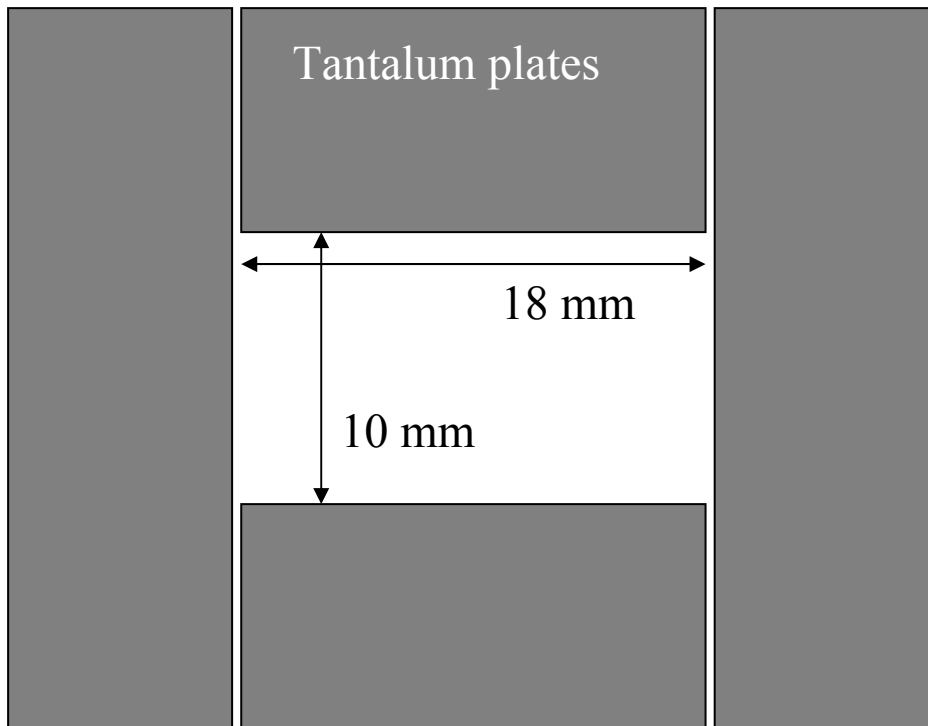
Figure 4.10 Schematic of the tantalum aperture system used to measure aperture current and shape the beam pattern for sample irradiation.
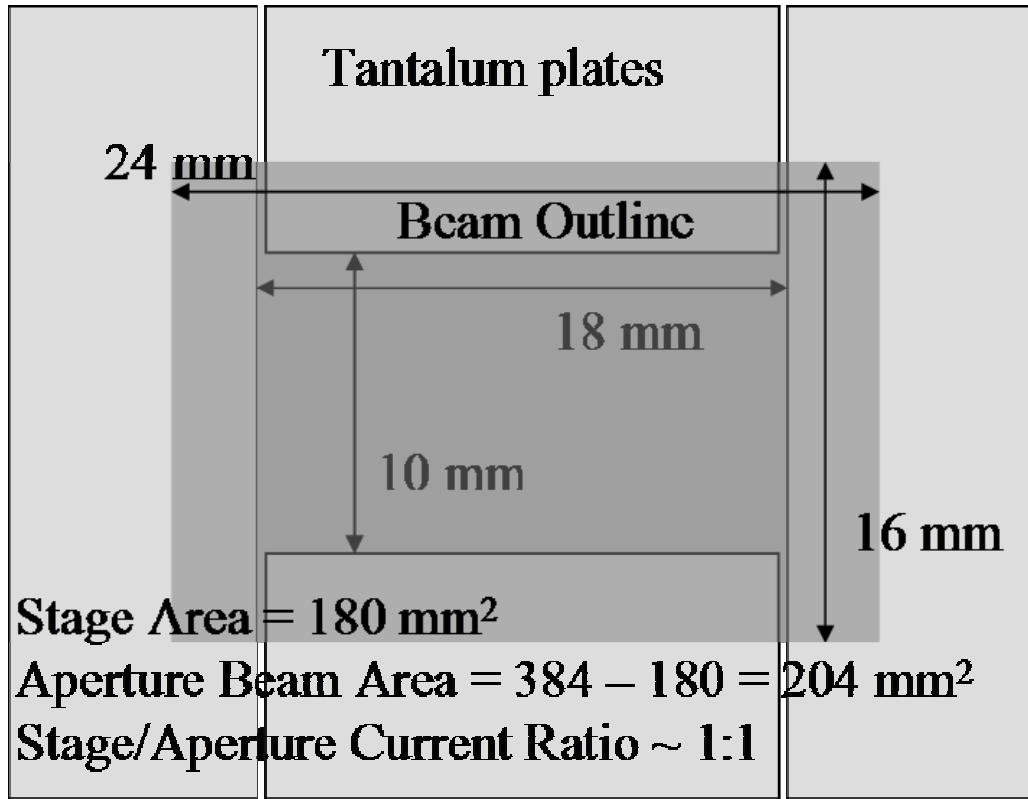
Figure 4.11 Schematic of beam-on-aperture overlap, with the resulting stage-to-aperture current ratio using a 3-mm beam size.

Path of center of beam

$f_y = 2061$ Hz
$T_y = 0.48$ ms

$f_x = 255$ Hz
$T_x = 3.92$ ms

Apertures
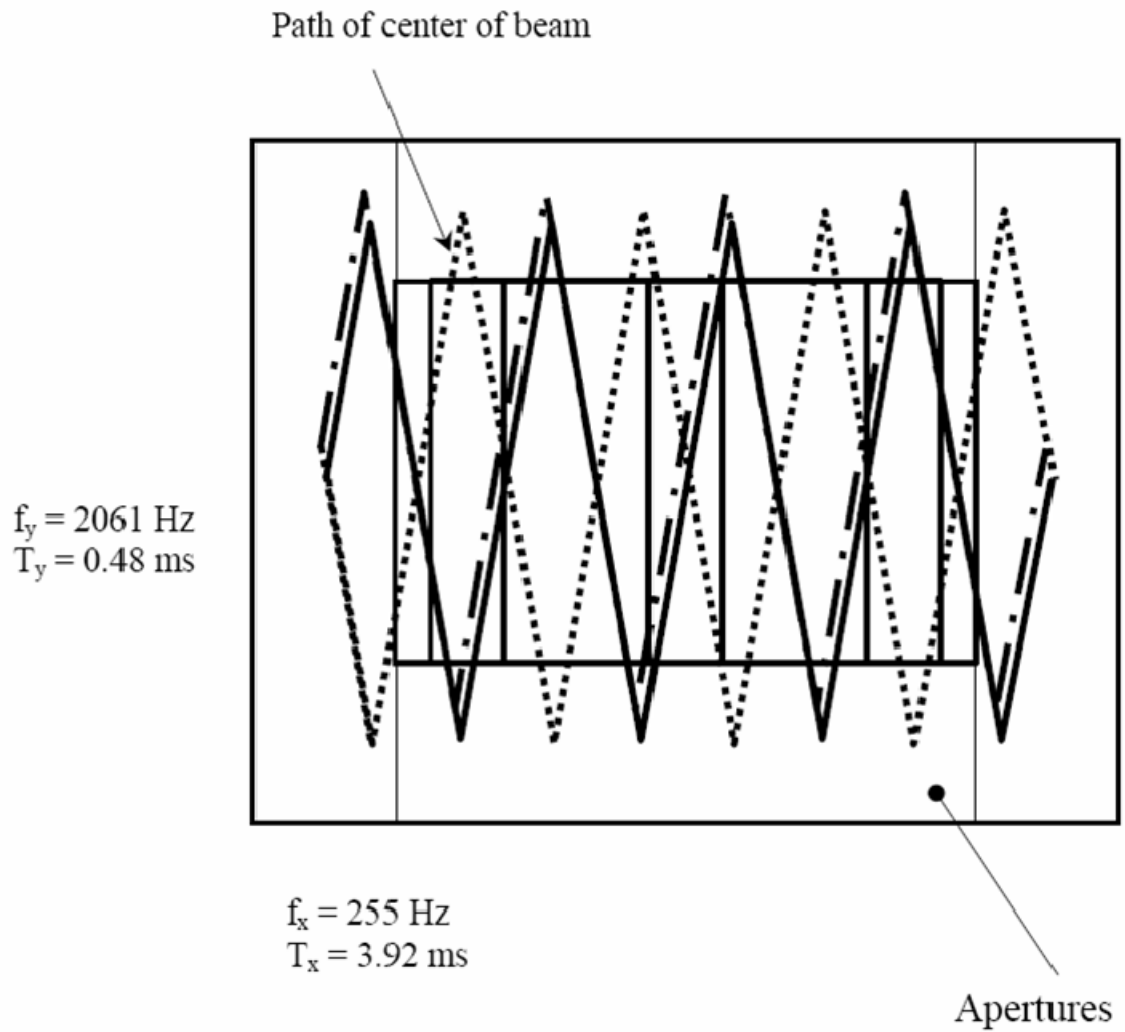
Figure 4.12 Beam scanning pattern of the raster scanner used during proton irradiation, taken from [17].

Figure 4.13 Beam profile monitor, including the beam selector knob set at 'beam profile' for beam size measurements.
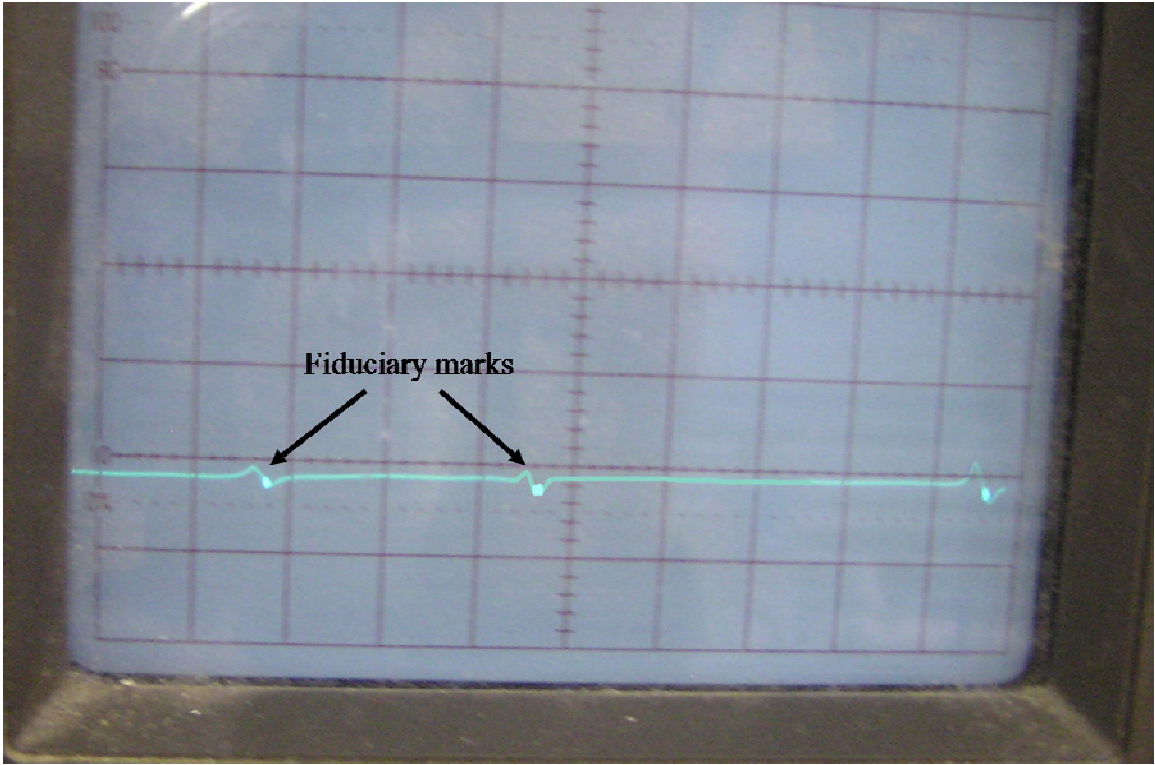
Figure 4.14 Image of the oscilloscope showing the positions of the fiduciary marks.
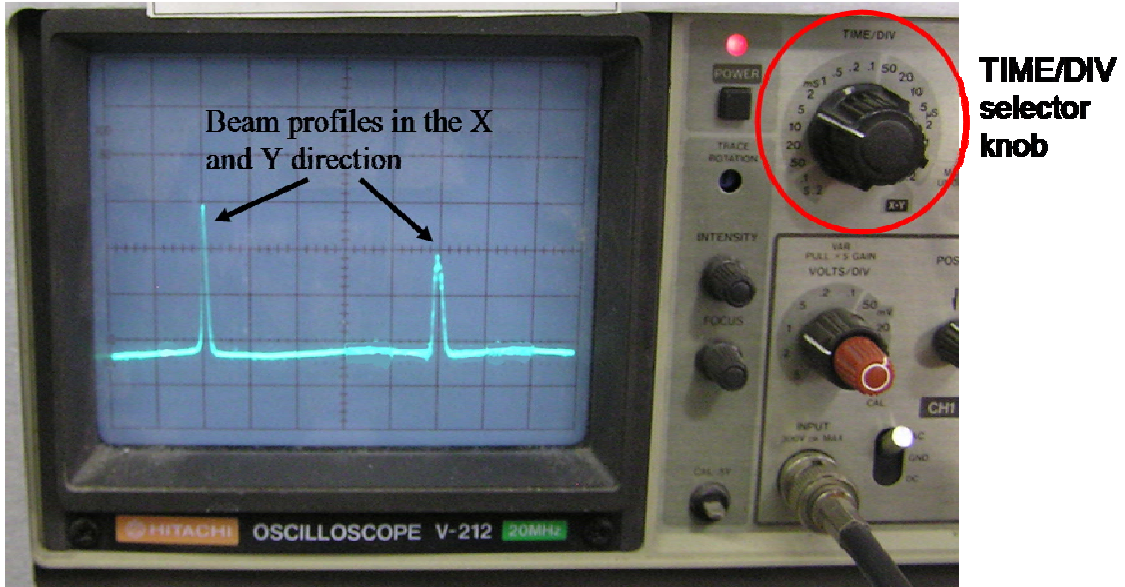
Figure 4.15 Oscilloscope image showing BPM current signal for beam size measurements.
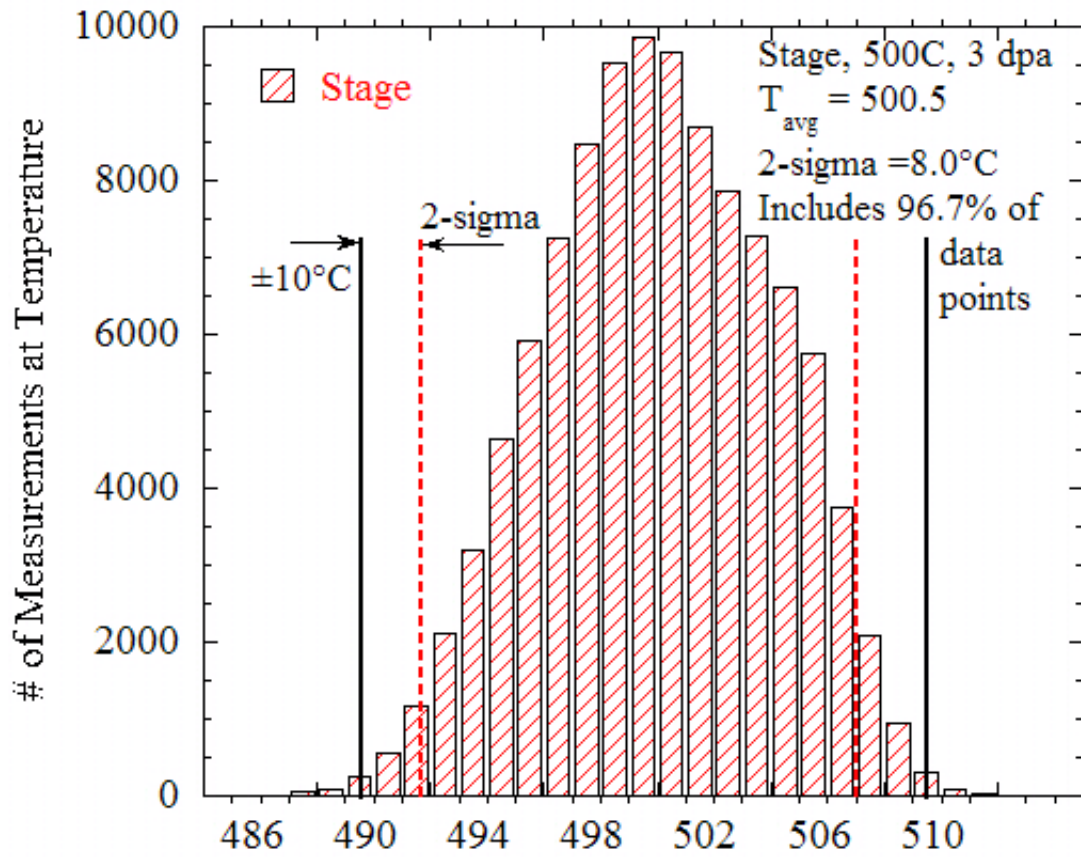
Figure 4.16 Stinger pyrometer temperature history for an irradiation, showing the number of measured temperature data points for all samples on the irradiation stage.
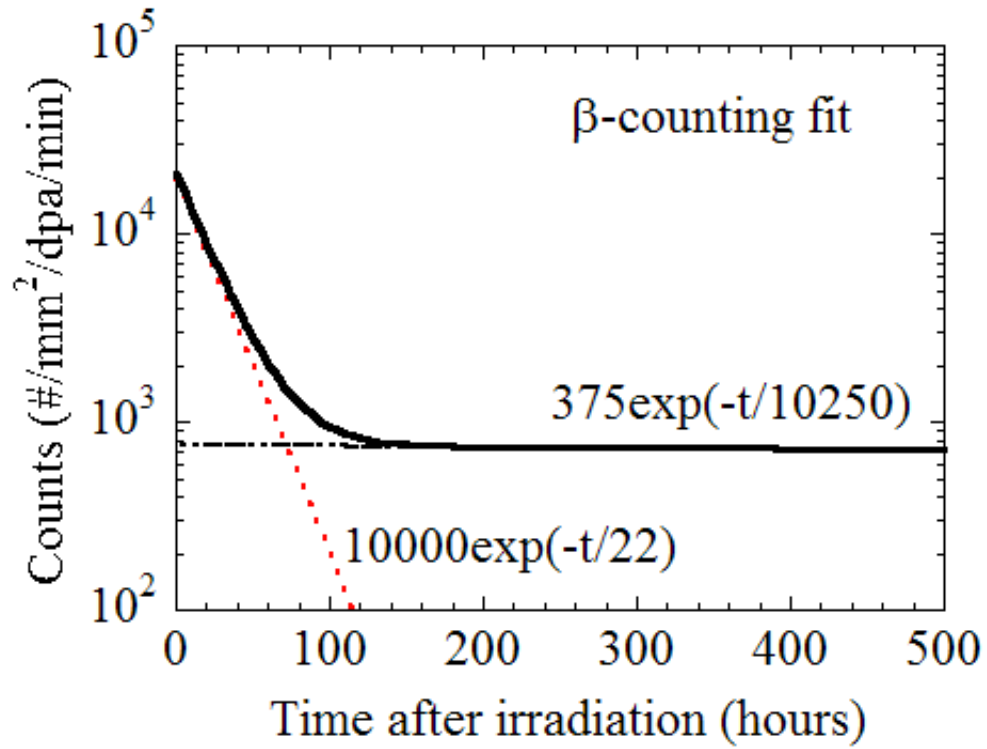
Figure 4.17 Beta activity model for predicting the number of beta counts as a function of time expected for an irradiation using 3.2 MeV p$^+$ of austenitic stainless steels. The combination of both exponential equations provided in the figure is used to predict the number of beta counts.

Resulting shape of TEM disc after slurry drill cutting from TEM bar

Shape of slurry drill cutting of TEM disc from irradiated sample
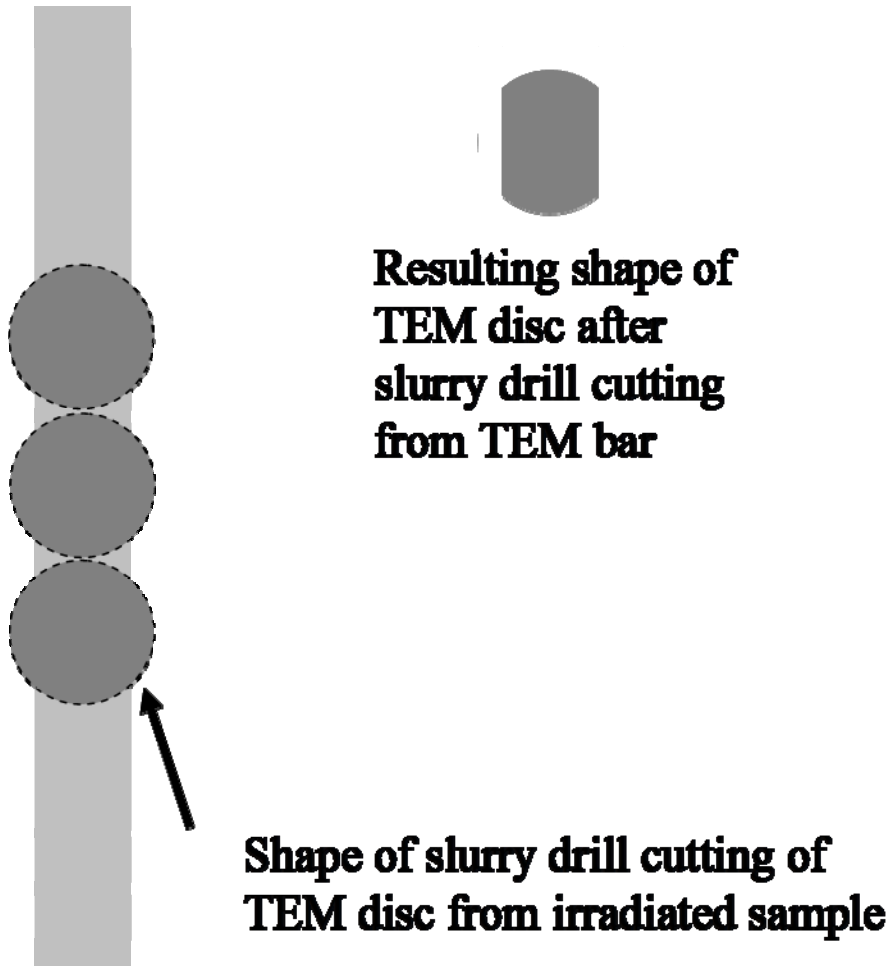
Figure 4.18 Illustration of TEM discs cut from an irradiated TEM bar.
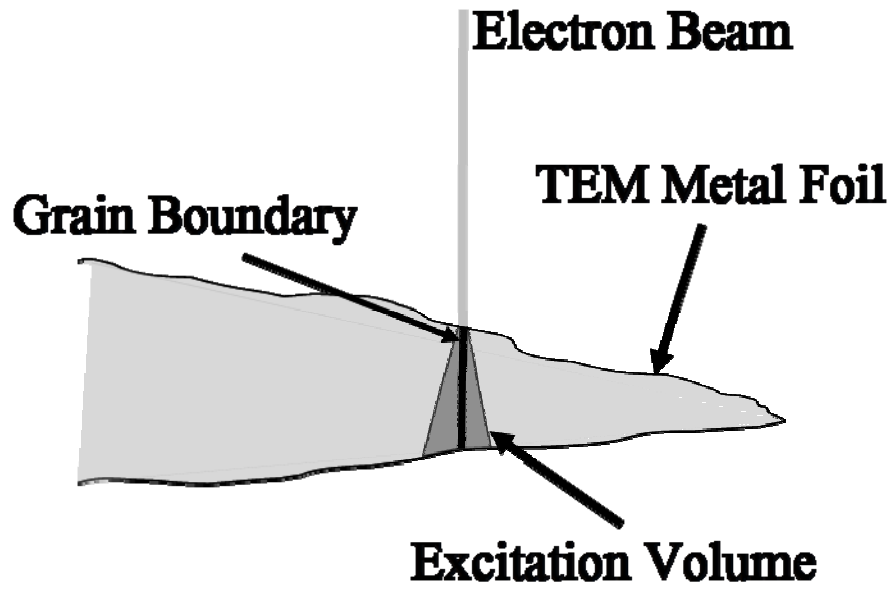
Figure 4.19 Sample foil with grain boundary aligned edge-on and the excitation volume of the electron beam as it passes through the specimen.
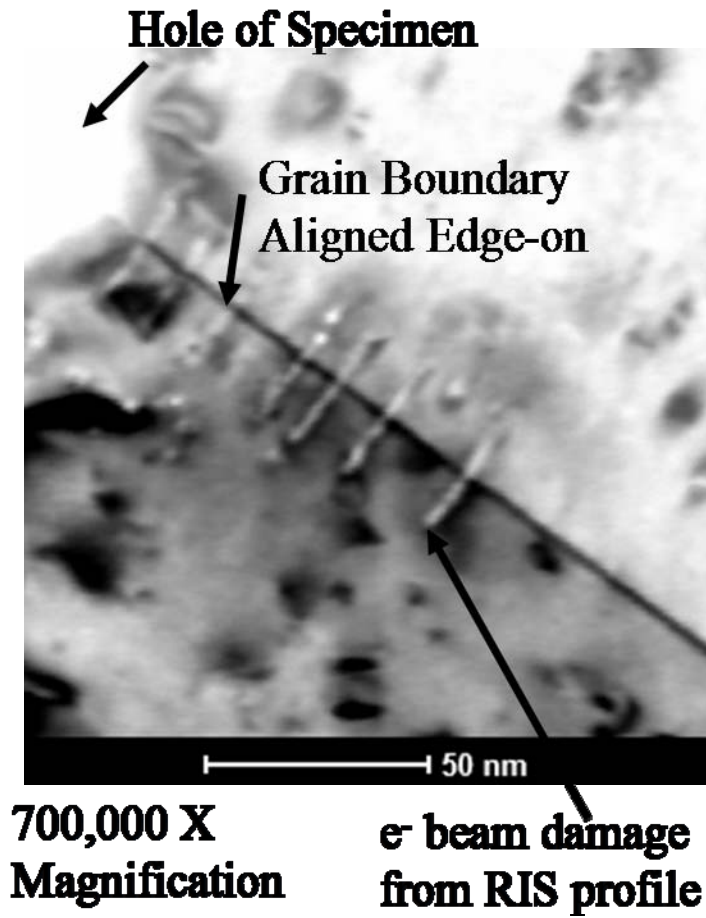
Figure 4.20 STEM image of a properly aligned grain boundary, with the boundary defined as a high-contrast line, including beam damage from STEM/EDS RIS measurements across the boundary.
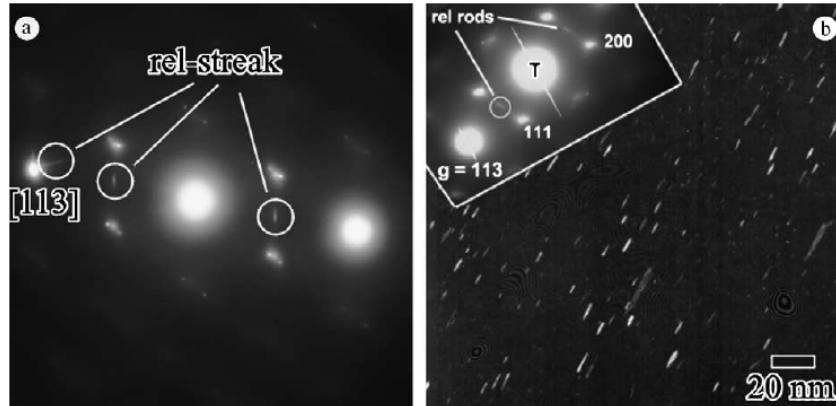
Figure 4.21 Relrod streaks, in (a) and (b), representing faulted dislocation loops, appear between the 111 and 200 spots along the g = 113 reflection for the [0 1 1] zone axis [36].
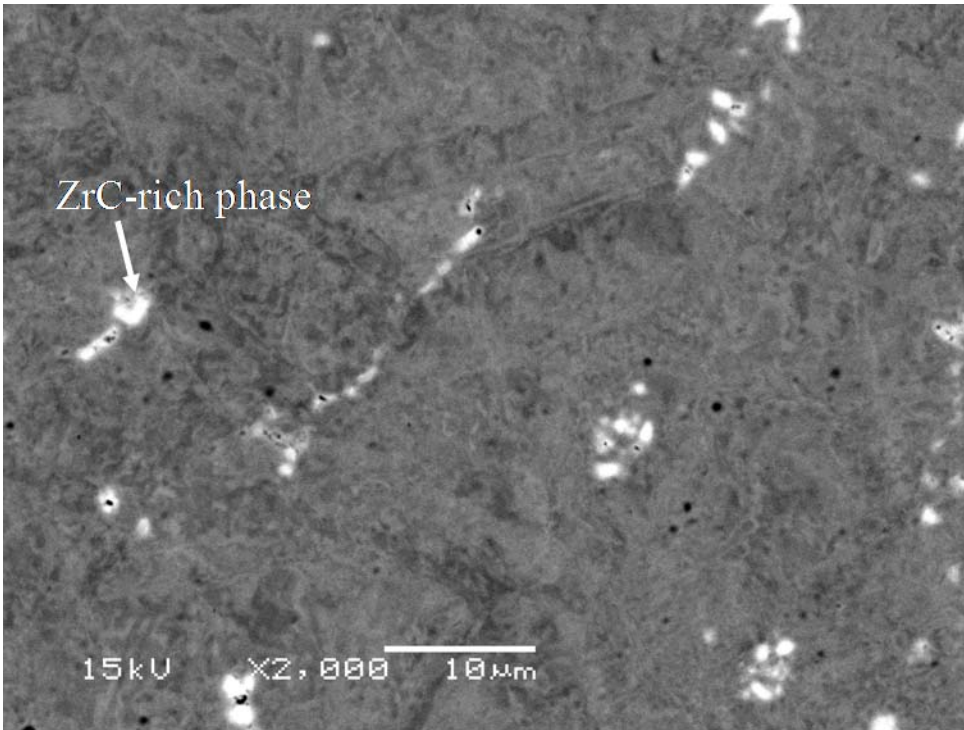
Figure 4.22 ZrC precipitate phase in 316+HiZr, imaged using a BSE detector in SEM.

CHAPTER 5

EXPERIMENTAL RESULTS

In the first section of this chapter, grain boundary segregation measurements are presented for the alloys Ref-Zr, LoZr, HiZr, Ref-Hf, LoHf, and HiHf. Data are presented for the following elements: Fe, Cr, Ni, Mn, Si and Zr in the +Zr alloys and Fe, Cr, Ni, Mn, Si, and Mo in the +Hf alloys, and figures show concentration profiles for Cr and the changes in grain boundary Ni and Cr concentrations as a function of dose for two different temperatures.

The second section of this chapter presents the dislocation loop measurements for each of the six alloys after irradiation to 400°C and doses of 3 and 7 dpa. Measurements include the loop size distributions and the resulting average loop diameters, dislocation densities, and total loop line lengths.

Finally, results are provided on the determination of oversized solute concentration in solution for the alloys LoZr, HiZr, LoHf and HiHf. Three different techniques are used for this analysis, which divides the last section into three parts. The first part describes the x-ray diffraction (XRD) results. XRD is performed on all four of the oversized solute alloys in the unirradiated condition. The purpose is to determine the nature of the precipitates present in the alloys. In addition, the fraction of precipitate in the alloy enables an estimate of the amount of oversized solute in the precipitates. From the atom fraction of the oversized solute in precipitates, an estimate is made of the amount of oversized solute remaining in solution.

The second part of this section presents the SEM images to confirm the presence of carbide precipitates in the matrix of the oversized solute alloys, and TEM imaging in the HiHf and HiZr alloys to determine the mean size and density of HfC and ZrC

precipitates, respectively. The precipitate microstructure results are used to calculate the amount of Hf remaining in solution in the alloy prior to irradiation.

The last part of this final section highlights results from an atom probe study of the four oversized solute alloys. These alloys are studied both in the unirradiated condition and also the irradiated condition at 400°C for 3 and 7 dpa. The purpose is to quantify the amount of oversized solute still in solution. In addition, samples are analyzed as a function of radiation dose to determine if there is a trend in solute concentration as a function of dose.

5.1 Radiation-Induced Segregation Results

This section presents RIS measurements of all irradiated alloys. STEM-EDS measurements are performed on grain boundaries that have first been aligned edge-on so that the optic axis of the microscope is in the grain boundary plane. Composition profile measurements are made in a direction perpendicular to the grain boundary, with profile line lengths of 30 nm and step sizes of 1.5 nm. The result is an intensity profile that can be converted into a concentration profile.

Samples of all alloys are irradiated with 2 or 3.2 MeV protons at 400°C to doses of 3, 7 and 10 dpa and at 500°C to doses of 1 and 3 dpa. In chapter 4.2.2, the differences in defect damage rate between 2 MeV and 3.2 MeV proton irradiations were described. As will be shown in chapter 7, there is no measurable difference in segregation results between 2 MeV and 3.2 MeV irradiations. Consequently, all RIS measurements of the same sample condition, regardless of proton energy, are averaged together to provide an average RIS value. No distinction is made between 2 MeV and 3.2 MeV segregation values when presenting the results as no major differences are found between the two data sets for any of the alloys.

The results in this section are divided by temperature and alloy. Results of impurity segregation are presented first. Then all RIS data is presented for the 400°C irradiations, which includes doses of 3, 7 and 10 dpa, first for the +Zr alloys, then for the +Hf alloys. This is followed by the 500°C irradiations to doses of 1 and 3 dpa, first for the +Zr alloys, then for the +Hf alloys.

5.1.1 Grain Boundary Segregation

In reporting the RIS data, the values of greatest interest are the amount of Ni enrichment and Cr depletion, as these can be used as easy points of comparison between the different alloys and different doses. For every irradiation condition Fe depletes at the grain boundary. Some of the minor elements also segregate at the grain boundary. Therefore, all of the measured segregation data is presented. For the +Zr alloys, this includes the major alloying elements Fe, Cr and Ni, plus the minor alloying element Mn and impurity Si, in addition to Zr for LoZr and HiZr. For the +Hf alloys, the measured segregation data includes Fe, Cr, Ni, Mn, Mo and Si.

For the +Zr alloys, no Mo data is reported because the alloy concentration is too low to be measured, and since Mo tends to deplete at the grain boundary in austenitic stainless steel, any changes will not alter the grain boundary composition significantly.

For LoHf and HiHf, no measurements of Hf are recorded for any of the spectra. The Hf $M\alpha_1$ X-ray peak, at 1.645 eV, overlaps with Si $K\alpha_1$ and $K\alpha_2$ x-rays at 1.739 and 1.740 eV. Since Si is known to enrich at the grain boundary, and Si concentrations are similar to Hf concentrations, any signal in a Hf energy window to determine the Hf concentration would inevitably show an increased signal due to grain boundary enrichment of Si.

Since the $K\alpha$ and $K\beta$ X-rays are too high in energy for detection, only the L X-rays remain for detection. The Hf $L\alpha_1$ and $L\alpha_2$ energies are 7.899 and 7.8445 eV, respectively, which makes them sufficiently close in energy to overlap in the same energy window. Using the neighboring Ni $K\beta_1$ X-ray peak at 8.265 keV to neglect detector efficiency, a ratio of the signals of Ni to Hf gives a minimum detectable concentration of ~ 1.7 at% Hf. Any grain boundary enrichment of Hf above this concentration should be detectable. Since no Hf was detected in any of the measured spectra, it can be assumed that enrichment of Hf above 1.7 at% did not occur for the LoHf or HiHf alloys. The details of this calculation are given in Appendix C.

Since the objective of this work is to focus on the effects of Zr and Hf on segregation behavior, this is best accomplished by analyzing trends in Cr depletion and Ni enrichment. Fe depletion also occurs for every alloy condition, but it can be largely inferred by the difference between Cr depletion and Ni enrichment. Segregation of the

other minor elements is not significant. Mn depletion is always less than 1 at% for any of the +Zr or +Hf alloys at either 400°C or 500°C. Mo depletion is likewise less than 1 at% for all conditions in the +Hf alloys. Si enrichment ranges from 0.04 to 1.13 at% for the +Hf alloys and from 0.48 to 3.43 at% for the +Zr alloys. The higher amount of Si enrichment in the +Zr alloys relative to the +Hf alloys is due to a bulk Si level that is three times more than the +Hf alloys. Since the minor elements have a small amount of segregation, the effects of oversized solutes on segregation of the minor elements will also be small.

As for changes in oversized solute concentration, it has been stated already that Hf concentrations are not measured explicitly because no Hf is detected at the grain boundary. As for Zr, the element is measured in all spectra, and changes in grain boundary concentration ranges from -0.01 to 0.78 at% for both 400°C and 500°C measurements of the +Zr alloys. No notable trends in grain boundary Zr concentration are detected, and any enrichment that does occur does not represent a significant enrichment of Zr at the grain boundary.

5.1.2 RIS in the +Zr Alloys at 400°C

Table 5.1 gives all 400°C RIS measurement values for the +Zr alloys. The results are normalized to Fe + Cr + Ni + Mn + Si +Zr = 1. The table lists the measurements by alloy and presents both the grain boundary concentrations and the matrix concentrations. In addition, the number of individual grain boundaries measured and the total number of segregation profiles for each alloy condition are listed in the tables.

Table 5.2(a) reports the amount of segregation at the grain boundary for the +Zr alloys at 400°C. The amount of segregation at the grain boundary is defined as the difference between the grain boundary concentration and the matrix concentration. Table 5.2(b) shows the error of the measurement for the segregation results. Measurement error is calculated using propagation of error defined in section 4.8. The errors for both matrix and grain boundary concentration measurements are the standard deviation (σ) of the measurement. These errors are propagated to give the segregation error in the tables.

In chapter 6 an RIS model is used to calculate segregation for a ternary Fe-Cr-Ni alloy. In order to make comparisons between model and experiment later, the Fe, Cr and

Ni concentrations must be renormalized to Fe + Cr + Ni = 1. These results are given in table 5.3, which gives the matrix and grain boundary concentrations for Fe, Cr and Ni and the amount of grain boundary segregation.

A representative concentration profile for the Ref-Zr alloy irradiated at 400°C to 3 dpa is given in figure 5.1 to illustrate the changes in concentration for Fe, Cr, and Ni as a function of distance from either side of the grain boundary. Fe concentration is given on the left y-axis shown in red while Cr and Ni are shown on the right y-axis in green and orange, respectively. The distance of 0 nm represents the grain boundary plane. From this figure, depletion of both Fe and Cr is clearly observed, and these are offset by a large enrichment in Ni.

The remaining figures for concentration profiles in this chapter focus on the changes in Cr concentrations. Figure 5.2(a), (b) and (c) shows concentration profiles as a function of distance from the grain boundary for the +Zr alloys at 3, 7 and 10 dpa, respectively. Ref-Zr is shown in grey and LoZr and HiZr are shown in shades of red. For each irradiation condition, Cr and Fe always deplete and Ni always enriches. The raw data for all RIS intensity profile measurements in this study are provided in Appendix D.

The changes in grain boundary Ni and Cr concentrations for the +Zr alloys after irradiation at 400°C to 3, 7 and 10 dpa are shown in figure 5.3. Ref-Zr is shown in grey with LoZr and HiZr in shades of red. Throughout this work, all bar plots of measured segregation are shown using solid bars. In addition, the shading pattern for the reference and the oversized solute alloys will be consistent for RIS data throughout this chapter. The error bars for each measurement represent one standard deviation.

At the lowest dose of 3 dpa, there is a large difference in the amount of Cr depletion between Ref-Zr and both LoZr and HiZr. Ref-Zr shows a Cr depletion of 6.81 at% compared to just 1.70 at% for LoZr and 2.43 at% for HiZr. The difference between reference and LoZr and HiZr alloys is more than 5 at%. Meanwhile, LoZr and HiZr differ by less than the range of the experimental error of their measurements.

By 7 dpa, there is no measurable difference in grain boundary Cr concentration between Ref-Zr and LoZr and only a small difference from HiZr. LoZr has a similar amount of Cr depletion, at 6.13 at%, as Ref-Zr, with 6.81 at%.   HiZr is still about 2 at%

less than this, at 4.68 at% Cr depletion. Although RIS in Ref-Zr is not measured at 10 dpa, it did not change substantially between 3 and 7 dpa for this alloy, so the results at 10 dpa are expected to be similar to 7 dpa results. Likewise, RIS in LoZr and HiZr did not change beyond their measurement errors from 7 to 10 dpa, with LoZr measuring 5.74 at% Cr depletion and HiZr again about 2 at% less at 3.47 at%.

Also shown in figure 5.3, the Ni enrichment for Ref-Zr is 21.12 at% at 3 dpa and only 2.68 at% for LoZr and 3.96 at% for HiZr. At 7 dpa, Ni enrichment increases substantially for LoZr and HiZr, consistent with the Cr depletion results. But while Cr depletion between Ref-Zr and LoZr shows little difference at 7 and 10 dpa, the results for Ni concentrations show that a difference in segregation among the alloys still exists. At 7 dpa Ref-Zr measures 18.02 at% Ni enrichment compared to just 12.84 at% for LoZr and 9.11 at% for HiZr. At 10 dpa, RIS measurements of grain boundary Ni are not available for Ref-Zr. Ni enrichment for LoZr measures 9.25 at% and HiZr has just 6.56 at% Ni enrichment. These results suggest that Ni enrichment would still be lower for LoZr and HiZr compared to Ref-Zr at 10 dpa. They confirm a difference in RIS that occurs with Zr addition, even up to higher doses, and that HiZr consistently measures less segregation than LoZr.

5.1.3 RIS in the +Hf Alloys at 400°C

Table 5.4 gives all 400°C RIS measurement values for the +Hf alloys. The results are normalized to Fe + Cr + Ni + Mo + Mn + Si = 1. The table lists the measurements by alloy and presents both the grain boundary concentrations and the matrix concentrations. In addition, the number of individual grain boundaries measured and the total number of segregation profile measurements for each alloy condition are listed in the tables.

Table 5.5(a) reports the amount of segregation at the grain boundary for the +Hf alloys at 400°C. Error measurements for the segregation results are shown in table 5.5(b).

To make comparisons with model calculations, Fe, Cr and Ni concentrations are again renormalized to Fe + Cr + Ni = 1. These results are given in table 5.6 for the +Hf alloys and gives the matrix and grain boundary concentrations for Fe, Cr and Ni and the amount of grain boundary segregation.

Figure 5.4(a), (b) and (c) shows Cr concentration profiles as a function of distance from the grain boundary for the +Hf alloys at 3, 7 and 10 dpa, respectively. Ref-Hf is shown in dark grey and LoHf and HiHf are shown in shades of blue. For each irradiation condition, Cr and Fe always deplete and Ni always enriches, and again, RIS intensity profile measurements are provided in Appendix D.

Ni and Cr segregation results for the +Hf alloys are shown in figure 5.5, which plots the changes in grain boundary Ni and Cr concentrations for doses of 3, 7 and 10 dpa. At 3 dpa, Cr depletion for Ref-Hf measures 7.60 at% compared to 6.43 at% for LoHf and 4.93 at% for HiHf. The difference between Ref-Hf and LoHf is less than the range of their measurement errors. Even for HiHf, Cr depletion is only about 3 at% lower than Ref-Hf.

The behavior of Ni enrichment in the +Hf alloys conveys similar information as the Cr depletion data, except that they point to larger difference in RIS at 3 dpa. With Ref-Hf measuring 11.04 at% Ni enrichment, the LoHf alloy is 3 at% less at 8.21 at%. HiHf is just 5.66 at% Ni enrichment, for a difference of nearly 6 at% from the reference alloy.

At 3 dpa, segregation decreases with increasing Hf concentration, where Ref-Hf has the most segregation and HiHf has the least segregation. At 7 dpa, however, segregation behavior is not the same. HiHf has the most segregation, with 8.60 at% Cr depletion and 13.29 at% Ni enrichment, and LoHf has the least segregation, with 5.56 at% Cr depletion and 8.65 at% Ni enrichment. Segregation for Ref-Hf is somewhere in between, with 7.45 at% Cr depletion and 13.23 a% Ni enrichment.

By 10 dpa, the trend in segregation behavior is more similar to the behavior at 3 dpa. Cr depletion is again lowest for the HiHf alloy, with 6.88 at% Cr depletion for Ref-Hf, 7.62 at% for LoHf, and 6.40 at% for HiHf. Ni enrichment is also lowest for HiHf and similar for Ref-Hf and LoHf, with 11.75 at% Ni enrichment for Ref-Hf, 12.37 at% for LoHf and 8.85 at% for HiHf. The segregation behavior at 10 dpa shows that 7 dpa segregation results are contradictory to the results at the other two doses. The segregation behavior at 7 dpa will be addressed more fully in chapter 7.

5.1.4 RIS in the +Zr Alloys at 500°C

For irradiations at 500°C, all alloys were irradiated to doses of 1 and 3 dpa. All 1 dpa irradiations were done with 2 MeV protons and all 3 dpa irradiations were done with 3.2 MeV protons. Table 5.7 gives all 500°C RIS measurement values for the +Zr alloys. The measurements cover doses of 1 and 3 dpa. The results are again normalized to Fe + Cr +Ni + Mn + Si + Zr = 1. The table lists grain boundary concentrations and the matrix concentrations, in addition to the number of individual grain boundaries measured and the total number of segregation profile measurements for each alloy condition. Table 5.8(a) reports the amount of segregation at the grain boundary for the +Zr alloys, and error measurements for the segregation results are shown in table 5.8(b).

Fe, Cr and Ni concentrations are again renormalized to Fe + Cr + Ni = 1 for the +Zr alloys at 500°C. These results are given in table 5.9 for the matrix and grain boundary concentrations for Fe, Cr and Ni and the amount of grain boundary segregation.

Figure 5.6(a), (b) and (c) shows Cr concentration profiles as a function of distance from the grain boundary for the +Zr alloys at 1 and 3 dpa, respectively. Ref-Zr is again shown in grey with LoZr and HiZr shown in shades of red.

Changes in grain boundary Cr and Ni concentrations for the +Zr alloys are plotted in figure 5.7. A substantial difference exists between Ref-Zr and both LoZr and HiZr, at 1 dpa, where Cr depletion is 8.82 at% for Ref-Zr, 4.72 at% for LoZr and 3.56 at% for HiZr. The Ref-Zr alloy reflects twice the Cr depletion for LoZr and more than twice the amount for HiZr, showing that Zr addition again causes less Cr depletion.

The results at 3 dpa show that only HiZr has a measurable difference from Ref-Zr, with 8.15 at% Cr depletion for Ref-Zr and 5.48 at% for HiZr. Meanwhile, LoZr measured slightly more Cr depletion than the reference alloy at 9.69 at%.

Similar trends for the +Zr alloys can be found when examining Ni enrichment, also shown in figure 5.7. Ref-Zr has a Ni enrichment of 17.29 at% at 1 dpa compared to the 14.51 at% for LoZr and 10.61 at% for HiZr. By 3 dpa, Ni enrichment at the grain boundary has increased for all alloys, with 20.80 at% for Ref-Zr, 22.17 at% for LoZr, and less than half the amount for HiZr at just 9.60 at%.

5.1.5 RIS in the +Hf Alloys at 500°C

Table 5.10 gives all 500°C RIS measurement values for the +Hf alloys. The measurements cover doses of 1 and 3 dpa. The results are again normalized to Fe + Cr +Ni + Mo + Mn + Si = 1. The table presents both the grain boundary concentrations and the matrix concentrations, along with the number of individual grain boundaries measured and the total number of segregation profile measurements for each alloy condition. Table 5.11(a) gives the amount of grain boundary segregation for the +Hf alloys at 500°C, while error measurements for the segregation results are shown in table 5.11(b).

Fe, Cr and Ni concentrations are again renormalized to Fe + Cr + Ni = 1 to compare with model calculations. The results are given in table 5.12 for the +Hf alloys which lists the matrix and grain boundary concentrations for Fe, Cr and Ni along with the amount of grain boundary segregation.

Figures 5.8(a) and (b) show Cr concentration profiles as a function of distance from the grain boundary for the +Hf alloys at 1 and 3 dpa, respectively. Ref-Hf is again shown in dark grey and LoHf and HiHf are shown in shades of blue.

Segregation results for Cr depletion and Ni enrichment for the +Hf alloys are shown in figure 5.9. No data is available for Ref-Hf at 1 dpa. Based on the results for Ref-Zr, for which Cr depletion is slightly higher at 1 dpa than at 3 dpa, it is expected that RIS will not change much between 1 and 3 dpa for 500°C. For the purposes of this study, Ref-Hf RIS results at 3 dpa are replicated for 1 dpa in figure 5.9, represented by striped bars, as this at least provides a point of comparison with LoHf and HiHf at 1 dpa.

For the 1 dpa data, only 5.96 at% Cr depletion is measured for LoHf, and even less for HiHf at 4.72 at%, compared to the 10.49 at% Cr depletion for Ref-Zr. These results would indicate some difference between the +Hf alloys and the reference alloy at 1 dpa. By 3 dpa, the Cr depletion results are virtually identical for all three of the +Hf alloys. Ref-Hf, as mentioned, measured 10.49 at% Cr depletion, with 10.09 at% and 10.46 at% for LoHf and HiHf, respectively. The 500°C, 3 dpa Cr depletion values show no difference in RIS at 3 dpa.

Ni enrichment results for the +Hf alloys offer the same perspective on the data. The difference between Ref-Hf and both LoHf and HiHf is substantial. Ni enrichment

158

for Ref-Hf is 19.37 at% compared to just 11.41 at% for LoHf and 9.10 at% for HiHf. But by 3 dpa, there is remarkable similarity in results between the alloys, with Ni enrichment values of 19.37 at%, 20.23 at% and 23.02 at% for Ref-Hf, LoHf and HiHf, respectively.

5.2 Results from Dislocation Loop Imaging

The dislocation loop microstructure of the irradiated alloys is examined at doses of 3 and 7 dpa at 400°C. The temperature and doses are chosen in order to provide a picture of how the loop microstructure changes in the same regime in which RIS changes in order to more broadly assess the effects of oversized solutes on point defect trapping.

Loop imaging is performed on the JEOL 2010F at the University of Michigan's Electron Microscopy and Analysis Laboratory using the reciprocal lattice rod (rel-rod) dark-field imaging technique. This section presents the results from this examination, starting with the +Zr alloys at 3, then 7 dpa, providing loop size distributions, average loop diameters and densities, and total loop line lengths. The same results are then presented for the +Hf alloys.

5.2.1 Dislocation Loops for the +Zr Alloys

Dark-field loop images are shown in figure 5.10 which are representative of the +Zr alloys irradiated at 400°C to 3 dpa. Figure 5.10(a) is for Ref-Zr, (b) for LoZr and (c) for HiZr. From the figures, Ref-Zr shows more loops than either LoZr or HiZr. The loop image for Ref-Zr also shows some larger loops which are actually just a collection of loops located close to one another in the image.

Dark-field loop images for the +Zr alloys at 7 dpa are provided in figure 5.11, with Ref-Zr in figure 5.11(a), LoZr in (b) and HiZr in (c). The Ref-Zr image does not show overlapping loops quite to the extent that they did at 3 dpa; nevertheless, the total number of loops in the image visually appears similar as compared to 3 dpa. These results are in contrast to that of the LoZr and HiZr alloys, for which the number of loops has visibly increased.

Loop size distributions reveal information about the loop microstructure. Size distributions are presented for the +Zr alloys in figure 5.12(a) – (f) which covers both the

3 dpa and 7 dpa samples to offer a direct comparison for loop morphology as a function of dose. For the 3 dpa samples, figure 5.12(a) shows Ref-Zr, (b) for LoZr and (c) for HiZr. For the 7 dpa samples, figure 5.12(d) gives Ref-Zr, (e) for LoZr and (f) for HiZr. Generally, the size distributions show a broadening of the loop distribution with increasing dose. This is especially true for LoZr and HiZr. For HiZr, there is a much larger fraction of loops below 7 nm, with a peak from 6 – 7 nm at 3 dpa. By 7 dpa, the distribution is broader, with a peak now from 10 – 11 nm.

Table 5.13 lists the values for all of the dislocation loop measurements for Ref-Zr, LoZr and HiZr at 3 and 7 dpa, presenting the average loop diameter, average loop density with standard deviation, and loop line length for each alloy.

The average loop diameter is plotted in figure 5.13 for the +Zr alloys from 3 – 7 dpa. Ref-Zr is shown in grey and LoZr and HiZr are shown in shades of red. The figure shows similar loop sizes for all of the +Zr alloys, with diameters of 10.0 nm for Ref-Zr, 8.0 nm for LoZr, and 9.0 nm for HiZr at 3 dpa. Loop sizes also do not change significantly from 3 to 7 dpa for the alloys, with diameters of 8.7 nm for Ref-Zr, 8.0 nm for LoZr, and 9.9 nm for HiZr.

Figure 5.14 shows the average loop density for the +Zr alloys. At 3 dpa there is a significant difference in average loop density among the alloys, with Ref-Zr at 5.06 x 10^{22} m^{-3} compared to 1.08 x 10^{22} m^{-3} for LoZr and 8.73 x 10^{21} m^{-3} for HiZr. By 7 dpa Ref-Zr has little change in loop density at 5.48 x 10^{22} m^{-3}. LoZr and HiZr show more significant changes in loop density, however, with increases of 50 – 60% over the 3 dpa densities. The loop densities are now 1.72 x 10^{22} m^{-3} for LoZr and 1.32 x 10^{22} m^{-3} for HiZr.

The total loop line length is an arbitrary measure of the total interstitial dislocation loop damage in the microstructure. The loop line length is a combination of the average loop circumference times the dislocation density, with units of m^{-2}.

The total loop line lengths are shown in figure 5.15 for the +Zr alloys from 3 – 7 dpa and give a measure of the total loop morphology as a function of dose. Notice that loop line length is fairly constant from 3 to 7 dpa for Ref-Zr, from 15.9 x 10^{14} m^{-2} to 14.9 x 10^{14} m^{-2}. The small decrease in loop line length from 3 to 7 dpa for Ref-Zr reflects a saturation of the loop microstructure. At the same time, the loop line length shows a

large increase of 60% or more for LoZr and HiZr from 3 to 7 dpa, demonstrating significant changes in the loop microstructure, particularly the loop density, between 3 and 7 dpa. LoZr increases from 2.72 x 10^{14} m^{-2} to 4.35 x 10^{14} m^{-2} while HiZr is less than LoZr but increases similarly, from 2.47 x 10^{14} m^{-2} to 4.10 x 10^{14} m^{-2}.

5.2.2 Dislocation Loops for the +Hf Alloys

Images of dislocation loops for the +Hf alloys at 3 dpa, 400°C are given in figure 5.16(a) for Ref-Hf, (b) for LoHf and (c) for HiHf. Both LoHf and HiHf clearly show fewer loops than the Ref-Hf alloy, although LoHf shows more loops than HiHf. Very few loops for HiHf at 3 dpa were imaged because the density of loops is so low.

The final dislocation loop images are shown in figure 5.17(a) for Ref-Hf, (b) for LoHf, and (c) for HiHf at 400°C, 7 dpa. These images are interesting because the loop microstructure for LoHf at this dose appears nearly identical to Ref-Hf. Meanwhile, HiHf still has visibly fewer loops as compared to either Ref-Hf or LoHf, but from 3 to 7 dpa, the number of loops shows a large increase.

Loop size distributions for the +Hf alloys are again used to give more information on the loop microstructure. Size distributions are presented for the +Hf alloys in figure 5.18(a) – (f) which covers both the 3 dpa and 7 dpa samples to offer a direct comparison for loop morphology as a function of dose. For the 3 dpa samples, figure 5.18(a) shows Ref-Hf, (b) for LoHf and (c) for HiHf. For the 7 dpa samples, figure 5.18(d) gives Ref-Hf, (e) for LoHf and (f) for HiHf. Generally, the size distributions show a broadening of the loop distribution with increasing dose. This is perhaps less true for Ref-Hf, where there appears to be only small changes from 3 to 7 dpa in the size distribution. But LoHf and HiHf both demonstrate a shift of the peak size upward, with a broadening of the size distribution overall.

Loop microstructure data for the +Hf alloys is listed in table 5.14, including the total number of loops imaged, the average diameters, average loop densities with standard deviations, and total loop line lengths for each alloy at 3 and 7 dpa.

Figure 5.19 plots the average loop diameters for the +Hf alloys from 3 – 7 dpa, with Ref-Hf shown in grey and LoHf and HiHf shown in shades of blue. Diameters among the +Hf alloys are similar at both 3 and 7 dpa. At 3 dpa, Ref-Hf has a loop

diameter of 9.4 nm, with LoHf at just 7.2 nm and HiHf at 7.2 nm. The loop diameter remains fairly constant for Ref-Hf at 7 dpa but increases slightly for LoHf and HiHf. Loop diameters are now 9.9 nm for Ref-Hf, 8.9 nm for LoHf and 10.4 nm for HiHf.

Average loop densities for the +Hf alloys are shown in figure 5.20. A large difference in loop density exists among the +Hf alloys at 3 dpa, with 40% lower loop density for LoHf and 70% lower for HiHf compared to Ref-Hf. At 3 dpa Ref-Hf has a loop density of 2.29×10^{22} m^{-3} compared to 1.38×10^{22} m^{-3} for LoHf and 6.32×10^{21} m^{-3} for HiHf. The loop density for Ref-Hf remains constant up to 7 dpa with a value of 2.32×10^{22} m^{-3}. Both LoHf and HiHf measure large changes between 3 – 7 dpa. LoHf at 7 dpa has a similar loop density as Ref-Hf at 2.38×10^{22} m^{-3}. Loop density for HiHf increases by nearly 50% from 3 to 7 dpa, for a loop density of 9.32×10^{21} m^{-3}.

The loop microstructure results are also reflected in the total loop line lengths for the +Hf alloys as a function of dose in figure 5.21. Substantial differences exist between the alloys, with lower loop line lengths for LoHf and HiHf compared to Ref-Hf at 3 dpa. Ref-Hf has a loop line length of 6.74×10^{14} m^{-2} while LoHf is at 3.11×10^{14} m^{-2}. HiHf is only 20% of the value for Ref-Hf, at 1.43×10^{14} m^{-2}.

By 7 dpa, the loop line lengths for Ref-Hf and LoHf are similar, at 7.03×10^{14} and 6.64×10^{14} m^{-2}, respectively. The values reflect a similar loop microstructure for Ref-Hf and LoHf by 7 dpa. And HiHf has increased substantially to 3.05×10^{14} m^{-2}, though the line length is still less than Ref-Hf or LoHf. The higher loop line length values for LoHf and HiHf reflect a changing loop microstructure from 3 to 7 dpa.

5.3 Determination of the Amount of Oversized Solute in Solution

This section is separated in three distinct parts, all of which seek to answer the questions 1) how much of the oversized solute is in solution? and 2) does the amount change with irradiation? This is important because the purpose of Hf or Zr additions is to reduce the effects of radiation damage through point defect trapping and enhanced recombination. The mechanism, however, relies not on the amount of oversized solute in the alloy but rather on the amount of solute remaining in solution. Solute that has been incorporated into incoherent precipitates or other solute-rich phases or has migrated

toward other sinks will no longer exert the lattice strain that attracts vacancy defects and allows them to be trapped by the solute atoms. Only the solute atoms in solution will play a role in enhancing recombination and reducing RIS.

A precipitate microstructure is revealed through imaging, both in SEM and TEM, of the oversized solute alloys. Analysis of the precipitates with EDS revealed them to be rich in oversized solute. Since the oversized solute formed precipitates in the alloys even before irradiation, understanding the effectiveness of the oversized solute requires, in part, knowledge of the amount of solute in solution. This is achieved through four separate analyses, which are separated by technique.

The first part is for a study using x-ray diffraction (XRD). XRD was performed at the Knolls Atomic Power Laboratory on each of the oversized solute alloys in the unirradiated condition. The results here present the diffraction patterns and describe the types of phases that are detected, as well as an estimate of the relative amounts of the precipitate phases.

The second part focuses on imaging of the carbide precipitates in the oversized solute alloys using SEM. The purpose is to confirm the presence of the precipitates as detected by XRD and to determine the distribution of the precipitates in the alloys.

The third part is an estimate of the mean precipitate size and density in HiHf based on TEM imaging from a series of low magnification images to measure and count the precipitates. Based on the size and density of carbides, the amount of Hf remaining in solution can be determined. The values for size and density and the concentration of Hf remaining in solution in the unirradiated condition are used in chapter 7 as an important parameter in a diffusion analysis to explain the precipitate growth during irradiation.

The final part describes the work performed using the local electrode atom probe (LEAP) at the Oak Ridge National Laboratory. By preparing samples using focused ion beam (FIB) from the irradiated portions of proton-irradiated TEM discs, three-dimensional atom mapping could be performed for each of the alloys. Although the atom probe results are only semi-quantitative, positive identification of Zr or Hf in the atom maps for some of the alloy conditions confirmed the presence of oversized solute still remaining in solution.

5.3.1 X-ray Diffraction

To help determine the type of precipitate phase present in the oversized solute alloys, a study of the alloys was performed using X-ray diffraction (XRD) at Lockheed Martin's Knolls Atomic Power Laboratory using a Bruker D8 Discover GADDS and a Rigaku Dmax B. Multiple scans were made of each of the six alloys, including all oversized solute alloys and the reference alloys, to ensure the accuracy of results. A search was made for peaks to identify both the matrix phase (austenite) and the presence of the precipitate phases.

In particular, the presence of ZrC or $ZrNi_5$ in the +Zr alloys and HfC or $HfNi_5$ in the +Hf alloys is sought. These particular phases were identified based on previous work by Ohnuki et al. [86] who identified the presence of solute-rich carbides present in both +Zr and +Hf alloys. Meanwhile, more recent work by Allen et al. [83] qualitatively characterized precipitate phases in both +Zr and +Hf alloys as being $ZrNi_5$ or $HfNi_5$. Knowledge of the types of precipitate phases to expect in the alloys made identification in the diffraction pattern significantly easier.

For the LoZr and HiZr alloys, ZrC is detected. Similarly, HfC is identified in the HiHf alloy only. No secondary phases with peaks above the background could be seen in the diffraction pattern for LoHf, even though precipitates have been observed in the microstructure. Table 5.15 gives the 2θ diffraction angles, relative intensities for the four highest-diffracting angles, and (hkl) planes of each diffraction angle for ZrC and HfC [98, 99]. The table includes the powder diffraction number (PDF#) from the International Centre for Diffraction Data (IDCC) [100].

Figures 5.22 – 5.27 present the diffraction patterns for each of the six alloys in this study. Each of these figures shows x-ray intensity as a function of diffraction angle and is for scans covering 2θ angles from 20 – 70°. Starting with Ref-Zr in figure 5.22, only two peaks are visible which correspond to the FCC austenite. No other peaks are identified. Figures 5.23 and 5.24 are for LoZr and HiZr, respectively. These figures also have the two austenite peaks in addition to four additional peaks from ZrC, with 2θ angles corresponding to those shown in table 5.15. Although the peaks are small due to the low mass fraction of precipitate, the peaks with highest intensity for both alloys are at ~ 33° and ~ 38.3°, which represents the two most strongly diffracting angles for ZrC.

These diffraction angles have the highest relative intensity. The other diffracting angles have lower intensity, and though they are still observed in the diffraction pattern, they are more difficult to identify above the background signal.

Ref-Hf in figure 5.25 again has only two peaks visible for the austenite. No secondary peaks are identified for this reference alloy either. Figure 5.26 is for LoHf, which shows only the austenite in the diffraction pattern, without any secondary phases detected. Figure 5.27 for HiHf shows the two austenite peaks in addition to four additional peaks from HfC, with 2θ angles corresponding to those shown in table 5.15. The intensity for the peaks is again low due to the low mass fraction of precipitate, but the relative intensities of each HfC peak corresponds to the relative intensity shown in table 5.15. As a result, the HfC peaks become less pronounced with increasing 2θ angle as the relative peak intensity decreases.

The diffraction patterns are used to calculate the mass fraction of precipitate phase for LoZr, HiZr and HiHf. The results in table 5.16 include an estimate of the wt% of each phase detected in the alloy. The lattice parameter calculations of the matrix and the estimated concentrations of the HfC and ZrC phases were performed using the Jade Whole Pattern Fitting software package [96]. These values should be taken only as estimates of the amount of precipitate. The very low concentrations of the precipitate in the alloys prevent a truly quantitative determination of their mass fraction.

5.3.2 SEM Imaging of Carbides

Imaging of the oversized solute alloys is performed using SEM-BSE to confirm the presence of carbides in the matrix of each of the alloys. The purpose was to image the carbide phases in the alloys, even in LoHf where XRD did not detect HfC, and to identify whether they are distributed throughout the material or are located only along grain boundaries. Representative images are shown in figure 5.28 for the (a) LoZr, (b) HiZr, (c) LoHf, and (d) HiHf alloys, respectively. These images highlight the high-contrast precipitates present in the alloy due to solute-rich carbides and show that the carbides are distributed throughout the matrix of the alloys.

5.3.3 TEM Imaging Analysis

A TEM imaging study is used to image the HfC and ZrC precipitates in the HiHf and HiZr alloys, respectively. The objective is to determine the precipitate density and calculate the atom fraction of Hf or Zr in carbides for the unirradiated condition. A series of five TEM images for each alloy were used to determine the mean precipitate size and density, and representative images of the precipitate microstructures are shown in figure 5.29 for the HiHf alloy and figure 5.30 for the HiZr alloy. The mean precipitate density for HiHf is 7 x 10^{19} m^{-3}. The mean size is 62 nm ± 36 nm, and the precipitate size distribution is shown in figure 5.31. For the HiZr alloy, the mean precipitate density is 2.5 x 10^{19} m^{-3} with a mean size of 81 nm ± 32 nm. The precipitate size distribution for for the HiZr alloy is shown in figure 5.32.

Fournier et al. [25] measured a precipitate density of 8.6 x 10^{20} m^{-3} with an average size of 25 nm for the same alloy heat as HiHf after a 900°C anneal for 20 minutes prior to irradiation. A separate sample was annealed at 1100°C for 30 minutes and the precipitate density was measured at 1 x 10^{19} m^{-3} with an average size of 150 nm. The anneal for HiHf in this study was at 1000°C for 1 hour which is in between the annealing temperatures used by Fournier et al. [25], and the precipitate density and size for HiHf is also in between the precipitate densities and sizes measured by Fournier et al.

To calculate the amount of solute in the carbide precipitates, each precipitate is assumed to be spherical. The atom percent of solute, $at\%_{solute}$, can be calculated by the following:

$$at\%_{solute} = \frac{1}{2}\rho_{ppt.}\cdot\frac{4}{3}\pi\left(\frac{d_{ppt.}}{2}\right)^3\cdot\left(\frac{a_{austenite}}{a_{ppt.}}\right)^3\cdot100, \tag{5.1}$$

where $\rho_{ppt.}$ is the precipitate density, $d_{ppt.}$ is the average precipitate size, and $a_{austenite}$ and $a_{ppt.}$ are the lattice parameters of the austenite and precipitate phases, respectively. Eq. 5.1 accounts for the increased atomic volume for the precipitate phases due to the larger lattice parameters for HfC and ZrC. Lattice parameters for HfC, ZrC and austenite are provided in table 5.17 [98, 99]. Note that Eq. 5.1 assumes that is the carbides are stoichiometric and ½ of the atoms are Hf or Zr. The amount of solute in the precipitates before irradiation is calculated to be 0.21 at% Hf for HiHf and 0.17 at% Zr for HiZr. The

amount remaining in solution is the difference from the bulk solute content and the amount remaining in solution in the unirradiated condition. For HiHf, with a bulk Hf content of 0.37 at% and 0.21 at% in precipitates, then 0.16 at% Hf remains in solution. For HiZr, with a bulk Zr content of 0.28 at% and 0.17 at% in precipitates, then 0.11 at% Zr remains in solution. Results for the mean precipitate size and density along with the amount of Hf in precipitates and in solution are provided in table 5.18.

These results require that a sufficient amount of C, above the C solubility limit, be present to form these carbides. Based on work by Ohnuki et al. [86] even a C level of 0.002 wt% still resulted in the formation of HfC and ZrC precipitates during irradiation, so it is assumed that all of the C can come out of solution to form carbides. For LoHf and LoZr alloys, there is more C than oversized solute, with 0.17 at% C and 0.05 at% Hf in the LoHf alloy, and 0.23 at% C and 0.19 at% Zr in the LoZr alloy. For the HiZr alloy, there is more Zr, at 0.28 at%, than C, at 0.23 at%, although there is enough C to account for the measured precipitates. Meanwhile, the HiHf alloy has just 0.14 at% C, which is less than the 0.21 at% C measured in HfC precipitates. The higher level of C in precipitates indicates that either the alloy has more bulk C than was measured by chemical analysis, or some of the precipitates are intermetallics rather than carbides. The presence of Hf intermetallics in stainless steel has been reported elsewhere [83]. In conclusion, the amount of C in the alloys is sufficient to form carbides with most or all of the oversized solute in the alloys, with the possible formation of intermetallics taking the remaining oversized solute from solution.

5.3.4 LEAP Analysis

The final technique aimed at quantifying the amount of oversized solute in solution is through the use of field ion microscopy (FIM) using a local-electrode atom probe (LEAP). All four oversized solute alloys are analyzed with LEAP. Sample tips for analysis were prepared using either electropolishing or focused ion beam (FIB) microscopy. Unirradiated samples of each of the four alloys were prepared using electropolishing because of the ease of preparation of sample tips. Due to the limited irradiated region of the irradiated alloys, irradiated sample tips had to be prepared using a sample lift-out method from TEM foils. Only three of the oversized solute alloys are

analyzed in the irradiated condition, namely LoZr, HiZr and HiHf. Of these, data are obtained for both LoZr and HiZr at 3 and 7 dpa. Meanwhile, analysis is completed for HiHf at 3 dpa only. No irradiated data are collected on the alloy LoHf because the very low concentration of Hf, at 0.05 at%, made detection of Hf in the FIB-prepared specimens unlikely. Furthermore, only data sets in excess of 1 million atoms for a sample are considered relevant for data analysis.

The primary goal of the LEAP analysis is to qualitatively verify the presence of oversized solute in the unirradiated alloys. This goal is met in the LoZr, HiZr and HiHf alloys; for the LoHf alloy, no above-background peaks from Hf isotopes are evident. Given that the amount of Hf in LoHf is only 0.05 at%, and furthermore that HfC precipitates further reduce this concentration of solute in the matrix, the lack of signal peaks from Hf is not unexpected.

A secondary goal of the LEAP analysis is to quantify the amount of solute in in solution. In principle, this should have been achievable. Unfortunately there are several complicating factors, which will be discussed later, that prevent a reliable quantification, so quantitative results on the amount of oversized solute in the matrix are not presented.

The peaks in the mass/charge ratio spectrum must align with each of the isotopes of a particular element in order for a positive identification of that element to be made. The individual isotope peak intensities are assumed to be proportional to the isotopic abundances for each element. The assumption requires that there is no bias for the extraction or detection of a particular element from the sample tip, and this depends principally on the specimen temperature and the voltage pulse fraction used to extract atoms from the specimen tip. The LEAP was optimized for stainless steels to ensure that all atoms are extracted and detected without bias. In addition, ionization energies for Fe, Cr and Ni are similar to the oversized solute atoms Zr and Hf, so there is no significant bias in the extraction of the oversized solutes. However, given low concentrations of an element, only the more abundant isotopes may appear while the less-abundant isotopes may not be detectable above the background signals. If the elemental concentration is low enough, it may not be detected above the background signal at all. The mass/charge ratios for Ni, Mo, Zr and Hf isotopes are shown in tables 5.19 – 5.22, respectively, based on either a +2 or +3 charge for the isotopes.

The mass/charge ratios for Ni^{2+} overlap with the ratios for Zr^{3+}. Given the relative concentrations between Ni and Zr, it was not possible to identify Zr among the Ni peaks. Identification of Zr, then, relied upon intensity peaks from the Zr^{2+} ions. Unfortunately, detector efficiency decreases with increasing mass/charge ratio, so the higher mass/charge ratios for Zr^{2+} relative to Zr^{3+} increases the minimum amount of Zr in solution necessary for identification of intensity peaks above background. Moreover, Mo^{2+} ratios also overlap with some of the Zr^{2+} ratios, although it does not overlap with the most abundant Zr isotope, Zr^{90}. Since Hf^{2+} and Hf^{3+} ions also have a higher mass/charge ratio than Zr^{2+} ions, detection of small amounts of Hf is also difficult.

The first of many figures to be presented is the mass/charge spectra for the oversized solute alloys. These spectra reveal qualitatively whether or not the oversized solute is present in the matrix material. None of the specimens analyzed using LEAP contains carbide precipitates, which are quite common in the matrix of the oversized solute alloys. Evidence of HfC or ZrC precipitates simply required atom maps to visualize both the C and the Hf or Zr and assess the presence of precipitate clusters of these elements. No carbide, or even oxide, precipitates are evident in any of the samples, which indicate that particle densities are low enough that they are not in the sample volumes analyzed. Therefore, any Hf or Zr detected in the spectrum must be in solution.

Figures 5.33 and 5.34 present the mass/charge spectra for both LoZr and HiZr, respectively, in the unirradiated condition and at doses of 3 and 7 dpa. Some of the spectra show the peaks for Zr^{90} isotopes, but the other Zr peaks, being both less abundant than Zr^{90} and overlapping with Mo isotope intensity peaks, cannot be seen. Nevertheless, the peak at the mass/charge ratio of roughly 45 corresponds to the Zr^{2+} ion of Zr^{90}. Other unidentified peaks can be seen in figure 5.34(b), (c) and (d) at mass/charge ratio of 43.5. Although the peak is rather large, it cannot be attributed to any particular isotope. The origin of such unidentified peaks is discussed later.

Figure 5.35 is similar to figures 5.33 and 5.34 except the spectra are for the +Hf alloys. There are no overlapping peaks of concern with the Hf; however, high mass/charge ratios mean the efficiency for detection is relatively low, making the Hf peaks above background less pronounced. Peaks with a mass/charge ratio of $59-60$ comprise most of the Hf. With mass/charge ratios close in value, the peaks will not be

distinct. A lack of signal for LoHf is not surprising since 0.05 at% would be difficult to detect. Since carbide precipitates are present in the matrix, though not detected in the LEAP samples, less Hf in solution means detection is unlikely.

In figure 5.35(c) there are multiple unidentified peaks with mass/charge ratios ranging from 54 – 59. There are only a few potential elements that could match some of these ratios, including Cd, In and Yb. None of them are perfect matches for these peaks, and In especially only fits one of the three peaks here. Moreover, there is no reason why any of these elements would have been in the sample or the spectrum. Finally, none of these elements match the peaks between 59 – 60, yet the peaks in this range do not match Hf well, either, so identification of Hf is not certain.

Table 5.23 shows the results from all successful sample analyses using LEAP. The table includes the unique sample ID used to identify each sample since, for several cases, there are multiple analyses of the same sample condition. In some cases, there are several usable data sets of the same alloy condition. For each sample analyzed, the question of whether or not oversized solute could be confirmed in the spectra is answered. In one case, for LoZr, 3 unirradiated specimens yielded valuable data sets, and in only two of the three data sets is the presence of Zr verified. The oversized solute is 'verified' if there are above-background peaks clearly visible which match the solute's expected mass/charge ratio, with relative intensities corresponding to the isotopic abundances of the element.

The results of LEAP analysis confirm the presence of Zr in solution in LoZr and HiZr in the unirradiated condition. At 3 and 7 dpa, Zr remaining in solution is only confirmed for the HiZr alloy. The LoZr alloy does not show any Zr peaks above the background signal, so Zr cannot be detected in LoZr after irradiation. For the +Hf alloys, LEAP analysis fails to identify any Hf above the background signal for the LoHf alloy in the unirradiated condition or at 3 dpa. The alloy was not measured at 7 dpa. For the HiHf alloy, Hf is detected in solution in the unirradiated condition. At 3 dpa, the identification of Hf is uncertain, and at 7 dpa, there is no Hf detected in the HiHf alloy.

It is worth mentioning that even in the cases where Zr or Hf could not be verified in the spectra, it does not mean there was no oversized solute in the matrix, but rather that

it is below the detectable limit. There are several factors which can affect what that detectable limit may be.

There are a variety of factors which make the detection of the Zr and Hf a difficult problem. First and foremost, of course, their low concentration, especially of the amount remaining in solution, makes identification a challenge. Their high mass/charge ratio is also a challenge due to lower detector efficiency in this range. This is especially true in the case of Zr, in which only the +2 ions provide unique intensity peaks due to the presence of Ni. It should be noted that the ratio for Hf^{3+} ions is still higher than Zr^{2+} ions and thus has a lower efficiency for detection.

A more intrinsic problem affects the samples prepared using FIB. The instrument is used to shape the sharp tips that are fabricated from the sample lift-out method. During the ion milling process using Ga^+ ions, some of the ions are implanted in the sample and end up in the sample's mass/charge spectrum. The problem can be circumvented by using low currents for ion imaging (to prepare for ion milling cuts), and by using low voltages to prevent the ions from being embedded deeply into the sample. However, ion imaging can be especially difficult or even impossible at low voltages, so a higher voltage is required to adequately visualize the sample and prepare for the final cuts. This means that some degree of Ga^+ ion implantation is inevitable. In preparation for the final annular milling, imaging the sample tip in the FIB must be done with as few scans as possible, ideally with a single scan, to limit the amount of Ga^+ implantation. As seen in figure 5.36 for a 30 kV image, the result is less than perfect unless sample focusing is performed, but this would require additional scans. Lowering the voltage would not only produce a lower quality image but would also require more scanning for sample focusing.

A final problem that should be highlighted has more to do with imperfections in the sample tip fabrication process. Ideally, only a single sharp tip would extend from the sample base. Often times during the milling process with FIB, however, multiple secondary tips can be created around the base of the primary sample tip. This has the effect of distorting the applied electric field and increasing the voltage required for evaporation of the sample tip [101]. It also causes the evaporation of ions from the secondary tips, which will then have a different time-of-flight path to the detector. The spectrometer will then misinterpret the mass of the rogue ions and bin them improperly in

the mass/charge spectrum. The effect, essentially, is to increase the background intensity spectrum and perhaps even create false, minor intensity peaks in the spectrum which will be both unidentifiable and cause the identification of some minor elements in the sample to become more difficult.

Three-dimensional atom maps of the samples help to reveal some additional information about the alloys. Figure 5.36(a), (b) and (c) displays atoms maps for Ni prior to irradiation for HiZr in (a), after 3 dpa for LoZr in (b), and after 7 dpa for HiZr in (c), while figure 5.36(a) – (c) shows the same alloy conditions for Si. Notice that prior to irradiation, the Ni and Si are uniformly distributed, but after irradiation, there is a clear association between Ni and Si, with clustering likely coinciding with dislocation loops in the matrix. Although difficult to visualize with the Ni atom maps, the areas of high Ni density correspond to the same areas of high Si density.

Finally, although low in concentration, the distribution of Zr and Hf atoms are shown in figure 5.39 for some of the samples in which the oversized solute is visible in the mass/charge ratio spectrum. There appears to be no difference in distribution of the atoms from the unirradiated to the irradiated specimens, nor is there any sign of clustering or precipitation in any of the sample volumes that were analyzed.

Despite the limitations for identifying Zr or Hf in these particular alloys, there is still value to be derived from the LEAP analysis. The analysis verified that oversized solute did remain in solution in LoZr, HiZr and HiHf prior to irradiation; Hf could not be detected above the background signal for LoHf. After irradiation to 3 dpa and 7 dpa, oversized solute in solution was confirmed only for the HiZr alloy. No solute was detected in solution for LoZr, LoHf or HiHf after irradiation.

Table 5.1 Grain boundary (GB) measurements of concentration for the +Zr alloys irradiated with protons at 400°C to doses of 3, 7 and 10 dpa
NM: Not Measured

Alloy		Dose (dpa)	# of GB's	# of Meas.	Measured Concentration (at%)					
					Fe	Cr	Ni	Mn	Si	Zr
Ref-Zr	GB	3	2	15	53.40	8.54	34.04	0.58	3.44	-
	Matrix				69.71	15.35	12.92	1.24	0.78	-
	GB	7	2	6	55.31	9.15	30.82	0.53	4.19	-
	Matrix				69.83	15.37	12.80	1.24	0.76	-
	GB	10	-	-	NM					
	Matrix									
LoZr	GB	3	2	15	66.51	13.70	15.52	1.52	2.57	0.18
	Matrix				69.50	15.40	12.84	1.32	0.75	0.19
	GB	7	2	7	62.40	9.25	25.71	0.52	1.86	0.25
	Matrix				69.43	15.38	12.87	1.37	0.76	0.19
	GB	10	3	14	62.94	9.63	22.14	1.18	3.13	0.98
	Matrix				69.35	15.37	12.89	1.33	0.86	0.20
HiZr	GB	3	4	13	67.56	12.42	16.73	0.89	1.58	0.83
	Matrix				69.93	14.85	12.77	1.24	0.83	0.39
	GB	7	4	27	64.51	10.18	21.92	0.73	2.23	0.43
	Matrix				69.97	14.86	12.81	1.21	0.82	0.32
	GB	10	2	18	66.65	11.40	19.38	0.65	1.58	0.35
	Matrix				70.03	14.87	12.82	1.20	0.80	0.28

Table 5.2(a) Grain boundary segregation and measurement error for the +Zr alloys irradiated with protons at 400°C to doses of 3, 7 and 10 dpa
NM: Not Measured

Alloy	Dose (dpa)	Grain Boundary Segregation (at%)					
		Fe	Cr	Ni	Mn	Si	Zr
Ref-Zr	3	-16.31	-6.81	21.12	-0.66	2.66	-
	7	-14.52	-6.22	18.02	-0.71	3.43	-
	10			NM			
LoZr	3	-2.99	-1.70	2.68	0.20	1.82	-0.01
	7	-7.03	-6.13	12.84	-0.84	1.10	0.06
	10	-6.41	-5.74	9.25	-0.14	2.26	0.78
HiZr	3	-2.37	-2.43	3.96	-0.35	0.75	0.44
	7	-5.46	-4.68	9.11	-0.48	1.41	0.11
	10	-3.39	-3.47	6.56	-0.55	0.78	0.07

Table 5.2(b) Error in the segregation measurements calculated using error propagation from the standard deviations (σ) of the grain boundary and matrix measurements for the +Zr alloys at 400°C to doses of 3, 7 and 10 dpa

Alloy	Dose (dpa)	Measurement Error (at%)					
		Fe	Cr	Ni	Mn	Si	Zr
Ref-Zr	3	3.07	0.60	4.70	0.31	0.77	-
	7	0.88	0.63	0.76	0.16	0.13	-
	10			NM			
LoZr	3	0.47	0.29	0.34	0.20	0.17	0.11
	7	0.90	0.77	0.98	0.34	0.18	0.06
	10	3.29	0.67	2.25	0.42	0.71	0.21
HiZr	3	0.72	0.41	0.84	0.19	0.05	0.09
	7	3.13	1.20	3.35	0.19	0.13	0.63
	10	2.34	0.81	2.56	0.28	0.08	0.31

Table 5.3 Grain boundary measurements of concentration for the +Zr alloys irradiated with protons at 400°C to doses of 3, 7 and 10 dpa, normalized to Fe + Cr + Ni = 1.

Alloy		Dose (dpa)	Measured Concentration (at%)			Grain Boundary Segregation (at%)		
			Fe	Cr	Ni	Fe	Cr	Ni
Ref-Zr	GB	3	55.63	8.90	35.47	-15.52	-6.77	22.28
	Matrix		71.15	15.67	13.19			
	GB	7	58.05	9.60	32.35	-13.20	-6.08	19.28
	Matrix		71.25	15.69	13.06			
	GB	10				NM		
	Matrix							
LoZr	GB	3	69.47	14.31	16.21	-1.63	-1.44	3.08
	Matrix		71.11	15.76	13.14			
	GB	7	64.09	9.50	26.41	-6.99	-6.24	13.23
	Matrix		71.08	15.75	13.18			
	GB	10	66.45	10.17	23.38	-4.60	-5.58	10.17
	Matrix		71.05	15.75	13.21			
HiZr	GB	3	69.86	12.84	17.30	-1.83	-2.38	4.21
	Matrix		71.69	15.22	13.09			
	GB	7	66.77	10.54	22.69	-4.89	-4.68	9.57
	Matrix		71.66	15.22	13.12			
	GB	10	68.41	11.70	19.89	-3.26	-3.52	6.77
	Matrix		71.66	15.22	13.12			

Table 5.4 Grain boundary (GB) measurements of concentration for the +Hf alloys irradiated with protons at 400°C to doses of 3, 7 and 10 dpa
NM: Not Measured

Alloy		Dose (dpa)	# of GB's	# of Meas.	Measured Concentration (at%)					
					Fe	Cr	Ni	Mn	Mo	Si
Ref-Hf	GB	3	4	21	61.15	11.51	24.37	0.61	1.19	1.17
	Matrix				64.87	19.11	13.33	1.09	1.33	0.27
	GB	7	4	12	59.76	11.65	26.57	0.50	0.66	0.86
	Matrix				64.86	19.10	13.34	1.06	1.37	0.27
	GB	10	2	12	61.18	12.24	25.06	0.44	0.45	0.63
	Matrix				64.90	19.12	13.31	1.06	1.33	0.27
LoHf	GB	3	2	15	65.00	12.32	21.09	0.43	0.74	0.42
	Matrix				65.75	18.75	12.88	1.05	1.29	0.28
	GB	7	2	8	63.36	13.19	21.56	0.53	0.82	0.54
	Matrix				65.73	18.75	12.91	1.05	1.28	0.28
	GB	10	2	10	60.94	11.11	25.24	0.55	0.69	1.46
	Matrix				65.68	18.73	12.87	1.06	1.32	0.34
HiHf	GB	3	4	28	65.72	13.47	18.74	0.66	0.99	0.42
	Matrix				65.83	18.40	13.08	1.06	1.41	0.22
	GB	7	4	20	61.89	9.92	26.04	0.59	0.75	0.41
	Matrix				65.74	18.52	13.15	1.06	1.32	0.21
	GB	10	2	12	64.15	12.13	21.99	0.51	0.84	0.38
	Matrix				65.73	18.53	13.14	1.06	1.32	0.22

Table 5.5(a) Grain boundary segregation for the +Hf alloys irradiated with protons at 400°C to doses of 3, 7 and 10 dpa

Alloy	Dose (dpa)	Grain Boundary Segregation (at%)					
		Fe	Cr	Ni	Mn	Mo	Si
Ref-Hf	3	-3.72	-7.60	11.04	-0.47	-0.14	0.90
	7	-5.10	-7.45	13.23	-0.55	-0.71	0.58
	10	-3.73	-6.88	11.75	-0.63	-0.88	0.36
LoHf	3	-0.76	-6.43	8.21	-0.61	-0.55	0.14
	7	-2.38	-5.56	8.65	-0.51	-0.46	0.25
	10	-4.73	-7.62	12.37	-0.51	-0.63	1.13
HiHf	3	-0.11	-4.93	5.66	-0.40	-0.42	0.20
	7	-3.85	-8.60	13.29	-0.46	-0.57	0.20
	10	-1.57	-6.40	8.85	-0.55	-0.48	0.16

Table 5.5(b) Error in the segregation measurements calculated using error propagation from the standard deviations (σ) of the grain boundary and matrix measurements for the +Hf alloys at 400°C to doses of 3, 7 and 10 dpa

Alloy	Dose (dpa)	Measurement Error (at%)					
		Fe	Cr	Ni	Mn	Mo	Si
Ref-Hf	3	1.60	0.83	1.82	0.20	0.21	0.05
	7	1.97	0.88	2.27	0.26	0.32	0.16
	10	0.68	0.35	0.70	0.27	0.16	0.10
LoHf	3	1.71	1.03	2.02	0.22	0.32	0.17
	7	0.79	1.09	1.48	0.20	0.32	0.05
	10	2.50	1.36	3.03	0.39	0.49	0.37
HiHf	3	1.13	1.03	1.20	0.21	0.17	0.05
	7	1.46	0.52	1.91	0.09	0.07	0.05
	10	0.85	0.91	1.48	0.18	0.21	0.05

Table 5.6 Grain boundary measurements of concentration for the +Hf alloys irradiated with protons at 400°C to doses of 3, 7 and 10 dpa, normalized to Fe + Cr + Ni = 1.

Alloy		Dose (dpa)	Measured Concentration (at%)			Grain Boundary Segregation (at%)		
			Fe	Cr	Ni	Fe	Cr	Ni
Ref-Hf	GB	3	63.03	11.86	25.12	-3.64	-7.78	11.41
	Matrix		66.66	19.63	13.70			
	GB	7	60.99	11.89	27.12	-5.67	-7.74	13.41
	Matrix		66.66	19.63	13.71			
	GB	10	62.12	12.43	25.45	-4.56	-7.21	11.77
	Matrix		66.68	19.64	13.68			
LoHf	GB	3	66.05	12.52	21.44	-1.47	-6.74	8.21
	Matrix		67.52	19.25	13.23			
	GB	7	64.58	13.45	21.98	-2.92	-5.81	8.72
	Matrix		67.49	19.25	13.25			
	GB	10	62.64	11.42	25.94	-4.88	-7.84	12.72
	Matrix		67.52	19.25	13.23			
HiHf	GB	3	67.11	13.75	19.14	-0.54	-5.15	5.69
	Matrix		67.65	18.91	13.44			
	GB	7	62.99	10.10	26.91	-4.49	-8.92	13.41
	Matrix		67.49	19.03	13.50			
	GB	10	65.28	12.34	22.37	-2.20	-6.68	8.88
	Matrix		67.48	19.03	13.49			

Table 5.7 Grain boundary (GB) measurements of concentration for the +Zr alloys irradiated with protons at 500°C to doses of 1 and 3 dpa

Alloy		Dose (dpa)	# of GB's	# of Meas.	Measured Concentration (at%)					
					Fe	Cr	Ni	Mn	Si	Zr
Ref-Zr	GB	1	2	6	60.74	6.54	30.07	0.73	1.93	-
	Matrix				69.76	15.36	12.78	1.25	0.85	-
	GB	3	2	6	56.92	7.22	33.60	0.69	1.57	-
	Matrix				69.82	15.37	12.80	1.25	0.76	-
LoZr	GB	1	2	7	58.11	10.66	27.73	1.78	1.44	0.27
	Matrix				68.90	15.38	13.22	1.53	0.77	0.20
	GB	3	2	10	55.48	5.70	35.00	0.64	2.81	0.37
	Matrix				69.51	15.39	12.83	1.32	0.77	0.19
HiZr	GB	1	2	13	62.22	11.39	23.52	1.07	1.29	0.52
	Matrix				69.82	14.95	12.91	1.22	0.81	0.29
	GB	3	2	12	64.68	9.40	22.38	0.67	2.37	0.49
	Matrix				70.04	14.88	12.78	1.19	0.83	0.28

Table 5.8(a) Grain boundary segregation for the +Zr alloys irradiated with protons at 500°C to doses of 1 and 3 dpa

Alloy	Dose (dpa)	Grain Boundary Segregation (at%)					
		Fe	Cr	Ni	Mn	Si	Zr
Ref-Zr	1	-9.02	-8.82	17.29	-0.52	1.08	-
	3	-12.90	-8.15	20.80	-0.56	0.81	-
LoZr	1	-10.79	-4.72	14.51	0.25	0.67	0.08
	3	-14.03	-9.69	22.17	-0.67	2.05	0.18
HiZr	1	-7.61	-3.56	10.61	-0.16	0.48	0.23
	3	-5.35	-5.48	9.60	-0.52	1.54	0.21

Table 5.8(b) Error in the segregation measurements calculated using error propagation from the standard deviations (σ) of the grain boundary and matrix measurements for the +Zr alloys at 500°C to doses of 1 and 3 dpa

Alloy	Dose (dpa)	Measurement Error (at%)					
		Fe	Cr	Ni	Mn	Si	Zr
Ref-Zr	1	1.56	0.60	1.35	0.22	1.03	-
	3	1.93	0.52	1.77	0.21	0.26	-
LoZr	1	1.96	0.97	1.87	0.75	0.08	0.33
	3	1.47	0.81	2.37	0.08	0.05	0.37
HiZr	1	2.81	0.85	1.99	0.21	0.59	0.95
	3	2.00	0.38	2.40	0.11	0.28	0.71

Table 5.9 Grain boundary measurements of concentration for the +Zr alloys irradiated with protons at 500°C to doses of 1 and 3 dpa, normalized to Fe + Cr + Ni = 1.

Alloy		Dose (dpa)	Measured Concentration (at%)			Grain Boundary Segregation (at%)		
			Fe	Cr	Ni	Fe	Cr	Ni
Ref-Zr	GB	1	62.39	6.72	30.89	-8.86	-8.97	17.83
	Matrix		71.26	15.69	13.05			
	GB	3	58.24	7.39	34.38	-13.02	-8.30	21.31
	Matrix		71.25	15.69	13.06			
LoZr	GB	1	60.22	11.05	28.74	-10.45	-4.73	15.18
	Matrix		70.67	15.77	13.56			
	GB	3	57.68	5.93	36.39	-13.45	-9.82	23.27
	Matrix		71.12	15.75	13.13			
HiZr	GB	1	64.05	11.73	24.22	-7.42	-3.58	11.00
	Matrix		71.48	15.31	13.22			
	GB	3	67.05	9.74	23.20	-4.64	-5.49	10.12
	Matrix		71.69	15.23	13.08			

Table 5.10 Grain boundary (GB) measurements of concentration for the +Hf alloys irradiated with protons at 500°C to doses of 1 and 3 dpa
NM: Not Measured

Alloy		Dose (dpa)	# of GB's	# of Meas.	Measured Concentration (at%)					
					Fe	Cr	Ni	Mn	Mo	Si
Ref-Hf	GB	1	2	5			NM			
	Matrix									
	GB	3	2	13	56.89	8.63	32.73	0.58	0.65	0.51
	Matrix				64.91	19.12	13.36	1.05	1.32	0.24
LoHf	GB	1	2	6	60.77	12.80	24.24	0.69	1.05	0.45
	Matrix				65.80	18.76	12.83	1.05	1.28	0.28
	GB	3	2	6	56.62	8.67	33.08	0.49	0.58	0.56
	Matrix				65.78	18.76	12.85	1.05	1.28	0.28
HiHf	GB	1	2	6	61.75	13.82	22.22	0.84	1.10	0.27
	Matrix				65.76	18.54	13.12	1.09	1.29	0.20
	GB	3	2	12	54.52	8.09	36.15	0.44	0.55	0.25
	Matrix				65.78	18.55	13.13	1.04	1.29	0.21

Table 5.11(a) Grain boundary segregation for the +Hf alloys irradiated with protons at 500°C to doses of 1 and 3 dpa

Alloy	Dose (dpa)	Grain Boundary Segregation (at%)					
		Fe	Cr	Ni	Mn	Mo	Si
Ref-Hf	1	NM					
	3	-8.02	-10.49	19.37	-0.47	-0.66	0.27
LoHf	1	-5.02	-5.96	11.41	-0.36	-0.24	0.16
	3	-9.32	-10.11	20.14	-0.56	-0.70	0.28
HiHf	1	-4.02	-4.72	9.10	-0.24	-0.19	0.07
	3	-11.27	-10.46	23.03	-0.61	-0.73	0.04

Table 5.11(b) Error in the segregation measurements calculated using error propagation from the standard deviations (σ) of the grain boundary and matrix measurements for the +Zr alloys at 500°C to doses of 1 and 3 dpa

Alloy	Dose (dpa)	Measurement Error (at%)					
		Fe	Cr	Ni	Mn	Mo	Si
Ref-Hf	1	NM					
	3	2.19	1.00	2.59	0.16	0.13	0.10
LoHf	1	0.82	0.49	0.82	0.15	0.13	0.08
	3	2.00	0.59	2.22	0.26	0.28	0.27
HiHf	1	0.83	0.56	0.76	0.25	0.14	0.03
	3	2.86	0.33	2.90	0.11	0.04	0.07

Table 5.12 Grain boundary measurements of concentration for the +Hf alloys irradiated with protons at 500°C to doses of 1 and 3 dpa, normalized to Fe + Cr + Ni = 1.

Alloy		Dose (dpa)	Measured Concentration (at%)			Grain Boundary Segregation (at%)		
			Fe	Cr	Ni	Fe	Cr	Ni
Ref-Hf	GB	1			NM			
	Matrix							
	GB	3	57.90	8.78	33.31	-8.75	-10.85	19.59
	Matrix		66.65	19.63	13.72			
LoHf	GB	1	62.13	13.09	24.78	-5.43	-6.18	11.61
	Matrix		67.56	19.26	13.18			
	GB	3	57.55	8.82	33.63	-9.99	-10.45	20.43
	Matrix		67.54	19.26	13.19			
HiHf	GB	1	63.15	14.13	22.72	-4.36	-4.90	9.25
	Matrix		67.50	19.03	13.47			
	GB	3	55.20	8.19	36.60	-12.29	-10.84	23.13
	Matrix		67.50	19.03	13.47			

Table 5.13 Measured dislocation loop data for the +Zr alloys after 400°C irradiation at doses of 3 and 7 dpa

Alloy	Dose (dpa)	# of Loops Measured	Avg. Loop Diameter (nm)	Avg. Loop Density x 10^{21} (m^{-3})	Loop Density Error (m^{-3})	Total Loop Line Length (m^{-2})
Ref-Zr	3	88	10.0	50.6×10^{21}	9.75×10^{21}	15.9×10^{14}
	7	303	8.7	54.8×10^{21}	4.51×10^{21}	14.9×10^{14}
LoZr	3	77	8.0	11.1×10^{21}	2.23×10^{21}	2.72×10^{14}
	7	318	8.0	17.2×10^{21}	2.00×10^{21}	4.35×10^{14}
HiZr	3	59	9.0	8.73×10^{21}	2.82×10^{21}	2.47×10^{14}
	7	282	9.9	13.2×10^{21}	2.79×10^{21}	4.1×10^{14}

Table 5.14 Measured dislocation loop data for the +Hf alloys after 400°C irradiation at doses of 3 and 7 dpa. Loop density error represents the standard deviation of the loop density measurements.

Alloy	Dose (dpa)	# of Loops Measured	Avg. Loop Diameter (nm)	Average Loop Density (m^{-3})	Loop Density Error (m^{-3})	Total Loop Line Length (m^{-2})
Ref-Hf	3	388	9.4	22.9×10^{21}	3.58×10^{21}	6.74×10^{14}
	7	208	9.6	23.2×10^{21}	4.01×10^{21}	7.03×10^{14}
LoHf	3	124	7.2	13.8×10^{21}	2.20×10^{21}	3.11×10^{14}
	7	289	8.9	23.8×10^{21}	2.53×10^{21}	6.64×10^{14}
HiHf	3	42	7.2	6.32×10^{21}	0.43×10^{21}	1.43×10^{14}
	7	87	10.4	9.32×10^{21}	1.16×10^{21}	3.05×10^{14}

Table 5.15 IDCC data for ZrC and HfC including 2θ diffraction angles, inter-planar distance (d), relative intensities, and (hkl) planes

Phase	2θ	d (nm)	Relative Intensity	(hkl) Plane
ZrC PDF# 00-035-0784	33.041	0.27089	100	(111)
	38.338	0.23459	82	(200)
	55.325	0.16592	62	(220)
	65.969	0.14149	50	(311)
HfC PDF# 00-039-1491	33.438	0.26776	100	(111)
	38.802	0.23189	69	(200)
	56.026	0.16401	44	(220)
	66.855	0.13983	37	(311)

Table 5.16 XRD results of the bulk lattice parameter and phases detected for the oversized solute alloys and the reference alloys, along with an estimated mass fraction of the secondary XC phases present in the oversized solute alloys
N/D: Not Detected

Alloy	ZrC	HfC	Bulk Lattice Parameter (nm)
Ref-Zr	N/D	N/D	0.35876 +/- .0001
LoZr	0.3 wt%	N/D	0.35894 +/- .0001
HiZr	0.4 wt%	N/D	0.35879 +/- .0001
Ref-Hf	N/D	N/D	0.35933 +/- .0001
LoHf	N/D	N/D	0.35934 +/- .0001
HiHf	N/D	0.5 wt%	0.35937 +/- .0001

Table 5.17 Experimental lattice parameters for austenite and HfC

Phase	Austenite	HfC	ZrC
Lattice Parameter (nm)	0.359	0.464	0.469

Table 5.18 Mean size and density of HfC and ZrC precipitates (ppts.) in HiHf and HiZr, respectively, with the amount of Hf/Zr in the precipitates and remaining in solution

Mean Size	Standard Deviation	Mean Density	Density Error	Hf/Zr in Ppts.	Hf/Zr in Solution
62 nm	± 36 nm	7.0E+19 m^{-3}	± 2.2E+19 m^{-3}	0.21 at%	0.16 at%
81 nm	± 32 nm	2.5E+19 m^{-3}	± 1.1E+19 m^{-3}	0.17 at%	0.11 at%

Table 5.19 Ni^{2+} mass/charge ratios with isotopic abundances. The Ni^{2+} ratios overlap with the Zr^{3+}

Ni Isotope	Ni-58	Ni-60	Ni-61	Ni-62	Ni-64
+2 mass/charge ratio	28.97	29.97	30.47	30.96	31.96
Isotopic abundance (%)	*68.08*	*26.22*	*1.14*	*3.63*	*0.93*

Table 5.20 Mo^{2+} mass/charge ratios with isotopic abundances. Some of the Mo^{2+} ratios overlap with Zr^{2+} ratios

Mo Isotope	Mo-92	Mo-94	Mo-95	Mo-96	Mo-97	M-98	Mo-100
+2 mass/charge ratio	45.95	46.95	47.45	47.95	48.45	48.95	49.95
Isotopic Abundance (%)	*14.84*	*9.25*	*15.92*	*16.68*	*9.55*	*24.13*	*9.83*

Table 5.21 Zr^{2+} and Zr^{3+} mass/charge ratios with isotopic abundances. Mass/charge ratios for both Mo and Ni overlap with Zr, making identification of Zr difficult.

Zr Isotope	Zr-90	Zr-91	Zr-92	Zr-94	Zr-96
+2 mass/charge ratio	44.95	45.45	45.95	46.95	47.95
+3 mass/charge ratio	29.97	30.30	30.64	31.30	31.97
Isotopic abundance (%)	*51.45*	*11.22*	*17.15*	*17.38*	*2.80*

Table 5.22 The Hf^{2+} and Hf^{3+} mass/charge ratios with isotopic abundances. High mass/charge ratios for Hf make detection more difficult at low concentrations.

Hf Isotope	Hf-174	Hf-176	Hf-177	Hf-178	Hf-179	Hf-180
+2 mass/charge ratio	86.97	87.97	88.47	88.97	89.47	89.97
+3 mass/charge ratio	57.98	58.65	58.98	59.31	59.65	59.98
Isotopic abundance (%)	*0.16*	*5.26*	*18.60*	*27.28*	*13.62*	*35.08*

Table 5.23 Results from the identification of oversized solute in LEAP sample analysis.

Sample ID	Alloy	Dose (dpa)	Oversize Solute Verified?
5031	LoZr	0	No
5033	LoZr	0	Yes
5034	LoZr	0	Yes
5239	LoZr	3	No
5246	LoZr	7	No
5058	HiZr	0	Yes
5099	HiZr	3	Yes
5100	HiZr	3	Yes
5104	HiZr	7	Yes
5096	LoHf	0	No
5098	HiHf	0	Yes
5103	HiHf	3	Unknown*

* Unidentified peaks with a lower mass/charge ratio than Hf make identification of Hf for HiHf at 3 dpa uncertain.
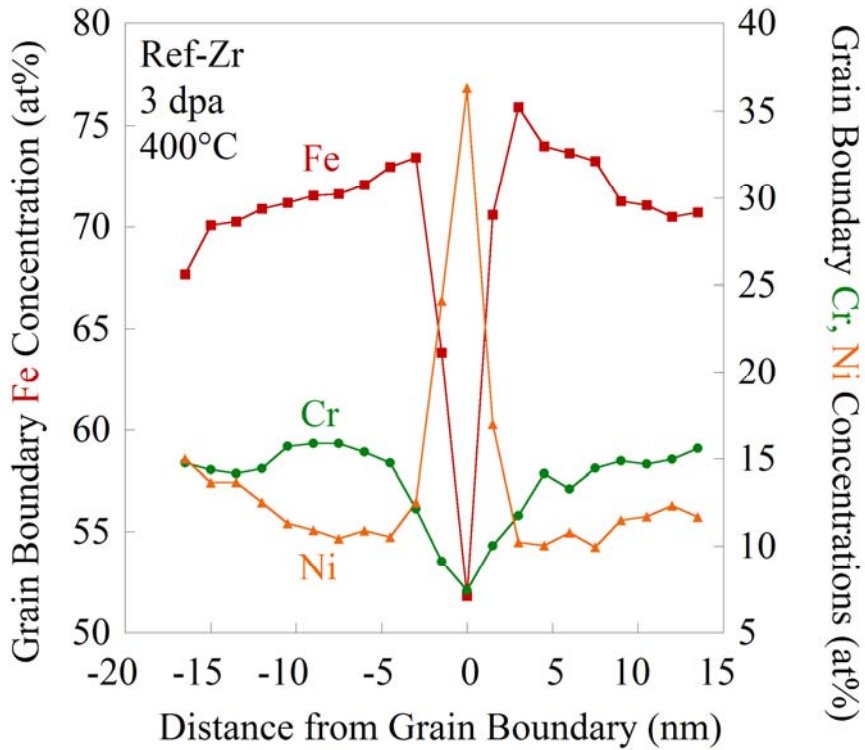
Figure 5.1 Concentration profile as a function of distance from the grain boundary for Fe, Cr and Ni for the Ref-Zr alloy irradiated at 400°C to 3 dpa. The left y-axis is for Fe concentration while Cr and Ni concentrations are plotted on the right y-axis.
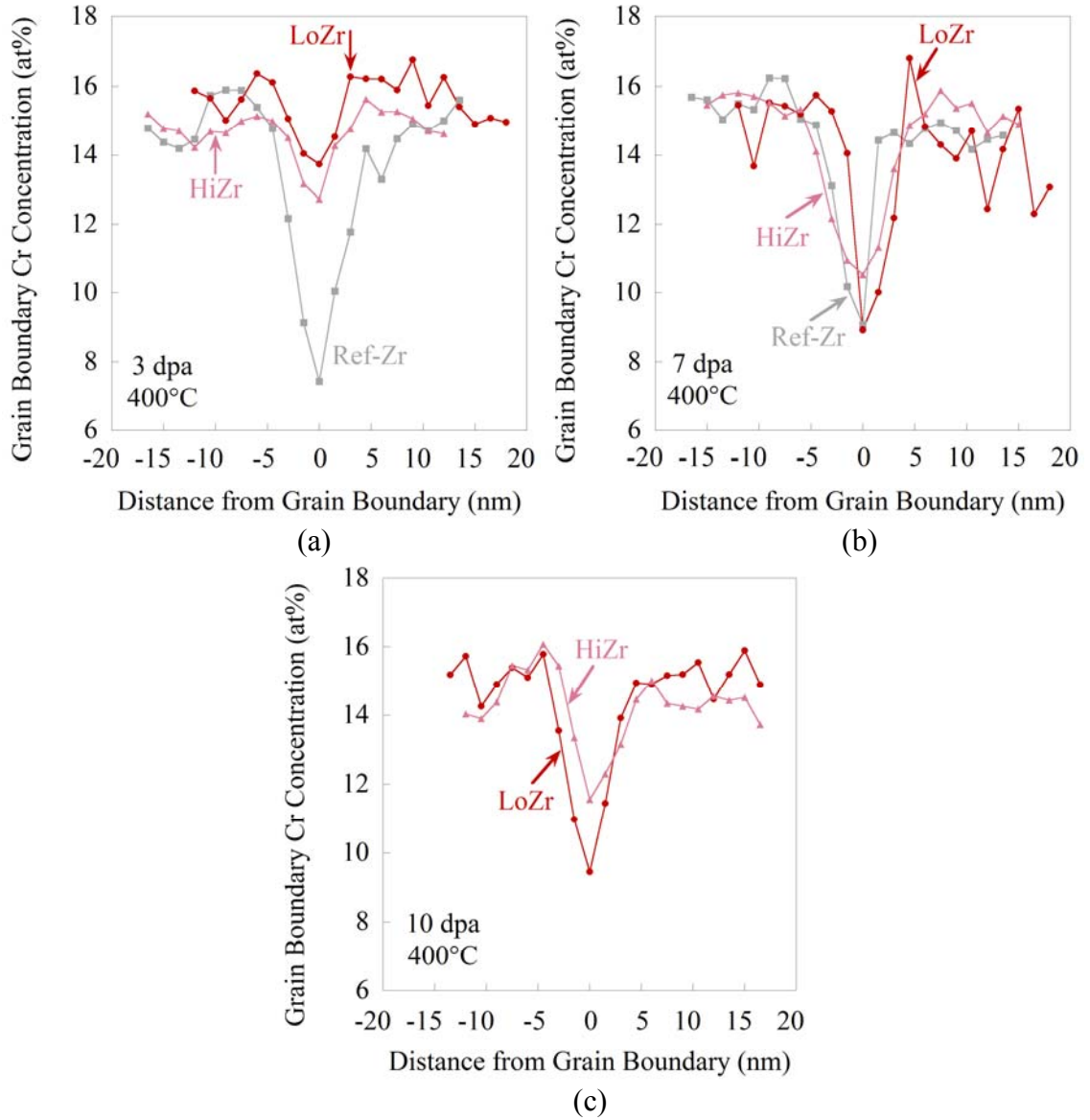
Figure 5.2 Cr concentration profiles as a function of distance from the grain boundary at 400°C for Ref-Zr, LoZr and HiZr, at doses of (a) 3 dpa, (b) 7 dpa, and (c) 10 dpa.
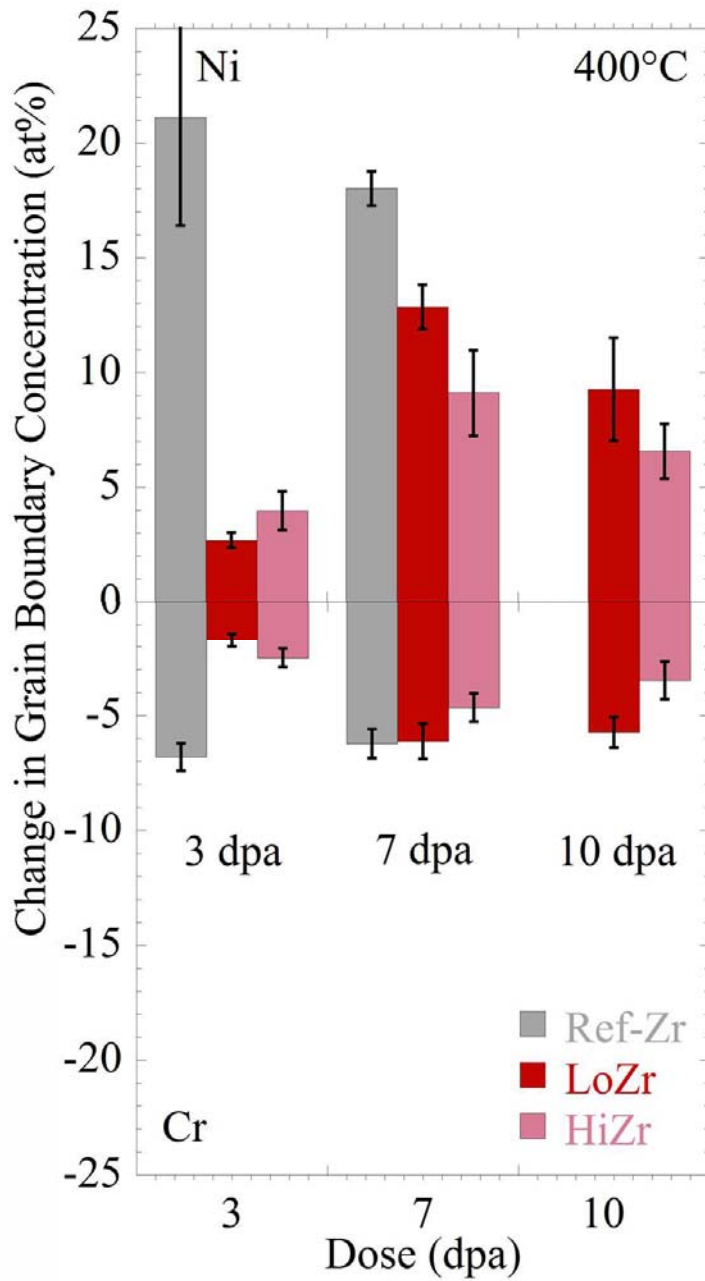
Figure 5.3 Change in grain boundary Ni and Cr concentration for the +Zr alloy series after proton irradiation at 400°C to doses of 3, 7 and 10 dpa.
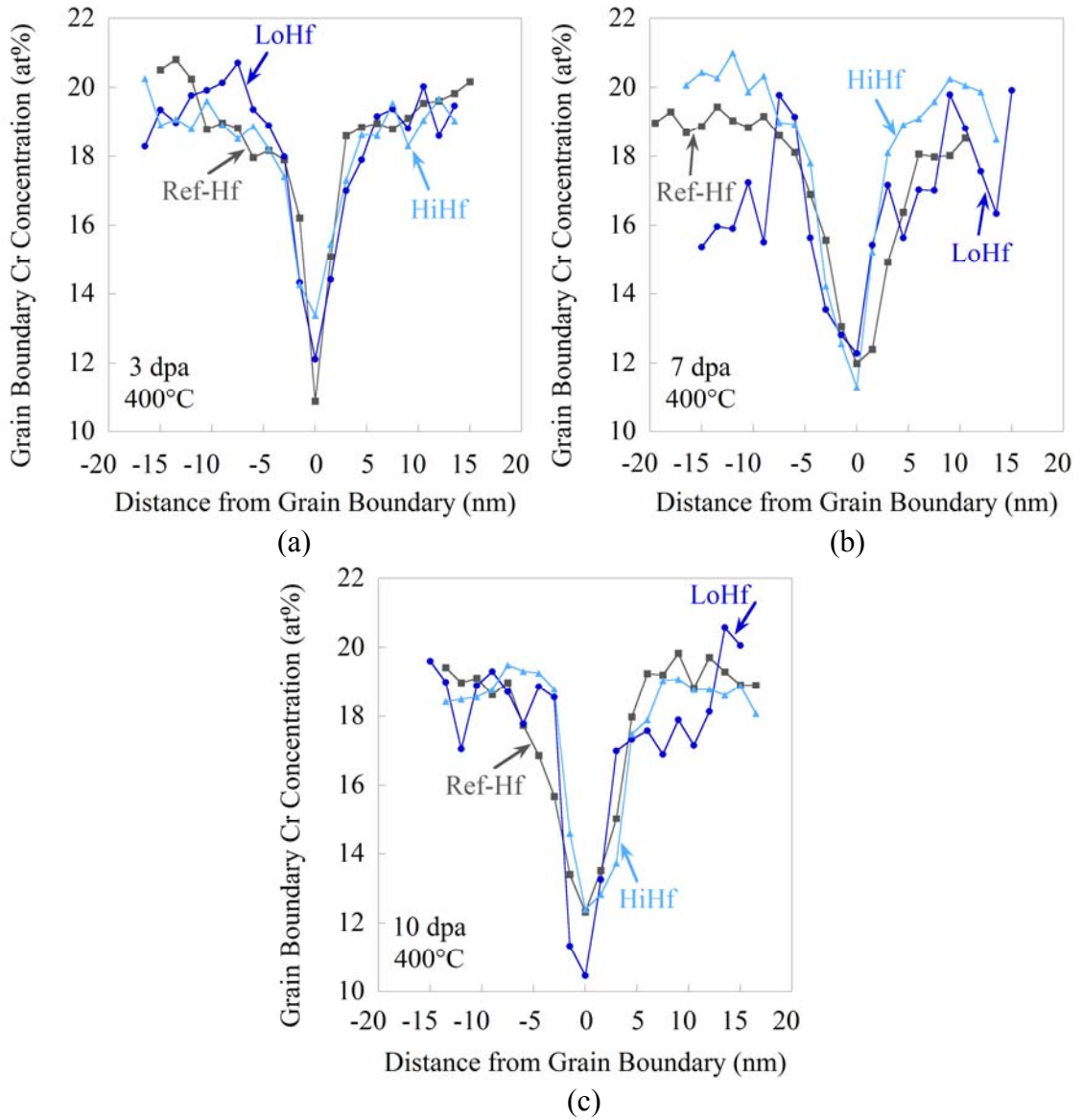
Figure 5.4 Cr concentration profiles as a function of distance from the grain boundary at 400°C for Ref-Hf, LoHf and HiHf, at doses of (a) 3 dpa, (b) 7 dpa, and (c) 10 dpa.
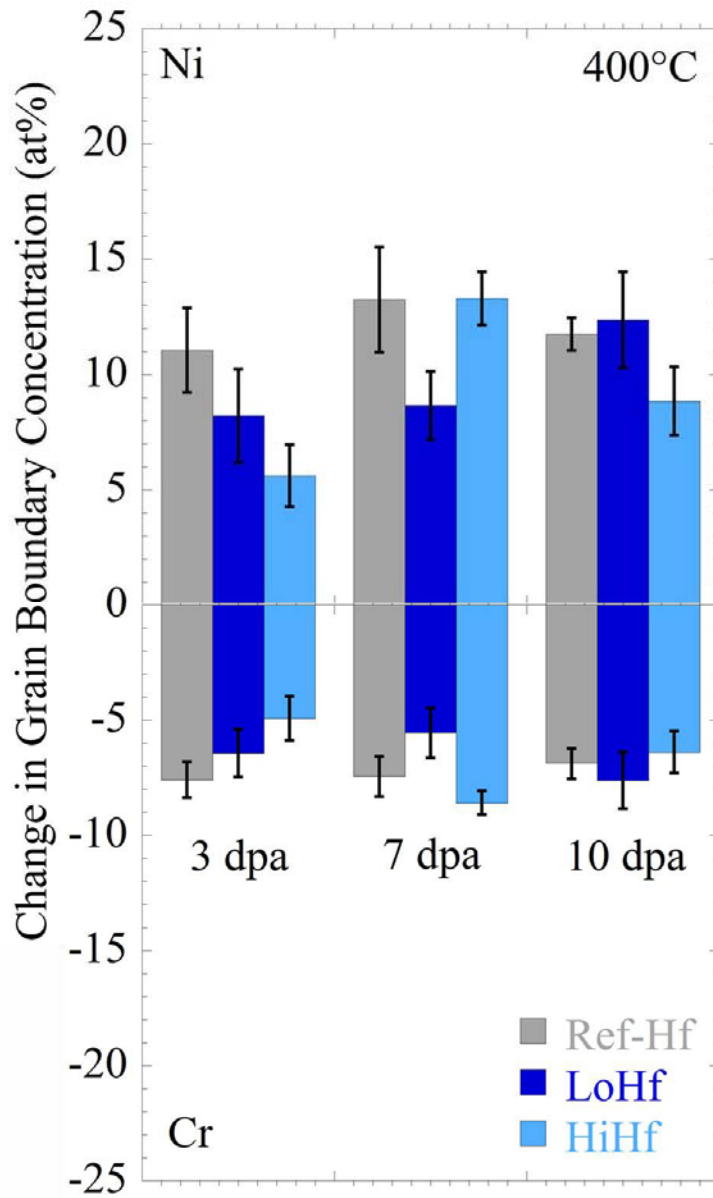
Figure 5.5 Change in grain boundary Ni and Cr concentration for the +Hf alloy series after proton irradiation at 400°C to doses of 3, 7 and 10 dpa.
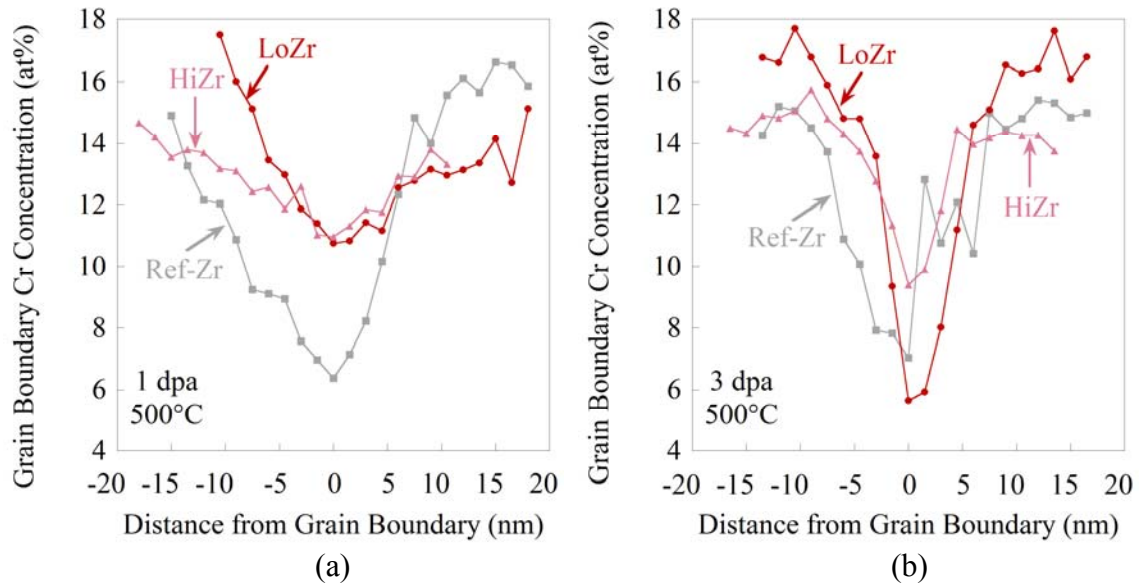
Figure 5.6 Cr concentration profiles as a function of distance from the grain boundary at 500°C for Ref-Zr, LoZr and HiZr, at doses of (a) 1 dpa and (b) 3 dpa.
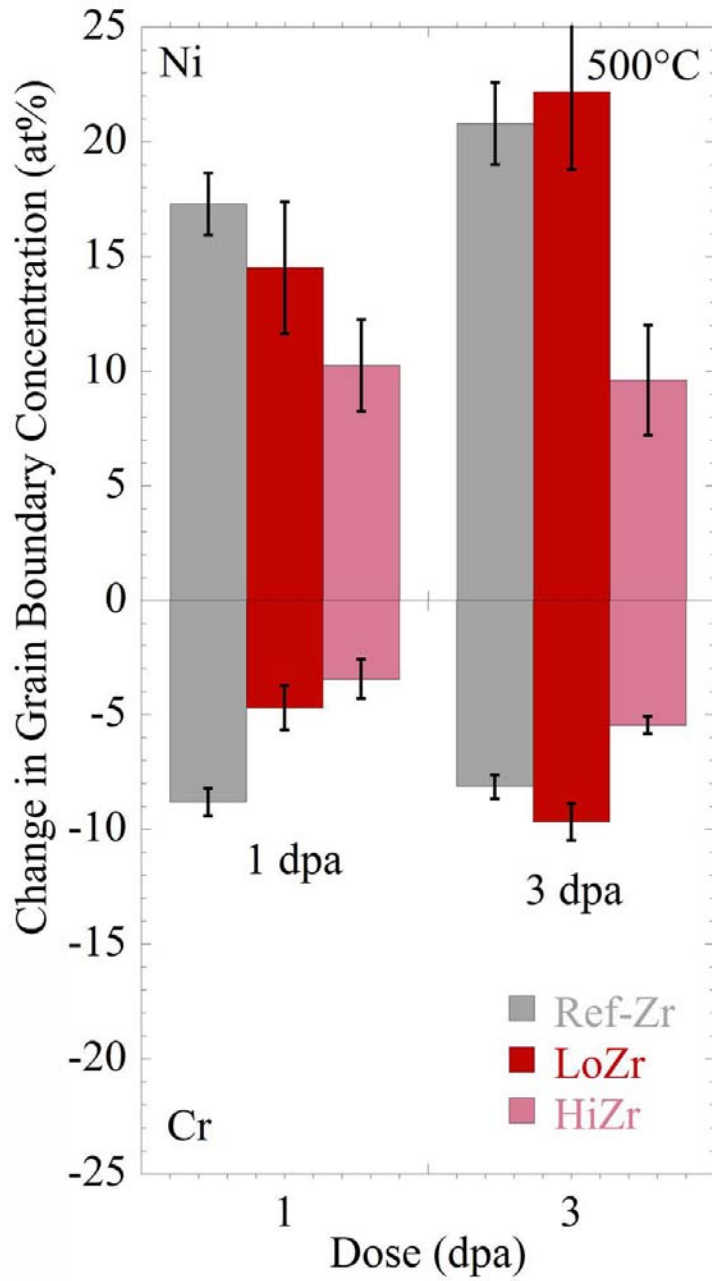
Figure 5.7 Change in grain boundary Ni and Cr concentration for the +Hf alloy series after proton irradiation at 500°C to doses of 1 and 3 dpa.

(a)   (b)
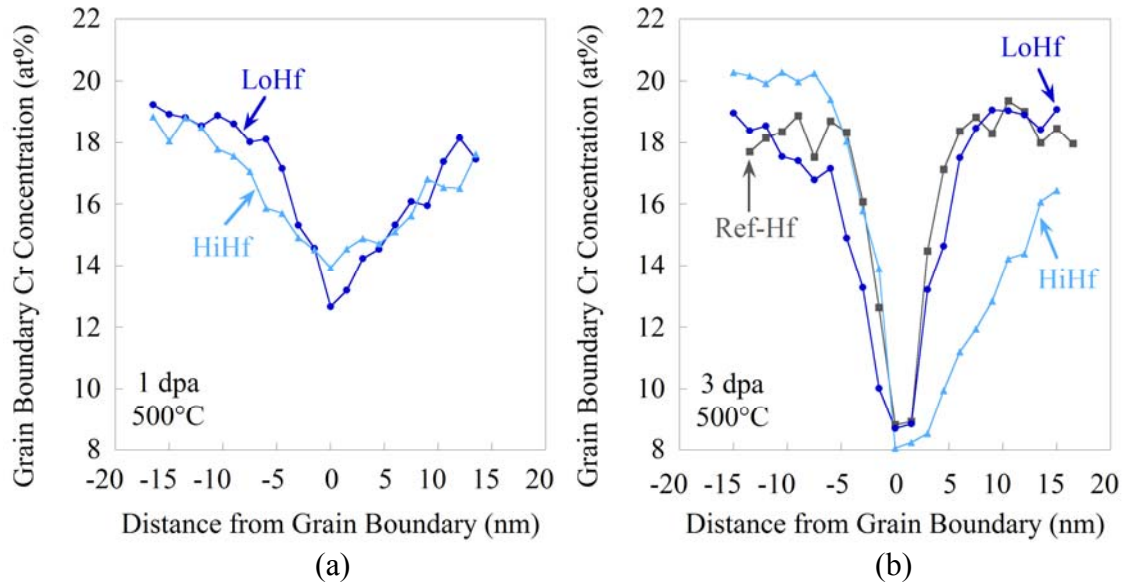
Figure 5.8 Cr concentration profiles as a function of distance from the grain boundary at 500°C for Ref-Hf, LoHf and HiHf, at doses of (a) 1 dpa and (b) 3 dpa.
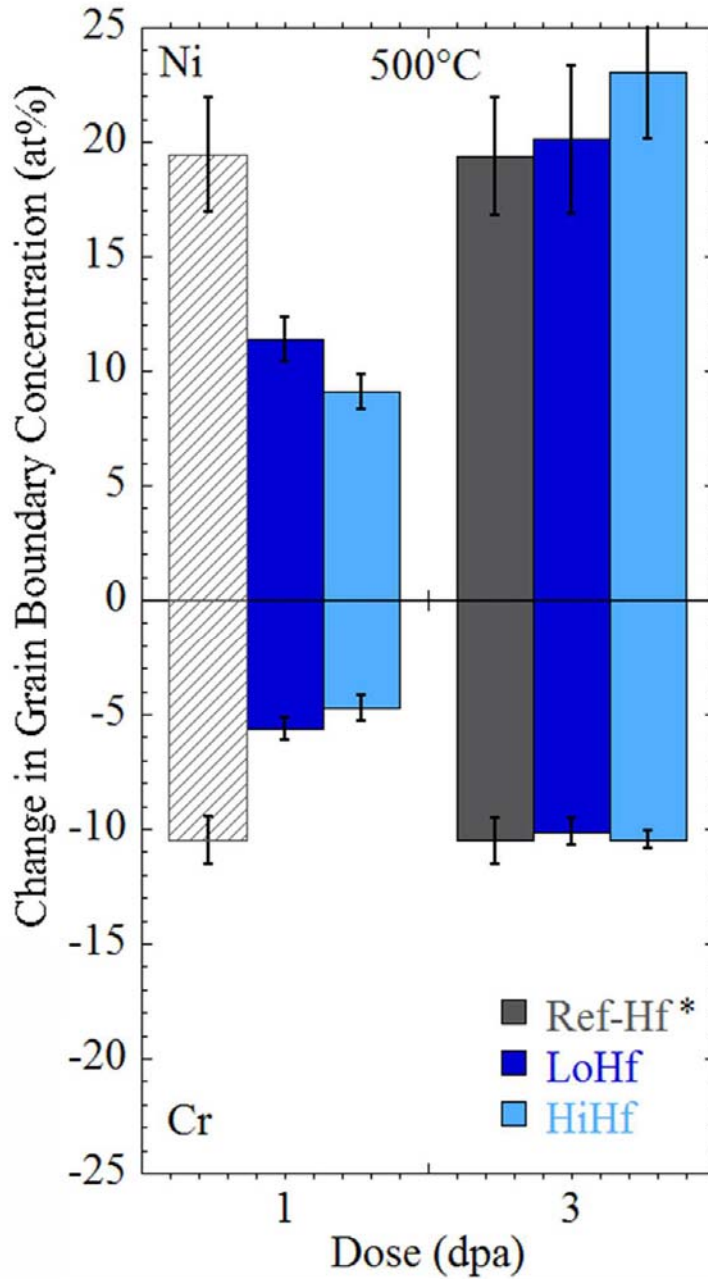
* Ref-Hf at 1 dpa was not measured. The values shown are for Ref-Hf at 3 dpa, which will serve as an estimate of the expected Cr depletion and Ni enrichment at 1 dpa.

Figure 5.9 Change in grain boundary Ni and Cr concentration for the +Hf alloy series after proton irradiation at 500°C to doses of 1 and 3 dpa.

(a)   (b)

(c)
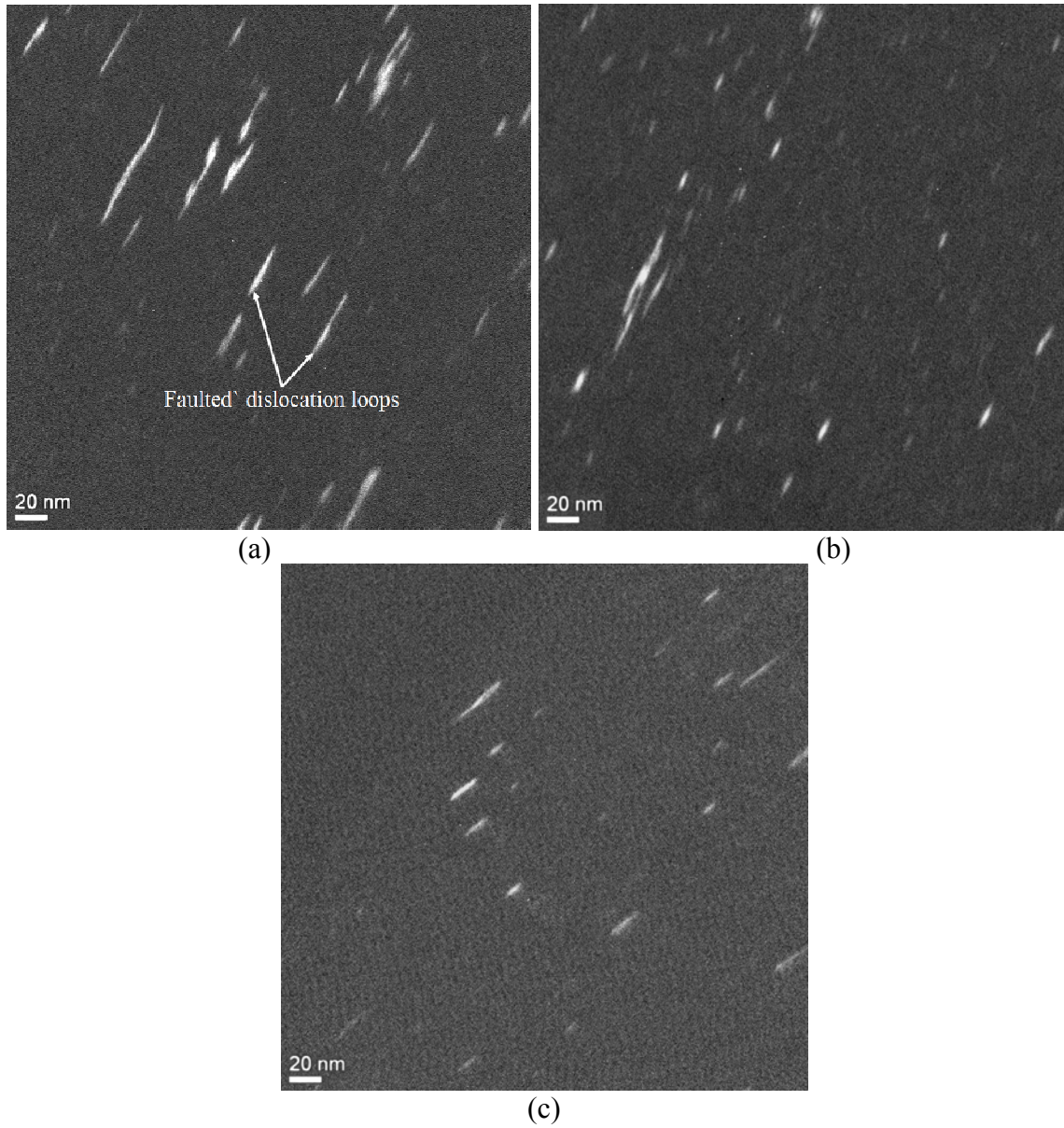
Figure 5.10 Dislocation loop images at 400°C, 3 dpa of (a) Ref-Zr, (b) LoZr, and (c) HiZr

(a)   (b)

(c)
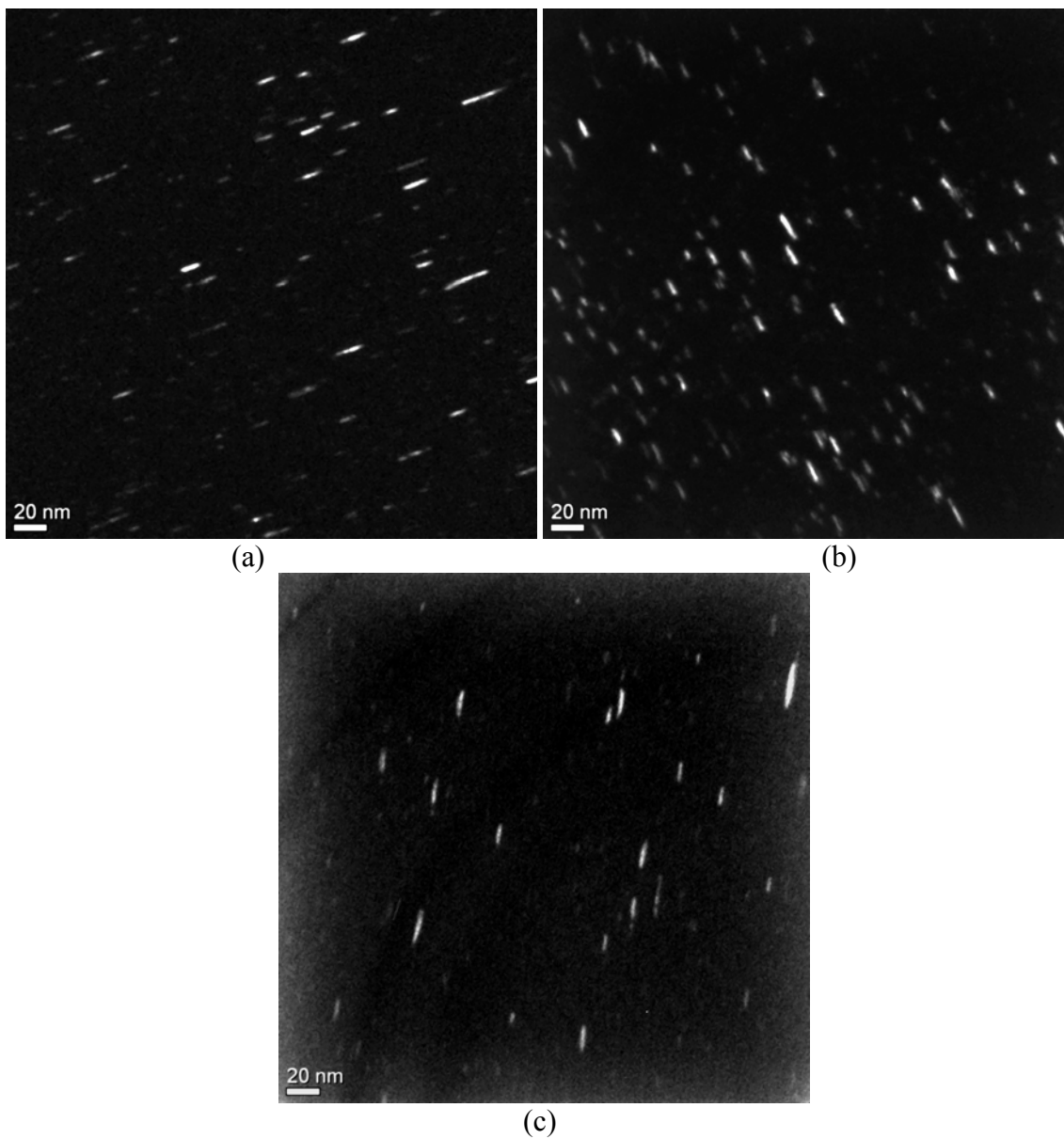
Figure 5.11 Dislocation loop images at 400°C, 7 dpa of (a) Ref-Zr, (b) LoZr, and (c) HiZr
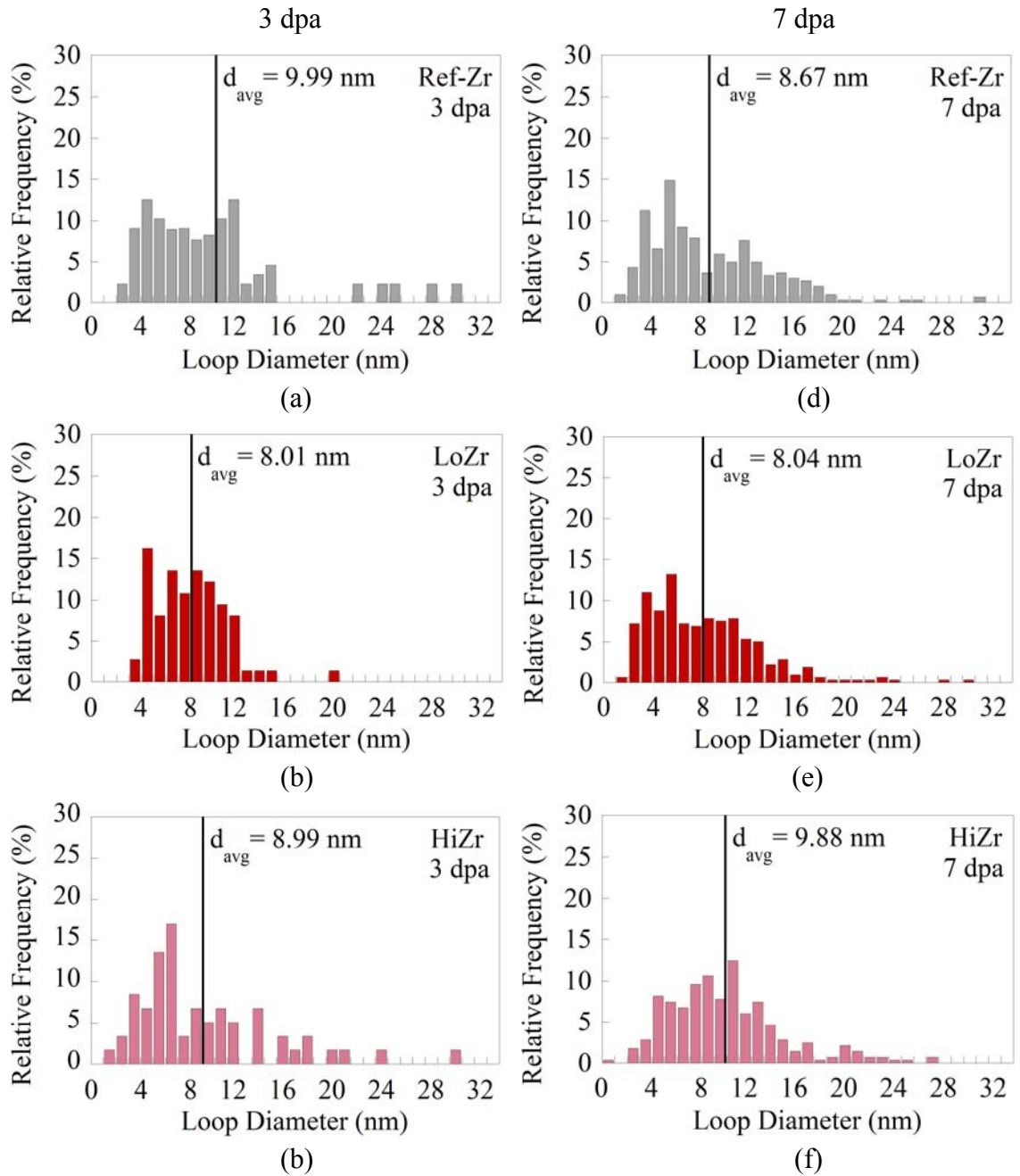
Figure 5.12 Dislocation loop size distributions of the relative frequency of loop diameter for the +Zr alloys after 400°C irradiation to 3 dpa for (a) Ref-Zr, (b) LoZr, and (c) HiZr, and to 7 dpa for (d) Ref-Zr, (e) LoZr, and (f) HiZr. Vertical lines denote the average loop diameter.
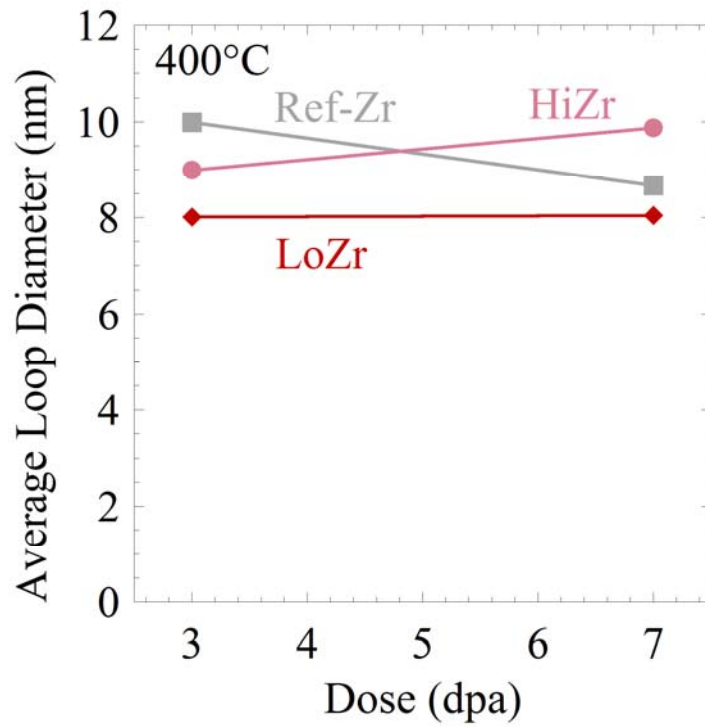
Figure 5.13 Average dislocation loop diameter for the +Zr alloys as a function of dose from 3 – 7 dpa after proton irradiation at 400°C.
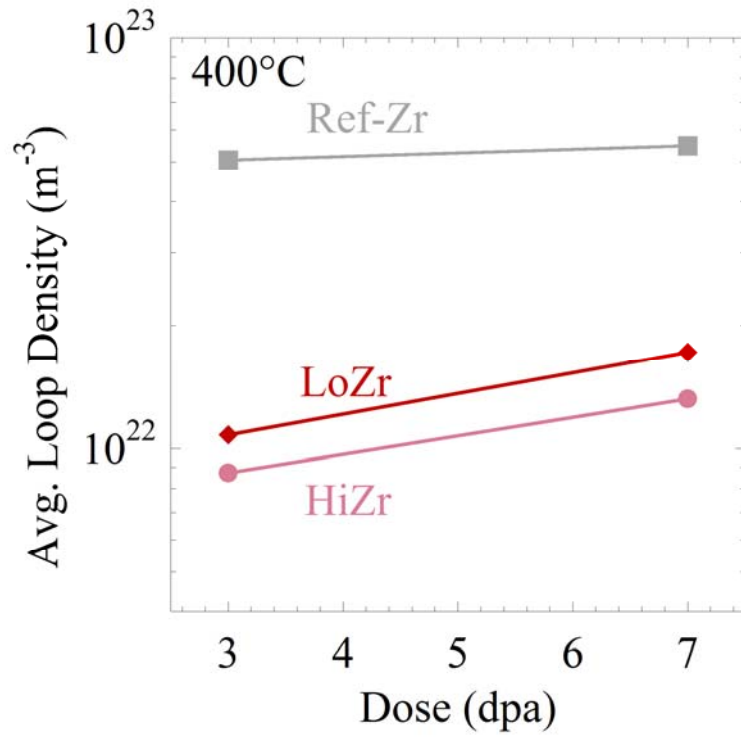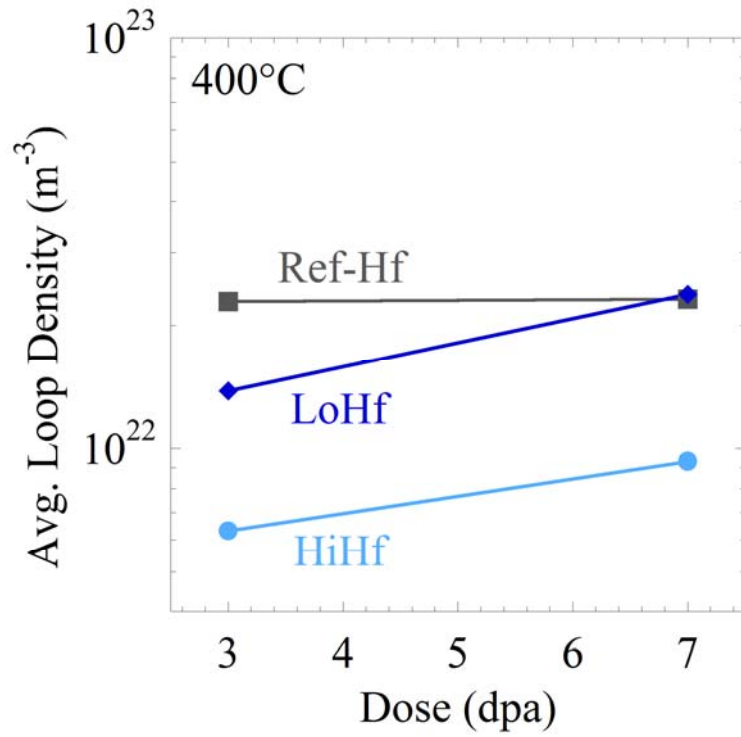
Figure 5.14 Average dislocation loop density for the +Zr alloys as a function of dose from 3 – 7 dpa after proton irradiation at 400°C.
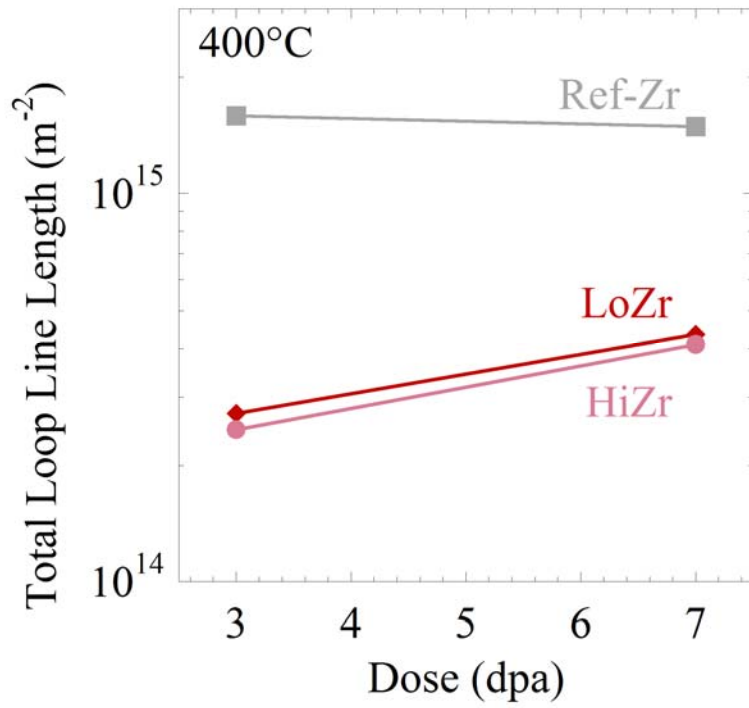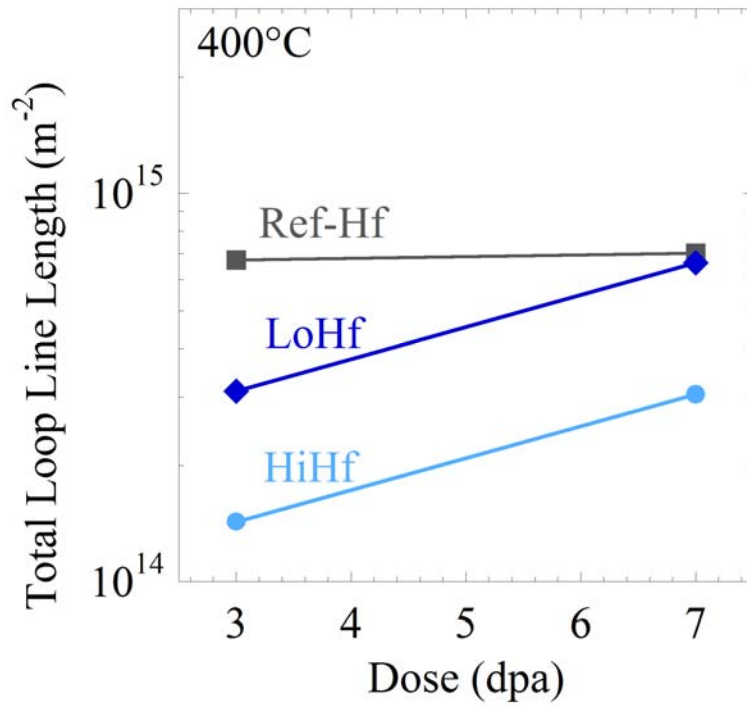
Figure 5.15 Total loop line length for the +Zr alloys as a function of dose from 3 – 7 dpa after 400°C proton irradiation.

(a)

(b)

(c)
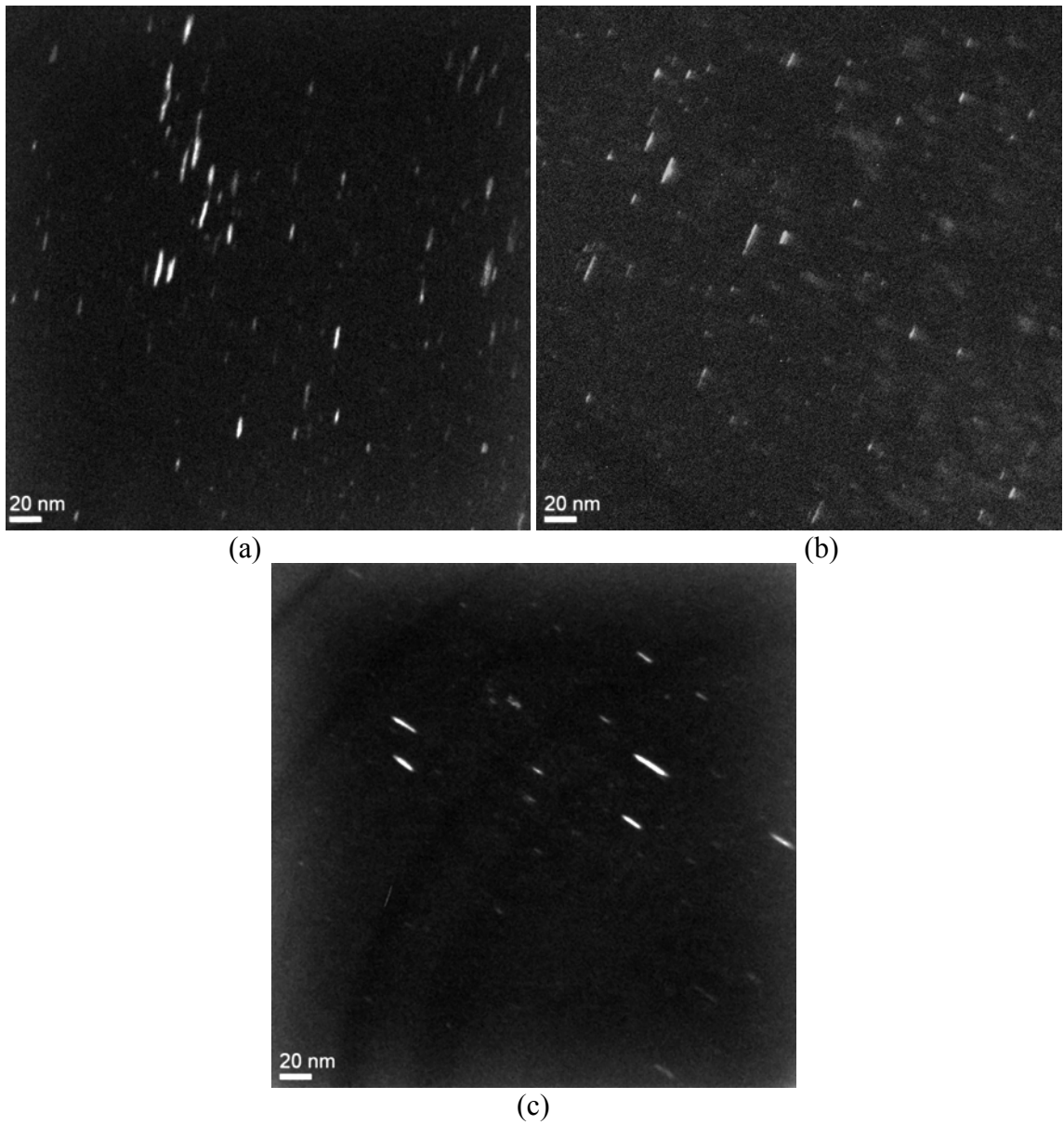
Figure 5.16 Dislocation loop images at 400°C, 3 dpa of (a) Ref-Hf, (b) LoHf, and (c) HiHf

(a)

(b)

(c)
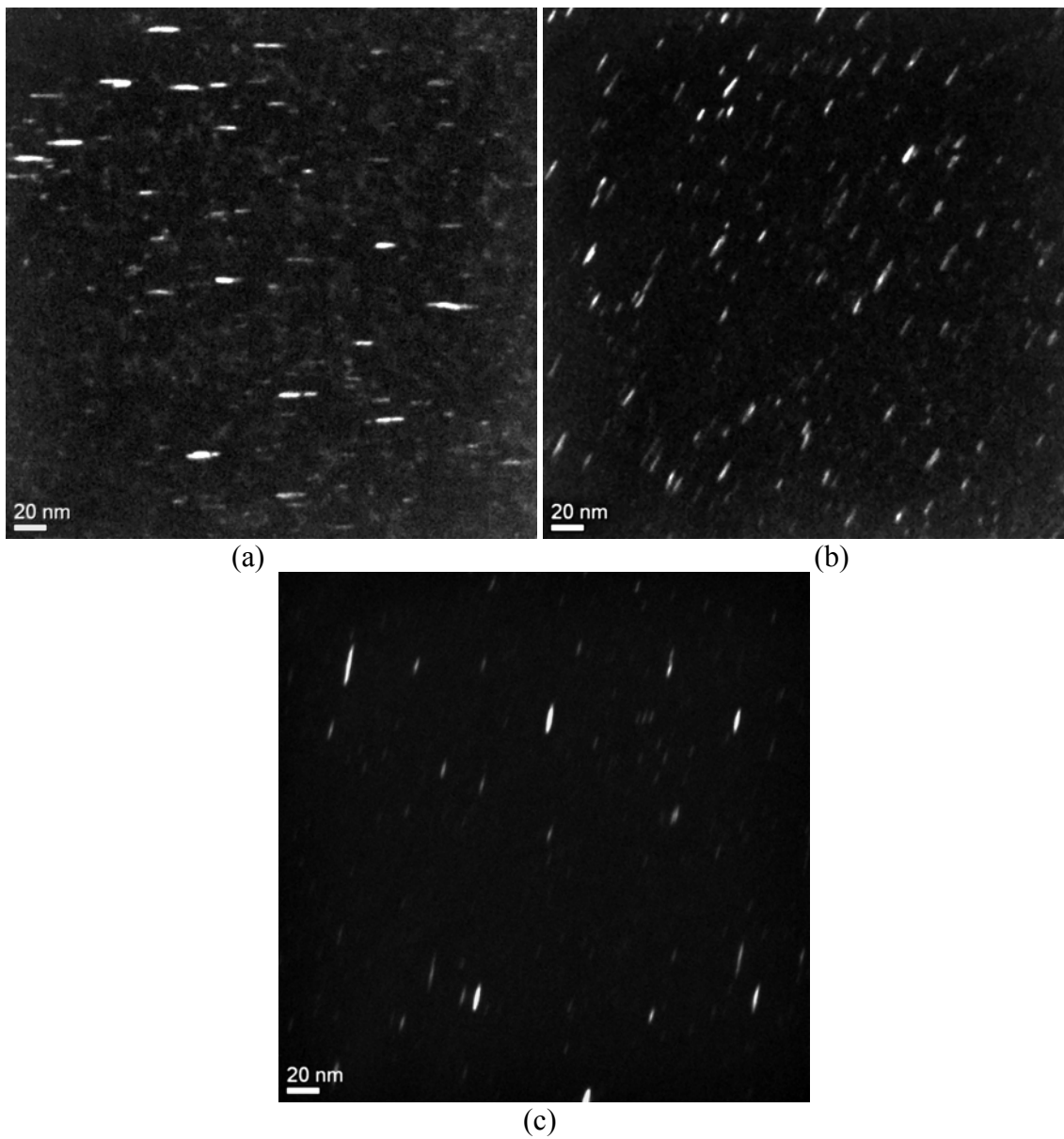
Figure 5.17 Dislocation loop images at 400°C, 7 dpa of (a) Ref-Hf, (b) LoHf, and (c) HiHf
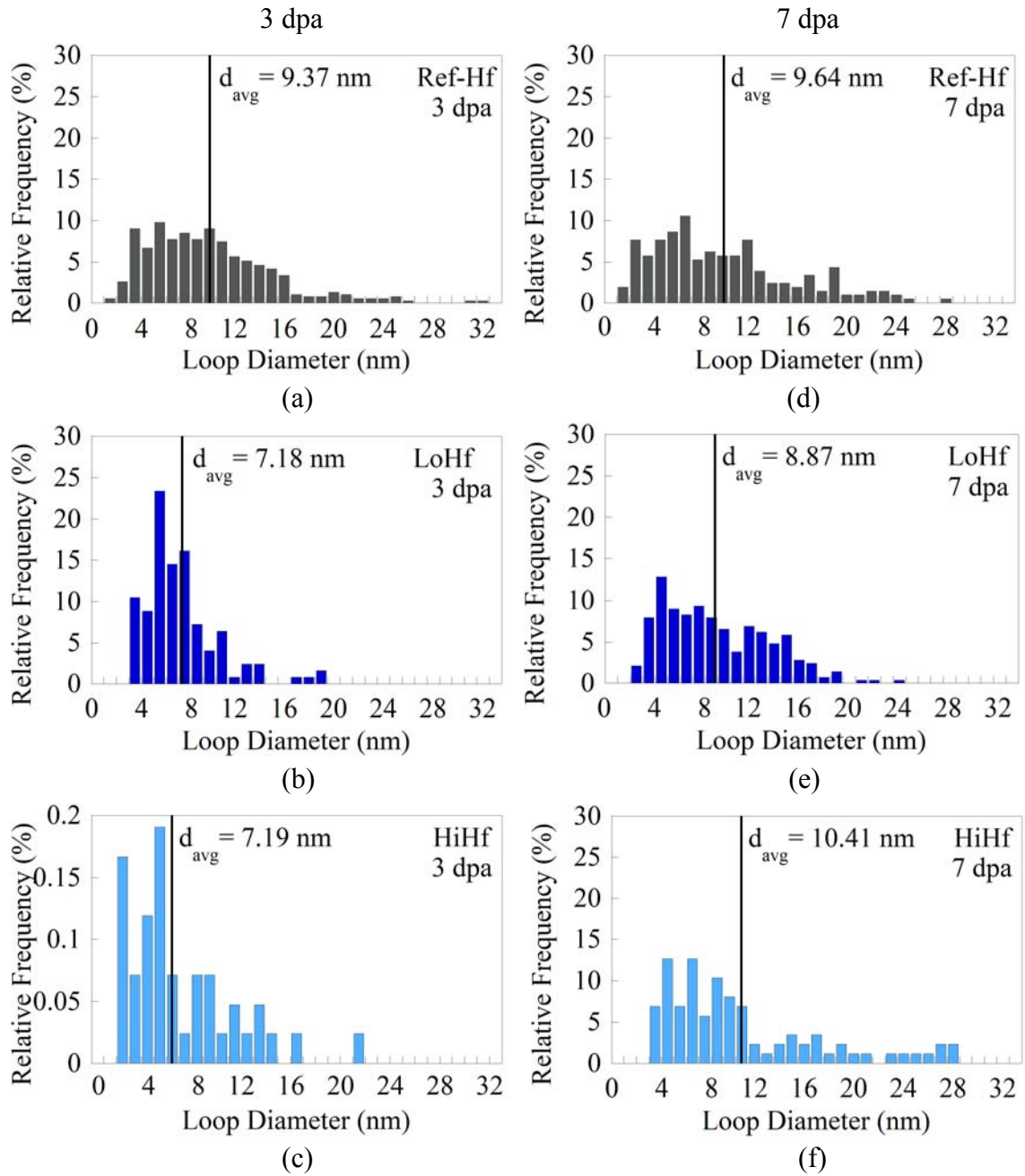
Figure 5.18 Dislocation loop size distributions of the relative frequency of loop diameter for the +Zr alloys after 400°C irradiation to 3 dpa for (a) Ref-Hf, (b) LoHf, and (c) HiHf, and to 7 dpa for (d) Ref-Hf, (e) LoHf, and (f) HiHf. Vertical lines denote the average loop diameter.
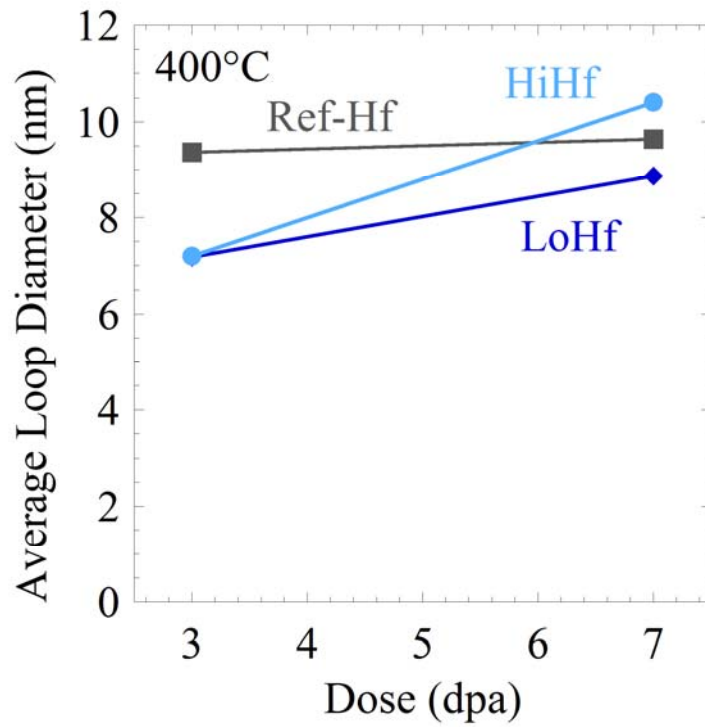
Figure 5.19 Average dislocation loop diameter for the +Hf alloys as a function of dose from 3 – 7 dpa after proton irradiation at 400°C.

Figure 5.20 Average dislocation loop density for the +Hf alloys as a function of dose from 3 – 7 dpa after proton irradiation at 400°C.

Figure 5.21 Total loop line length for the +Hf alloys as a function of dose from 3 – 7 dpa after 400°C proton irradiation.
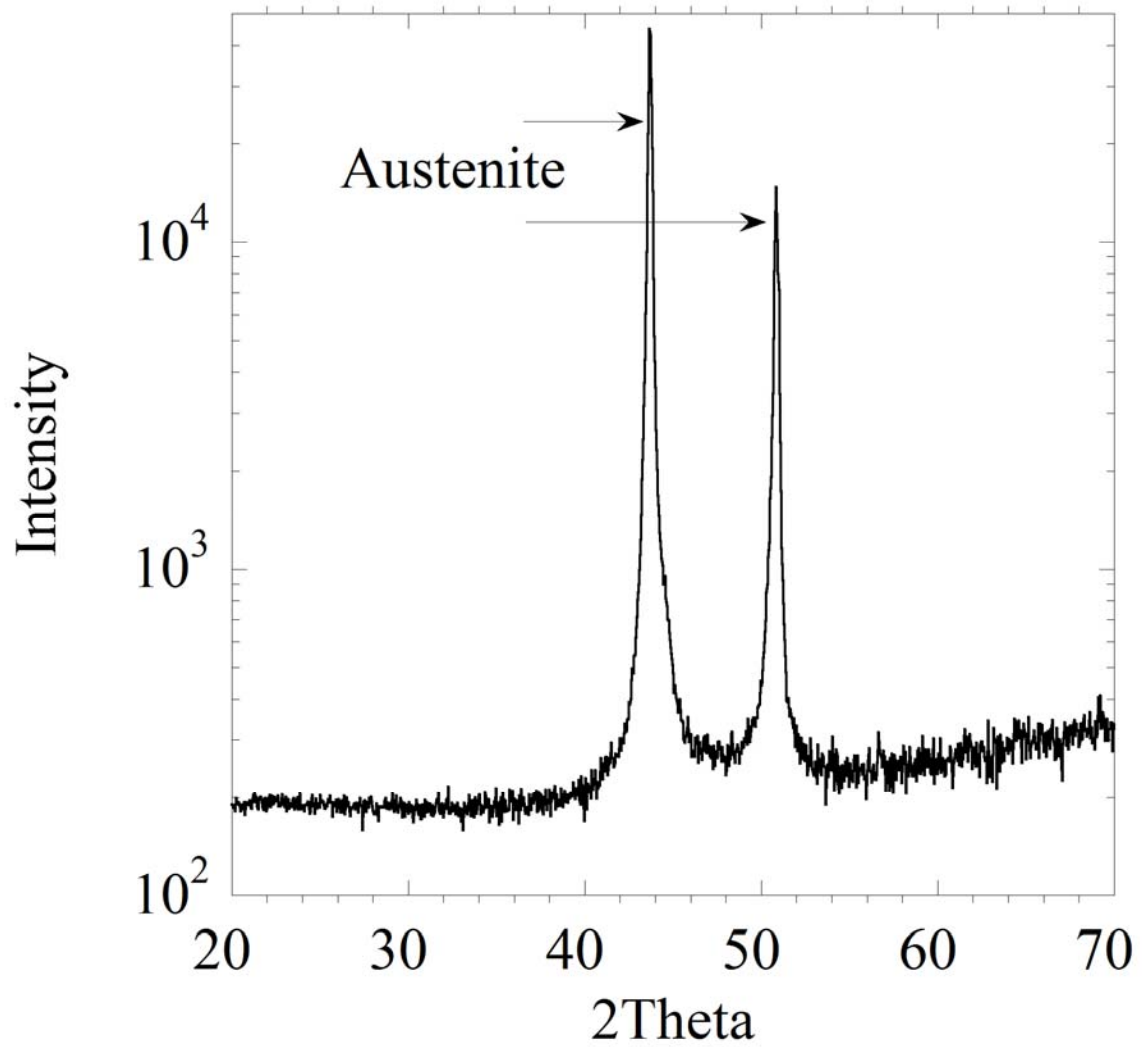
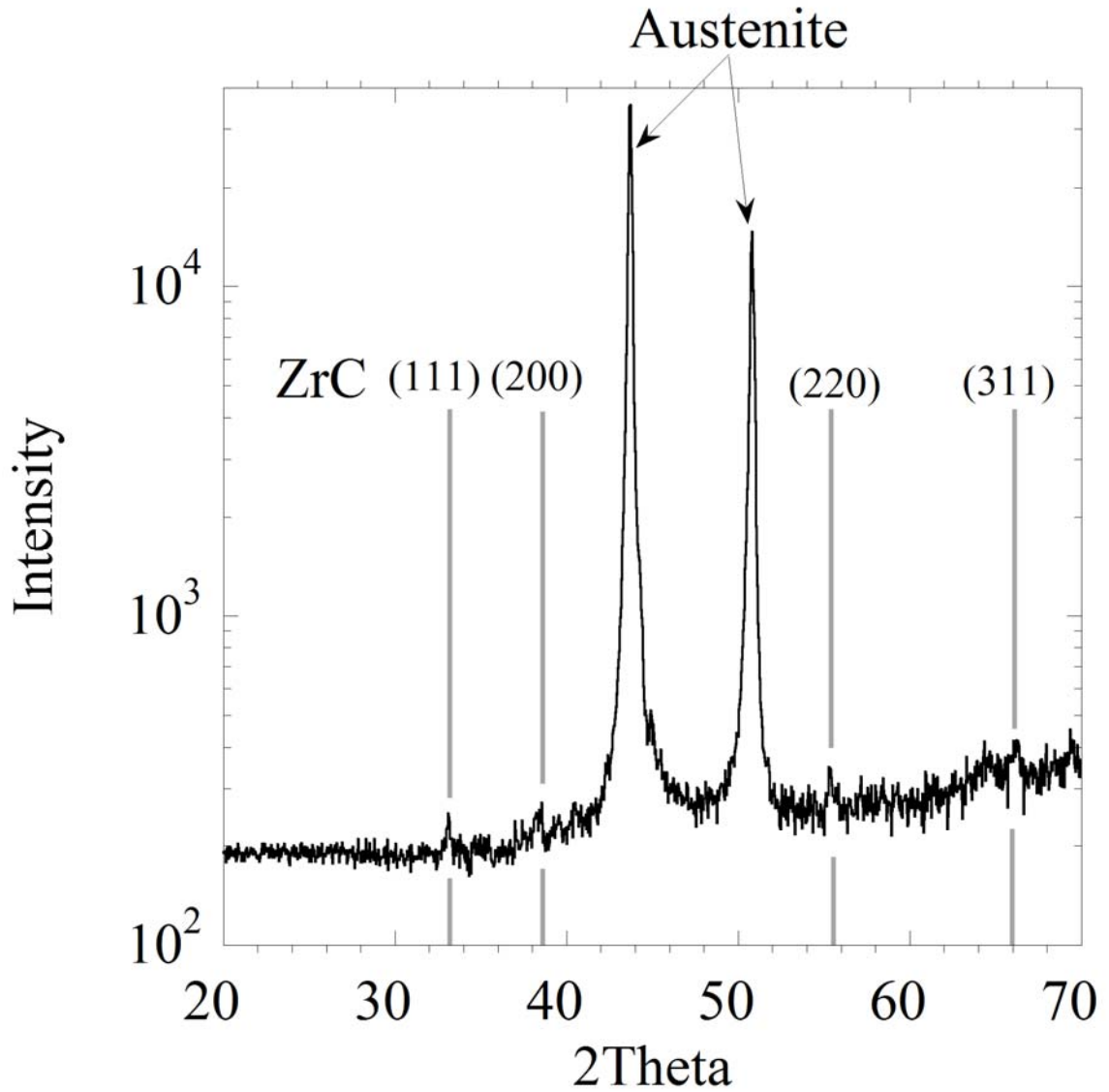Figure 5.22 XRD pattern for Ref-Zr showing intensity as a function of 2θ, scanned from 2θ = 20 - 70°. The peaks for austenite are highlighted by arrows.
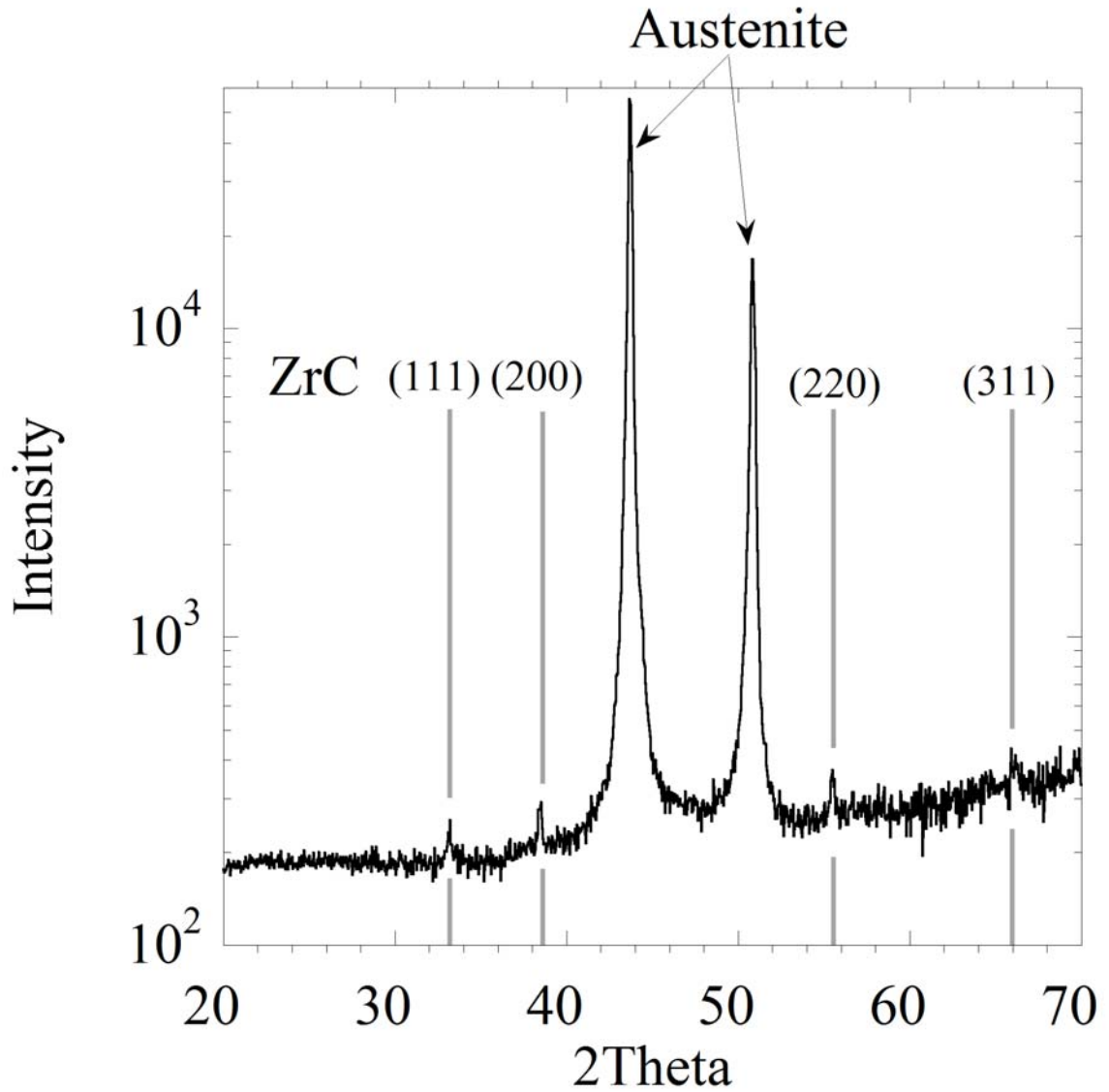
Figure 5.23 XRD pattern for LoZr showing intensity as a function of 2θ, scanned from 2θ = 20 - 70°. The peaks for austenite are highlighted by arrows. The gray lines represent the most strongly diffracting (highest intensity) 2θ angles for ZrC in this 2θ range and include the (hkl) planes for each line.

Figure 5.24 XRD pattern for HiZr showing intensity as a function of 2θ, scanned from 2θ = 20 - 70°. The peaks for austenite are highlighted by arrows. The gray lines represent the most strongly diffracting (highest intensity) 2θ angles for ZrC in this 2θ range and include the (hkl) planes for each line.
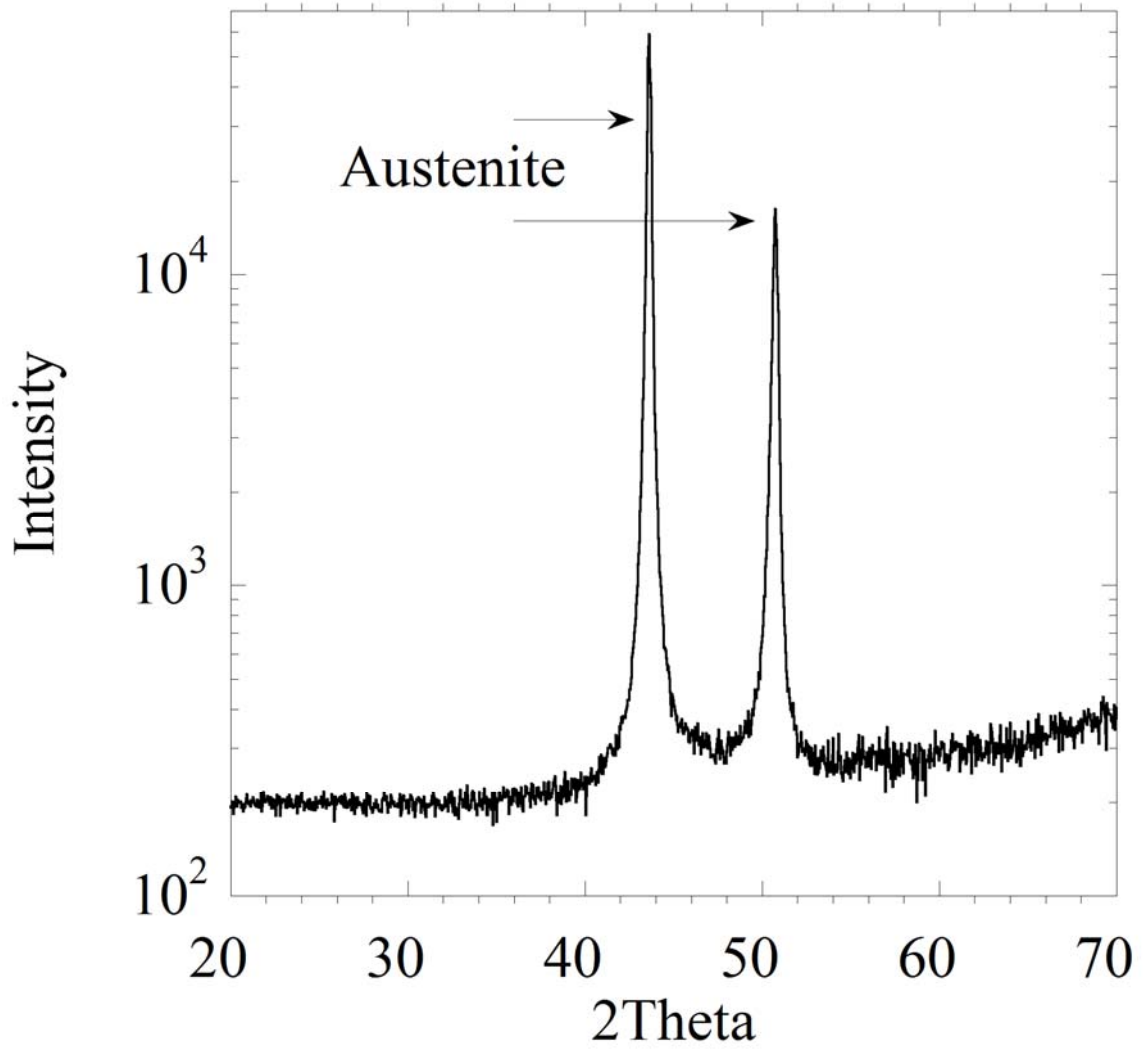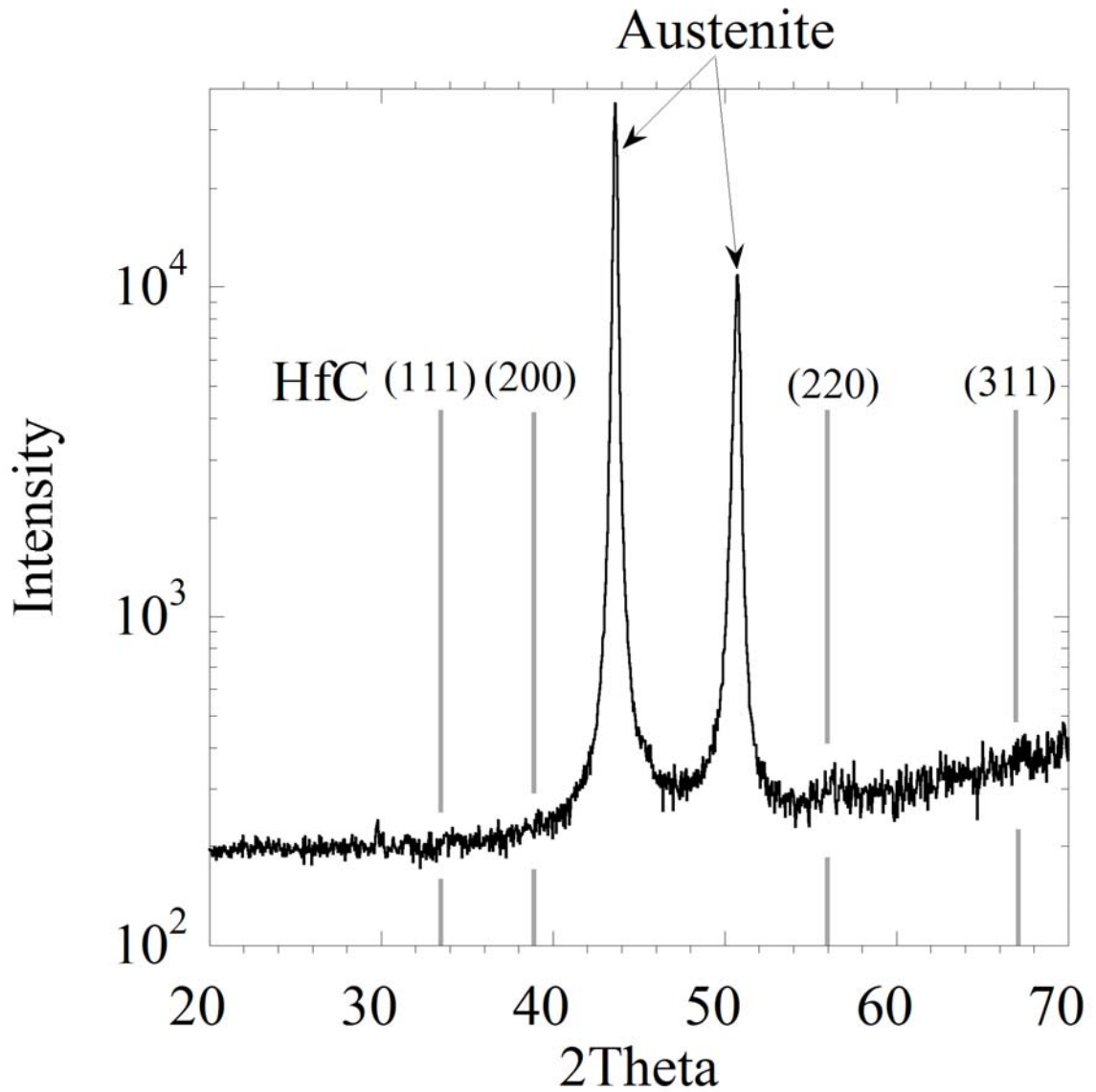
Figure 5.25 XRD pattern for Ref-Zr showing intensity as a function of 2θ, scanned from 2θ = 20 - 70°. The peaks for austenite are highlighted by arrows.

Figure 5.26 XRD pattern for LoHf showing intensity as a function of 2θ, scanned from 2θ = 20 - 70°. The peaks for austenite are highlighted by arrows. The gray lines represent the most strongly diffracting (highest intensity) 2θ angles for HfC in this 2θ range and include the (hkl) planes for each line. Note that these lines do not correspond to any diffraction peaks, meaning that no HfC was identified.
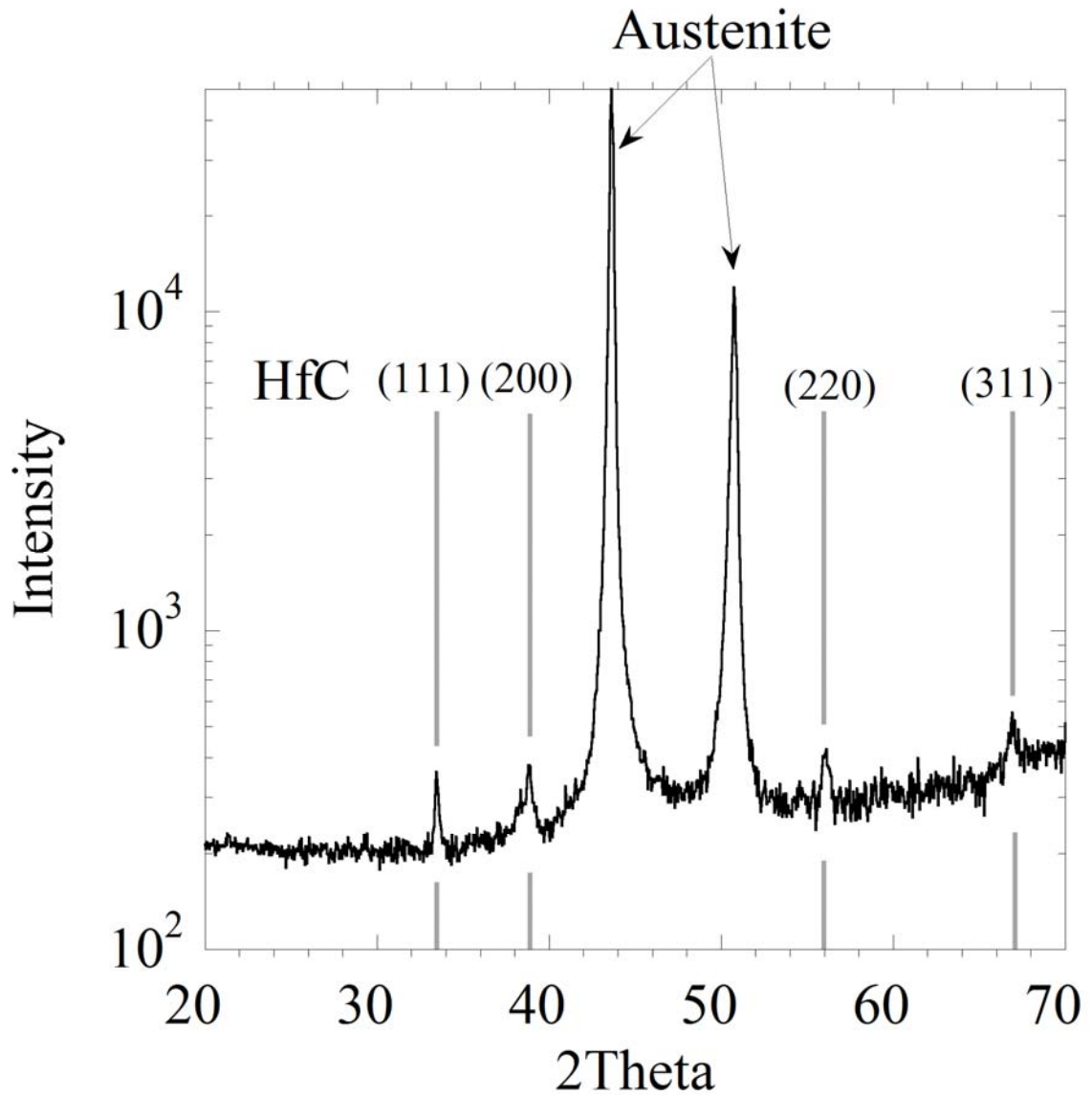
Figure 5.27 XRD pattern for HiHf showing intensity as a function of 2θ, scanned from 2θ = 20 - 70°. The peaks for austenite are highlighted by arrows. The gray lines represent the most strongly diffracting (highest intensity) 2θ angles for HfC in this 2θ range and include the (hkl) planes for each line.